

**Flutter Stabilization of Long Span  
Suspension Bridges with Slender Deck  
–Study on the Improvement of Aerodynamic Properties from  
Unsteady Pressure Characteristics Point of View–**

**Robby Permata**

**2014**



# Abstract

As the bridge spans getting longer, the structure becoming more flexible and new concept of structure and element are needed to face the new challenges. The history of development of long span suspension bridges shows an endless conflict between economy and structural performance constraint, in which aerodynamic stability concern plays major role. This field of study is relatively new and still developing as the need for longer bridges are increasing. Flutter is one of the major aerodynamic instability phenomena that need special attention, since it can lead to total collapse of the bridge.

Aerodynamic derivatives are the only aerodynamic properties that need to be measured experimentally in order to understand flutter stability of bridge deck sections. However, aerodynamic derivatives do not provide any information about flow field around body. Therefore, the physical explanation behind the aerodynamic performance of deck sections cannot be obtained. Moreover, it is hard to improve stability of any deck based on aerodynamic derivatives only without trial and error experiment, since each countermeasures give different effects to the aerodynamic properties of the deck.

Surface pressure distribution on the body in wind flow is important for the study of aerodynamic stability. Each aero-elastic phenomenon has unique mechanism that directly related with flow field around the body. Pressure distribution information can give more comprehensive understanding about the physical process behind destabilization or stabilization of the body. Aerodynamic derivatives can also be expressed with unsteady pressure of the deck, since the total lift and moment are integration of surface pressure along the width. Therefore, it is logical that efforts to find more stable bridge deck started from unsteady pressure point of view.

In this research, rectangular prism cross section with side ratio  $B/D=20$  is used as basic section. Slots and porous cavities are used as countermeasures with consideration of unsteady pressure distribution of basic section. The results show that slots with proper arrangement and size can produce deck with superior performance for flutter stability, but improper arrangement of slots can lead to unstable bridge deck. Therefore, fairings and winglets are studied as additional countermeasures to assure flutter stability of deck with slot.

It was concluded that slender bridge deck with double slot and winglets can be proposed as alternative for future long span bridge deck. The unsteady pressure characteristics data of several alternatives from experiments also presented to explain the process behind the aerodynamic performance for each section.





# Contents

Chapter 1 Introduction .....	I - 1
1.1 Motivation.....	I - 1
1.2 Problems Statement and Approach .....	I - 2
1.3 Overall Organization of Dissertation .....	I - 3
Bibliography .....	I - 5
Chapter 2 General Background.....	II - 1
2.1 Development of Long Span Bridges.....	II - 1
2.1.1 Suspension Bridges .....	II - 1
2.1.2 Cable-stayed Bridges.....	II - 5
2.2 Aero-elastic Problems in Long Span Bridges.....	II - 6
2.3 Flutter Instability in Long Span Bridge Decks .....	II - 11
2.3.1 Mathematical Model of Flutter and Aerodynamic Derivatives .....	II - 11
2.3.2 Obtaining Aerodynamic Derivatives.....	II - 14
2.3.3 Unsteady Pressure Characteristics .....	II - 16
2.4 Concluding Remarks.....	II - 21
Bibliography .....	II - 23
Chapter 3 Overview of Flutter Analysis and Stabilization for Long Span Bridge Deck... III - 1	III - 1
3.1 Analysis Method for Flutter Stability Problem of Bridge Deck .....	III - 1
3.1.1 Complex Eigenvalue (CEV) Analysis.....	III - 5
3.1.2 Step-by-step (SBS) Analysis.....	III - 7
3.1.2.1 Torsional Branch .....	III - 8

3.1.2.2 Heaving Branch .....	III - 17
3.1.3 Simplified Closed Form Formula: Selberg Formula.....	III - 29
3.2 Flutter Stabilization of Long Span Bridge Deck.....	III - 32
3.3 Concluding Remarks.....	III - 33
Bibliography .....	III - 34
Chapter 4 Effects of Double Slot and Porous Cavity to Unsteady Pressure Characteristics and Flutter Stability of Slender Rectangular Prism .....	IV - 1
4.1 Background.....	IV - 1
4.1.1 Double Slot.....	IV - 2
4.1.2 Porous Cavity .....	IV - 3
4.2 Description of Experiment and Models .....	IV - 3
4.3 Results: Unsteady Pressure Characteristics and Aerodynamic Derivatives .....	IV - 10
4.3.1 Unsteady Pressure Characteristics and Aerodynamic Derivatives of Prism with Double Slot.....	IV - 10
4.3.2 Unsteady Pressure Characteristics and Aerodynamic Derivatives of Prism with Porous Cavity .....	IV - 38
4.4 Results: Flutter Stability .....	IV - 59
4.5 Concluding Remarks.....	IV - 60
Bibliography .....	IV - 61
Chapter 5 Flutter Stabilization of Slender Bridge Deck Section Using Combination of Double Slot with Fairings and Winglets.....	V - 1
5.1 Background.....	V - 2
5.2 Description of Experiment and Models .....	V - 2
5.3 Results: Aerodynamic Derivatives and Unsteady Pressure Characteristics .....	V - 7
5.3.1 Comparison of Aerodynamic Derivatives from Pressure Measurement and Direct Force Measurement.....	V - 7

5.3.2 Aerodynamic Derivatives of Prism Using Combination of Double Slot with Fairings and Winglets.....	V - 13
5.3.3 Unsteady Pressure Characteristics of Prism Using Combination of Double Slot with Fairings and Winglets.....	V - 22
5.4 Results: Flutter Stability .....	V - 26
5.5 Concluding Remarks.....	V - 29
Bibliography .....	V - 31
Chapter 6 Feasibility of Using Slender Deck for Long Span Suspension Bridges.....	VI - 1
6.1 Problems of Slender Bridge Deck.....	VI - 1
6.2 Approach of Study .....	VI - 2
6.2.1 Analysis of Suspension Bridge .....	VI - 3
6.2.1.1 Theory of Cable .....	VI - 4
6.2.1.2 Theory of Suspension Bridge: Deflection Theory and Solution by Wollmann	VI - 4
6.2.1.3 Finite Element Model of Suspension Bridge.....	VI - 7
6.2.2 Live Load for Long Span Bridge .....	VI - 9
6.3 Results and Discussion .....	VI - 10
6.3.1 Weight of Steel Deck and Main Cable .....	VI - 10
6.3.2 Stress and Deflection at Mid-span due to Live Load .....	VI - 11
6.3.3 Structural Dynamic Properties.....	VI - 12
6.3.4 Frequency Ratio of Long Span Suspension Bridge Using Slotted Deck .....	VI - 14
6.4 Concluding Remarks.....	VI - 15
Bibliography .....	VI - 16
Chapter 7 Concluding Remarks .....	VII - 1

Appendix A Cross Section of Deck for Long Span Suspension Bridges .....A - 1

Appendix B Scientific Production .....A - 1

# Acknowledgements

The idea of studying bridge aerodynamics as research for higher degree started when I was in my first bridge project. But, at that time I never thought of coming to Japan and get a chance of becoming a PhD student in one of the leading national university. I would not able to ‘survive’ without help and support from many people, and I would like to express my gratitude for everything.

Before coming to Japan, I had great support from my superior in Indonesia: Mr. Jodi Firmansjah, PhD and Ms. Arvila Delitriana at PT. Cipta Graha Abadi, who taught me everything about bridge engineering and encouraged me to pursue PhD degree. I received recommendation letters from Prof. Amrinsyah Nasution (my supervisor in master course), and Ms. Puti Farida Marzuki, PhD (Dean of Civil Engineering and Planning Faculty at Institut Teknologi Bandung).

Prof. Hiromichi Shirato gave me warm welcome to the Bridge Engineering Laboratory – Kyoto University. He not just guided me in my research, but also helped me in many ways that made me feel comfortable in my early days as PhD student and foreigner in Japan. I also very much appreciate his understanding when I faced several hard times: my wife get hospitalized before the birth of my son, my son get hospitalized 3 times, my dad passed away, and when I have to continue finishing my thesis in Indonesia. Those are times when I could not focus on my research, and Prof. Shirato’s willing to help is essential so I can continue and finish my research. Thank you very much for everything.

I also say thank you very much for other senseis in Kyoto University: Hiroshi Hattori, PhD, who helped me so much in taking care of administration problems when I arrived in Japan; Prof. Tomomi Yagi, who gave me many valuable input in my research and thesis; Prof. Toyoaki Miyagawa from Structural Material Engineering laboratory, for the comments and questions to the draft of my thesis.

Thank you to the students of Bridge Engineering Laboratory, who helped me in using the wind tunnel facilities. Especially for the flutter team: Hong Jin Wuk and Kazuhide Yonamine; Mr. Shinjo, Mr. Zam and Mr. Hafidz for helping me in the final stage of my experiments; Mr. Yasuaki Ito for always be there when I had questions; senpai Mr. Cristiano Trein who helped me to understand the basic concept of unsteady pressure characteristics. It is a great experience to become part of the big family of Bridge Engineering Lab. member. Also for Mr. Miyasaka who helped me in preparing the model for my experiment; and Ms. Soda for helping me dealing with administration in the campus.

Also thank you for Indonesian students: members of PPI Kyoto and PPI Kobe, who made me feel like home.

Last but surely not least, I would like to thank my family: my wife and son, who always give me joy and happiness, also for the understanding and patience during the hard times in our stay in Japan; my family in Indonesia in for the continuous support. Finally to my parents, my mom and my late dad: this is for you.

# Chapter 1

## Introduction

### 1.1 Motivation

The history of development of long span suspension bridges shows an endless conflict between economy and structural performance constraint, as described by Kawada (2010). The use of deflection theory, which allows very slender deck for static load, shifted the design trend at that time from rigid truss to slender edge girder deck and led to Tacoma Narrows Bridge (853 m) disaster in 1940 (Buonopane & Billington, 1993). This event had raised awareness of bridge aerodynamic subject, and wind-structure interaction, especially flutter instability, had been an important topic for research in bridge engineering since then.

Tacoma Narrow Bridge underwent unstable oscillation that later known as torsional flutter. Researchers and engineers learned from that event, and managed to overcome torsional flutter for the next generation of long span bridges. Scott (2001) and Kawada (2010) summarized the efforts in building long span bridges after Tacoma Narrow Bridge disaster. In general, there are two approach to prevent flutter instability: modifying aerodynamic properties of deck and modifying dynamic properties of the whole bridge structure.

As the length of main span increased, the effects of deck stiffness become less significant to the total stiffness of the suspension bridge. In the case of super long span suspension bridges (main span more than 2000 m), deck element acts as element to collect live loads and distribute them to hangers. Cable becomes the predominant structural element, therefore the overall behavior of the bridge is significantly influenced by it. In this condition, modifying deck shape or structural configuration for improving stiffness is not effective for flutter stabilization. Related issues are (Brancaleoni *et al.*, 2010):

#### 1. Cable self weight

Cable element becomes the heaviest and most expensive structural part for suspension bridges with main span more than 2500 m. Therefore, minimizing the size of cable is the main concern for super long span suspension bridge. One way to achieve that is by minimizing the weight of the deck by using slender section. Use of heavy truss deck like in Akashi Kaikyo Bridge (1991 m) is not feasible in this case. Another way is by increasing the strength of cable element, or by selecting proper sag ratio.

#### 2. Dynamic properties

In the case of super long span bridges with slender deck, the behavior of the overall bridge is becoming more like stand alone cable element. Heaving and torsional mode shape of the deck are simply in-phase and out-of-phase motion of the main cable. It means that the

torsional frequency becomes lower, and frequency ratio between torsional and heaving mode shape approaches unity ( $f_\phi/f_\eta \rightarrow 1$ ). This is an unfavorable condition for flutter instability.

Based on these conditions, feasible deck for super long span suspension bridges must have the following properties:

1. Slender cross section, so the weight is kept relatively low.
2. Superior aerodynamic properties, so flutter instability is avoided even for low torsional frequency and frequency ratio almost 1.

Many researchers already proposed alternatives for deck of super long span suspension bridges, such as:

1. Messina Bridge team: Brancaleoni *et al.*, 2010.
2. Japanese researchers for future super long span bridges in Japan: Sato *et al.*, 2002; Tokoro *et al.*, 2002.
3. Chinese researchers, for Xihoumen Bridge, Runyang Bridge and study for suspension bridge with main span 5000 m: Ge & Xiang, 2009.
4. Some of the proposed deck section are summarized in Matsumoto *et al.* (2007).

The latest development is utilizing wide slot or gap to produce multi box girder as for Messina Bridge or twin box girder as for Xihoumen Bridge and future long super long span bridge in Japan. Box girder with wide slot raises another concern related to cost of the bridge. The wide slot, which its width can be more than 30% or more of total width of the deck, gives the total cost of the bridge more expensive. Sato *et al.* (1994) and Yoneda *et al.* (1996) studied aerodynamic performance of box girder with various position and size of slot. The results showed that aerodynamic performance is very sensitive to the size and position of the slot. Improper size or position of the slot might result in more unstable deck.

This study attempts to study alternatives of slender deck for future super long span bridges. The focus is study the aerodynamic derivatives and unsteady pressure characteristics of deck with countermeasures and tracing the effects of countermeasures to suppress flutter instability.

## 1.2 Problems Statement and Approach

Based on brief explanation above, questions for more stable slender deck for super long span suspension bridge are straightforward:

1. In the case of box girder with slot, what are the physical processes behind stabilization or destabilization of deck? By knowing the physical processes involved, further study for developing more stable bridge deck is possible in more rational way instead of trial and error using series of wind tunnel tests.
2. What are another deck shapes or aerodynamic countermeasures that produce superior aerodynamic properties and cheaper than wide slot box girder?
3. What are the effects of wider or narrower deck to the structural properties of the whole bridge?



Rectangular prism with B/D=20 is selected as basic section for studying countermeasures to achieve more stable deck. The reasons are:

1. This section is considered as very slender, therefore it suits the slenderness criteria for future super long span suspension bridge.
2. This section has similar aerodynamic properties with thin plate, which its aerodynamic derivatives can be calculated analytically using Theodorsen formula. Also this section is prone to coupled flutter instability at relatively low reduced wind velocity, which is the same problem for traditional single box girder deck. Therefore it is an ideal section as a starting point.

Several tests and analysis will be performed to answer the questions in problem statement above:

1. Analysis of proposed countermeasures

Unsteady surface pressure will be measured to obtain unsteady pressure characteristics: amplitude of unsteady pressure  $\tilde{C}_p(x^*)$  and phase difference  $\psi(x^*)$ . The physical processes of flow around deck could be analyzed by knowing these parameters, instead of focusing only to aerodynamic derivatives. Many studies has been published about this approach. Matsumoto (1996) can be said as the pioneer of using unsteady pressure characteristics to explain aerodynamic instability. His work explained aerodynamic properties of rectangular section with B/D from 1 to 20. Matsumoto *et al.* (2004) explained how unsteady pressure characteristics can be used to explain flutter stability of proposed deck section for future super long span bridge in Japan, that is rectangular prism with fairings, central wide slot and central vertical plate. Trein & Shirato (2011) developed optimum distribution of amplitude of unsteady pressure  $\tilde{C}_p(x^*)$  and phase difference  $\psi(x^*)$  along bridge deck width to produce superior aerodynamic properties.

2. Effects of deck geometry to structural parameters

Many studies about flutter stabilization by modifying aerodynamic properties of deck used the same structural/dynamics parameters (mass, stiffness and therefore frequency). So the effectiveness of the countermeasures can be evaluated by using flutter stability index, that is the ratio between critical reduced velocity of the deck and critical reduced velocity of thin plate or  $U_{r\ cr\ model}/U_{r\ cr\ thin\ plate}$ . This approach is sufficient as long as the deck being investigated have comparable size and weight, but it will be inaccurate if the models have different size or width and weight. In the case of deck section with slot, different size and position of slot influence the value of structural dynamic parameters. Therefore, the structural parameter data will be obtained from finite element modelling with member size being designed properly.

### **1.3 Overall Organization of Dissertation**

This thesis is divided into six chapters:

Chapter 1 Introduction → background and scope of this thesis is introduced.

Chapter 2 *General Background* → development of long span bridges is explained, along with aero-elastic phenomena that govern the design with focus on flutter instability

Chapter 3 *Overview of Flutter Analysis and Stabilization of Long Span Bridge Deck* → include detail explanation about flutter instability and several analytical method to solve flutter problem, and summary of stabilization proposed or used by researchers and engineers.

Chapter 4 *Effects of Double Slot and Porous Cavity to Unsteady Pressure Characteristics and Flutter Stability of Slender Rectangular Prism* → flutter stabilization or destabilization by using slots and porous cavities are studied from unsteady pressure characteristics point of view.

Chapter 5 *Flutter Stabilization of Slender Rectangular Prism Using Combination of Double Slot with Fairings and Winglets* → this chapter is continuation from chapter 4, where additional countermeasures (fairings and winglets) are used in order to obtain more stable deck section.

Chapter 6 *Feasibility of Using Slender Deck for Long Span Suspension Bridges* → the applicability of slender deck under gravity load are studied, along with the effects of position of slot to dynamic properties of structures .

## Bibliography

- Brancaleoni, F., Diana, G., Faccioli, E., Fiammenghi, G., Firth, I. P. T., Gimsing, N. J., Jamiolkowski, M., Sluszkza, P., Solari, G., Valensise, G., and Vullo, E. (2010) *'The Messina Strait Bridge : a challenge and a dream'*, CRC Press.
- Buonopane, S. G., and Billington, D. (1993) 'Theory and history of suspension bridge design from 1823 to 1940', *Journal of Structural Engineering*, 119(3), pp. 954-977.
- Ge, Y. J., Xiang, H. F. (2009) 'Aerodynamic stabilization for box-girder suspension bridges with super-long span', *EACWE 5*, Florence, Italy, July 19-23 2009.
- Kawada, T. (2010) *'History of the modern suspension bridges : solving the dilemma between economy and stiffness'*, ASCE Press.
- Matsumoto, M. (1996) 'Aerodynamic damping of prisms', *Journal of Wind Engineering and Industrial Aerodynamics*, 59, pp. 159-175.
- Matsumoto, M., Shijo, R., Eguchi, A., Hikida, T., Tamaki, H., Mizuno, K. (2004) 'On the flutter characteristics of separated two box girders', *Wind and Structures – An International Journal*, 7 (4), pp. 281-291.
- Matsumoto, M., Mizuno, K., Okubo, K., Ito, Y., and Matsumiya, H. (2007) 'Flutter instability and recent development in stabilization of structures', *Journal of Wind Engineering and Industrial Aerodynamics*, 95, pp. 888-907.
- Sato, H., Toriumi, R., Sekiya, M., Watanabe., S. (1994), 'Study on Aerodynamic Stability of Super Long-span Bridge', *Proceeding of 13<sup>th</sup> National Symposium on Wind Engineering, Japan Association for Wind Engineering*, pp. 419-424 (in Japanese).
- Sato, H., Hirahara, N., Fumoto, K., Hirano, S., and Kusuhara, S. (2002) 'Full aeroelastic model test of a super long-span bridge with slotted box girder', *Journal of Wind Engineering and Industrial Aerodynamics*, 90, pp. 2023-2032.
- Scott, R. (2001) *'In the wake of Tacoma bridge : suspension bridges and the quest for aerodynamic stability'*, ASCE Press.
- Tokoro, S., Honda, A., Masuda, I., Nakashima, Y., Murakoshi, J., Fumoto, K. (2002), 'Aerodynamic Improvement of One Box Girder for Super Long Suspension Bridge', *The 2<sup>nd</sup> International Symposium on Wind and Structures*, Busan, Korea, August 21-23 2002, pp. 235-242.
- Trein, C. A., Shirato, H. (2011) 'Coupled flutter stability from unsteady pressure characteristics point of view', *Journal of Wind Engineering and Industrial Aerodynamics*, 99 (2), pp. 114-122.
- Yoneda, M., Ohno, K., Tamaki, Y., Kimura., K., Miyachi, S. (1996), 'On aerodynamic stability of a 2500m class streamlined box girder suspension bridge with open spaces or open gratings of bridge deck', *Proceeding of 14<sup>th</sup> National Symposium on Wind Engineering, Japan Association for Wind Engineering*, pp. 401-406 (in Japanese).



# Chapter 2

## General Background

### 2.1 Development of Long Span Bridges

The term ‘long span’ for bridges has relative standard around the world. For some countries, main span more than 200 m is considered as ‘long span’, while main span of 500 m is still considered as ‘moderate’ in other countries. Nevertheless, cable supported bridge type (cable-stayed bridge and suspension bridge) are accepted worldwide as common solution for long span bridges, especially for span with more than 1000 m where other types are not feasible or even technically not possible. The current longest span for several type of long span bridges are shown in Fig. 2.1.

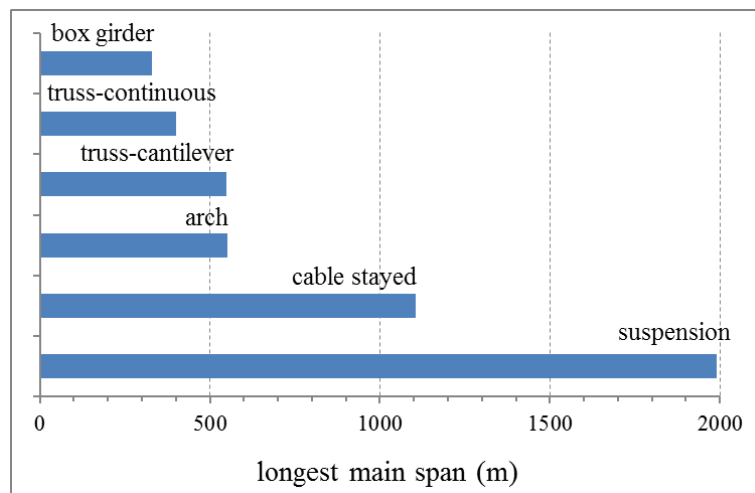


Fig. 2.1 Longest span for different bridge type

#### 2.1.1 Suspension Bridges

Carrying load by utilizing suspended rope had been used since ancient time. This is the basic concept for suspension bridges, and its history for traffic to connect islands started in 1826 when Menai Bridge (176 m) in UK was opened. Menai Bridge used chain as supporting element. Wire cable was used later in Grand Pond Suspendu (273 m, completed in 1834) in Swiss. Menai Bridge later suffered excessive vertical vibration due to cross wind flow, and repair works were needed. British engineers suggested use of stiffening truss to avoid this vibration (Buonopane & Billington, 1993).

The next major milestone for suspension bridge was the construction of Wheeling Bridge (308 m, completed in 1849) in US. Although wind-related problems to long span bridges had been recognized at that time, but engineers still did not take it as critical aspect. Original Wheeling Bridge used shallow deck that did not provide enough stiffness and it failed under windstorm in 1854. Many suspension bridges built in 19<sup>th</sup> century suffered from damages or even collapsed especially due to strong wind (Scott, 2001). These events led to judgment that suspension bridges were risky and unreliable. Improvements were made by engineers and then using stiffening girder became a common practice.

The opening of Brooklyn Bridge (486 m) in 1883 was the starting point for large scale suspension bridge construction industry. This bridge employs stay cables as additional stiffener, resulting more rigid deck with high redundant structures that was hard to be analyzed at that time. This idea concept already applied for Niagara Falls Bridge (251 m, completed in 1855). Next generation of suspension bridges used deep rigid truss instead of additional stay cables to provide stiffness and stability. This type of structure could be analyzed at that time using linear theory. Advance analysis method, deflection theory, was introduced in practical use for Manhattan Bridge (448 m, completed in 1909). This analysis takes into account the nonlinear elastic effect related to the displacement of cable due to live load, thus bending moments in deck are reduced significantly (Gimsing & Georgakis, 2011).

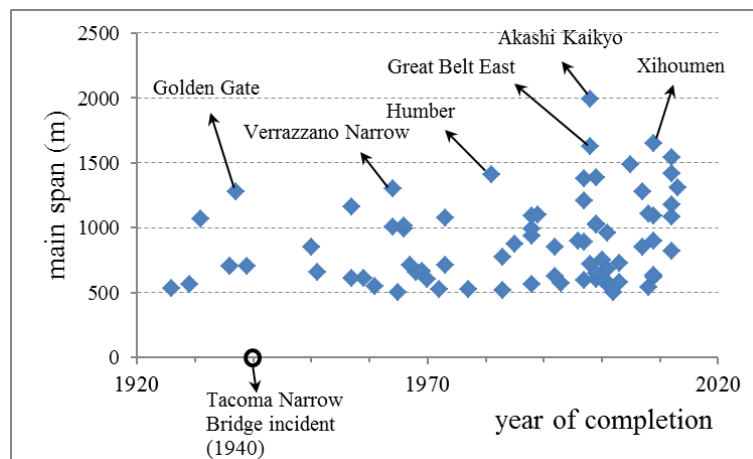


Fig. 2.2 Development of long span suspension bridges (main span > 500 m)

In the early 20<sup>th</sup> century, only modest improvement achieved in suspension bridges construction. The golden era of suspension bridges in US started in 1930s, with the opening of George Washington Bridge (1067 m) in 1931 and Golden Gate Bridge (1280 m) in 1937. Another improvement of analysis also achieved when deflection theory was applied to analyze suspension bridge under lateral load. This led to use of more slender bridge deck, and unfortunately contributed to the collapse of Tacoma Narrow Bridge (853 m) in 1940.

Tacoma Narrow Bridge was designed to resist static wind load up to wind speed of 54 m/s, but it collapsed under 19 m/s wind after underwent divergent oscillations later known as torsional flutter. It was found that this phenomenon was related to the lack of stiffness of the bridge structure and poor aerodynamic properties of the deck. This event raised awareness to wind-structure interaction and aerodynamic behavior of long span bridge deck, and since then aerodynamic and aero-elastic analysis became important for long span bridge design.

Immediate response after this event was back to rigid truss deck and increase deck mass to increase stiffness of the bridge as used in New Tacoma Narrow Bridge (completed in 1950). Strengthening and retrofitting works also carried out for several other bridges that already had been built.

Rigid truss deck dominated the suspension bridge designs in 1950-1960. In 1960s, new trend for suspension started in UK when Severn bridge (988 m) was completed in 1966. This bridge has slender streamlined box girder deck, and diagonal hangers instead of traditional vertical ones. Its slender and light deck brought significant cost reduction compared to US-style designs. Other bridges in Europe such as First Bosphorus bridge (1074 m, completed in 1973) and Humber Bridge (1410 m, completed in 1981) followed Severn Bridge design. However, later in 1980s, Severn Bridge started to suffer from structural problems due to wind induced vibration of its diagonal hangers. The repairing cost 2.5 times its construction cost. Based on experiences from this event, next generation of suspension bridges still adopted streamlined slender box girder but abandoned the diagonal hangers and use heavier deck to add mass and consequently, stiffness (Kawada, 2010).

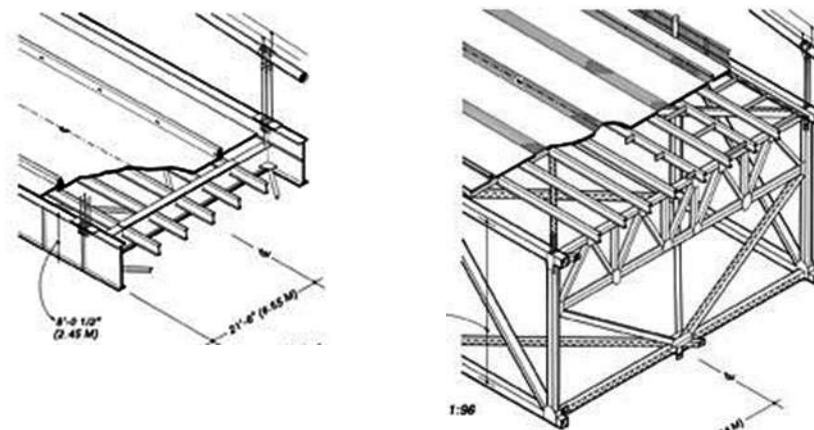


Fig. 2.3 Comparison of original (left) and new (right) deck of Tacoma Narrow Bridge

Next significant leap came when Akashi Kaikyo and Great Belt East (1624 m) were completed in 1998. These bridges represented the latest development of US-style rigid truss deck (Akashi Kaikyo) and UK-style streamlined slender box girder (Great Belt East) at that time. Akashi Kaikyo uses high tensile strength wire of 1800 MPa (significant development from previous record of 1600 MPa) so excessive size and amount of main cables can be avoided (Kitagawa, 2004).

Several problems were also noticed in these bridges:

1. Based on full model wind tunnel test, large lateral deflection of Akashi Kaikyo was found under static wind load, equivalent to prototype scale about 30 m with  $4^0$  torsional displacement at 74 m/s wind speed (Miyata & Yamaguchi, 1993). This was due to high value of drag force coefficient which is typical problem for deep truss deck.

- Great Belt East experienced vortex-induced vibration or VIV, and guide vanes were installed to suppress this oscillation (Larsen *et al.*, 2000).

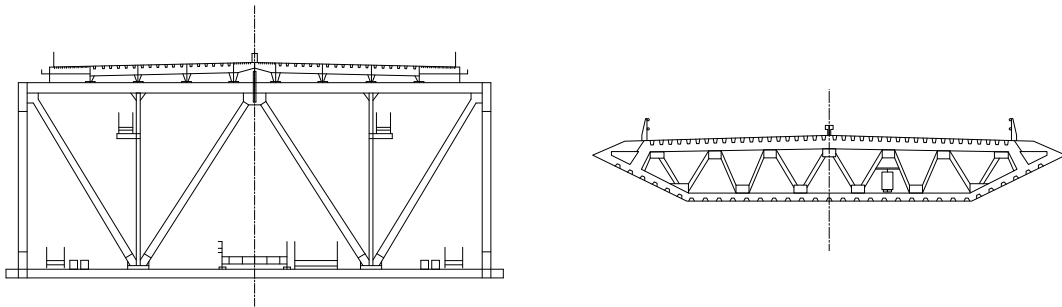


Fig. 2.4 Deck section of Akashi Kaikyo Bridge (left) and Great Belt East Bridge (right)

Akashi Kaikyo and Great Belt East are considered as the limit span for each type. Rigid truss deck is not applicable for span longer than 2000 m due to its heavy self-weight. Streamlined box girder has good aerodynamic properties, but not excellent. Application of this deck to longer span will result relatively low performance against coupled flutter instability. Thus, new type of deck is required to fulfill the need of future long span bridges. One proposed solution is using multi box girder or slotted box girder as used in design of Messina Bridge (3300 m). Another type of slotted box girder is center-slotted box girder or twin box girder. This concept is used in Xihoumen Bridge (1650 m, completed in 2009). Modification of twin box girder with additional countermeasures such as vertical plate at the center and horizontal plates also proposed by other researchers for future super long span suspension bridges in Japan with main span 2000-3000 m (Sato *et al.*, 2002; Ueda *et al.*, 1998). Streamlined box girder can also be modified by adding vertical central stabilizer to improve its aerodynamic properties without using any slot, as used in Runyang Bridge (1490 m, completed in 2005). Runyang Bridge is the longest single box girder bridge now, and also has largest side ratio with  $B/D=12$  (B: deck width, D: deck depth). Intensive studies also carried out by Japanese researchers to improve aerodynamic properties of single box girder with narrow slot (Tokoro *et al.*, 2002).

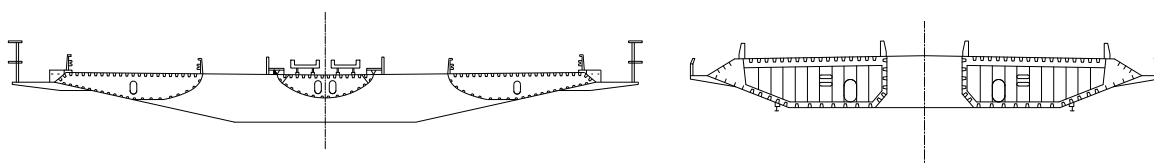


Fig. 2.5 Deck section of Messina Bridge (left) and Xihoumen Bridge (right)

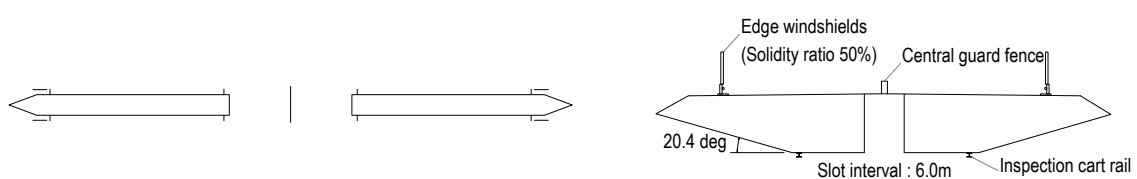


Fig. 2.6 Deck section of future super long span bridge in Japan (left) and narrow center-slotted deck proposed by Tokoro *et al.*, 2002 (right)



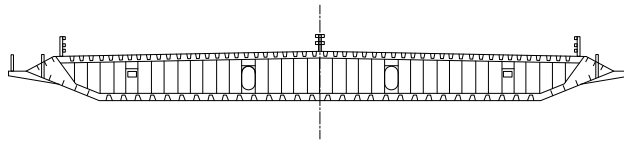


Fig. 2.7 Deck section of Runyang Bridge

Future suspension bridges will face the challenge of longer main span up to 5000 m. Several proposal of deck shape had been proposed for this need such as twin box girder with wide slot (Richardson, 1988; Brown, 1998; Ge & Xiang, 2009) and elliptical cross section (Astiz & Andersen, 1990; Matsumoto *et al.*, 1995). More detail explanation about shape of deck and countermeasures against aero-elastic phenomena are presented in Appendix A.

### 2.1.2 Cable-stayed Bridges

The main idea of cable-stayed bridge, that is supporting a bridge deck by inclined tension elements, had been known for centuries. The first permanent bridge using this concept is King Meadow Bridge in 1817. Like early suspension bridges, early examples of cable-stayed bridges in 19<sup>th</sup> century also suffered from damage and collapse (Svensson, 2012).

As mentioned earlier, engineers in the 19<sup>th</sup> century used this concept to provide additional stiffness of suspension bridges. This idea was not popular at that time due to limitation of analysis technique to solve high redundant structure problems. In 1950s, thank to the improvement of technique in structural analysis, this concept was applied to Stromsund Bridge (183 m, completed in 1956). Since then, cable-stayed bridges were popular for span about 200-400 m. Completion of St. Nazaire Bridge (404 m) in 1975 marked a further step as the first cable-stayed bridge with main span more than 400 m.

Further improvement of numerical calculation technique and increasing capability of computer to support numerical structural analysis code had great impact to development of modern cable-stayed bridges. Major milestone was construction of Normandy Bridge (856 m, completed in 1995). At the beginning of the new millennium, 1000 m main span limit was surpassed by Sutong Bridge (1088 m, completed in 2008), Stonecutter Bridge (1018 m, completed in 2009) and Russky Bridge (1104 m, completed in 2012).

Zhu *et al.* (2011), demonstrated that flutter stability of 1400 m cable-stayed bridge is very good with use of traditional streamlined single box girder and additional minor countermeasures. Ge & Xiang (2008) suggested that most dominant aerodynamic problem for long span cable-stayed bridge is not flutter stability or VIV of the deck, but wind induced vibration of stay cables . Another factor that have to be considered carefully is the limitation of length of stay cable element due to its self-weight (Clemente, 1998).

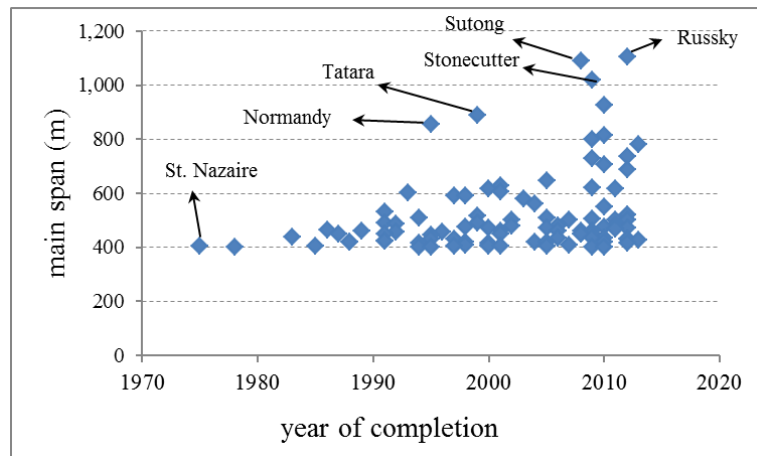


Fig. 2.8 Development of long span cable-stayed bridges (main span > 400 m)

## 2.2 Aero-elastic Problems in Long Span Bridges

From the brief history as explained in the previous section, it is clear that aerodynamic related problems are important subject and governing factor in the design of long span bridges. Future long span bridges with longer span, taller pylons and longer cable elements will be very flexible and sensitive when subjected to wind flows.

The term aero-elasticity is concerned with the interaction between fluid flow and solid body elastically suspended in the fluid. When the flow meets a bluff body such as bridge deck, the flow field around body generates the flow-induced forces and these forces excite the flow-induced vibrations. Moreover, these vibrations change the flow field and then generate new modified forces. These new forces then again excite modified flow-induced vibration and so on. Continuous interactions between flow field, forces and vibrations are known as aero-elastic phenomena.

Flow around body can be divided into 2 main categories: non-separated flow and separated flow. Non-separated flow mostly studied in aeronautic field because flow around airfoil section does not have separation. In this case, potential theory can be used to analyze aerodynamic forces. On the other hand, bluff body aerodynamics are characterized by separation of flow, flow reattachment and flow non-reattachment. The differences between airfoil (and thin plate) with bluff body aerodynamics are shown in Fig 2.9. Typical flow around bluff body with large side ratio or B/D (common case for long span bridge deck) is shown in Fig. 2.10. Understanding these aerodynamic phenomena is important as basic to study aero-elastic problems in long span bridges.

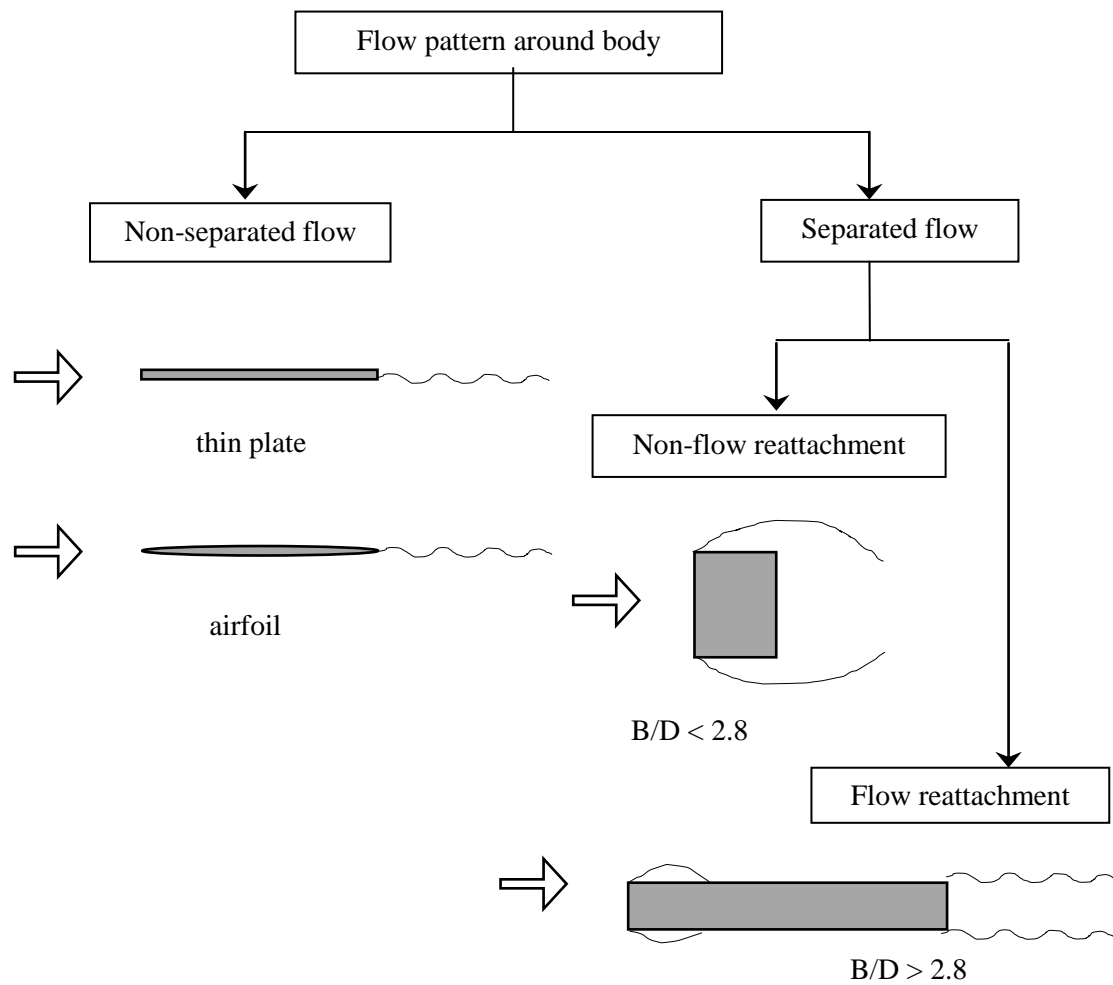


Fig. 2.9 Flow fields around bodies (reproduced from Matsumoto, 2000)

Aero-elastic phenomena can be classified by their origin and characteristics such as proposed by Naudascher & Rockwell (1994):

1. EIE: Extraneously-induced excitation, where vibration is generated by unsteadiness of oncoming flow such as turbulent and other type of time varying oncoming flow
2. IIE: Instability-induced excitation, where flow instability inherent to the flow created by the body under consideration such as excitation induced by Karman vortex.
3. MIE: Movement-induced excitation, where aerodynamic forces arising from the movement of the body such as galloping and flutter.

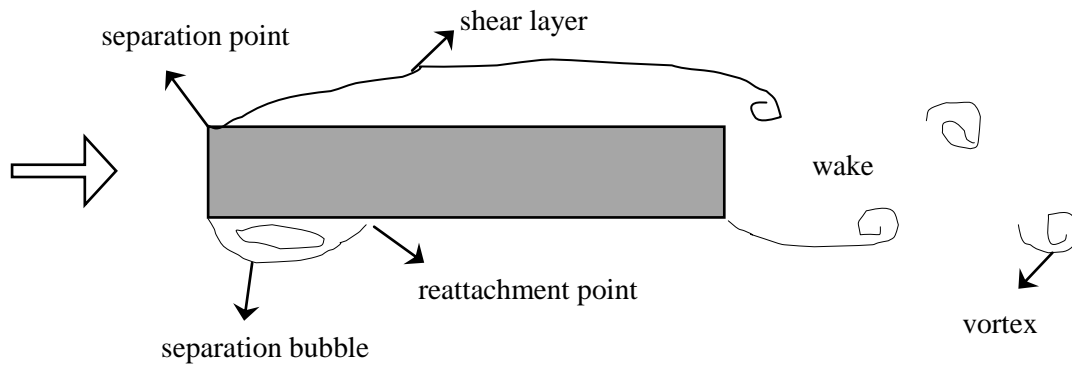


Fig. 2.10 Flow fields around bluff body with large side ratio or  $B/D$  (reproduced from Matsumoto, 2000)

The most popular aero-elastic phenomenon in long span bridges is flutter. This is attributed to the failure of Tacoma Narrow Bridge which demonstrated that flutter instability could lead to total collapse of the bridge deck. Flutter stability criteria is the main concern for design of long span bridges, and a dominant factor to assess feasibility of future super long span bridges. Other relevant aero-elastic phenomena for bridge engineering are vortex-induced vibration or VIV (IIE) and galloping (MIE). This thesis is focused on flutter stability of slender deck for long span bridges and also only deal with smooth flow, therefore EIE phenomena such as buffeting forces due to turbulent wind flow is not explained here.

Vortex-induced vibration or VIV is one of major issue in long span bridges. This vibration is self-limited and does not cause direct instability or failure to the structural element. It may cause fatigue damage and unacceptable vibration for serviceability of the bridges. In general, the mechanism of VIV may be explained as synchronization of frequency of vortex shedding with the natural frequency of the body. Detail explanation of the mechanism of VIV was reported by Shiraishi & Matsumoto (1983) and Deniz & Staubli (1997) whom found that certain type of VIV can also be classified as combination of IIE and MIE). This movement-induced VIV can be said as vibration phenomena due to separation of vortex at the leading edge is generated by the motion of the body itself and its growth up by amalgamating with another separation vortex at trailing edge. Development of mathematical model for analysis of VIV is also still an attractive topic for research, as reported by Mashnad & Jones (2013).

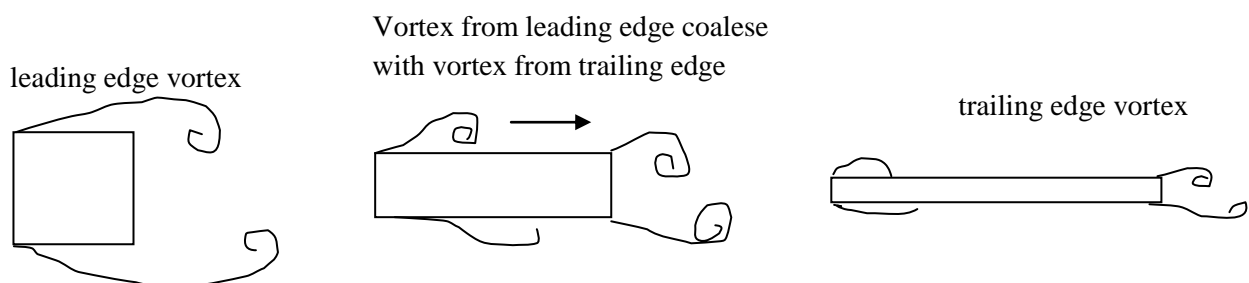


Fig. 2.11 Mechanism of various type of VIV

VIV mainly occurs on cable elements of the bridge, deck and pylon. VIV on cables usually has small amplitudes and can be suppressed by adding damper. The occurrence of VIV on deck along with its countermeasures had been reported in several bridges such as Kansai International Airport Access Bridge (Honda *et al.*, 1993), Great Belt East Bridge (Larsen *et al.*, 2000), Rio-Niteroi Bridge (Battista & Pfeil, 2000), Trans Tokyo Bay Bridge (Fujino & Yoshida, 2002), Second Severn Crossing Bridge (Macdonald *et al.*, 2002), Osteroy Bridge (Larsen & Poulin, 2005) and Volgograd Bridge (Weber & Maslanka, 2012). Most of VIV on pylon occurred during construction stage, where the pylons were still as free-standing structure. A rare case of along wind VIV on pylon of completed bridge was observed on Hakucho Bridge (Siringoringo & Fujino, 2012).

Galloping instability is a single-degree of freedom cross-flow divergent type vibration, therefore its stabilization is important for design of structural element. Galloping occurs when the direction of quasi-steady lift force corresponding to the relative angle of attack is identical with the direction of heaving vibration. Use of quasi-steady theory for galloping is based on assumption that period of oscillation is long compared to time taken for the flow to pass along the body. Based on Fig. 2.12, instability occurs when:

$$\frac{dF_y}{d\alpha} > 0 \quad (2.1)$$

or in other words, galloping instability occurs when lift force and heaving velocity has the same direction.

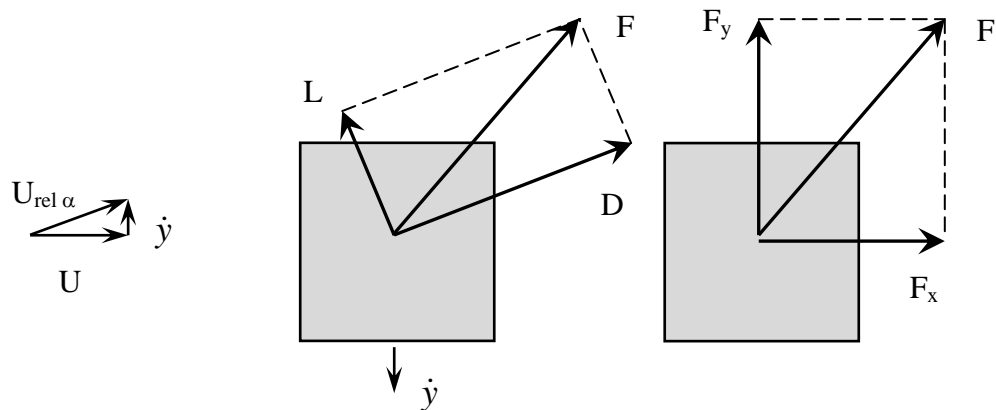


Fig. 2.12 Forces on a prism subjected to cross-flow  $U$  and undergoing transverse oscillation

From superposition and decomposition of forces in Fig. 2.12,  $F_y$  can be formulated as:

$$F_y = -L \cdot \cos \alpha - D \cdot \sin \alpha \quad (2.2)$$

Then:

$$\frac{dF_y}{d\alpha} = \left( L - \frac{dD}{d\alpha} \right) \sin \alpha + \left( -\frac{dL}{d\alpha} - D \right) \cos \alpha \quad (2.3)$$

By assuming  $\alpha$  is small, eq, (2.3) can be simplified as:

$$\frac{dF_y}{d\alpha} = -\left(\frac{dL}{d\alpha} + D\right) \quad (2.4)$$

Thus the criterion for galloping instability, also known as Den Hartog criterion is obtained:

$$\frac{dL}{d\alpha} + D < 0 \quad (2.5)$$

The physical process behind the same direction of heaving velocity and transverse lift force can be seen in Fig. 2.13. The inner circulatory flow on the lower surface of the body will produce large value of negative pressure (suction), while upper surface has lower value of negative surface pressure. Resultant of these pressures are downward transverse force or positive  $F_y$ .

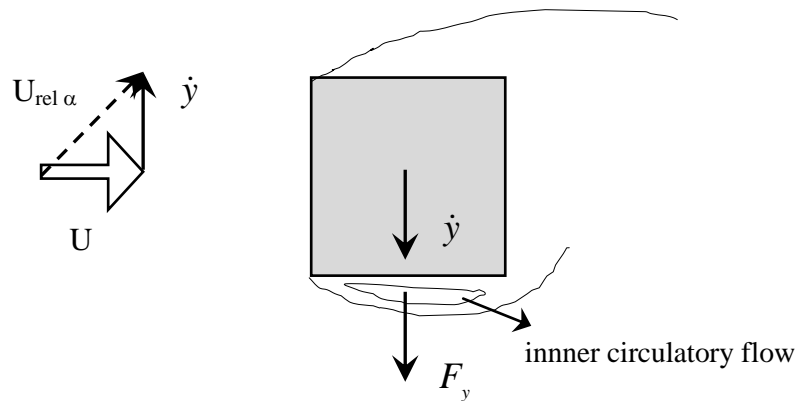


Fig. 2.13 Inner circulatory flow related to mechanism of galloping

Galloping can occur on bridge elements such as deck, pylon and stay cable. Bluff deck section such as non-streamlined box girder with small B/D are susceptible to galloping instability. Several countermeasures against galloping instability had been reported such as in Tozaki Viaduct girder and Nihimaya Bridge girder (Fujino et al., 2012) and pylon of Higashi Kobe Bridge (Shiraishi, 1988).

For cable-stayed bridges, wind-vibration occurred mainly on stay cables. Cables are prone to vibrate under wind flow due to its low mechanical damping. Many efforts had been made to clarify the mechanism and to find the mitigation solution. Rapid development of cable-stayed bridges brings identification of new type instability for stay cable such as rain-wind vibration, high-speed vortex excitation and dry inclined galloping (Fujino *et al.*, 2012).

## 2.3 Flutter Instability in Long Span Bridge Decks

Flutter is a flow-induced and self-excited divergent aerodynamic instability phenomenon, for which mass, stiffness, damping and geometrical shape of the body, as well as characteristics of the flow such as velocity and angle of attack play fundamental role (Trein, 2009). This definition mentions three factors that influenced flutter instability:

1. structural properties (mass, stiffness, damping)
2. geometrical shape of the body
3. oncoming flow

Since the oncoming flows are controlled by environmental aspect, then flutter stability of bridge deck can be improved by modifying structural properties and shape of the deck.

Flutter has almost the same condition with galloping: aerodynamic forces due to movement of the body act feeding energy to the oscillation, or known as negative damping that imposed to the body-flow system, increasing the amplitude of oscillations and leading to failure of the structure. Nowadays, two major types of flutter are recognized: torsional flutter and coupled flutter. Torsional flutter is single degree of freedom instability (torsional motion), and coupled flutter consists of two degree of freedom motion: heaving and torsional motion.

Matsumoto *et al.* (2002) introduced more complete classification of flutter based on the shape of the cross section and mechanism:

1. low speed flutter, occurs in bluff sections like rectangular cylinder with B/D=5
2. high speed torsional flutter, occurs still in bluff sections but with higher side ratio like rectangular cylinder with B/D=10
3. torsional branch coupled flutter, occurs in slender section like rectangular cylinder with B/D=20, and most common type of flutter for streamlined box girder
4. heaving branch coupled flutter
5. hybrid branch coupled flutter

The last 2 types are not common in practice, therefore they are not widely known.

### 2.3.1 Mathematical Model of Flutter and Aerodynamic Derivatives

A bridge deck of long span bridge immersed in smooth wind flow can be modeled as dynamic system of 2 degree of freedom (2-DOF) as shown in Fig. 2.14. The equation of motion is:

$$m.\ddot{\eta} + c_{\eta}.\dot{\eta} + k_{\eta}.\eta = L(t) \quad (2.6a)$$

$$I.\ddot{\varphi} + c_{\varphi}.\dot{\varphi} + k_{\varphi}.\varphi = M(t) \quad (2.6b)$$

where  $m$ ,  $I$ : mass, mass moment of inertia per unit span;  $\eta$ ,  $\varphi$ : heaving displacement, torsional displacement;  $c_{\eta}$ ,  $c_{\varphi}$ : damping constant for heaving motion, torsional motion;  $k_{\eta}$ ,  $k_{\varphi}$ : heaving stiffness, torsional stiffness;  $L(t)$ ,  $M(t)$ : unsteady aerodynamic lift, moment per unit span.

Sign convention for positive values of  $\eta$ ,  $\varphi$ ,  $L(t)$ ,  $M(t)$  are as shown in Fig. 2.14. The oncoming wind flow is from the left side of the body.

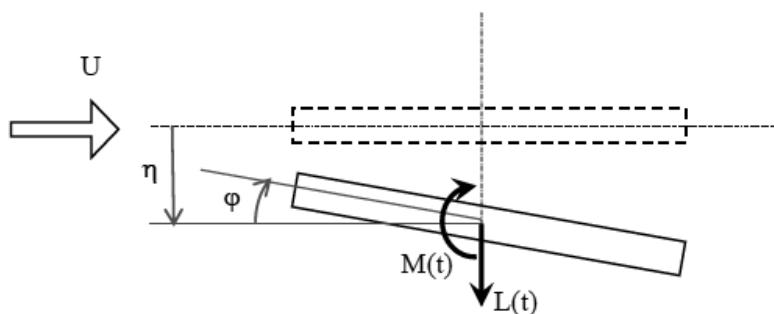


Fig. 2.14 Dynamic system of 2-DOF body under wind load

Early works on flutter analysis were in aeronautics field. Theodorsen derived closed-form analytic solution for aerodynamic forces (lift and torsional moment) for thin plate based on potential theory:

$$L = -\pi \cdot \rho \cdot b^2 (U \cdot \dot{\varphi} + \dot{\eta}) - 2 \cdot \pi \cdot \rho \cdot b \cdot U \cdot C(k) \left( U \cdot \varphi + \dot{\eta} + \frac{b \cdot \dot{\varphi}}{2} \right) \quad (2.7a)$$

$$M = -\pi \cdot \rho \cdot b^2 \left( U \frac{b \cdot \dot{\varphi}}{2} + \frac{b^2 \cdot \ddot{\varphi}}{8} \right) + \pi \cdot \rho \cdot b^2 \cdot U \cdot C(k) \left( U \cdot \dot{\varphi} + \dot{\eta} + \frac{b \cdot \dot{\varphi}}{2} \right) \quad (2.7b)$$

where:  $\rho$ : density of air,  $b$ : half width of deck,  $C(k)$ : Theodorsen function with  $k$ : reduced frequency,  $k = b \cdot \omega / U$  with  $\omega$  is circular frequency =  $2 \cdot \pi \cdot f$

$$C(k) = \frac{H_1^{(2)}(k)}{H_1^{(2)}(k) + iH_0^{(2)}(k)} F(k) - iG(k) \quad (2.8)$$

where  $H_v^{(2)}$  is the Hankel function of second kind. The value of  $C(k)$  could be approximated by using equation proposed by R. T. Jones as follows:

$$C(k) = 1 - \frac{a \cdot k^2}{b^2 + k^2} - \frac{c \cdot k^2}{d^2 + k^2} - i \left( \frac{k \cdot a \cdot b}{b^2 + k^2} + \frac{k \cdot c \cdot d}{d^2 + k^2} \right) \quad (2.9)$$

where:  $a=0.165$ ,  $b=0.0455$ ,  $c=0.335$ ,  $d=0.3$ . Eq. (2.7a) and (2.7b) are for aerodynamic forces of thin airfoil or thin flat plate undergoes heaving and torsional motion, where the forces are function of displacement, velocity and acceleration. Linear analysis is based on the assumption of small amplitude. From Eq. (2.8), it can be seen that Theodorsen function is complex value which means the inclusion of phase lag from quasi-steady aerodynamic forces to the unsteady ones.

Aerodynamic forces formula using Theodorsen function could not be applied for bridge aerodynamics. Theodorsen function was derived mathematically from from airfoil or thin



plate section that are categorized as non-separated flow, while most of elements in bridge structure, especially deck, are bluff body and categorized as separated flow cases (Fig. 2.7). There is no closed form analytic solution for aerodynamic of bluff body, at least until now. One approach to model aerodynamic forces in bluff body is by doing wind tunnel test. Scanlan & Tomko (1971) proposed 8 aerodynamic derivatives for structural sections in 2-D dynamic system as follows:

$$L(t) = \frac{1}{2} \cdot \rho \cdot (2b) U^2 \left\{ k \cdot H_1^* \cdot \frac{\dot{\eta}}{U} + k \cdot H_2^* \cdot b \cdot \frac{\dot{\phi}}{U} + k^2 \cdot H_3^* \cdot \varphi + k^2 \cdot H_4^* \cdot \frac{\eta}{b} \right\} \quad (2.10a)$$

$$M(t) = \frac{1}{2} \cdot \rho \cdot (2b^2) U^2 \left\{ k \cdot A_1^* \cdot \frac{\dot{\eta}}{U} + k \cdot A_2^* \cdot b \cdot \frac{\dot{\phi}}{U} + k^2 \cdot A_3^* \cdot \varphi + k^2 \cdot A_4^* \cdot \frac{\eta}{b} \right\} \quad (2.10b)$$

where  $H_i^*$  and  $A_i^*$  ( $i=1$  to 4) are aerodynamic derivatives. For case of thin plate, its aerodynamic derivatives can be calculated by substitution of Eq. (2.7a), (2.7b), (2.9), (2.10a) and (2.10b) for harmonic motion  $\eta = \eta_0 \cdot e^{i\omega t}$  and  $\varphi = \varphi_0 \cdot e^{i\omega t}$ . In this case, aerodynamic derivatives can be written as follows:

$$H_1^* = -\frac{2\pi}{k} F(k) \quad (2.11a)$$

$$H_2^* = -\frac{2\pi}{k} \left( \frac{1}{2} + \frac{F(k)}{2} - \frac{G(k)}{k} \right) \quad (2.11b)$$

$$H_3^* = -\frac{2\pi}{k} \left( \frac{F(k)}{k} + \frac{G(k)}{k} \right) \quad (2.11c)$$

$$H_4^* = -\frac{2\pi}{k} G(k) \quad (2.11d)$$

$$A_1^* = \frac{\pi}{k} F(k) \quad (2.11e)$$

$$A_2^* = \frac{\pi}{k} \left( -\frac{1}{2} + \frac{F(k)}{2} - \frac{G(k)}{k} \right) \quad (2.11f)$$

$$A_3^* = \frac{\pi}{k} \left( \frac{F(k)}{k} + \frac{G(k)}{2} \right) \quad (2.11g)$$

$$A_4^* = \frac{\pi}{k} G(k) \quad (2.11h)$$

Aerodynamic derivatives of thin plate calculated from Eq. (2.11a) to (2.11h) are often referred as ‘aerodynamic derivatives from Theodorsen function’. Although these derivatives are not suitable for bridge deck, but they are used in practice as benchmark for bridge deck derivatives to assess flutter stability. Also from these equations, it can be said that flutter derivatives of thin plate are not independent mutually. They are defined by  $F(k)$  and  $G(k)$ , and interdependence between them is an important factor for flutter stabilization.

Flutter is an unsteady flow phenomenon, so aerodynamic forces for its mathematical model must take into account the unsteady forces. Despite the unsteadiness of forces, some researchers proposed quasi-steady model with modification for flutter analysis (Øiseth *et al.*, 2010; Borri & Costa, 2004; Brancaloni *et al.*, 2010).

### 2.3.2 Obtaining Aerodynamic Derivatives

As explained in the previous section, aerodynamic derivatives for bluff body such as bridge deck can be obtained by wind tunnel test. Although several researchers already studied the possibility of computer numerical simulation under field of computational fluid dynamics or CFD (Walther & Larsen, 1997; Larsen & Walther, 1998; Šarkić *et al.*, 2012), wind tunnel tests still regarded as the more reliable technique. System identification is needed to extract the aerodynamic derivatives data from the wind tunnel test. Several system identification method had been proposed and used such as by Sarkar *et al.* (1992), Iwamoto & Fujino (1995), Gu *et al.* (2000), Chen *et al.* (2002), Chowdury & Sarkar (2003). Free vibration test is less expensive but need complicated system identification, forced vibration on the other hand is straightforward but need expensive motor system. Forced vibration technique is used in this thesis.

In forced vibration test, load cells and laser sensor are used to measure time history of aerodynamic forces and displacements for each 1-DOF motion (heaving only and torsional only). The aerodynamic forces and displacements are evaluated as:

For 1-DOF heaving motion:

$$L_{\eta}(t) = L_{\eta 0} \cdot \cos(\omega_{\eta} \cdot t - \psi_{L_{\eta}}) \quad (2.12a)$$

$$M_{\eta}(t) = M_{\eta 0} \cdot \cos(\omega_{\eta} \cdot t - \psi_{M_{\eta}}) \quad (2.12b)$$

$$\eta(t) = \eta_0 \cdot \cos(\omega_{\eta} \cdot t) \quad (2.12c)$$

For 1-DOF torsional motion:

$$L_{\varphi}(t) = L_{\varphi 0} \cdot \cos(\omega_{\varphi} \cdot t - \psi_{L_{\varphi}}) \quad (2.12d)$$

$$M_{\varphi}(t) = M_{\varphi 0} \cdot \cos(\omega_{\varphi} \cdot t - \psi_{M_{\varphi}}) \quad (2.12e)$$

$$\varphi(t) = \varphi_0 \cdot \cos(\omega_{\varphi} \cdot t) \quad (2.12f)$$

where:  $L_{\eta 0}$ ,  $L_{\varphi 0}$ : amplitude of lift force due to heaving motion  $\eta$  and torsional motion  $\varphi$ ;  $M_{\eta 0}$ ,  $M_{\varphi 0}$ : amplitude of torsional moment due to heaving motion  $\eta$  and torsional motion  $\varphi$ ;  $\omega_{\eta}$ ,  $\omega_{\varphi}$ : circular frequency of heaving motion  $\eta$  and torsional motion  $\varphi$ ;  $\psi_{L_{\eta}}$ ,  $\psi_{M_{\eta}}$ : phase lag from maximum heaving displacement to maximum lift force and torsional moment;  $\psi_{L_{\varphi}}$ ,  $\psi_{M_{\varphi}}$ : phase lag from maximum torsional displacement to maximum lift force and torsional moment.

In the case of 1-DOF heaving and torsional motion, Eq. (2.10) becomes:

For 1-DOF heaving motion:

$$L(t) = \frac{1}{2} \cdot \rho \cdot (2b) U^2 \left\{ k \cdot H_1^* \cdot \frac{\dot{\eta}}{U} + k^2 \cdot H_4^* \cdot \frac{\eta}{b} \right\} \quad (2.13a)$$

$$M(t) = \frac{1}{2} \cdot \rho \cdot (2b^2) U^2 \left\{ k \cdot A_1^* \cdot \frac{\dot{\eta}}{U} + k^2 \cdot A_4^* \cdot \frac{\eta}{b} \right\} \quad (2.13b)$$

For 1-DOF torsional motion:

$$L(t) = \frac{1}{2} \cdot \rho \cdot (2b) U^2 \left\{ k \cdot H_2^* \cdot b \cdot \frac{\dot{\varphi}}{U} + k^2 \cdot H_3^* \cdot \varphi \right\} \quad (2.13c)$$

$$M(t) = \frac{1}{2} \cdot \rho \cdot (2b^2) U^2 \left\{ k \cdot A_2^* \cdot b \cdot \frac{\dot{\varphi}}{U} + k^2 \cdot A_3^* \cdot \varphi \right\} \quad (2.13d)$$

The values of aerodynamic derivatives can be calculated by combining and rearranging Eq. (2.12) and (2.13):

$$H_1^* = -\frac{L_{\eta 0} \cdot \sin \psi_{L\eta}}{\rho \cdot b^2 \cdot \omega_\eta^2 \cdot \eta_0} \quad (2.14a)$$

$$H_2^* = -\frac{L_{\varphi 0} \cdot \sin \psi_{L\varphi}}{\rho \cdot b^3 \cdot \omega_\varphi^2 \cdot \varphi_0} \quad (2.14b)$$

$$H_3^* = \frac{L_{\varphi 0} \cdot \cos \psi_{L\varphi}}{\rho \cdot b^3 \cdot \omega_\varphi^2 \cdot \varphi_0} \quad (2.14c)$$

$$H_4^* = \frac{L_{\eta 0} \cdot \cos \psi_{L\eta}}{\rho \cdot b^2 \cdot \omega_\eta^2 \cdot \eta_0} \quad (2.14d)$$

$$A_1^* = -\frac{M_{\eta 0} \cdot \sin \psi_{M\eta}}{\rho \cdot b^3 \cdot \omega_\eta^2 \cdot \eta_0} \quad (2.14e)$$

$$A_2^* = -\frac{M_{\varphi 0} \cdot \sin \psi_{M\varphi}}{\rho \cdot b^4 \cdot \omega_\varphi^2 \cdot \varphi_0} \quad (2.14f)$$

$$A_3^* = \frac{M_{\varphi 0} \cdot \cos \psi_{M\varphi}}{\rho \cdot b^4 \cdot \omega_\varphi^2 \cdot \varphi_0} \quad (2.14g)$$

$$A_4^* = \frac{M_{\eta 0} \cdot \cos \psi_{M\eta}}{\rho \cdot b^3 \cdot \omega_\eta^2 \cdot \eta_0} \quad (2.14h)$$

This derivatives extraction technique is applicable to any kind of geometry even models with many small size appendages.

### 2.3.3 Unsteady Pressure Characteristics

Aerodynamic derivatives are the only aerodynamic properties that need to be measured experimentally in order to assess flutter stability of bridge deck sections analytically. However, aerodynamic derivatives do not provide any information about flow field around body. Therefore, the physical explanation behind the aerodynamic performance of deck sections cannot be obtained. Moreover, it is hard to improve stability of any deck based on aerodynamic derivatives only without trial and error experiment, since each countermeasures give different effects to the aerodynamic properties of the deck.

Surface pressure distribution on the body in wind flow is important for the study of aerodynamic stability. As explained in section 2.2, each aero-elastic phenomenon has unique mechanism that directly related with flow field around the body. Pressure distribution information can give more comprehensive understanding about the physical process behind destabilization or stabilization of the body. Aerodynamic derivatives can also be expressed with unsteady pressure of the deck, since the total lift and moment are integration of surface pressure along the width. However, measuring the surface pressure to get aerodynamic derivatives is considered not practical and only applicable for model with simple geometry, so direct measurement using load cell is still a more common method.

Pressure on the surface of a harmonically oscillating body can be explained as in Fig. 2.15. For each position  $x^*$  (position from mid-chord, normalized with half width of the body, b), the pressure consists of steady part  $\bar{P}$  and unsteady part  $\tilde{P}$ .  $\bar{P}$  is constant while  $\tilde{P}$  is varied with time, or in mathematic expression:

$$P(x^*, t) = \bar{P}(x^*) + \tilde{P}(x^*, t) \quad (2.15)$$

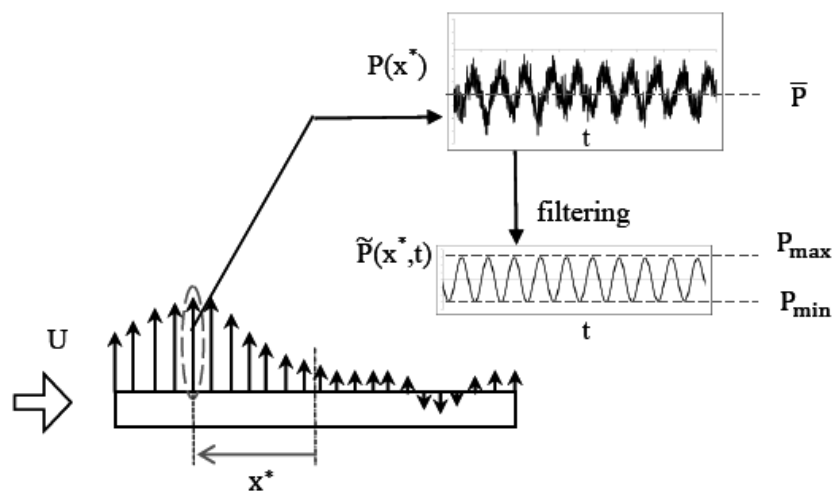


Fig. 2.15 Surface pressure of a dynamic system under wind load

Since Eq. (2.10) are for unsteady forces, so the steady part is canceled out. Unsteady pressure can be represented by two variables: amplitude of unsteady pressure,  $\tilde{C}_p(x^*)$  and phase lag,

$\psi(x^*)$ , therefore these two variables are called unsteady pressure characteristics.  $\tilde{C}_p(x^*)$  is the peak to peak amplitude of unsteady pressure, and normalized by dynamic pressure:

$$\tilde{C}_p(x^*) = \frac{P_{\max}(x^*) - P_{\min}(x^*)}{\frac{1}{2} \cdot \rho \cdot U^2} \quad (2.16)$$

$\psi(x^*)$  is phase difference between maximum relative angle of attack and maximum negative pressure. For torsional motion, maximum relative angle of attack is simply maximum rotation and for heaving motion is at maximum heaving velocity. Positive value of  $\psi(x^*)$  indicates a delay of pressure fluctuation at point  $x^*$  in relation to the motion of the body. Physical description of  $\tilde{C}_p(x^*)$  and  $\psi(x^*)$  for heaving and torsional motion can be seen in Fig. 2.16 and Fig 2.17.

Unsteady or fluctuating pressure on the surface at position  $x^*$  can be formulated as:

For 1-DOF heaving motion:

$$\tilde{C}_p(x^*, t) = \frac{\tilde{C}_p(x^*)}{2} \cdot \sin(\omega_\eta \cdot t - \psi(x^*)) \quad (2.17a)$$

For 1-DOF torsional motion:

$$\tilde{C}_p(x^*, t) = \frac{\tilde{C}_p(x^*)}{2} \cos(\omega_\varphi \cdot t - \psi(x^*)) \quad (2.17b)$$

Positive pressures act as ‘push’ to the surface and negative pressures act as ‘suction’.

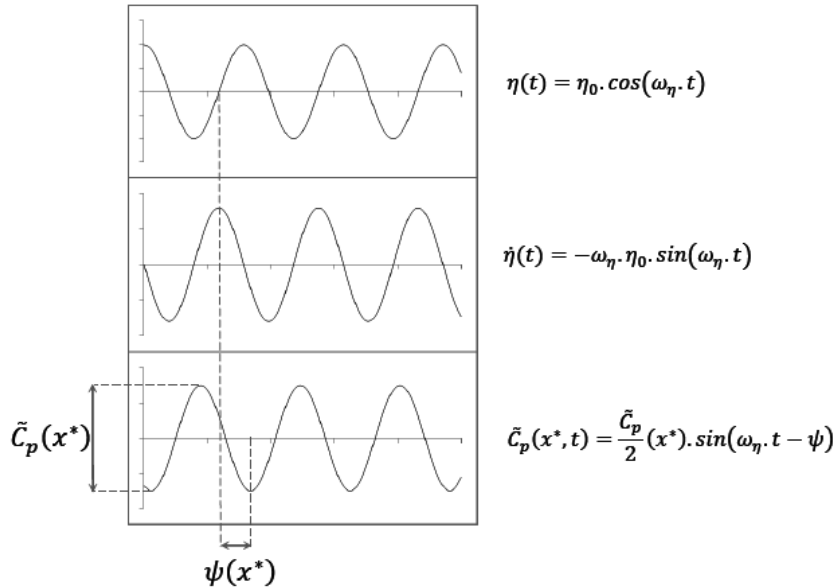


Fig. 2.16  $\tilde{C}_p(x^*)$  and  $\psi(x^*)$  for heaving motion

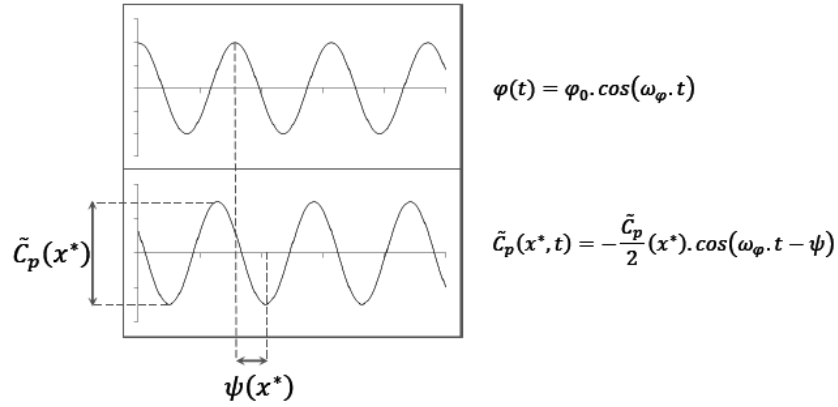


Fig. 2.17  $\tilde{C}_p(x^*)$  and  $\psi(x^*)$  for torsional motion

In order to obtain the total lift force and torsional moment due to unsteady pressure, Eq. (2.17a) and eq. (2.17b) should be integrated over the whole surface of the body.

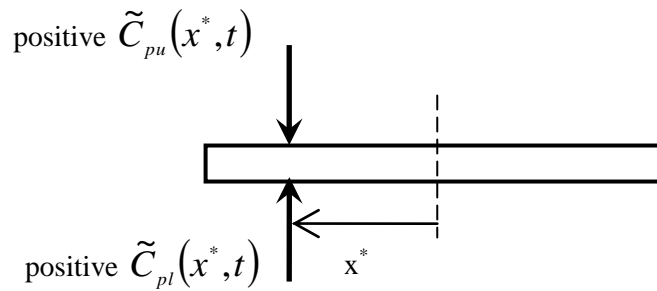


Fig. 2.18  $\tilde{C}_p(x^*, t)$  for upper and lower surface

For 1-DOF heaving motion:

$$L_\eta(t) = \frac{1}{2} \cdot \rho \cdot U^2 \cdot b \left\{ \int_{-1}^1 \frac{\tilde{C}_{pu}(x^*)}{2} \cdot \sin(\omega_\eta \cdot t - \psi_u(x^*)) dx^* - \int_{-1}^1 \frac{\tilde{C}_{pl}(x^*)}{2} \cdot \sin(\omega_\eta \cdot t - \psi_l(x^*)) dx^* \right\} \quad (2.18a)$$

$$M_\eta(t) = \frac{1}{2} \cdot \rho \cdot U^2 \cdot b^2 \left\{ \int_{-1}^1 x^* \cdot \frac{\tilde{C}_{pu}(x^*)}{2} \cdot \sin(\omega_\eta \cdot t - \psi_u(x^*)) dx^* - \int_{-1}^1 x^* \cdot \frac{\tilde{C}_{pl}(x^*)}{2} \cdot \sin(\omega_\eta \cdot t - \psi_l(x^*)) dx^* \right\} \quad (2.18b)$$

For 1-DOF torsional motion:

$$L_\varphi(t) = \frac{1}{2} \cdot \rho \cdot U^2 \cdot b \left\{ \int_{-1}^1 -\frac{\tilde{C}_{pu}(x^*)}{2} \cdot \cos(\omega_\varphi \cdot t - \psi_u(x^*)) dx^* - \int_{-1}^1 -\frac{\tilde{C}_{pl}(x^*)}{2} \cdot \cos(\omega_\varphi \cdot t - \psi_l(x^*)) dx^* \right\} \quad (2.18c)$$

$$M_\varphi(t) = \frac{1}{2} \cdot \rho \cdot U^2 \cdot b^2 \left\{ \int_{-1}^1 x^* \cdot -\frac{\tilde{C}_{pu}(x^*)}{2} \cdot \cos(\omega_\varphi \cdot t - \psi_u(x^*)) dx^* - \int_{-1}^1 x^* \cdot -\frac{\tilde{C}_{pl}(x^*)}{2} \cdot \sin(\omega_\varphi \cdot t - \psi_l(x^*)) dx^* \right\} \quad (2.18d)$$

The values of aerodynamic derivatives can be calculated by combining and rearranging Eq. (2.13a) to Eq. (2.13d) with (Eq. (2.18a) to Eq. (2.18d):

$$H_1^* = -\frac{U}{2 \cdot k \cdot \omega_\eta \cdot \eta_0} \int_{-1}^1 \left( \frac{\tilde{C}_{pu}(x^*)}{2} \cdot \cos \psi_u(x^*) - \frac{\tilde{C}_{pl}(x^*)}{2} \cdot \cos \psi_l(x^*) \right) dx^* \quad (2.19a)$$

$$H_2^* = \frac{1}{2 \cdot k^2 \cdot \varphi_0} \int_{-1}^1 \left( \frac{\tilde{C}_{pu}(x^*)}{2} \cdot \sin \psi_u(x^*) - \frac{\tilde{C}_{pl}(x^*)}{2} \cdot \sin \psi_l(x^*) \right) dx^* \quad (2.19b)$$

$$H_3^* = -\frac{1}{2 \cdot k^2 \cdot \varphi_0} \int_{-1}^1 \left( \frac{\tilde{C}_{pu}(x^*)}{2} \cdot \cos \psi_u(x^*) - \frac{\tilde{C}_{pl}(x^*)}{2} \cdot \cos \psi_l(x^*) \right) dx^* \quad (2.19c)$$

$$H_4^* = -\frac{1}{2 \cdot k \cdot \omega_\eta \cdot \eta_0} \int_{-1}^1 \left( \frac{\tilde{C}_{pu}(x^*)}{2} \cdot \sin \psi_u(x^*) - \frac{\tilde{C}_{pl}(x^*)}{2} \cdot \sin \psi_l(x^*) \right) dx^* \quad (2.19d)$$

$$A_1^* = -\frac{U}{2 \cdot k \cdot \omega_\eta \cdot \eta_0} \int_{-1}^1 x^* \left( \frac{\tilde{C}_{pu}(x^*)}{2} \cdot \cos \psi_u(x^*) - \frac{\tilde{C}_{pl}(x^*)}{2} \cdot \cos \psi_l(x^*) \right) dx^* \quad (2.19e)$$

$$A_2^* = \frac{1}{2 \cdot k^2 \cdot \varphi_0} \int_{-1}^1 x^* \left( \frac{\tilde{C}_{pu}(x^*)}{2} \cdot \sin \psi_u(x^*) - \frac{\tilde{C}_{pl}(x^*)}{2} \cdot \sin \psi_l(x^*) \right) dx^* \quad (2.19f)$$

$$A_3^* = -\frac{1}{2 \cdot k^2 \cdot \varphi_0} \int_{-1}^1 x^* \left( \frac{\tilde{C}_{pu}(x^*)}{2} \cdot \cos \psi_u(x^*) - \frac{\tilde{C}_{pl}(x^*)}{2} \cdot \cos \psi_l(x^*) \right) dx^* \quad (2.19g)$$

$$A_4^* = -\frac{1}{2 \cdot k \cdot \omega_\eta \cdot \eta_0} \int_{-1}^1 x^* \left( \frac{\tilde{C}_{pu}(x^*)}{2} \cdot \sin \psi_u(x^*) - \frac{\tilde{C}_{pl}(x^*)}{2} \cdot \sin \psi_l(x^*) \right) dx^* \quad (2.19h)$$

Eq. (2.19a) to (2.19h) are used for general section with different shape between upper and lower surface. For symmetric section (between upper and lower surface), 2 conditions are occurred for one position  $x^*$  :

$$\tilde{C}_{pu}(x^*) = \tilde{C}_{pl}(x^*) = \tilde{C}_p(x^*) \quad (2.20)$$

$$|\psi_u(x^*) - \psi_l(x^*)| = 180^\circ \quad (2.21)$$

Therefore, symmetric section has more simple equations:

$$H_1^* = -\frac{U}{2.k.\omega_\eta.\eta_0} \int_{-1}^1 \tilde{C}_p(x^*) \cos \psi(x^*) dx^* \quad (2.22a)$$

$$H_2^* = \frac{1}{2.k^2.\varphi_0} \int_{-1}^1 \tilde{C}_p(x^*) \sin \psi(x^*) dx^* \quad (2.22b)$$

$$H_3^* = -\frac{1}{2.k^2.\varphi_0} \int_{-1}^1 \tilde{C}_p(x^*) \cos \psi(x^*) dx^* \quad (2.22c)$$

$$H_4^* = -\frac{1}{2.k.\omega_\eta.\eta_0} \int_{-1}^1 \tilde{C}_p(x^*) \sin \psi(x^*) dx^* \quad (2.22d)$$

$$A_1^* = -\frac{U}{2.k.\omega_\eta.\eta_0} \int_{-1}^1 x^* . \tilde{C}_p(x^*) \cos \psi(x^*) dx^* \quad (2.22e)$$

$$A_2^* = \frac{1}{2.k^2.\varphi_0} \int_{-1}^1 x^* . \tilde{C}_p(x^*) \sin \psi(x^*) dx^* \quad (2.22f)$$

$$A_3^* = -\frac{1}{2.k^2.\varphi_0} \int_{-1}^1 x^* . \tilde{C}_p(x^*) \cos \psi(x^*) dx^* \quad (2.22g)$$

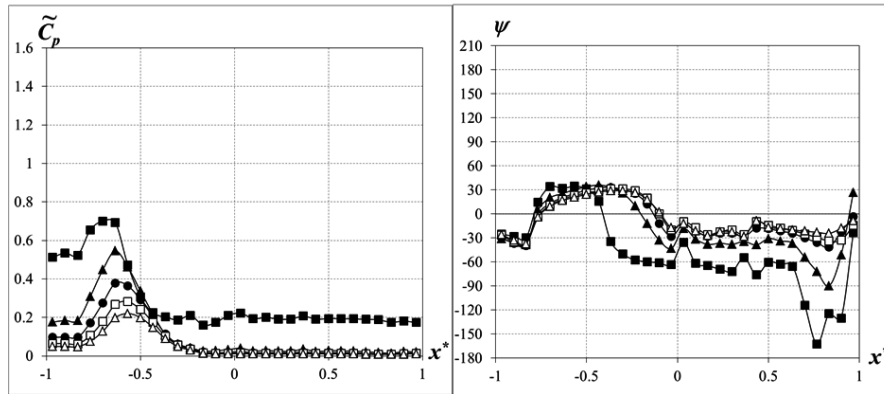
$$A_4^* = -\frac{1}{2.k.\omega_\eta.\eta_0} \int_{-1}^1 x^* . \tilde{C}_p(x^*) \sin \psi(x^*) dx^* \quad (2.22h)$$

Unsteady pressure characteristics for rectangular prism with B/D=20 are shown in Fig. 2.19. Aerodynamic derivatives of thin plate (from Theodorsen function) and rectangular prism with B/D=20 are shown in Fig. 2.20. From Fig. 2.20, it can be said that aerodynamic derivatives from direct forces measurement using load cell are in good agreement with values from integration of unsteady pressure.

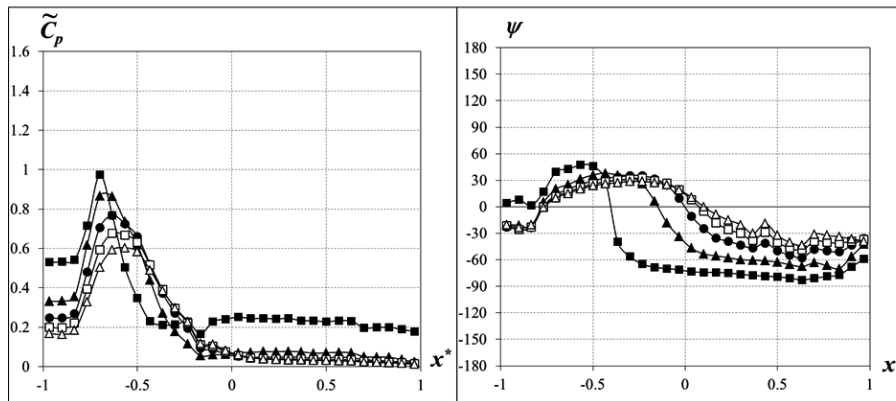


## 2.4 Concluding Remarks

A brief overview about significance of aerodynamic-related problems, especially flutter to the history and future development of long span bridge was presented. Also, basic explanation about flutter can be found in this chapter: definition and basic theory, mathematical modelling, obtaining aerodynamic derivatives and unsteady pressure characteristics. These are important terms that used in this thesis.



(a) heaving



(b) torsional



Fig. 2.19  $\tilde{C}_p(x^*)$  and  $\psi(x^*)$  of rectangular prism with  $B/D=20$

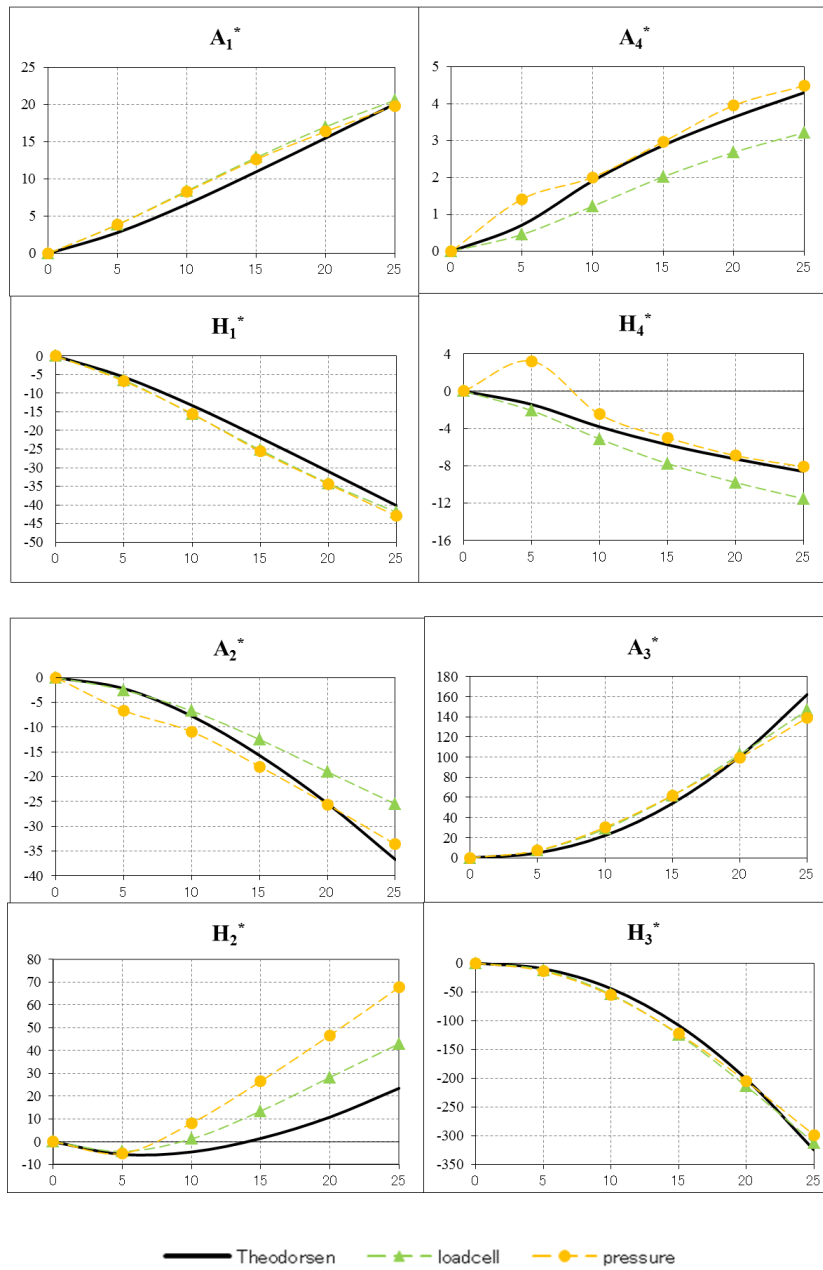


Fig. 2.20 Comparison of aerodynamic derivatives of thin plate (from Theodorsen function) with rectangular prism with  $B/D=20$  (from experiment using load cell and pressure measurement)

## Bibliography

- Astiz, M. A., Andersen, E. Y. (1990) 'On wind stability of very long spans in connection with a bridge across the Strait of Gibraltar', *Strait Crossings*, Rotterdam.
- Battista, R. C., Pfeil, M. S. (2000) 'Reduction of vortex-induced oscillations of Rio-Niteroi bridge by dynamic control devices', *Journal of Wind Engineering and Industrial Aerodynamics*, 84, pp. 273-288.
- Borri, C., Costa, C. (2004), 'Quasi-steady analysis of a bridge deck element', *Computer and Structures*, 82, pp. 993-1006.
- Brancaleoni, F., Diana, G., Faccioli, E., Fiammenghi, G., Firth, I. P. T., Gimsing, N. J., Jamiolkowski, M., Sluszk, P., Solari, G., Valensise, G., and Vullo, E. (2010) '*The Messina Strait Bridge : a challenge and a dream*', CRC Press.
- Buonopane, S. G., and Billington, D. (1993) 'Theory and history of suspension bridge design from 1823 to 1940', *Journal of Structural Engineering*, 119(3), pp. 954-977.
- Chen, A., He, X., Xiang, H. F. (2002) 'Identification of 18 flutter derivatives of bridge decks', *Journal of Wind Engineering and Industrial Aerodynamics*, 90 (12-15), pp. 2007-2022.
- Chowdhury, A. G., Sarkar, P. P. (2003) 'A new technique for identification of eighteen flutter derivatives using a three-degree-of-freedom section model', *Engineering and Structures*, 25 (14), pp. 1763-1772.
- Clemente, P. (1998), 'On the limit span of cable-stayed structures', *IABSE Report 79 (1998)*.
- Deniz, S., Staubli, T. (1997) 'Oscillating rectangular and octagonal profiles: interaction of leading- and trailing-edge vortex formation ', *Journal of Fluids and Structures*, 11, pp. 3-31.
- Fujino, Y., Yoshida, Y. (2002) 'Wind-induced vibration and control of Trans-Tokyo Bay crossing bridge', *Journal of Structural Engineering*, 128 (8), pp. 1012-1025.
- Fujino, Y., Kimura, K., Tanaka, H. (2012), '*Wind resistant design of bridges in Japan: development and practices*', Springer.
- Ge, Y. J., Xiang, H. F. (2008), 'Aerodynamic challenges in long-span bridges', *Proceedings of the Centenary Conference of the Institution of Structural Engineers*, Hong Kong, China, January 24-26 2008.
- Ge, Y. J., Xiang, H. F. (2009) 'Aerodynamic stabilization for box-girder suspension bridges with super-long span', *EACWE 5*, Florence, Italy, July 19-23 2009.
- Gimsing, N. J., Georgakis, C. T. (2011) '*Cable supported bridges : concept and design 3ed.*', Wiley.
- Gu, M., Zhang, R., Xiang, H. F. (2000) 'Identification of flutter derivatives of bridge decks', *Journal of Wind Engineering and Industrial Aerodynamics*, 84 (2), pp. 151-162.
- Honda, A., Shiraishi, N., Matsumoto, M., Fuse, Y., Sumi, K., Sasaki, N. (1993) 'Aerodynamic stability of Kansai International Airport access bridge', *Journal of Wind Engineering and Industrial Aerodynamics*, 49, pp. 533-542.
- Iwamoto, M., Fujino, Y. (1995) 'Identification of flutter derivatives of bridge deck from free vibration data', *Journal of Wind Engineering and Industrial Aerodynamics*, 54-55, pp. 55-63.

- Kawada, T. (2010) *'History of the modern suspension bridges : solving the dilemma between economy and stiffness'*, ASCE Press.
- Kitagawa, M. (2004) 'Technology of the Akashi Kaikyo bridge', *Structural Control and Health Monitoring*, 11 (2), pp. 75-90.
- Larsen, A., Eisdahl, S., Andersen, J. E., and Vejrum, T. (2000) 'Storebælt suspension bridge – vortex shedding excitation and mitigation by guide vanes', *Journal of Wind Engineering and Industrial Aerodynamics*, 88, pp. 283-296.
- Larsen, A., Poulin, S. (2005), 'Vortex-shedding excitation of box-girder bridges and mitigation', *Structure Engineering International*, 4, pp. 258-263.
- Larsen, A., Walther, J. H. (1998) 'Discrete vortex simulation of flow around five generic bridge deck sections', *Journal of Wind Engineering and Industrial Aerodynamics*, 77&78, pp. 591-602.
- Macdonald, J. H. G., Irwin, P. A., Fetcher, M. S. (2002), 'Vortex-induced vibrations of the Second Severn Crossing cable-stayed bridge – full scale and wind tunnel measurements', *Proc. ICE Struct. Build.*, 152 (2), pp. 123-143.
- Matsumoto, M., Kobayashi, Y., Niihara, Y., Shirato, H., Hamasaki, H. (1995), 'Flutter mechanism and its stabilization of bluff bodies', *The 9<sup>th</sup> International Conference on Wind Engineering*, New Delhi, India, pp. 827-838.
- Matsumoto, M. (2000), *'Aeroelasticity and bridge aerodynamics: text for international course'*, Genova, Italy.
- Matsumoto, M., Taniwaki, Y., Shijo, R. (2002) 'Frequency characteristics in various flutter instabilities of bridge girders', *Journal of Wind Engineering and Industrial Aerodynamics*, 90, pp. 1973-1980.
- Miyata, T., and Yamaguchi, K. (1993) 'Aerodynamic of wind effects on the Akashi Kaikyo bridge', *Journal of Wind Engineering and Industrial Aerodynamics*, 48, pp. 287-315.
- Naudascher, E., Rockwell, D. (1994), *'Flow-induced vibration: an engineering guide'*, A. A Balkema, Rotterdam.
- Øiseth, O., Rönquist, A., Sigbjörnsson, R. (2010) 'Simplified prediction of wind-induced response and stability limit of slender long-span suspension bridges, based on modified quasi-steady theory: a case study', *Journal of Wind Engineering and Industrial Aerodynamics*, 98 (12), pp. 730-741.
- Richardson, R. (1988), 'Radical deck design for ultra long span suspension bridges, Congress Report IABSE 13<sup>th</sup> Congress', Helsinki, Finland.
- Sato, H., Hirahara, N., Fumoto, K., Hirano, S., and Kusuhara, S. (2002) 'Full aeroelastic model test of a super long-span bridge with slotted box girder', *Journal of Wind Engineering and Industrial Aerodynamics*, 90, pp. 2023-2032.
- Sarkar, P. P., Jones, N. P., Scanlan, R. H. (1992) 'System identification for estimation of flutter derivatives', *Journal of Wind Engineering and Industrial Aerodynamics*, 42 (1-3), pp. 1243-1254.
- Šarkić, A., Fisch, R., Höffer, R., Bletzinger, K. (2012) 'Bridge flutter derivatives based on computed, validated pressure fields', *Journal of Wind Engineering and Industrial Aerodynamics*, 104-106, pp. 141-151.
- Scott, R. (2001) *'In the wake of Tacoma bridge : suspension bridges and the quest for aerodynamic stability'*, ASCE Press

- Svensson, H. (2012), *'Cable-stayed bridges: 40 years of experience worldwide'*, Ernst & Sohn.
- Tokoro, S., Honda, A., Masuda, I., Nakashima, Y., Murakoshi, J., and Fumoto, K. (2002), *'Aerodynamic Improvement of One Box Girder for Super Long Suspension Bridge'*, *The 2<sup>nd</sup> International Symposium on Wind and Structures*, Busan, Korea, August 21-23 2002, pp. 235-242.
- Trein, C. A. (2009), *'Study on the unsteady pressure characteristics of bluff bodies focusing on flutter stabilization of long-span bridges'*, PhD thesis, Kyoto University.
- Ueda, T., Tanaka, H., Matsushita, Y. (1998), *'Aerodynamic stabilization for super long span suspension bridges'*, *IABSE Symposium Report vol. 79*, Kobe, Japan.
- Scanlan, R. H., and Tomko, J. J. (1971) *'Airfoil and bridge deck flutter derivatives'*, *Journal of Engineering Mechanics Division*, ASCE 97, EM6, pp. 1717-1737.
- Shiraishi, N., Matsumoto, M. (1983) *'On classification of vortex-induced oscillation and its application for bridge structures'*, *Journal of Wind Engineering and Industrial Aerodynamics*, 14, pp. 419-430.
- Shiraishi, N., Matsumoto, M., Shirato, H., Ishizaki, H. (1988) *'On aerodynamic stability effects for bluff rectangular cylinders by their corner-cut'*, *Journal of Wind Engineering and Industrial Aerodynamics*, 28, pp. 371-380.
- Siringoringo, D. M., Fujino, Y. (2012) *'Observed along-wind vibration of a long-span suspension bridge tower'*, *Journal of Wind Engineering and Industrial Aerodynamics*, 103, pp. 107-121.
- Walther, J. H., Larsen, A. (1997) *'Two dimensional discrete vortex method for application to bluff body aerodynamics'*, *Journal of Wind Engineering and Industrial Aerodynamics*, 67&68, pp. 183-193.
- Weber, F., Maslanka, M. (2012), *'Frequency and damping adaptation of a TMD with controlled MR damper'*, *Smart Materials and Structures*, 21 (5) 055011.
- Zhu, L. D., Zhang, H. J., Guo, Z. S., Hu, X. H. (2011), *'Flutter performance and control measures of a 1400 m-span cable-stayed bridge scheme with steel box deck'*, *The 13<sup>th</sup> International Conference on Wind Engineering*, Amsterdam, Netherlands.



# Chapter 3

## Overview of Flutter Analysis and Stabilization for Long Span Bridge Deck

Shortly before the collapse of Tacoma Narrow Bridge, Farquharson studied the vibration of the bridge under wind loading and had proposed several aerodynamic countermeasures to suppress it. Unfortunately, the retrofitting work never took place due to the collapse of the bridge. One year before, in 1939, two suspension bridges with smaller size: Thousand Island Bridge (244 m) and Deer Isle Bridge (329 m) were strengthened with stay cables to control their excessive vibration (Scott, 2001). These were among the first attempt to stabilize bridge against vibration due to wind loading that based on analytic or experimental results. Since then, the field of bridge aerodynamic, especially flutter instability, had been improved significantly. New knowledge about flutter mechanism, mathematical model and analysis technique has contributed to better solution for stabilization. This chapter describes several stabilization solutions that had been proposed by researchers or engineers for modern long span bridges. A brief review about analysis method for flutter problem also outlined, since improvement in the stabilization solutions follows development in analytic method.

### 3.1 Analysis Method for Flutter Stability Problem of Bridge Deck

Analysis of flutter can be classified generally into three major techniques:

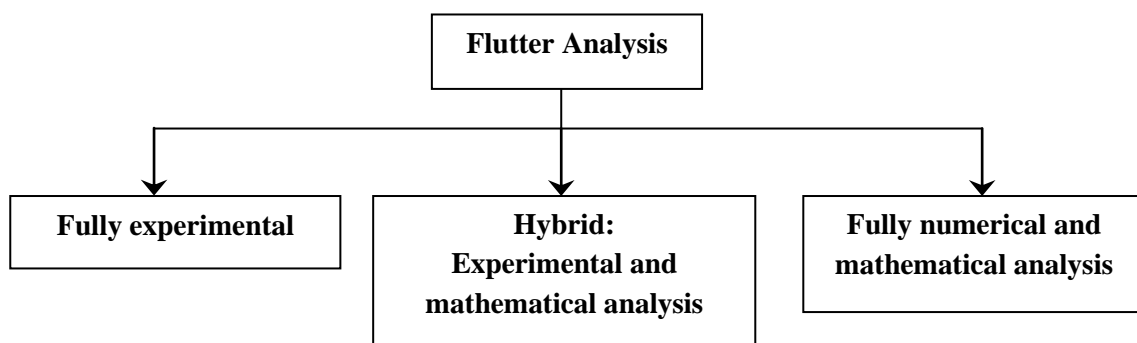


Fig. 3.1 General classification of flutter analysis technique

Fully experimental technique employs wind tunnel test to obtain flutter on set velocity of the bridge deck. This method is rigorous and requires intensive preparation and data analysis. Response of the model of the bridge can be measured by full model bridge test or

modifying the structure into section model test or taut-strip model test. However, even for very much simpler section model test, intensive and complicated works is needed for preparation, data extraction and data analysis. Hybrid technique employs section model test to obtain aerodynamic derivatives of the deck, and then solve the flutter formula numerically to get the flutter onset velocity. This technique is very much easier than fully experimental one if forced vibration technique is used to obtain aerodynamic derivatives.

The rapid increase of computer's capability to solve large numerical problems also generates the rapid improvement in field of computational fluid dynamics (CFD). Several CFD methods already developed to simulate moving body under wind flow and extract aerodynamic derivatives data. This technique is very attractive due to elimination of experimental works, and also more data about flow field can be obtained directly. However, numerical modeling of moving body under wind flow is still far from practical and require CFD specialist to do it.

In practice, hybrid technique is used in design stage of a bridge project. Much simpler model section test to obtain only aerodynamic derivatives facilitates engineers to try several alternatives of bridge deck section and make optimization. The most feasible section will be tested to confirm the flutter onset velocity, either using bridge section test only or full model test. This thesis deals only with hybrid technique, thus term 'flutter analysis' used in this thesis refers to hybrid technique.

Numerical analysis of flutter can be divided according to several ways:

1. Based on mathematical formulation of flutter model:
  - unsteady model
  - quasi-steady model
2. Based on analysis domain:
  - time domain
  - frequency domain
3. Based on assumption of amplitude of motion:
  - linear model
  - non-linear model
4. Based on degree of freedom:
  - n-DOF analysis: consider global structure model, such as direct method, multi-mode method and full-mode method
  - 2-DOF analysis or bi-modal analysis: consider heaving and torsional mode
  - 3-DOF analysis: consider heaving, torsional and sway mode

Equation of motion for a 3-D finite element model of a long span bridge under smooth wind flow can be written as follows:



$$[M]\{\ddot{u}\} + [C]\{\dot{u}\} + [K]\{u\} = [F_v]\{\dot{u}\} + [F_d]\{u\} \quad (3.1a)$$

or:

$$[M]\{\ddot{u}\} + [C']\{\dot{u}\} + [K']\{u\} = 0 \quad (3.1b)$$

where  $[M]$ ,  $[C]$ ,  $[K]$ : mass, damping and stiffness matrices;  $\{u\}$ : displacement vector;  $[F_v]$  and  $[F_d]$  are aerodynamic forces associated with velocity and displacement, respectively.  $[C']=[C]-[F_v]$  and  $[K']=[K]-[F_d]$ .

Eq (3.1b) can be transformed into modal coordinate  $\{q\}$  that is defined as:

$$\{u\} = [\Phi]\{q\} \quad (3.2)$$

where  $[\Phi]$ : orthonormal mode shape matrix;  $\{q\}$ : generalized coordinate vector. Equation (3.1b) in modal coordinate becomes:

$$[\bar{M}]\{\ddot{q}\} + [\bar{C}']\{\dot{q}\} + [\bar{K}']\{q\} = 0 \quad (3.3)$$

where  $[\bar{M}] = [\Phi]^T [M] [\Phi]$ ,  $[\bar{C}'] = [\Phi]^T [C'] [\Phi]$ , and  $[\bar{K}'] = [\Phi]^T [K'] [\Phi]$ , which are the generalized mass, generalized damping and generalized stiffness matrices, respectively. Assume  $\{q\} = \{q_0\} e^{\lambda t}$ ,  $\lambda = \lambda_R + \lambda_I$ , then characteristics equation from Eq. (3.3) is:

$$\det(\lambda^2 [\bar{M}] + \lambda [\bar{C}'] + [\bar{K}']) = 0 \quad (3.4)$$

Eq (3.4) can be solved as a complex eigenvalue problem. At the flutter condition, damping becomes zero ( $\xi_F=0$ , so  $\lambda_R=0$ ), and flutter frequency is the imaginary part of the complex eigenvalue ( $\omega_F=\lambda_I$ ). Flutter onset velocity can be calculated as wind speed  $U$  that gives one of the mode (say mode- $j$ ) zero real eigenvalue or  $\lambda_{Rj}=0$ .

Fujino *et al.* (2012) recommended flow chart for flutter analysis as in Fig. 3.2:

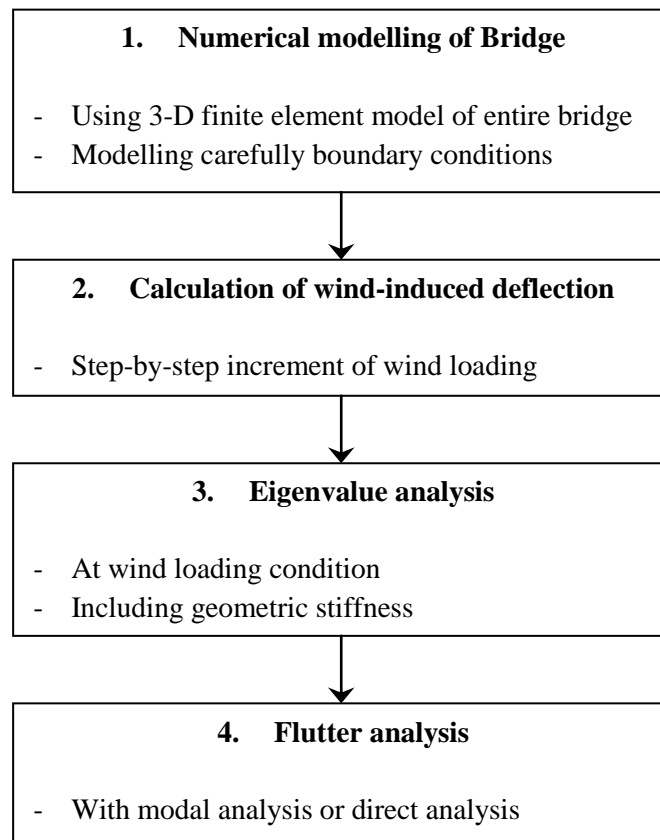


Fig. 3.2 Flow chart for flutter analysis (Fujino *et al.*, 2012)

Several notes about flow chart in Fig. 3.2:

1. Accurate calculation for deflection of deck under wind loading is needed, because flutter occurred at high wind speed and relatively large static deflection will be induced at center span under such condition. Some problems may arise:
  - aerodynamic derivatives and static coefficient of deck section are strongly affected by angle of attack. Therefore accurate static torsional deflection will be the angle of attack for each wind velocity level and proper aerodynamic derivatives can be applied.
  - large static deflection may change modal properties
2. Taking into account all of mode shapes of the bridge in Eq. (3.1) to (3.4) as formulated by Miyata & Yamada (1990) requires a large computer capacity and tends to be time consuming. Multi-mode method (Agar, 1989) is more preferred.
3. Simplification can be made by using bi-modal flutter analysis (Bartoli & Mannini, 2005). This simplification is valid for most of cases of long span bridges with deck that have low drag coefficient. Use of bi-modal flutter analysis for bridge with deck that have large value of drag coefficient will lead to overestimation of flutter onset velocity. This is due to the sway deformation (also accompanied by torsional deformation) effects flutter

stability significantly. Akashi Kaikyo Bridge is one example which large sway deformation due to large drag of deep truss deck must be taken into account for flutter analysis (Katsuchi *et al.*, 1999; Matsumoto *et al.*, 2010). In case of streamlined deck with low drag value, such as Messina Bridge, flutter is strongly characterized by torsional and heaving mode only, and also effect of deformed mode shape could be neglected (D'Asdia & Sepe, 1998). Chen (2007) stated that bi-modal flutter is sufficiently accurate and useful tool for finding best bridge deck section with superior aerodynamic properties.

Bi-modal flutter analysis is used in this thesis. Formulation for linear-unsteady model of flutter in 2-DOF is combination of Eq. (2.6a), (2.6b) with Eq. (2.10a) and (2.10b) as follows:

$$m.\ddot{\eta} + c_{\eta}.\dot{\eta} + k_{\eta}.\eta = \frac{1}{2}.\rho.(2b)U^2 \left\{ k.H_1^*.\frac{\dot{\eta}}{U} + k.H_2^*.b.\frac{\dot{\phi}}{U} + k^2.H_3^*.\phi + k^2.H_4^*.\frac{\eta}{b} \right\} \quad (3.5a)$$

$$I.\ddot{\phi} + c_{\phi}.\dot{\phi} + k_{\phi}.\phi = \frac{1}{2}.\rho.(2b^2)U^2 \left\{ k.A_1^*.\frac{\dot{\eta}}{U} + k.A_2^*.b.\frac{\dot{\phi}}{U} + k^2.A_3^*.\phi + k^2.A_4^*.\frac{\eta}{b} \right\} \quad (3.5b)$$

Complex eigenvalue method as Eq. (3.4) also widely used in 2-DOF flutter problem (Simiu & Scanlan, 1978; Ge & Tanaka, 2000). This approach is accurate to predict flutter onset velocity, but has drawback such as lack of explanation about mechanism of flutter and influence of each aerodynamic derivatives. Matsumoto *et al.* (1994) introduced step-by-step (SBS) analysis in order to capture mechanism behind the onset of flutter instability.

### 3.1.1 Complex Eigenvalue (CEV) Analysis

Eq. (3.5a) and (3.5b) can be rewritten as:

$$m.\ddot{\eta} + c_{\eta}.\dot{\eta} + k_{\eta}.\eta = \rho.b^2.\omega.H_1^*.\dot{\eta} + \rho.b^3.\omega.H_2^*.\dot{\phi} + \rho.b^3.\omega^2.H_3^*.\phi + \rho.b^2.\omega^2.H_4^*.\eta \quad (3.6a)$$

$$I.\ddot{\phi} + c_{\phi}.\dot{\phi} + k_{\phi}.\phi = \rho.b^3.\omega.A_1^*.\dot{\eta} + \rho.b^4.\omega.A_2^*.\dot{\phi} + \rho.b^4.\omega^2.A_3^*.\phi + \rho.b^3.\omega^2.A_4^*.\eta \quad (3.6b)$$

Eq. (3.6a) and (3.6b) can be rearranged and rewritten in similar form with Eq. (3.1b):

$$[M]\{\ddot{u}\} + [C]\{\dot{u}\} + [K]\{u\} = 0 \quad (3.1b)$$

with:

$$[M] = \begin{bmatrix} m & 0 \\ 0 & I \end{bmatrix}$$

$$[C'] = \begin{bmatrix} c_\eta & 0 \\ 0 & c_\varphi \end{bmatrix} - \begin{bmatrix} \rho b^2 \cdot \omega \cdot H_1^* & \rho b^3 \cdot \omega \cdot H_2^* \\ \rho b^3 \cdot \omega \cdot A_1^* & \rho b^4 \cdot \omega \cdot A_2^* \end{bmatrix}$$

$$[K'] = \begin{bmatrix} k_\eta & 0 \\ 0 & k_\varphi \end{bmatrix} - \begin{bmatrix} \rho b^2 \cdot \omega^2 \cdot H_4^* & \rho b^3 \cdot \omega^2 \cdot H_3^* \\ \rho b^3 \cdot \omega^2 \cdot A_4^* & \rho b^4 \cdot \omega^2 \cdot A_3^* \end{bmatrix}$$

$$\{u\} = \begin{Bmatrix} \eta_0 \\ \varphi_0 \end{Bmatrix} e^{\lambda t} = \{u_0\} e^{\lambda t}, \quad \{\dot{u}\} = \lambda \{u\}, \quad \{\ddot{u}\} = \lambda^2 \{u\}$$

then:

$$[M] \lambda^2 \{u\} + [C'] \lambda \{u\} + [K'] \{u\} = 0 \quad (3.7)$$

In order to solve eigen-problem of Eq. (3.7), mathematical manipulation is needed so it can be solved with method applicable to the eigenvalue solution of an undamped case (Ge & Tanaka, 2000). Additional equation is added:

$$[M] \lambda \{u\} + [0] \{u\} = [M] \lambda \{u\} \quad (3.8)$$

Rearrange Eq. (3.7) and combine with Eq. (3.8), then:

$$\begin{aligned} [C'] \lambda \{u\} + [M] \lambda^2 \{u\} &= -[K'] \{u\} \\ [M] \lambda \{u\} + [0] \{u\} &= [M] \lambda \{u\} \end{aligned}$$

or in matrix form:

$$\begin{bmatrix} [C'] & [M] \\ [M] & [0] \end{bmatrix} \lambda \begin{Bmatrix} \{u\} \\ \lambda \{u\} \end{Bmatrix} = - \begin{bmatrix} [K'] & [0] \\ [0] & -[M] \end{bmatrix} \begin{Bmatrix} \{u\} \\ \lambda \{u\} \end{Bmatrix} \quad (3.9)$$

Eq. (3.9) is rearranged into general form of eigen-problem:

$$[A^*]\{Y\} = \lambda\{Y\} \quad (3.10)$$

where:

$$[A^*] = - \begin{bmatrix} [C'] & [M] \\ [M] & [0] \end{bmatrix}^{-1} \begin{bmatrix} [K'] & [0] \\ [0] & -[M] \end{bmatrix}$$

$$\{Y\} = \begin{Bmatrix} \{u\} \\ \lambda\{u\} \end{Bmatrix}$$

Because  $\{Y\} \neq \{0\}$ , we get  $[[A] - \lambda[I]] = 0$ . Solution of this equation is two groups of conjugate eigenvalues:

$$\begin{aligned} \lambda_j &= \lambda_{Rj} \pm i\lambda_{Ij} \\ &= -\zeta_j \cdot \omega_j \pm i\sqrt{1 - \zeta_j^2} \cdot \omega_j \end{aligned} \quad (3.11)$$

Where:

$\zeta_j$ : damping ratio of mode-j,  $\omega_j$ : circular frequency of mode-j. Flutter occurred when logarithmic damping equal to zero or  $\delta_j=0$ , which  $\delta_j=2 \cdot \pi \cdot \zeta_j$ . In other words, flutter occurred when  $\zeta_j$  equals zero or negative.

Substitute eigenvalues into Eq. (3.10) then we get eigenvector:

$$\{Z_{0j}\} = \begin{Bmatrix} \eta_{0j} \\ \varphi_{0j} \end{Bmatrix} \quad (3.12)$$

Amplitude ratio  $R_j$  and phase lag  $\psi_j$  from the largest heaving displacement to the largest torsional displacement of each mode is as follows:

$$C_{Rj} + iC_{Ij} = \frac{\eta_{0j}}{\varphi_{0j}} \quad (3.13)$$

$$R_j = \frac{|\eta_{0j}|}{|\varphi_{0j}|}, \quad \psi_j = \tan^{-1} \frac{C_{Ij}}{C_{Rj}} \quad (3.14)$$

### 3.1.2 Step-by-step (SBS) Analysis

Flutter onset velocity can be calculated with fair accuracy by using CEV, but it still has drawbacks such as lack of explanation about the mechanism involved, and no information about role of each aerodynamic derivatives to the stabilization or destabilization. Matsumoto introduced step-by-step (SBS) analysis to overcome this problems. SBS analysis can split the analysis into torsional branch and heaving branch.

### 3.1.2.1 Torsional Branch

#### Step 1

Assume harmonic torsional motion:

$$\varphi = \varphi_0 \cdot \sin(\omega_\varphi \cdot t) \quad (3.15)$$

$$\dot{\varphi} = \omega_\varphi \cdot \varphi_0 \cdot \cos(\omega_\varphi \cdot t) \quad (3.16)$$

Equation of motion becomes:

$$I \cdot \ddot{\varphi} + c_\varphi \cdot \dot{\varphi} + k_\varphi \cdot \varphi = \rho \cdot b^4 \cdot \omega_F \cdot A_2^* \cdot \dot{\varphi} + \rho \cdot b^4 \cdot \omega_F^2 \cdot A_3^* \cdot \varphi \quad (3.17)$$

Say  $\frac{k_\varphi}{I} = \omega_{\varphi 0}^2$  and  $c_\varphi = 0$  (no structural damping), then Eq. (3.17) becomes:

$$\ddot{\varphi} + \left( -\frac{\rho \cdot b^4}{I} \omega_F \cdot A_2^* \right) \dot{\varphi} + \left( \omega_{\varphi 0}^2 - \frac{\rho \cdot b^4}{I} \omega_F^2 \cdot A_3^* \right) \varphi = 0 \quad (3.18)$$

Recall the equation of motion for 1-DOF torsional free vibration :

$$\ddot{\varphi} + 2\zeta_\varphi \cdot \omega_\varphi \cdot \dot{\varphi} + \omega_\varphi^2 \cdot \varphi = 0 \quad (3.19)$$

Compare Eq. (3.18) with Eq. (3.19), then:

$$\zeta_\varphi = \frac{-\frac{\rho \cdot b^4}{I} \omega_F \cdot A_2^*}{2\omega_\varphi} \quad (3.20)$$

$$\omega_\varphi = \sqrt{\omega_{\varphi 0}^2 - \frac{\rho \cdot b^4}{I} \omega_F^2 \cdot A_3^*} \quad (3.21)$$

$$\omega_\varphi' = \sqrt{\left\{ \omega_{\varphi 0}^2 - \frac{\rho \cdot b^4}{I} \omega_F^2 \cdot A_3^* \right\} (1 - \zeta_\varphi^2)} \quad (3.22)$$

#### Step 2

Because of the effect of coupled derivatives, in the case of 2-DOF motion, heaving motion and lift force is induced by torsional motion:

$$m.\ddot{\eta} + c_\eta.\dot{\eta} + k_\eta.\eta = \rho.b^2.\omega_F.H_1^*.\dot{\eta} + \rho.b^3.\omega_F.H_2^*.\dot{\varphi} + \rho.b^3.\omega_F^2.H_3^*.\varphi + \rho.b^2.\omega_F^2.H_4^*.\eta \quad (3.23)$$

Say  $\frac{k_\eta}{m} = \omega_{\eta 0}^2$  and  $c_\eta = 0$  (no structural damping), then Eq. (3.23) becomes:

$$\ddot{\eta} + \left( -\frac{\rho.b^2}{m}\omega_F.H_1^* \right) \dot{\eta} + \left( \omega_{\eta 0}^2 - \frac{\rho.b^2}{m}\omega_F^2.H_4^* \right) \eta = \frac{\rho.b^3}{m}\omega_F.H_2^*.\dot{\varphi} + \frac{\rho.b^3}{m}\omega_F^2.H_3^*.\varphi \quad (3.24)$$

Recall the equation of motion for 1-DOF heaving forced vibration:

$$\ddot{\eta} + 2\zeta_\eta^*.\omega_\eta^*.\dot{\eta} + \omega_\eta^{*2}.\eta = F \quad (3.25)$$

Compare Eq. (3.25) with Eq. (3.24), then:

$$\zeta_\eta^* = \frac{-\frac{\rho.b^2}{m}\omega_F.H_1^*}{2\omega_\eta} \quad (3.26)$$

$$\omega_\eta^* = \sqrt{\omega_{\eta 0}^2 - \frac{\rho.b^2}{m}\omega_F^2.H_4^*} \quad (3.27)$$

$$\omega_\eta^{*'} = \sqrt{\left\{ \omega_{\eta 0}^2 - \frac{\rho.b^2}{m}\omega_F^2.H_4^* \right\} \left( 1 - \zeta_\eta^{*2} \right)} \quad (3.28)$$

$$F = \frac{\rho.b^3}{m}\omega_F.H_2^*.\dot{\varphi} + \frac{\rho.b^3}{m}\omega_F^2.H_3^*.\varphi \quad (3.29)$$

Here, torsional displacement is written as:

$$\varphi = \bar{\varphi}.\sin(\omega_\varphi.t) \quad (3.30)$$

$$\dot{\varphi} = \omega_\varphi.\bar{\varphi}.\cos(\omega_\varphi.t) = \omega_\varphi.\bar{\varphi}.\sin(\omega_\varphi.t + 90^\circ) \quad (3.31)$$

Substitute Eq. (3.30) and (3.31) to (3.29):

$$F = \frac{\rho b^3}{m} \omega_F H_2^* \dot{\varphi} + \frac{\rho b^3}{m} \omega_F^2 H_3^* \varphi = \frac{\rho b^3}{m} \omega_F \bar{\varphi} (H_2^* \omega_\varphi \sin(\omega_\varphi t + 90^\circ) + \omega_F H_3^* \sin(\omega_\varphi t)) \quad (3.32)$$

or:

$$F = \frac{\rho b^3}{m} \omega_F H_2^* \dot{\varphi} + \frac{\rho b^3}{m} \omega_F^2 H_3^* \varphi = \frac{\rho b^3}{m} \omega_F \bar{\varphi} \sqrt{(\omega_\varphi H_2^*)^2 + (\omega_F H_3^*)^2} \sin(\omega_\varphi t - \Delta) \quad (3.33)$$

where:

$\Delta$  = phase difference between maximum torsional displacement to maximum lift force due to torsional motion

$$\Delta = \tan^{-1} \left( -\frac{\omega_\varphi H_2^*}{\omega_F H_3^*} \right) \quad (3.34)$$

$$\cos \Delta = \frac{\omega_F H_3^*}{\sqrt{(\omega_\varphi H_2^*)^2 + (\omega_F H_3^*)^2}} \quad (3.35)$$

$$\sin \Delta = \frac{-\omega_\varphi H_2^*}{\sqrt{(\omega_\varphi H_2^*)^2 + (\omega_F H_3^*)^2}} \quad (3.36)$$

From Eq. (3.25), (3.29) and (3.32), the equation of heaving motion due to torsional motion is:

$$\ddot{\eta} + 2\zeta_\eta^* \omega_\eta^{*2} \dot{\eta} + \omega_\eta^{*2} \eta = \frac{\rho b^3}{m} \omega_F \bar{\varphi} (H_2^* \omega_\varphi \sin(\omega_\varphi t + 90^\circ) + \omega_F H_3^* \sin(\omega_\varphi t)) \quad (3.37)$$

Eq. (3.37) is solved by decomposing it into 2 components:  $\eta_1 \rightarrow$  in-phase velocity component and  $\eta_2 \rightarrow$  in-phase displacement component.

(1) in-phase velocity component

$$\ddot{\eta}_1 + 2\zeta_\eta^* \omega_\eta^{*2} \dot{\eta}_1 + \omega_\eta^{*2} \eta_1 = \frac{\rho b^3}{m} \omega_F \bar{\varphi} H_2^* \omega_\varphi \sin(\omega_\varphi t + 90^\circ) \quad (3.38)$$



Solution for Eq. (3.38) is:

$$\eta_1 = \frac{\frac{\rho \cdot b^3}{m} \omega_F \cdot \omega_\varphi \cdot H_2^* \cdot \bar{\varphi}}{\sqrt{(\omega_\eta^{*2} - \omega_\varphi^2)^2 + 4\zeta_\eta^{*2} \cdot \omega_\eta^{*2} \cdot \omega_\varphi^2}} \sin(\omega_\varphi \cdot t + 90^\circ - \theta) \quad (3.39)$$

Where:

$\theta$  = phase difference between maximum lift force due to torsional motion to maximum heaving displacement.

$$\theta = \tan^{-1} \left( \frac{2\zeta_\eta^* \cdot \omega_\eta^* \cdot \omega_\varphi}{\omega_\eta^{*2} - \omega_\varphi^2} \right) \quad (3.40)$$

$$\cos \theta = \frac{\omega_\eta^{*2} - \omega_\varphi^2}{\sqrt{(\omega_\eta^{*2} - \omega_\varphi^2)^2 + 4\zeta_\eta^{*2} \cdot \omega_\eta^{*2} \cdot \omega_\varphi^2}} \quad (3.41)$$

$$\sin \theta = \frac{2\zeta_\eta^* \cdot \omega_\eta^* \cdot \omega_\varphi}{\sqrt{(\omega_\eta^{*2} - \omega_\varphi^2)^2 + 4\zeta_\eta^{*2} \cdot \omega_\eta^{*2} \cdot \omega_\varphi^2}} \quad (3.42)$$

Amplitude of in-phase velocity heaving motion is:

$$\bar{\eta}_1 = \frac{\frac{\rho \cdot b^3}{m} \omega_F \cdot \omega_\varphi \cdot |H_2^*| \cdot \bar{\varphi}}{\sqrt{(\omega_\eta^{*2} - \omega_\varphi^2)^2 + 4\zeta_\eta^{*2} \cdot \omega_\eta^{*2} \cdot \omega_\varphi^2}} \quad (3.43)$$

$$\text{If } H_2^* > 0, \eta_1 = \bar{\eta}_1 \cdot \sin(\omega_\varphi \cdot t + 90^\circ - \theta) = \bar{\eta}_1 \cdot \sin(\omega_\varphi \cdot t - \theta_1) \quad \rightarrow \theta_1 = \theta - 90^\circ$$

$$H_2^* < 0, \eta_1 = \bar{\eta}_1 \cdot \sin(\omega_\varphi \cdot t + 90^\circ - \theta - 180^\circ) = \bar{\eta}_1 \cdot \sin(\omega_\varphi \cdot t - \theta_1) \quad \rightarrow \theta_1 = \theta + 90^\circ \quad (3.44)$$

Where:

$\theta_1$  = phase difference between maximum lift force due to torsional motion to maximum heaving displacement of in-phase velocity component.

(2) in-phase displacement component

$$\ddot{\eta}_2 + 2\zeta_{\eta}^* \omega_{\eta}^{*2} \dot{\eta}_2 + \omega_{\eta}^{*2} \eta_2 = \frac{\rho b^3}{m} \omega_F^2 \bar{\varphi} H_3^* \sin(\omega_{\varphi} t) \quad (3.45)$$

Solution for Eq. (3.45) is:

$$\eta_2 = \frac{\frac{\rho b^3}{m} \omega_F^2 H_3^* \bar{\varphi}}{\sqrt{(\omega_{\eta}^{*2} - \omega_{\varphi}^2)^2 + 4\zeta_{\eta}^{*2} \omega_{\eta}^{*2} \omega_{\varphi}^2}} \sin(\omega_{\varphi} t - \theta) \quad (3.46)$$

Amplitude of in-phase displacement heaving motion is:

$$\bar{\eta}_2 = \frac{\frac{\rho b^3}{m} \omega_F^2 |H_3^*| \bar{\varphi}}{\sqrt{(\omega_{\eta}^{*2} - \omega_{\varphi}^2)^2 + 4\zeta_{\eta}^{*2} \omega_{\eta}^{*2} \omega_{\varphi}^2}} \quad (3.47)$$

$$\text{If } H_3^* > 0, \eta_2 = \bar{\eta}_2 \cdot \sin(\omega_{\varphi} t - \theta) = \bar{\eta}_2 \cdot \sin(\omega_{\varphi} t - \theta_2) \quad \rightarrow \theta_2 = \theta$$

$$H_3^* < 0, \eta_2 = \bar{\eta}_2 \cdot \sin(\omega_{\varphi} t - \theta - 180^\circ) = \bar{\eta}_2 \cdot \sin(\omega_{\varphi} t - \theta_2) \quad \rightarrow \theta_2 = \theta + 180^\circ \quad (3.48)$$

where:

$\theta_2$  = phase difference between maximum lift force due to torsional motion to maximum heaving displacement of in-phase displacement component.

Total steady heaving response:

$$\eta = \eta_1 + \eta_2 = \bar{\eta}_1 \cdot \sin(\omega_{\varphi} t - \theta_1) + \bar{\eta}_2 \cdot \sin(\omega_{\varphi} t - \theta_2) \quad (3.49)$$

Phase difference from maximum lift force to maximum heaving displacement:

$$\psi = \Delta + \theta \quad (3.50)$$

### Step 3

Heaving motion affects torsional system, and the complete equation of torsional motion is:

$$\ddot{\varphi} + \omega_{\varphi 0}^2 \cdot \varphi = \frac{\rho \cdot b^4}{I} \omega_F \cdot A_2^* \cdot \dot{\varphi} + \frac{\rho \cdot b^4}{I} \omega_F^2 \cdot A_3^* \cdot \varphi + \frac{\rho \cdot b^3}{I} \omega_F \cdot A_1^* (\dot{\eta}_1 + \dot{\eta}_2) + \frac{\rho \cdot b^3}{I} \omega_F^2 \cdot A_4^* (\eta_1 + \eta_2) \quad (3.51)$$

Substitute heaving motion terms with Eq. (3.49) and its derivatives:

$$\begin{aligned} & \frac{\rho \cdot b^3}{I} \omega_F \cdot A_1^* (\dot{\eta}_1 + \dot{\eta}_2) + \frac{\rho \cdot b^3}{I} \omega_F^2 \cdot A_4^* (\eta_1 + \eta_2) = \\ & \frac{\rho \cdot b^3}{I} \omega_F \cdot A_1^* \cdot \omega_{\varphi} \left\{ \bar{\eta}_1 \cdot \cos(\omega_{\varphi} \cdot t - \theta_1) + \bar{\eta}_2 \cdot \cos(\omega_{\varphi} \cdot t - \theta_2) \right\} + \\ & \frac{\rho \cdot b^3}{I} \omega_F^2 \cdot A_4^* \left\{ \bar{\eta}_1 \cdot \sin(\omega_{\varphi} \cdot t - \theta_1) + \bar{\eta}_2 \cdot \sin(\omega_{\varphi} \cdot t - \theta_2) \right\} = \\ & \frac{\rho \cdot b^3}{I} \omega_F \cdot A_1^* \cdot \omega_{\varphi} \left\{ \bar{\eta}_1 \cdot \cos(\omega_{\varphi} \cdot t) \cos(\theta_1) + \bar{\eta}_1 \cdot \sin(\omega_{\varphi} \cdot t) \sin(\theta_1) + \bar{\eta}_2 \cdot \cos(\omega_{\varphi} \cdot t) \cos(\theta_2) + \bar{\eta}_2 \cdot \sin(\omega_{\varphi} \cdot t) \sin(\theta_2) \right\} + \\ & \frac{\rho \cdot b^3}{I} \omega_F^2 \cdot A_4^* \left\{ \bar{\eta}_1 \cdot \sin(\omega_{\varphi} \cdot t) \cos(\theta_1) - \bar{\eta}_1 \cdot \cos(\omega_{\varphi} \cdot t) \sin(\theta_1) + \bar{\eta}_2 \cdot \sin(\omega_{\varphi} \cdot t) \cos(\theta_2) - \bar{\eta}_2 \cdot \cos(\omega_{\varphi} \cdot t) \sin(\theta_2) \right\} \end{aligned} \quad (3.48)$$

We know that  $\varphi = \bar{\varphi} \cdot \sin(\omega_{\varphi} \cdot t) \rightarrow \sin(\omega_{\varphi} \cdot t) = \frac{\varphi}{\bar{\varphi}}$ , and

$$\dot{\varphi} = \omega_{\varphi} \cdot \bar{\varphi} \cdot \cos(\omega_{\varphi} \cdot t) \rightarrow \cos(\omega_{\varphi} \cdot t) = \frac{\dot{\varphi}}{\omega_{\varphi} \cdot \bar{\varphi}}$$

Then Eq. (3.48) becomes:

$$\begin{aligned} & \frac{\rho \cdot b^3}{I} \omega_F \cdot A_1^* (\dot{\eta}_1 + \dot{\eta}_2) + \frac{\rho \cdot b^3}{I} \omega_F^2 \cdot A_4^* (\eta_1 + \eta_2) = \\ & \frac{\rho \cdot b^3}{I} \omega_F \cdot A_1^* \cdot \omega_{\varphi} \left\{ \bar{\eta}_1 \frac{\dot{\varphi}}{\omega_{\varphi} \cdot \bar{\varphi}} \cos(\theta_1) + \bar{\eta}_1 \frac{\varphi}{\bar{\varphi}} \sin(\theta_1) + \bar{\eta}_2 \frac{\dot{\varphi}}{\omega_{\varphi} \cdot \bar{\varphi}} \cos(\theta_2) + \bar{\eta}_2 \frac{\varphi}{\bar{\varphi}} \sin(\theta_2) \right\} + \\ & \frac{\rho \cdot b^3}{I} \omega_F^2 \cdot A_4^* \left\{ \bar{\eta}_1 \frac{\varphi}{\bar{\varphi}} \cos(\theta_1) - \bar{\eta}_1 \frac{\dot{\varphi}}{\omega_{\varphi} \cdot \bar{\varphi}} \sin(\theta_1) + \bar{\eta}_2 \frac{\varphi}{\bar{\varphi}} \cos(\theta_2) - \bar{\eta}_2 \frac{\dot{\varphi}}{\omega_{\varphi} \cdot \bar{\varphi}} \sin(\theta_2) \right\} \end{aligned} \quad (3.49)$$

Substitute Eq. (3.47) and (3.43) into Eq. (3.49):

$$\begin{aligned}
& \frac{\rho b^3}{I} \omega_F \cdot A_1^* (\dot{\eta}_1 + \dot{\eta}_2) + \frac{\rho b^3}{I} \omega_F^2 \cdot A_4^* (\eta_1 + \eta_2) = \\
& \frac{\rho b^3}{I} \omega_F \cdot A_1^* \cdot \omega_\varphi \frac{\frac{\rho b^3}{m}}{\sqrt{(\omega_\eta^{*2} - \omega_\varphi^2)^2 + 4\zeta_\eta^{*2} \cdot \omega_\eta^{*2} \cdot \omega_\varphi^2}} \\
& \left\{ \omega_F \cdot \omega_\varphi \cdot |H_2^*| \cdot \bar{\varphi} \frac{\dot{\varphi}}{\omega_\varphi \cdot \bar{\varphi}} \cos(\theta_1) + \omega_F \cdot \omega_\varphi \cdot |H_2^*| \cdot \bar{\varphi} \frac{\varphi}{\bar{\varphi}} \sin(\theta_1) + \omega_F^2 \cdot |H_3^*| \cdot \bar{\varphi} \frac{\dot{\varphi}}{\omega_\varphi \cdot \bar{\varphi}} \cos(\theta_2) + \omega_F^2 \cdot |H_3^*| \cdot \bar{\varphi} \frac{\varphi}{\bar{\varphi}} \sin(\theta_2) \right\} \\
& + \frac{\rho b^3}{I} \omega_F^2 \cdot A_4^* \frac{\frac{\rho b^3}{m}}{\sqrt{(\omega_\eta^{*2} - \omega_\varphi^2)^2 + 4\zeta_\eta^{*2} \cdot \omega_\eta^{*2} \cdot \omega_\varphi^2}} \\
& \left\{ \omega_F \cdot \omega_\varphi \cdot |H_2^*| \cdot \bar{\varphi} \frac{\varphi}{\bar{\varphi}} \cos(\theta_1) - \omega_F \cdot \omega_\varphi \cdot |H_2^*| \cdot \bar{\varphi} \frac{\dot{\varphi}}{\omega_\varphi \cdot \bar{\varphi}} \sin(\theta_1) + \omega_F^2 \cdot |H_3^*| \cdot \bar{\varphi} \frac{\varphi}{\bar{\varphi}} \cos(\theta_2) - \omega_F^2 \cdot |H_3^*| \cdot \bar{\varphi} \frac{\dot{\varphi}}{\omega_\varphi \cdot \bar{\varphi}} \sin(\theta_2) \right\} \\
& \tag{3.50}
\end{aligned}$$

$$\begin{aligned}
& \Leftrightarrow \frac{\rho b^3}{I} \omega_F \cdot A_1^* (\dot{\eta}_1 + \dot{\eta}_2) + \frac{\rho b^3}{I} \omega_F^2 \cdot A_4^* (\eta_1 + \eta_2) = \\
& \frac{\left( \frac{\rho b^3}{I} \right) \left( \frac{\rho b^3}{m} \right)}{\sqrt{(\omega_\eta^{*2} - \omega_\varphi^2)^2 + 4\zeta_\eta^{*2} \cdot \omega_\eta^{*2} \cdot \omega_\varphi^2}} \\
& \left\{ \omega_F^2 \cdot \omega_\varphi \cdot A_1^* \cdot |H_2^*| \cdot \cos(\theta_1) \cdot \dot{\varphi} + \omega_F^2 \cdot \omega_\varphi^2 \cdot A_1^* \cdot |H_2^*| \cdot \sin(\theta_1) \cdot \varphi + \omega_F^3 \cdot A_1^* \cdot |H_3^*| \cdot \cos(\theta_2) \cdot \dot{\varphi} + \omega_F^3 \cdot \omega_\varphi \cdot A_1^* \cdot |H_3^*| \cdot \sin(\theta_2) \cdot \varphi \right\} \\
& + \frac{\left( \frac{\rho b^3}{I} \right) \left( \frac{\rho b^3}{m} \right)}{\sqrt{(\omega_\eta^{*2} - \omega_\varphi^2)^2 + 4\zeta_\eta^{*2} \cdot \omega_\eta^{*2} \cdot \omega_\varphi^2}} \\
& \left\{ \omega_F^3 \cdot \omega_\varphi \cdot A_4^* \cdot |H_2^*| \cdot \cos(\theta_1) \cdot \varphi - \omega_F^3 \cdot A_4^* \cdot |H_2^*| \cdot \sin(\theta_1) \cdot \dot{\varphi} + \omega_F^4 \cdot A_4^* \cdot |H_3^*| \cdot \cos(\theta_2) \cdot \varphi - \frac{\omega_F^4}{\omega_\varphi} \cdot A_4^* \cdot |H_3^*| \cdot \sin(\theta_2) \cdot \dot{\varphi} \right\}
\end{aligned}$$

$$\begin{aligned}
& \Leftrightarrow \frac{\rho b^3}{I} \omega_F \cdot A_1^* (\dot{\eta}_1 + \dot{\eta}_2) + \frac{\rho b^3}{I} \omega_F^2 \cdot A_4^* (\eta_1 + \eta_2) = \\
& \frac{\left( \frac{\rho b^3}{I} \right) \left( \frac{\rho b^3}{m} \right)}{\sqrt{(\omega_\eta^{*2} - \omega_\varphi^2)^2 + 4\zeta_\eta^{*2} \cdot \omega_\eta^{*2} \cdot \omega_\varphi^2}} \\
& \left\{ \omega_F^2 \cdot \omega_\varphi \cdot A_1^* \cdot |H_2^*| \cdot \cos(\theta_1) + \omega_F^3 \cdot A_1^* \cdot |H_3^*| \cdot \cos(\theta_2) - \omega_F^3 \cdot A_4^* \cdot |H_2^*| \cdot \sin(\theta_1) - \frac{\omega_F^4}{\omega_\varphi} \cdot A_4^* \cdot |H_3^*| \cdot \sin(\theta_2) \right\} \dot{\varphi} \\
& + \frac{\left( \frac{\rho b^3}{I} \right) \left( \frac{\rho b^3}{m} \right)}{\sqrt{(\omega_\eta^{*2} - \omega_\varphi^2)^2 + 4\zeta_\eta^{*2} \cdot \omega_\eta^{*2} \cdot \omega_\varphi^2}} \\
& \left\{ \omega_F^2 \cdot \omega_\varphi^2 \cdot A_1^* \cdot |H_2^*| \cdot \sin(\theta_1) + \omega_F^3 \cdot \omega_\varphi \cdot A_1^* \cdot |H_3^*| \cdot \sin(\theta_2) + \omega_F^3 \cdot \omega_\varphi \cdot A_4^* \cdot |H_2^*| \cdot \cos(\theta_1) + \omega_F^4 \cdot A_4^* \cdot |H_3^*| \cdot \cos(\theta_2) \right\} \varphi
\end{aligned}$$

Substitute this formula into Eq. (3.48):

$$\begin{aligned}
\ddot{\varphi} + \omega_{\varphi_0}^2 \cdot \varphi &= \frac{\rho \cdot b^4}{I} \omega_F \cdot A_2^* \cdot \dot{\varphi} + \frac{\rho \cdot b^4}{I} \omega_F^2 \cdot A_3^* \cdot \varphi \\
&+ \frac{\left(\frac{\rho \cdot b^3}{I}\right) \left(\frac{\rho \cdot b^3}{m}\right)}{\sqrt{\left(\omega_{\eta}^{*2} - \omega_{\varphi}^2\right)^2 + 4\zeta_{\eta}^{*2} \cdot \omega_{\eta}^{*2} \cdot \omega_{\varphi}^2}} \\
&\left\{ \omega_F^2 \cdot \omega_{\varphi} \cdot A_1^* \cdot |H_2^*| \cdot \cos(\theta_1) + \omega_F^3 \cdot A_1^* \cdot |H_3^*| \cdot \cos(\theta_2) - \omega_F^3 \cdot A_4^* \cdot |H_2^*| \cdot \sin(\theta_1) - \frac{\omega_F^4}{\omega_{\varphi}} \cdot A_4^* \cdot |H_3^*| \cdot \sin(\theta_2) \right\} \dot{\varphi} \\
&+ \frac{\left(\frac{\rho \cdot b^3}{I}\right) \left(\frac{\rho \cdot b^3}{m}\right)}{\sqrt{\left(\omega_{\eta}^{*2} - \omega_{\varphi}^2\right)^2 + 4\zeta_{\eta}^{*2} \cdot \omega_{\eta}^{*2} \cdot \omega_{\varphi}^2}} \\
&\left\{ \omega_F^2 \cdot \omega_{\varphi}^2 \cdot A_1^* \cdot |H_2^*| \cdot \sin(\theta_1) + \omega_F^3 \cdot \omega_{\varphi} \cdot A_1^* \cdot |H_3^*| \cdot \sin(\theta_2) + \omega_F^3 \cdot \omega_{\varphi} \cdot A_4^* \cdot |H_2^*| \cdot \cos(\theta_1) + \omega_F^4 \cdot A_4^* \cdot |H_3^*| \cdot \cos(\theta_2) \right\} \varphi
\end{aligned} \tag{3.51}$$

In flutter condition,  $\omega_{\varphi} = \omega_F$ , also a slight modification is introduced:

$$\frac{\left(\frac{\rho \cdot b^3}{I}\right) \left(\frac{\rho \cdot b^3}{m}\right)}{\sqrt{\left(\omega_{\eta}^{*2} - \omega_{\varphi}^2\right)^2 + 4\zeta_{\eta}^{*2} \cdot \omega_{\eta}^{*2} \cdot \omega_{\varphi}^2}} = \frac{\left(\frac{\rho \cdot b^3}{I}\right) \left(\frac{\rho \cdot b^3}{m}\right)}{\omega_{\eta}^{*2} \sqrt{\left(1 - \left(\frac{\omega_F}{\omega_{\eta}^*}\right)^2\right)^2 + 4\zeta_{\eta}^{*2} \left(\frac{\omega_F}{\omega_{\eta}^*}\right)^2}}$$

Eq. (3.51) becomes:

$$\begin{aligned}
\ddot{\phi} + \omega_{\phi_0}^2 \cdot \phi &= \frac{\rho \cdot b^4}{I} \omega_F \cdot A_2^* \cdot \dot{\phi} + \frac{\rho \cdot b^4}{I} \omega_F^2 \cdot A_3^* \cdot \phi \\
&+ \frac{\left(\frac{\rho \cdot b^3}{I}\right) \left(\frac{\rho \cdot b^3}{m}\right)}{\omega_{\eta}^{*2} \sqrt{\left(1 - \left(\frac{\omega_F}{\omega_{\eta}^*}\right)^2\right)^2 + 4\zeta_{\eta}^{*2} \left(\frac{\omega_F}{\omega_{\eta}^*}\right)^2}} \\
&\left\{ \omega_F^2 \cdot \omega_{\phi} \cdot A_1^* \cdot |H_2^*| \cdot \cos(\theta_1) + \omega_F^3 \cdot A_1^* \cdot |H_3^*| \cdot \cos(\theta_2) - \omega_F^3 \cdot A_4^* \cdot |H_2^*| \cdot \sin(\theta_1) - \frac{\omega_F^4}{\omega_{\phi}} \cdot A_4^* \cdot |H_3^*| \cdot \sin(\theta_2) \right\} \dot{\phi} \\
&+ \frac{\left(\frac{\rho \cdot b^3}{I}\right) \left(\frac{\rho \cdot b^3}{m}\right)}{\omega_{\eta}^{*2} \sqrt{\left(1 - \left(\frac{\omega_F}{\omega_{\eta}^*}\right)^2\right)^2 + 4\zeta_{\eta}^{*2} \left(\frac{\omega_F}{\omega_{\eta}^*}\right)^2}} \\
&\left\{ \omega_F^2 \cdot \omega_{\phi}^2 \cdot A_1^* \cdot |H_2^*| \cdot \sin(\theta_1) + \omega_F^3 \cdot \omega_{\phi} \cdot A_1^* \cdot |H_3^*| \cdot \sin(\theta_2) + \omega_F^3 \cdot \omega_{\phi} \cdot A_4^* \cdot |H_2^*| \cdot \cos(\theta_1) + \omega_F^4 \cdot A_4^* \cdot |H_3^*| \cdot \cos(\theta_2) \right\} \phi
\end{aligned} \tag{3.52}$$

Rearrange Eq. (3.52) into 1-DOF free vibration torsional motion as Eq. (3.19):

$$\ddot{\phi} + 2\zeta_{\phi} \omega_{\phi} \cdot \dot{\phi} + \omega_{\phi}^2 \cdot \phi = 0 \tag{3.19}$$

Where:

$$\begin{aligned}
2\zeta_{\phi} \omega_{\phi} &= -\frac{\rho \cdot b^4}{I} \omega_F \cdot A_2^* - \frac{\left(\frac{\rho \cdot b^3}{I}\right) \left(\frac{\rho \cdot b^3}{m}\right)}{\omega_{\eta}^{*2} \sqrt{\left(1 - \left(\frac{\omega_F}{\omega_{\eta}^*}\right)^2\right)^2 + 4\zeta_{\eta}^{*2} \left(\frac{\omega_F}{\omega_{\eta}^*}\right)^2}} \\
&\left\{ \omega_F^2 \cdot \omega_{\phi} \cdot A_1^* \cdot |H_2^*| \cdot \cos(\theta_1) + \omega_F^3 \cdot A_1^* \cdot |H_3^*| \cdot \cos(\theta_2) - \omega_F^3 \cdot A_4^* \cdot |H_2^*| \cdot \sin(\theta_1) - \frac{\omega_F^4}{\omega_{\phi}} \cdot A_4^* \cdot |H_3^*| \cdot \sin(\theta_2) \right\}
\end{aligned} \tag{3.53}$$

$$\begin{aligned}
\omega_{\phi}^2 &= -\frac{\rho \cdot b^4}{I} \omega_F^2 \cdot A_3^* - \frac{\left(\frac{\rho \cdot b^3}{I}\right) \left(\frac{\rho \cdot b^3}{m}\right)}{\omega_{\eta}^{*2} \sqrt{\left(1 - \left(\frac{\omega_F}{\omega_{\eta}^*}\right)^2\right)^2 + 4\zeta_{\eta}^{*2} \left(\frac{\omega_F}{\omega_{\eta}^*}\right)^2}} \\
&\left\{ \omega_F^2 \cdot \omega_{\phi}^2 \cdot A_1^* \cdot |H_2^*| \cdot \sin(\theta_1) + \omega_F^3 \cdot \omega_{\phi} \cdot A_1^* \cdot |H_3^*| \cdot \sin(\theta_2) + \omega_F^3 \cdot \omega_{\phi} \cdot A_4^* \cdot |H_2^*| \cdot \cos(\theta_1) + \omega_F^4 \cdot A_4^* \cdot |H_3^*| \cdot \cos(\theta_2) \right\}
\end{aligned}$$

(3.54)

We know  $\delta = 2\pi.\zeta$ , and at flutter condition  $\omega_F = \omega_\phi$ , then we get:

$$\delta_\phi = -\pi\left(\frac{\rho b^4}{I}\right)A_2^* - \pi\left(\frac{\rho b^4}{I}\right) \frac{\left(\frac{\rho b^2}{m}\right)\left(\frac{\omega_F}{\omega_\eta^*}\right)^2}{\sqrt{\left(1 - \left(\frac{\omega_F}{\omega_\eta^*}\right)^2\right)^2 + 4\zeta_\eta^{*2}\left(\frac{\omega_F}{\omega_\eta^*}\right)^2}} \left\{A_1^*|H_2^*|\cos(\theta_1) + A_1^*|H_3^*|\cos(\theta_2) - A_4^*|H_2^*|\sin(\theta_1) - A_4^*|H_3^*|\sin(\theta_2)\right\} \quad (3.55)$$

Let  $X = \pi\left(\frac{\rho b^4}{I}\right)$  and  $Y = \frac{\left(\frac{\rho b^2}{m}\right)\left(\frac{\omega_F}{\omega_\eta^*}\right)^2}{\sqrt{\left(1 - \left(\frac{\omega_F}{\omega_\eta^*}\right)^2\right)^2 + 4\zeta_\eta^{*2}\left(\frac{\omega_F}{\omega_\eta^*}\right)^2}}$ , then:

$$\delta_\phi = -X.A_2^* - \pi.X.Y\left\{A_1^*|H_2^*|\cos(\theta_1) + A_1^*|H_3^*|\cos(\theta_2) - A_4^*|H_2^*|\sin(\theta_1) - A_4^*|H_3^*|\sin(\theta_2)\right\} \quad (3.56)$$

Flutter occurred when  $\delta_\phi < 0$ , and  $\omega_\phi'$  is:

$$\omega_\phi' = \sqrt{\left\{\omega_{\phi_0}^2 - \left(\frac{X}{\pi}\right)\omega_F^2.A_3^* - \left(\frac{X.Y}{\pi}\right)\omega_F^2\left\{A_1^*|H_2^*|\sin(\theta_1) + A_1^*|H_3^*|\sin(\theta_2) + A_4^*|H_2^*|\cos(\theta_1) + A_4^*|H_3^*|\cos(\theta_2)\right\}\right\}}\left(1 - \zeta_\phi^2\right) \quad (3.57)$$

### 3.1.2.2 Heaving Branch

#### Step 1

Assume harmonic heaving motion:

$$\eta = \eta_0.\sin(\omega_\eta t) \quad (3.57)$$

$$\dot{\eta} = \omega_{\eta} \eta_0 \cdot \cos(\omega_{\eta} t) \quad (3.58)$$

Equation of motion becomes:

$$m \ddot{\eta} + c_{\eta} \dot{\eta} + k_{\eta} \eta = \rho b^2 \omega_F H_1^* \dot{\eta} + \rho b^2 \omega_F^2 H_4^* \eta \quad (3.59)$$

Say  $\frac{k_{\eta}}{m} = \omega_{\eta 0}^2$  and  $c_{\eta} = 0$  (no structural damping), then Eq. (3.59) becomes:

$$\ddot{\eta} + \left( -\frac{\rho b^2}{m} \omega_F H_1^* \right) \dot{\eta} + \left( \omega_{\eta 0}^2 - \frac{\rho b^2}{m} \omega_F^2 H_4^* \right) \eta = 0 \quad (3.60)$$

Recall the equation of motion for 1-DOF heaving free vibration :

$$\ddot{\eta} + 2\zeta_{\eta} \omega_{\eta} \dot{\eta} + \omega_{\eta}^2 \eta = 0 \quad (3.61)$$

Compare Eq. (3.61) with Eq. (3.60), then:

$$\zeta_{\eta} = \frac{-\frac{\rho b^2}{m} \omega_F H_1^*}{2\omega_{\eta}} \quad (3.62)$$

$$\omega_{\eta} = \sqrt{\omega_{\eta 0}^2 - \frac{\rho b^2}{m} \omega_F^2 H_4^*} \quad (3.63)$$

$$\omega_{\eta}' = \sqrt{\left\{ \omega_{\eta 0}^2 - \frac{\rho b^2}{m} \omega_F^2 H_4^* \right\} (1 - \zeta_{\eta}^2)} \quad (3.64)$$

## Step 2

Because of the effect of coupled derivatives, in the case of 2-DOF motion, torsional motion and torsional moment is induced by heaving motion:



$$I.\ddot{\varphi} + c_{\varphi}.\dot{\varphi} + k_{\varphi}.\varphi = \rho.b^3.\omega_F.A_1^*.\dot{\eta} + \rho.b^4.\omega_F.A_2^*.\dot{\varphi} + \rho.b^4.\omega_F^2.A_3^*.\varphi + \rho.b^3.\omega_F^2.A_4^*.\eta \quad (3.65)$$

Say  $\frac{k_{\varphi}}{I} = \omega_{\varphi 0}^2$  and  $c_{\varphi} = 0$  (no structural damping), then Eq. (3.65) becomes:

$$\ddot{\varphi} + \left( -\frac{\rho.b^4}{I}\omega_F.A_2^* \right) \dot{\varphi} + \left( \omega_{\varphi 0}^2 - \frac{\rho.b^4}{I}\omega_F^2.A_3^* \right) \varphi = \frac{\rho.b^3}{I}\omega_F.A_1^*.\dot{\eta} + \frac{\rho.b^3}{I}\omega_F^2.A_4^*.\eta \quad (3.66)$$

Recall the equation of motion for 1-DOF torsional forced vibration:

$$\ddot{\varphi} + 2\zeta_{\varphi}^*.\omega_{\varphi}^{*2}.\dot{\varphi} + \omega_{\varphi}^{*2}.\varphi = F \quad (3.67)$$

Compare Eq. (3.67) with Eq. (3.66), then:

$$\zeta_{\varphi}^* = \frac{-\frac{\rho.b^4}{I}\omega_F.A_2^*}{2\omega_{\varphi}} \quad (3.68)$$

$$\omega_{\varphi}^* = \sqrt{\omega_{\varphi 0}^2 - \frac{\rho.b^4}{I}\omega_F^2.A_3^*} \quad (3.69)$$

$$\omega_{\eta}^{*'} = \sqrt{\left\{ \omega_{\varphi 0}^2 - \frac{\rho.b^4}{I}\omega_F^2.A_3^* \right\} (1 - \zeta_{\varphi}^{*2})} \quad (3.70)$$

$$F = \frac{\rho.b^3}{I}\omega_F.A_1^*.\dot{\eta} + \frac{\rho.b^3}{I}\omega_F^2.A_4^*.\eta \quad (3.71)$$

Here, heaving displacement is written as:

$$\eta = \bar{\eta}.\sin(\omega_{\eta}t) \quad (3.72)$$

$$\dot{\eta} = \omega_{\eta}.\bar{\eta}.\cos(\omega_{\eta}t) = \omega_{\eta}.\bar{\eta}.\sin(\omega_{\eta}t + 90^0) \quad (3.73)$$

Substitute Eq. (3.72) and (3.73) to (3.71):

$$F = \frac{\rho.b^3}{I}.\omega_F.A_1^*.\dot{\eta} + \frac{\rho.b^3}{I}.\omega_F^2.A_4^*.\eta = \frac{\rho.b^3}{I}\omega_F.\bar{\eta}\left(A_1^*.\omega_\eta.\sin(\omega_\eta.t + 90^\circ) + \omega_F.A_4^*.\sin(\omega_\eta.t)\right) \quad (3.74)$$

Or:

$$F = \frac{\rho.b^3}{I}.\omega_F.A_1^*.\dot{\eta} + \frac{\rho.b^3}{I}.\omega_F^2.A_4^*.\eta = \frac{\rho.b^3}{I}\omega_F.\bar{\eta}\sqrt{(\omega_\eta.A_1^*)^2 + (\omega_F.A_4^*)^2}.\sin(\omega_\eta.t - \Delta) \quad (3.75)$$

Where:

$\Delta$  = phase difference between maximum heaving displacement to maximum torsional moment due to heaving motion

$$\Delta = \tan^{-1}\left(-\frac{\omega_\eta.A_1^*}{\omega_F.A_4^*}\right) \quad (3.76)$$

$$\cos \Delta = \frac{\omega_F.A_4^*}{\sqrt{(\omega_\eta.A_1^*)^2 + (\omega_F.A_4^*)^2}} \quad (3.77)$$

$$\sin \Delta = \frac{-\omega_\eta.A_1^*}{\sqrt{(\omega_\eta.A_1^*)^2 + (\omega_F.A_4^*)^2}} \quad (3.78)$$

From Eq. (3.67), (3.71) and (3.74), the equation of torsional motion due to heaving motion is:

$$\ddot{\varphi} + 2\zeta_\varphi^*.\omega_\varphi^{*2}.\dot{\varphi} + \omega_\varphi^{*2}.\varphi = \frac{\rho.b^3}{I}\omega_F.\bar{\eta}\left(A_1^*.\omega_\eta.\sin(\omega_\eta.t + 90^\circ) + \omega_F.A_4^*.\sin(\omega_\eta.t)\right) \quad (3.79)$$

Eq. (3.79) is solved by decomposing it into 2 components:  $\varphi_1 \rightarrow$  in-phase velocity component and  $\varphi_2 \rightarrow$  in-phase displacement component.

(1) in-phase velocity component

$$\ddot{\varphi}_1 + 2\zeta_\varphi^* \cdot \omega_\varphi^{*2} \cdot \dot{\varphi}_1 + \omega_\varphi^{*2} \cdot \varphi_1 = \frac{\rho b^3}{I} \omega_F \cdot A_1^* \cdot \omega_\eta \cdot \bar{\eta} \cdot \sin(\omega_\eta \cdot t + 90^\circ) \quad (3.80)$$

Solution for Eq. (3.80) is:

$$\varphi_1 = \frac{\frac{\rho b^3}{I} \omega_F \cdot \omega_\eta \cdot A_1^* \cdot \bar{\eta}}{\sqrt{(\omega_\varphi^{*2} - \omega_\eta^2)^2 + 4\zeta_\varphi^{*2} \cdot \omega_\varphi^{*2} \cdot \omega_\eta^2}} \sin(\omega_\eta \cdot t + 90^\circ - \theta) \quad (3.81)$$

Where:

$\theta$  = phase difference between maximum torsional moment due to heaving motion to maximum torsional displacement.

$$\theta = \tan^{-1} \left( \frac{2\zeta_\varphi^* \cdot \omega_\varphi^* \cdot \omega_\eta}{\omega_\varphi^{*2} - \omega_\eta^2} \right) \quad (3.82)$$

$$\cos \theta = \frac{\omega_\varphi^{*2} - \omega_\eta^2}{\sqrt{(\omega_\varphi^{*2} - \omega_\eta^2)^2 + 4\zeta_\varphi^{*2} \cdot \omega_\varphi^{*2} \cdot \omega_\eta^2}} \quad (3.83)$$

$$\sin \theta = \frac{2\zeta_\varphi^* \cdot \omega_\varphi^* \cdot \omega_\eta}{\sqrt{(\omega_\varphi^{*2} - \omega_\eta^2)^2 + 4\zeta_\varphi^{*2} \cdot \omega_\varphi^{*2} \cdot \omega_\eta^2}} \quad (3.84)$$

Amplitude of in-phase velocity heaving motion is:

$$\bar{\varphi}_1 = \frac{\frac{\rho b^3}{I} \omega_F \cdot \omega_\eta \cdot |A_1^*| \cdot \bar{\eta}}{\sqrt{(\omega_\varphi^{*2} - \omega_\eta^2)^2 + 4\zeta_\varphi^{*2} \cdot \omega_\varphi^{*2} \cdot \omega_\eta^2}} \quad (3.85)$$

$$\begin{aligned}
\text{If } A_I^* > 0, \varphi_1 &= \bar{\varphi}_1 \cdot \sin(\omega_\eta \cdot t + 90^\circ - \theta) = \bar{\varphi}_1 \cdot \sin(\omega_\eta \cdot t - \theta_1) & \rightarrow \theta_1 &= \theta - 90^\circ \\
A_I^* < 0, \varphi_1 &= \bar{\varphi}_1 \cdot \sin(\omega_\eta \cdot t + 90^\circ - \theta - 180^\circ) = \bar{\varphi}_1 \cdot \sin(\omega_\eta \cdot t - \theta_1) & \rightarrow \theta_1 &= \theta + 90^\circ
\end{aligned} \quad (3.86)$$

Where:

$\theta_I$  = phase difference between maximum torsional moment due to heaving motion to maximum torsional displacement of in-phase velocity component.

(2) in-phase displacement component

$$\ddot{\varphi}_2 + 2\zeta_\varphi^* \cdot \omega_\varphi^{*2} \cdot \dot{\varphi}_2 + \omega_\varphi^{*2} \cdot \varphi_2 = \frac{\rho \cdot b^3}{I} \omega_F^2 \cdot \bar{\varphi} \cdot A_4^* \cdot \sin(\omega_\eta \cdot t) \quad (3.87)$$

Solution for Eq. (3.87) is:

$$\varphi_2 = \frac{\frac{\rho \cdot b^3}{I} \omega_F^2 \cdot A_4^* \cdot \bar{\eta}}{\sqrt{(\omega_\varphi^{*2} - \omega_\eta^2)^2 + 4\zeta_\varphi^{*2} \cdot \omega_\varphi^{*2} \cdot \omega_\eta^2}} \sin(\omega_\eta \cdot t - \theta) \quad (3.88)$$

Amplitude of in-phase displacement heaving motion is:

$$\bar{\varphi}_2 = \frac{\frac{\rho \cdot b^3}{I} \omega_F^2 \cdot |A_4^*| \cdot \bar{\eta}}{\sqrt{(\omega_\varphi^{*2} - \omega_\eta^2)^2 + 4\zeta_\varphi^{*2} \cdot \omega_\varphi^{*2} \cdot \omega_\eta^2}} \quad (3.89)$$

$$\begin{aligned}
\text{If } A_4^* > 0, \varphi_2 &= \bar{\varphi}_2 \cdot \sin(\omega_\eta \cdot t - \theta) = \bar{\varphi}_2 \cdot \sin(\omega_\eta \cdot t - \theta_2) & \rightarrow \theta_2 &= \theta \\
A_4^* < 0, \varphi_2 &= \bar{\varphi}_2 \cdot \sin(\omega_\eta \cdot t - \theta - 180^\circ) = \bar{\varphi}_2 \cdot \sin(\omega_\eta \cdot t - \theta_2) & \rightarrow \theta_2 &= \theta + 180^\circ
\end{aligned} \quad (3.90)$$

Where:

$\theta_2$  = phase difference between maximum torsional moment due to heaving motion to maximum torsional displacement of in-phase displacement component.

Total steady torsional response:

$$\varphi = \varphi_1 + \varphi_2 = \bar{\varphi}_1 \cdot \sin(\omega_\eta t - \theta_1) + \bar{\varphi}_2 \cdot \sin(\omega_\eta t - \theta_2) \quad (3.91)$$

Phase difference from maximum torsional moment to maximum torsional displacement:

$$\psi = \Delta + \theta \quad (3.92)$$

### Step 3

Torsional motion affects heaving system, and the complete equation of heaving motion is:

$$\ddot{\eta} + \omega_{\eta 0}^2 \cdot \eta = \frac{\rho b^2}{m} \omega_F \cdot H_1^* \cdot \dot{\eta} + \frac{\rho b^2}{m} \omega_F^2 \cdot H_4^* \cdot \eta + \frac{\rho b^3}{m} \omega_F \cdot H_2^* (\dot{\varphi}_1 + \dot{\varphi}_2) + \frac{\rho b^3}{m} \omega_F^2 \cdot H_3^* (\varphi_1 + \varphi_2) \quad (3.93)$$

Substitute heaving motion terms with Eq. (3.91) and its derivatives:

$$\begin{aligned} & \frac{\rho b^3}{m} \omega_F \cdot H_2^* (\dot{\varphi}_1 + \dot{\varphi}_2) + \frac{\rho b^3}{m} \omega_F^2 \cdot H_3^* (\varphi_1 + \varphi_2) = \\ & \frac{\rho b^3}{m} \omega_F \cdot H_2^* \cdot \omega_\eta \{ \bar{\varphi}_1 \cdot \cos(\omega_\eta t - \theta_1) + \bar{\varphi}_2 \cdot \cos(\omega_\eta t - \theta_2) \} + \\ & \frac{\rho b^3}{m} \omega_F^2 \cdot H_3^* \{ \bar{\varphi}_1 \cdot \sin(\omega_\eta t - \theta_1) + \bar{\varphi}_2 \cdot \sin(\omega_\eta t - \theta_2) \} = \\ & \frac{\rho b^3}{m} \omega_F \cdot H_2^* \cdot \omega_\eta \{ \bar{\varphi}_1 \cdot \cos(\omega_\eta t) \cos(\theta_1) + \bar{\varphi}_1 \cdot \sin(\omega_\eta t) \sin(\theta_1) + \bar{\varphi}_2 \cdot \cos(\omega_\eta t) \cos(\theta_2) + \bar{\varphi}_2 \cdot \sin(\omega_\eta t) \sin(\theta_2) \} + \\ & \frac{\rho b^3}{m} \omega_F^2 \cdot H_3^* \{ \bar{\varphi}_1 \cdot \sin(\omega_\eta t) \cos(\theta_1) - \bar{\varphi}_1 \cdot \cos(\omega_\eta t) \sin(\theta_1) + \bar{\varphi}_2 \cdot \sin(\omega_\eta t) \cos(\theta_2) - \bar{\varphi}_2 \cdot \cos(\omega_\eta t) \sin(\theta_2) \} \end{aligned} \quad (3.94)$$

We know that  $\eta = \bar{\eta} \cdot \sin(\omega_\eta t) \rightarrow \sin(\omega_\eta t) = \frac{\eta}{\bar{\eta}}$ , and

$$\dot{\eta} = \omega_\eta \bar{\eta} \cdot \cos(\omega_\eta t) \rightarrow \cos(\omega_\eta t) = \frac{\dot{\eta}}{\omega_\eta \bar{\eta}}$$

Then Eq. (3.94) becomes:

$$\begin{aligned} & \frac{\rho b^3}{m} \omega_F H_2^* (\dot{\varphi}_1 + \dot{\varphi}_2) + \frac{\rho b^3}{m} \omega_F^2 H_3^* (\varphi_1 + \varphi_2) = \\ & \frac{\rho b^3}{m} \omega_F H_2^* \omega_\eta \left\{ \bar{\varphi}_1 \frac{\dot{\eta}}{\omega_\eta \bar{\eta}} \cos(\theta_1) + \bar{\varphi}_1 \frac{\eta}{\bar{\eta}} \sin(\theta_1) + \bar{\varphi}_2 \frac{\dot{\eta}}{\omega_\eta \bar{\eta}} \cos(\theta_2) + \bar{\varphi}_2 \frac{\eta}{\bar{\eta}} \sin(\theta_2) \right\} + \quad (3.95) \\ & \frac{\rho b^3}{m} \omega_F^2 H_3^* \left\{ \bar{\varphi}_1 \frac{\eta}{\bar{\eta}} \cos(\theta_1) - \bar{\varphi}_1 \frac{\dot{\eta}}{\omega_\eta \bar{\eta}} \sin(\theta_1) + \bar{\varphi}_2 \frac{\eta}{\bar{\eta}} \cos(\theta_2) - \bar{\varphi}_2 \frac{\dot{\eta}}{\omega_\eta \bar{\eta}} \sin(\theta_2) \right\} \end{aligned}$$

Substitute Eq. (3.85) and (3.89) into Eq. (3.95):

$$\begin{aligned} & \frac{\rho b^3}{m} \omega_F H_2^* (\dot{\varphi}_1 + \dot{\varphi}_2) + \frac{\rho b^3}{m} \omega_F^2 H_3^* (\varphi_1 + \varphi_2) = \\ & \frac{\rho b^3}{m} \omega_F H_2^* \omega_\eta \frac{\frac{\rho b^3}{I}}{\sqrt{(\omega_\phi^{*2} - \omega_\eta^2)^2 + 4\zeta_\phi^{*2} \omega_\phi^{*2} \omega_\eta^2}} \\ & \left\{ \omega_F \omega_\eta |A_1^*| \bar{\eta} \frac{\dot{\eta}}{\omega_\eta \bar{\eta}} \cos(\theta_1) + \omega_F \omega_\eta |A_1^*| \bar{\eta} \frac{\eta}{\bar{\eta}} \sin(\theta_1) + \omega_F^2 |A_4^*| \bar{\eta} \frac{\dot{\eta}}{\omega_\eta \bar{\eta}} \cos(\theta_2) + \omega_F^2 |A_4^*| \bar{\eta} \frac{\eta}{\bar{\eta}} \sin(\theta_2) \right\} \\ & + \frac{\rho b^3}{I} \omega_F^2 H_3^* \frac{\frac{\rho b^3}{I}}{\sqrt{(\omega_\phi^{*2} - \omega_\eta^2)^2 + 4\zeta_\phi^{*2} \omega_\phi^{*2} \omega_\eta^2}} \\ & \left\{ \omega_F \omega_\eta |A_1^*| \bar{\eta} \frac{\eta}{\bar{\eta}} \cos(\theta_1) - \omega_F \omega_\eta |H_2^*| \bar{\eta} \frac{\dot{\eta}}{\omega_\eta \bar{\eta}} \sin(\theta_1) + \omega_F^2 |A_4^*| \bar{\eta} \frac{\eta}{\bar{\eta}} \cos(\theta_2) - \omega_F^2 |A_4^*| \bar{\eta} \frac{\dot{\eta}}{\omega_\eta \bar{\eta}} \sin(\theta_2) \right\} \quad (3.96) \end{aligned}$$

$$\begin{aligned}
&\Leftrightarrow \frac{\rho b^3}{m} \omega_F H_2^*(\dot{\varphi}_1 + \dot{\varphi}_2) + \frac{\rho b^3}{m} \omega_F^2 H_3^*(\varphi_1 + \varphi_2) = \\
&\frac{\left(\frac{\rho b^3}{I}\right)\left(\frac{\rho b^3}{m}\right)}{\sqrt{\left(\omega_\varphi^{*2} - \omega_\eta^2\right)^2 + 4\zeta_\varphi^{*2} \omega_\varphi^{*2} \omega_\eta^2}} \\
&\left\{ \omega_F^2 \omega_\eta H_2^* |A_1^*| \cos(\theta_1) \dot{\eta} + \omega_F^2 \omega_\eta^2 H_2^* |A_1^*| \sin(\theta_1) \eta + \omega_F^3 H_2^* |A_4^*| \cos(\theta_2) \dot{\eta} + \omega_F^3 \omega_\eta H_2^* |A_4^*| \sin(\theta_2) \eta \right\} \\
&+ \frac{\left(\frac{\rho b^3}{I}\right)\left(\frac{\rho b^3}{m}\right)}{\sqrt{\left(\omega_\varphi^{*2} - \omega_\eta^2\right)^2 + 4\zeta_\varphi^{*2} \omega_\varphi^{*2} \omega_\eta^2}} \\
&\left\{ \omega_F^3 \omega_\eta H_3^* |A_1^*| \cos(\theta_1) \eta - \omega_F^3 H_3^* |A_1^*| \sin(\theta_1) \dot{\eta} + \omega_F^4 H_3^* |A_4^*| \cos(\theta_2) \eta - \frac{\omega_F^4}{\omega_\eta} H_3^* |A_4^*| \sin(\theta_2) \dot{\eta} \right\}
\end{aligned}$$

$$\begin{aligned}
&\Leftrightarrow \frac{\rho b^3}{m} \omega_F H_2^*(\dot{\varphi}_1 + \dot{\varphi}_2) + \frac{\rho b^3}{m} \omega_F^2 H_3^*(\varphi_1 + \varphi_2) = \\
&\frac{\left(\frac{\rho b^3}{I}\right)\left(\frac{\rho b^3}{m}\right)}{\sqrt{\left(\omega_\varphi^{*2} - \omega_\eta^2\right)^2 + 4\zeta_\varphi^{*2} \omega_\varphi^{*2} \omega_\eta^2}} \\
&\left\{ \omega_F^2 \omega_\eta H_2^* |A_1^*| \cos(\theta_1) + \omega_F^3 H_2^* |A_4^*| \cos(\theta_2) - \omega_F^3 H_3^* |A_1^*| \sin(\theta_1) - \frac{\omega_F^4}{\omega_\eta} H_3^* |A_4^*| \sin(\theta_2) \right\} \dot{\eta} \\
&+ \frac{\left(\frac{\rho b^3}{I}\right)\left(\frac{\rho b^3}{m}\right)}{\sqrt{\left(\omega_\varphi^{*2} - \omega_\eta^2\right)^2 + 4\zeta_\varphi^{*2} \omega_\varphi^{*2} \omega_\eta^2}} \\
&\left\{ \omega_F^2 \omega_\eta^2 H_2^* |A_1^*| \sin(\theta_1) + \omega_F^3 \omega_\eta H_2^* |A_4^*| \sin(\theta_2) + \omega_F^3 \omega_\eta H_3^* |A_1^*| \cos(\theta_1) + \omega_F^4 H_3^* |A_4^*| \cos(\theta_2) \right\} \eta
\end{aligned}$$

Substitute this formula into Eq. (3.94):

$$\begin{aligned}
\ddot{\eta} + \omega_{\eta 0}^2 \cdot \eta &= \frac{\rho \cdot b^2}{m} \omega_F \cdot H_1^* \cdot \dot{\eta} + \frac{\rho \cdot b^2}{m} \omega_F^2 \cdot H_4^* \cdot \eta \\
&+ \frac{\left(\frac{\rho \cdot b^3}{I}\right) \left(\frac{\rho \cdot b^3}{m}\right)}{\sqrt{\left(\omega_{\varphi}^{*2} - \omega_{\eta}^2\right)^2 + 4\zeta_{\varphi}^{*2} \cdot \omega_{\varphi}^{*2} \cdot \omega_{\eta}^2}} \\
&\left\{ \omega_F^2 \cdot \omega_{\eta} \cdot H_2^* \cdot |A_1^*| \cdot \cos(\theta_1) + \omega_F^3 \cdot H_2^* \cdot |A_4^*| \cdot \cos(\theta_2) - \omega_F^3 \cdot H_3^* \cdot |A_1^*| \cdot \sin(\theta_1) - \frac{\omega_F^4}{\omega_{\eta}} \cdot H_3^* \cdot |A_4^*| \cdot \sin(\theta_2) \right\} \dot{\eta} \\
&+ \frac{\left(\frac{\rho \cdot b^3}{I}\right) \left(\frac{\rho \cdot b^3}{m}\right)}{\sqrt{\left(\omega_{\varphi}^{*2} - \omega_{\eta}^2\right)^2 + 4\zeta_{\varphi}^{*2} \cdot \omega_{\varphi}^{*2} \cdot \omega_{\eta}^2}} \\
&\left\{ \omega_F^2 \cdot \omega_{\eta}^2 \cdot H_2^* \cdot |A_1^*| \cdot \sin(\theta_1) + \omega_F^3 \cdot \omega_{\eta} \cdot H_2^* \cdot |A_4^*| \cdot \sin(\theta_2) + \omega_F^3 \cdot \omega_{\eta} \cdot H_3^* \cdot |A_1^*| \cdot \cos(\theta_1) + \omega_F^4 \cdot H_3^* \cdot |A_4^*| \cdot \cos(\theta_2) \right\} \eta
\end{aligned} \tag{3.97}$$

In flutter condition,  $\omega_{\eta} = \omega_F$ , also a slight modification is introduced:

$$\frac{\left(\frac{\rho \cdot b^3}{I}\right) \left(\frac{\rho \cdot b^3}{m}\right)}{\sqrt{\left(\omega_{\varphi}^{*2} - \omega_{\eta}^2\right)^2 + 4\zeta_{\varphi}^{*2} \cdot \omega_{\varphi}^{*2} \cdot \omega_{\eta}^2}} = \frac{\left(\frac{\rho \cdot b^3}{I}\right) \left(\frac{\rho \cdot b^3}{m}\right)}{\omega_{\eta}^{*2} \sqrt{\left(1 - \left(\frac{\omega_F}{\omega_{\varphi}^*}\right)^2\right)^2 + 4\zeta_{\varphi}^{*2} \left(\frac{\omega_F}{\omega_{\varphi}^*}\right)^2}}$$

Eq. (3.97) becomes:



$$\begin{aligned}
\ddot{\eta} + \omega_{\eta 0}^2 \cdot \eta &= \frac{\rho \cdot b^2}{m} \omega_F \cdot H_1^* \cdot \dot{\eta} + \frac{\rho \cdot b^2}{m} \omega_F^2 \cdot H_4^* \cdot \eta \\
&+ \frac{\left(\frac{\rho \cdot b^3}{I}\right) \left(\frac{\rho \cdot b^3}{m}\right)}{\omega_{\eta}^{*2} \sqrt{\left(1 - \left(\frac{\omega_F}{\omega_{\varphi}^*}\right)^2\right)^2 + 4\zeta_{\varphi}^{*2} \left(\frac{\omega_F}{\omega_{\varphi}}\right)^2}} \\
&\left\{ \omega_F^2 \cdot \omega_{\eta} \cdot H_2^* \cdot |A_1^*| \cdot \cos(\theta_1) + \omega_F^3 \cdot H_2^* \cdot |A_4^*| \cdot \cos(\theta_2) - \omega_F^3 \cdot H_3^* \cdot |A_1^*| \cdot \sin(\theta_1) - \frac{\omega_F^4}{\omega_{\eta}} \cdot H_3^* \cdot |A_4^*| \cdot \sin(\theta_2) \right\} \dot{\eta} \\
&+ \frac{\left(\frac{\rho \cdot b^3}{I}\right) \left(\frac{\rho \cdot b^3}{m}\right)}{\omega_{\eta}^{*2} \sqrt{\left(1 - \left(\frac{\omega_F}{\omega_{\varphi}^*}\right)^2\right)^2 + 4\zeta_{\varphi}^{*2} \left(\frac{\omega_F}{\omega_{\varphi}}\right)^2}} \\
&\left\{ \omega_F^2 \cdot \omega_{\eta}^2 \cdot H_2^* \cdot |A_1^*| \cdot \sin(\theta_1) + \omega_F^3 \cdot \omega_{\eta} \cdot H_2^* \cdot |A_4^*| \cdot \sin(\theta_2) + \omega_F^3 \cdot \omega_{\eta} \cdot H_3^* \cdot |A_1^*| \cdot \cos(\theta_1) + \omega_F^4 \cdot H_3^* \cdot |A_4^*| \cdot \cos(\theta_2) \right\} \eta
\end{aligned} \tag{3.98}$$

Rearrange Eq. (3.98) into 1-DOF free vibration torsional motion as Eq. (3.61):

$$\ddot{\eta} + 2\zeta_{\eta} \cdot \omega_{\eta} \cdot \dot{\eta} + \omega_{\eta}^2 \cdot \eta = 0 \tag{3.61}$$

Where:

$$\begin{aligned}
2\zeta_{\eta} \cdot \omega_{\eta} &= -\frac{\rho \cdot b^2}{m} \omega_F \cdot H_1^* - \frac{\left(\frac{\rho \cdot b^3}{I}\right) \left(\frac{\rho \cdot b^3}{m}\right)}{\omega_{\eta}^{*2} \sqrt{\left(1 - \left(\frac{\omega_F}{\omega_{\varphi}^*}\right)^2\right)^2 + 4\zeta_{\varphi}^{*2} \left(\frac{\omega_F}{\omega_{\varphi}}\right)^2}} \\
&\left\{ \omega_F^2 \cdot \omega_{\eta} \cdot H_2^* \cdot |A_1^*| \cdot \cos(\theta_1) + \omega_F^3 \cdot H_2^* \cdot |A_4^*| \cdot \cos(\theta_2) - \omega_F^3 \cdot H_3^* \cdot |A_1^*| \cdot \sin(\theta_1) - \frac{\omega_F^4}{\omega_{\eta}} \cdot H_3^* \cdot |A_4^*| \cdot \sin(\theta_2) \right\}
\end{aligned} \tag{3.99}$$

$$\omega_{\eta}^2 = -\frac{\rho.b^2}{m}\omega_F^2.H_4^* - \frac{\left(\frac{\rho.b^3}{I}\right)\left(\frac{\rho.b^3}{m}\right)}{\omega_{\eta}^2 \sqrt{\left(1 - \left(\frac{\omega_F}{\omega_{\phi}^*}\right)^2\right)^2 + 4\zeta_{\phi}^{*2}\left(\frac{\omega_F}{\omega_{\phi}^*}\right)^2}} \left\{ \omega_F^2.\omega_{\eta}^2.H_2^*.|A_1^*|. \sin(\theta_1) + \omega_F^3.\omega_{\eta}.H_2^*.|A_4^*|. \sin(\theta_2) + \omega_F^3.\omega_{\eta}.H_3^*.|A_1^*|. \cos(\theta_1) + \omega_F^4.H_3^*.|A_4^*|. \cos(\theta_2) \right\} \quad (3.100)$$

We know  $\delta = 2\pi.\zeta$ , and at flutter condition  $\omega_F = \omega_{\eta}$ , then we get:

$$\delta_{\eta} = -\pi\left(\frac{\rho.b^2}{m}\right)H_1^* - \pi\left(\frac{\rho.b^2}{m}\right) \frac{\left(\frac{\rho.b^4}{I}\right)\left(\frac{\omega_F}{\omega_{\phi}^*}\right)^2}{\sqrt{\left(1 - \left(\frac{\omega_F}{\omega_{\phi}^*}\right)^2\right)^2 + 4\zeta_{\phi}^{*2}\left(\frac{\omega_F}{\omega_{\phi}^*}\right)^2}} \left\{ H_2^*.|A_1^*|. \cos(\theta_1) + H_2^*.|A_4^*|. \cos(\theta_2) - H_3^*.|A_1^*|. \sin(\theta_1) - H_3^*.|A_4^*|. \sin(\theta_2) \right\} \quad (3.101)$$

Let  $X = \pi\left(\frac{\rho.b^2}{m}\right)$  and  $Y = \frac{\left(\frac{\rho.b^4}{I}\right)\left(\frac{\omega_F}{\omega_{\phi}^*}\right)^2}{\sqrt{\left(1 - \left(\frac{\omega_F}{\omega_{\phi}^*}\right)^2\right)^2 + 4\zeta_{\phi}^{*2}\left(\frac{\omega_F}{\omega_{\phi}^*}\right)^2}}$ , then:

$$\delta_{\eta} = -X.H_1^* - X.Y\left\{H_2^*.|A_1^*|. \cos(\theta_1) + H_2^*.|A_4^*|. \cos(\theta_2) - H_3^*.|A_1^*|. \sin(\theta_1) - H_3^*.|A_4^*|. \sin(\theta_2)\right\} \quad (3.102)$$

Flutter occurred when  $\delta_{\eta} < 0$ , and  $\omega_{\eta}'$  is:

$$\omega_{\eta}' = \sqrt{\left\{ \omega_{\eta 0}^2 - \left(\frac{X}{\pi}\right)\omega_F^2.H_4^* - \left(\frac{X.Y}{\pi}\right)\omega_F^2\left\{H_2^*.|A_1^*|. \cos(\theta_1) + H_2^*.|A_4^*|. \cos(\theta_2) - H_3^*.|A_1^*|. \sin(\theta_1) - H_3^*.|A_4^*|. \sin(\theta_2)\right\}\right\}} \left(1 - \zeta_{\eta}^2\right) \quad (3.103)$$

### 3.1.3 Simplified Closed Form Formula: Selberg Formula

CEV and SBS analysis method are powerful tools for flutter analysis for practical use, however aerodynamic derivatives data are needed. Therefore in can not be used in preliminary design phase, where aerodynamic derivatives data of the proposed deck are unknown. In 1962, Selberg propose a simple analytic formula for calculation of flutter onset velocity, known as Selberg Formula.

$$U_{cr} = 3.71 \cdot f_{\varphi 0} \cdot B \sqrt{\frac{m \cdot r}{\rho \cdot B^3} \left\{ 1 - \left( \frac{f_{\eta 0}}{f_{\varphi 0}} \right)^2 \right\}} \quad (3.104)$$

Where:

$U_{cr}$ : flutter onset velocity;  $r$ : radius of gyration =  $\sqrt{I/m}$ ;  $f_{\varphi 0}/f_{\eta 0}$ : torsional/heaving frequency ratio;  $m/I$ : mass/mass inertia per unit length;  $B$ : width of deck;  $\rho$ : air density.

This formula was derived based from aerodynamics of two-dimensional thin plate or Theodorsen function. This raises questions:

1. Is Selberg Formula applicable for actual bridges with varied structural parameter data?
2. Is Selberg Formula applicable for deck section with aerodynamic derivatives values differ from thin plate data?

Matsumoto *et al.*, (2001) studied the applicability of Selberg Formula to several modern long span bridges. The derivatives are taken from Theodorsen function, but the structural parameter data ( $m$ ,  $r$ ,  $B$ ,  $f_{\varphi 0}$ ,  $f_{\eta 0}$ ) are taken from the bridges' actual data. The results surprisingly showed that Selberg Formula can predict flutter onset velocity with error less than 5% compared to results from CEV analysis. This showed that the structural data of nowadays long span bridge are within applicable range of Selberg Formula.

Two sections are studied as examples to study the applicability of Selberg Formula for section with varied aerodynamic derivatives: section NF-II-A and section SC. These section already tested in wind tunnels and reported by Trein (2009). Both section originated from rectangular prism with B/D=20. Section NF-II-A is equipped with vertical plates at both leading edge and trailing edge, while section SC is modified with semi-circular fairings. The aerodynamic derivatives of basic section is similar to Theodorsen function, but changed significantly due to the modifications. Aerodynamic derivatives values of NF-II-A and SC are presented in Fig. 3.4. Section NF-II-A is prone to torsional flutter at low wind velocity, and SC is susceptible to coupled flutter at high wind velocity (Permata *et al.*, 2011).

The results are presented in Fig. 3.5, 3.6 and 3.7. If the CEV results are assumed as more accurate analysis, it can be said that Selberg Formula only applicable for section with aerodynamic derivatives similar to thin plate. It failed to predict flutter onset velocity of section with aerodynamic derivatives differ from thin plate. It also can be seen that Selberg Formula is not applicable for frequency ratio less than 1.1, regardless the section aerodynamic properties. Structural parameter used are:  $B=0.3$  m;  $m=2.42$  kg/m;  $I=0.0181$  kg.m<sup>2</sup>/m.



Fig. 3.3 Section NF-II-A (left) and SC (right)

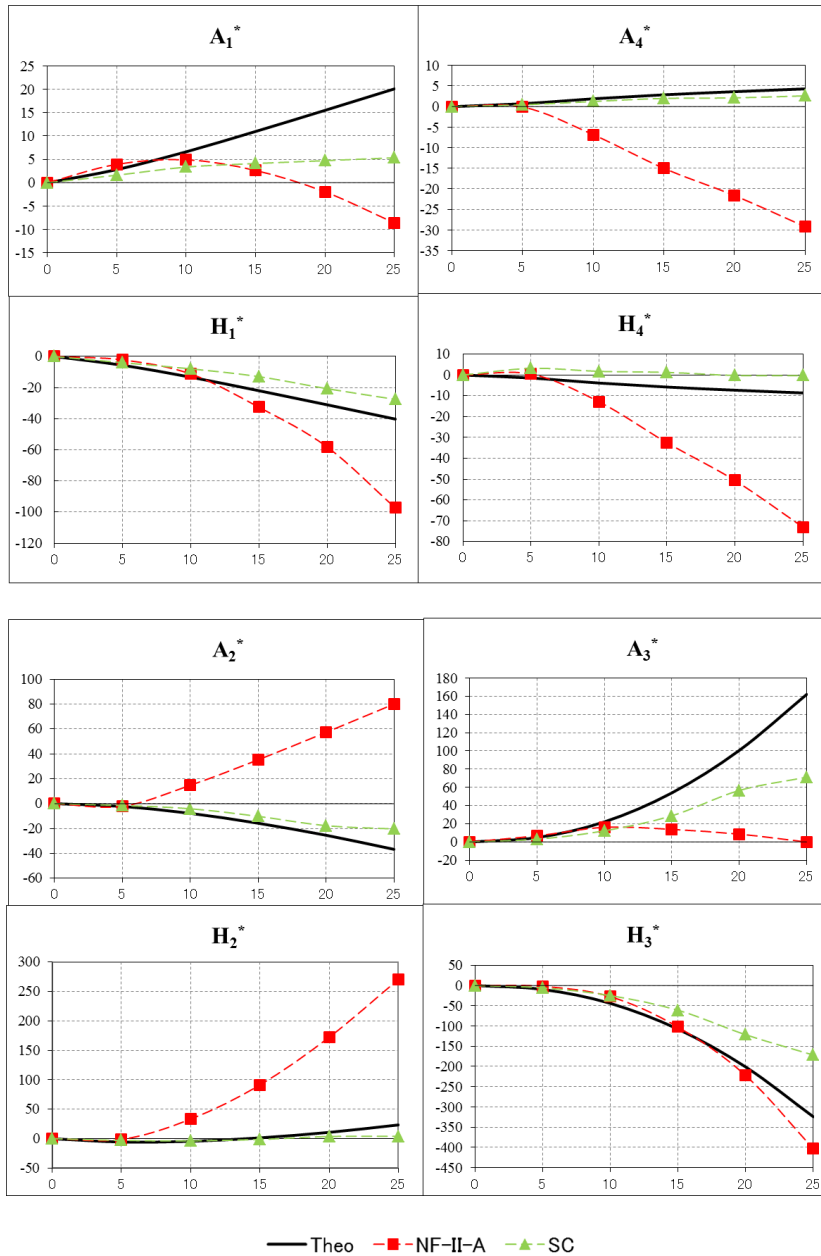


Fig. 3.4 Aerodynamic derivatives of section NF-II-A and SC, compared with Theodorsen function

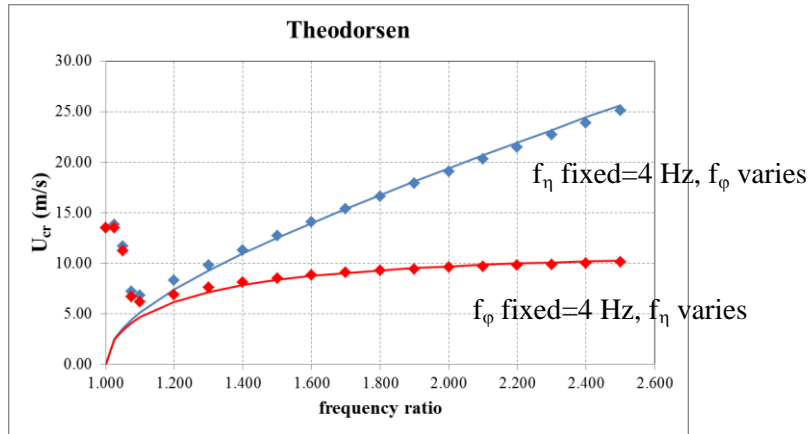


Fig. 3.5 Results of flutter onset velocity of thin plate (aerodynamic derivatives from Theodorsen function) using Selberg Formula (solid line) and CEV analysis (dotted)

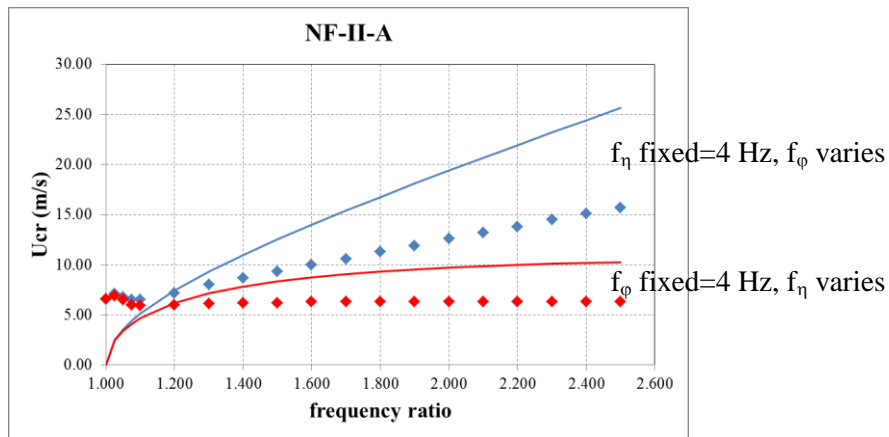


Fig. 3.6 Results of flutter onset velocity of section NF-II-A using Selberg Formula (solid line) and CEV analysis (dotted)

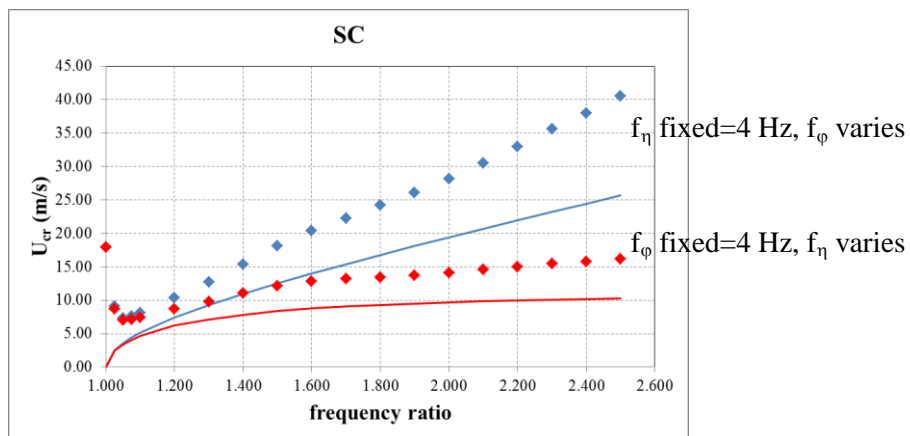


Fig. 3.7 Results of flutter onset velocity of section NF-II-A using Selberg Formula (solid line) and CEV analysis (dotted)

## 3.2 Flutter Stabilization of Long Span Bridge Deck

As can be seen in Fig. 3.5, 3.6 and 3.7 above, more stable bridge can be achieved by increasing torsional frequency and frequency ratio of the bridge, and using deck with superior aerodynamic properties (section SC). This is consistent with definition explained in Chapter 2.3. Therefore, there are two ways in practice to improve stability against flutter:

1. Modify structural configuration to improve structural parameter
2. Modify shape of deck to improve aerodynamic derivatives value

Modification of structural configuration has clear purpose: to increase torsional stiffness which produces larger torsional frequency. Flutter stabilization by modifying bridge structure had been reported by several researchers, such as:

1. Using cross-diagonal hanger or combination of vertical and horizontal crossed stays at several points to improve torsional stiffness (Ostenfeld & Larsen, 1992; Xiang & Ge, 2007)
2. Using new arrangement of cable system such as mono and spatial cable system (Xiang and Ge, 2007) and mono-duo cable system which reported increase flutter onset velocity up to 57% (Ostenfeld & Larsen, 1992)
3. Using optimum arrangement of sag ratio and side-span ratio, as studied by Miyata *et al.* (2001). Optimum value for sag ratio is more than 1.0 and side-span ratio around 0.3-0.35.

However, for longer span bridge, structural modification becomes less effective and also further researches and studies are needed to provide construction method for the new structural systems. More rational way to improve flutter stability is by improving aerodynamic properties of deck.

Matsumoto *et al.* (2002) pointed out that  $A_2^*$ ,  $H_1^*$ ,  $A_1^*$  and  $H_3^*$  are important aerodynamic derivatives for flutter.  $A_2^*$  is related with 1-DOF torsional instability, which positive value of  $A_2^*$  means the deck will undergo torsional flutter. The same case is applied for  $H_1^*$  for heaving motion.  $A_1^*$  and  $H_3^*$  are associated with coupled motion or 2-DOF motion.  $A_1^*$  related with the value of torsional moment induced by heaving velocity, and  $H_3^*$  related with lift force due to torsional motion. Therefore, strategy for flutter stabilization from aerodynamics point of view can be summarized as:

- negative  $A_2^*$  and  $H_1^*$
- low absolute value of  $A_1^*$  and  $H_3^*$

Results in Fig. 3.5, 3.6 and 3.7 clearly demonstrate the effectiveness of this strategy. Section NF-II-A that has positive  $A_2^*$  value is less stable than thin plate section, and section SC with low absolute value of  $A_1^*$  and  $H_3^*$  is the most stable section.

Matsumoto *et al.* (2007) summarized aerodynamic improvements for several proposed bridge deck section and confirmed the effectiveness of reducing absolute values of  $A_1^*$  and  $H_3^*$  to improve stability against flutter. Summary of flutter stabilization concept of several modern long span bridge decks and proposed concept for future use are presented in Appendix B.

### 3.3 Concluding Remarks

This chapter gives an overview about method for flutter analysis and the latest development in practice of bridge engineering for stabilization against flutter. It can be said that this chapter provides basic information as a starting point for studying flutter problems in long span bridges.

Complex Eigenvalue (CEV) Analysis will be used in this thesis. More rigorous Step-by-step (SBS) Analysis also explained to give insight about the differences between CEV and SBS. CEV is more like ‘purely’ mathematical approach to flutter problem, while SBS is based on the physics of the process that involved heaving and torsional branch of motion. CEV and SBS will give the same results for flutter onset velocity, which is the main concern of this thesis. But for future studies, SBS is a better option since it can give the information about role of each aerodynamic derivatives for damping of the motion.

Appendix A that related to this chapter give comprehensive information about deck shapes and countermeasures used in modern long span suspension bridges for flutter stabilization. This information is very important as a quick reference in studying flutter problems.

## Bibliography

- Agar, T. J. A. (1989) 'Aerodynamic flutter analysis of suspension bridges by a modal technique', *Engineering Structures*, 11, pp. 75-82.
- Bartoli, G., and Mannini, C. (2005) 'From multimodal to bimodal approach to flutter', *EURODYN 2005*, Millpress, Rotterdam, pp. 349-354.
- Chen, X. (2007) 'Improved Understanding of bimodal coupled bridge flutter based on closed-form solution', *Journal of Structural Engineering*, 133(1), pp. 22-31.
- D' Asdia, P., and Sepe, V. (1998) 'Aeroelastic instability of long-span suspended bridges : a multi-mode approach', *Journal of Wind Engineering and Industrial Aerodynamics*, 74-76, pp. 849-857.
- Fujino, Y., Kimura, K., Tanaka, H. (2012), '*Wind resistant design of bridges in Japan: development and practices*', Springer.
- Ge, Y. J., tanaka, H. (2000) 'Aerodynamic flutter analysis of cable-supported bridges by multi-mode and full-mode approaches', *Journal of Wind Engineering and Industrial Aerodynamics*, 86, pp. 123-153.
- Katsuchi, H., Jones, N. P., Scanlan, R. H. (1999) 'Multimode coupled flutter and buffeting analysis of the Akashi Kaikyo bridge', *Journal of Structural Engineering*, 125, pp. 60-70.
- Matsumoto, M., Taniwaki, Y., Shijo, R. (2002) 'Frequency characteristics in various flutter instabilities of bridge girders', *Journal of Wind Engineering and Industrial Aerodynamics*, 90, pp. 1973-1980.
- Matsumoto, M., Mizuno, K., Okubo, K., Ito, Y., and Matsumiya, H. (2007) 'Flutter instability and recent development in stabilization of structures', *Journal of Wind Engineering and Industrial Aerodynamics*, 95, pp. 888-907.
- Matsumoto, M., Matsumiya, H., Fujiwara, S., Ito, Y., and Matsumiya, H. (2010) 'New consideration on flutter properties based on step-by-step analysis', *Journal of Wind Engineering and Industrial Aerodynamics*, 98 (8-9), pp. 429-437.
- Matsumoto, M., Niihara, Y., Kobayashi, Y. (2010) 'On mechanism of flutter phenomena for structural sections', *Journal of Structural Engineering*, 40A, pp. 1019-1024.
- Miyata, T., Yamada, H. (1990) 'Coupled flutter estimate of a suspension bridge', *Journal of Wind Engineering and Industrial Aerodynamics*, 33 (1-2), pp. 341-348.
- Miyata, T., Yamada, H., Katsuchi, H., and Suangga, M. (2001) 'Optimum suspension bridge configuration against flutter and construction cost', *EASEC 8*, Singapore, December 5-7 2001.
- Ostenfeld, K. H., Larsen, A. (1992) 'Bridge engineering and aerodynamics', *Proceeding of the First international Symposium on Aerodynamics of Large Bridges*, Copenhagen, Denmark.
- Permata, R., Trein, C. A., Hong, J. W., Shirato, H., *Effects of Fairings and Vertical Plates on Unsteady Pressure Characteristics and Flutter Stability of B/D=20 Rectangular Prism*, 24<sup>th</sup> KKCNN Symposium on Civil Engineering, 2011, Hyogo, Japan.
- Simiu, E., Scanlan, R. H. (1978), '*Wind effect to structures: an introduction to wind engineering*', John Wiley & Sons.



- Scott, R. (2001) '*In the wake of Tacoma bridge : suspension bridges and the quest for aerodynamic stability*', ASCE Press.
- Trein, C. A. (2009), '*Study on the unsteady pressure characteristics of bluff bodies focusing on flutter stabilization of long-span bridges*', PhD thesis, Kyoto University.
- Xiang, H. F., and Ge, Y. J. (2007) '*Aerodynamic challenges in span length of suspension bridges*', *Front. Archit. Civ. Eng. China*, 1(2), pp. 153-162.



# Chapter 4

## Effects of Double Slot and Porous Cavity to Unsteady Pressure Characteristics and Flutter Stability of Slender Rectangular Prism

As explained in Chapter 3,  $A_1^*$  and  $H_3^*$  are the most important derivatives for coupled flutter instability as they play major role in coupled flutter excitation. Combination of  $A_1^*$  and  $H_3^*$  plays as destabilizing source, thus the reduction of absolute value of  $A_1^*$  and  $H_3^*$  decreases the exciting coupling force. Other important aerodynamic derivatives are  $A_2^*$  and  $H_1^*$  as aerodynamic damping for 1-SDOF torsional and heaving motion, respectively. Therefore, reducing absolute value of  $A_1^*$  and  $H_3^*$  while maintaining negative  $A_2^*$  and  $H_1^*$  is the appropriate strategy to avoid flutter instability. Unsteady pressure characteristics,  $\tilde{C}_p(x^*)$  and  $\psi(x^*)$  are the basis to modify the value of aerodynamic derivatives explain and to explain the physical process behind it. The basic deck section is rectangular prism with side ratio  $B/D=20$ .

### 4.1 Background

From unsteady pressure characteristics point of view, near leading edge zone of rectangular prism with  $B/D=20$  contributes predominantly to the value of  $A_1^*$ ,  $H_3^*$  and  $A_2^*$ . The near leading edge zone is coincide with the peak amplitude zone, located at  $x^*$  is between -0.8 and -0.4 (Fig. 4.1). Large pressure values in this zone are related with the occurrence of separation bubble. It is logical that manipulation of pressure in this zone will change the aerodynamic derivatives values more significantly.

Based on this condition, the introduction of countermeasures in this zone is expected to be able to change the flow and manipulate  $\tilde{C}_p(x^*)$  and  $\psi(x^*)$  to produce more stable deck section against coupled flutter. Two countermeasures are used in this study: slot and porous cavity. Both countermeasures are expected to manipulate unsteady pressure characteristics with different approach. Double slot (positioned near leading edge and trailing edge and symmetric to mid-chord) is expected to eliminate large pressure difference between upper and lower surface, thus reduce aerodynamic forces. Porous cavity is expected to reduce pressure level, thus reduce the value of  $\tilde{C}_p(x^*)$ .

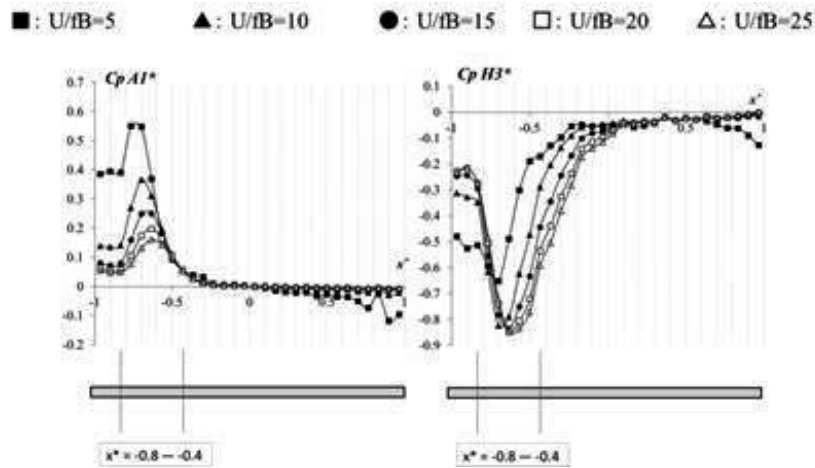


Fig.4.1  $\tilde{C}_p A_1^*(x^*)$  and  $\tilde{C}_p H_3^*(x^*)$  of rectangular prism with B/D=20

### 4.1.1 Double Slot

The idea of introducing slots or gap at bridge deck as countermeasure to achieve more stable deck section has been known since the seventies, firstly proposed as ‘vented deck’ system. The design of Messina Bridge deck was based at the first place on this idea (Brown, 1996). Study by Sato *et al.* (1994) and Yoneda *et al.* (1997) showed that the effects of slot were found to be sensitive to the location and width of the slot. Results of both studies have similarities:

1. Most stable deck section is achieved when relative wide slot (gap ratio more than 30%) is positioned at the center of the deck. Sato *et al.* (1994) used 47% gap ratio to achieve flutter onset velocity doubled from the original section (from 39 m/s to 80 m/s). Narrower slot with 20% gap ratio improved flutter onset velocity about 38% (from 39 m/s to 54 m/s). Yoneda *et al.* (1997) found that gap ratio 32% (with vertical plates at the slot area) increased flutter onset velocity about 80% (from 15 m/s to 27 m/s). Results of these studies are summarized in Table 4.1 and Table 4.2.
2. Introducing slot at near leading edge zone has unfavourable effect to flutter stability for most of the cases. As for Case 23 from Table 4.1 and Case W3 from Table 4.2, narrow slot near leading edge could produce more stable deck, although the increase in flutter onset velocities are less than 20%. But moving the slot closer to leading edge (Case W2 from Table 4.2) reduced the flutter onset velocity, while slot right beside fairings had insignificant effects (Case 17 from Table 4.1 and Case W1 from Table 4.2).
3. One important note is that both studies use slender rectangular prism with triangular fairings as basic section.

State of the art of using slot is utilization of relatively wide gap or space to form multi box girder section or twin box girder section, like used in design of Messina Bridge, design of future super long span bridges in Japan and Xihoumen Bridge. The wide space, means wider deck, gives rise to economical concern. Use of grating to allow the area of gap used for traffic

is considered not acceptable for practice due to comfort and safety reasons (Brancaleoni *et al.*, 2010). Tokoro *et al.* (2002) reported the study of using narrow slot at the center of single streamlined box girder to increase its stability about 40%. Therefore, possibility of using different arrangement of narrow slot to achieve more stable deck action is an attractive subject in bridge deck design.

#### 4.1.2 Porous Cavity

The use of porous surface with a cavity beneath it to reduce amplitude of surface pressure in reattachment area for very high velocity flow (transonic flow) was proposed by Kumar & Viswanath (2002). Reduction of rms surface pressure ( $C_{p\ rms}$ ) up to 35% was possible. The mechanism was related with the combination of suction at the leeward and blowing at the upward of the porous cavity, as shown in Fig. 4.2. Using this concept to moving bluff body under low speed flow is new and challenging, especially by considering the position of reattachment point for such case is not a fixed one.

### 4.2 Description of Experiment and Models

Series of wind tunnel test were performed to measure surface pressure of models. The wind tunnel used in the experiment was a room-circuit Eiffel type, with working section of 1.8 m height and 1.0 m width. Forced 1-DOF heaving and torsional oscillation method were conducted to each model under smooth flow. Frequency of motion was set to 2 Hz, and amplitude of motion was  $\eta_0=1$  cm for heaving and  $\varphi_0=2^\circ$  for torsional.

Pressure signals were carried from pressure taps to sensor box outside wind tunnel working section, through metal tubes inside the model and plastic tubes outside the model. The sensor box was positioned near the window of wind tunnel, so length of the plastic tubes were kept relatively short (about 60 cm) in order to minimize phase lag of the tubing system.

Fluctuating pressure data were obtained by band-pass filtering the pressure signal data, and calibrated with pressure data in no wind condition. Then the data were normalized with dynamic pressure as in Eq. (2.16). The values of  $\tilde{C}_p(x^*)$  were obtained by using statistic relationship: amplitude =  $2\sqrt{2}$  x standard deviation (peak to peak amplitude). The values of  $\psi(x^*)$  were calculated through cross-correlation with displacement data, which were acquired by using laser sensor. Details of these equipments are shown in Fig. 4.3 to 4.5.

Table 4.1 Results of study by Sato *et al.* (1994)

Section ID	Cross section	Void ratio	Flutter onset velocity $U_{cr}$ (m/s)	ratio $U_r$
1		0.00	39.0	1.00
2		0.00	38.0	0.97
3		0.00	37.0	0.95
4		0.00	37.0	0.95
5		0.20	51.0	1.31
6		0.20	37.0	0.95
7		0.20	47.0	1.21
8		0.20	25.0	0.64
9		0.20	21.0	0.54
10		0.40	19.0	0.49
11		0.20	18.0	0.46
12		0.20	53.0	1.36
13		0.20	53.0	1.36
14		0.00	27.0	0.69
15		0.20	16.0	0.41
16		0.00	39.0	1.00
17		0.13	38.0	0.97
18		0.20	54.0	1.38
19		0.33	51.0	1.31
20		0.47	80.0	2.05
21		0.27	62.0	1.59
22		0.40	57.0	1.46
23		0.13	46.0	1.18
24		0.47	64.0	1.64
25		0.73	74.0	1.90
26		0.33	68.0	1.74
27		0.40	69.0	1.77

Table 4.2 Results of study by Yoneda *et al.* (1997)

Section ID	Cross section	Void ratio	Flutter onset velocity $U_{cr}$ (m/s)	ratio $U_r$
Case - AD		0	15.0	1.00
Case - W1		0.08	15.0	1.00
Case - W2		0.08	11.0	0.73
Case - W3		0.08	17.5	1.17
Case - W4		0.08	17.5	1.17
Case - W5		0.08	16.0	1.07
Case - L3		0.08	16.0	1.07
Case - W3L3		0.16	18.5	1.23
Case - W3L3/50		0.16	18.0	1.20
Case - L5		0.08	16.5	1.10
Case - W5L5		0.16	19.0	1.27
Case - W5L5/50		0.16	18.5	1.23
Case - W4W5L4L5		0.32	27.0	1.80
Case - W4W5L4L5/50		0.32	25.5	1.70
Case - W4W5L4L5/70		0.32	23.0	1.53

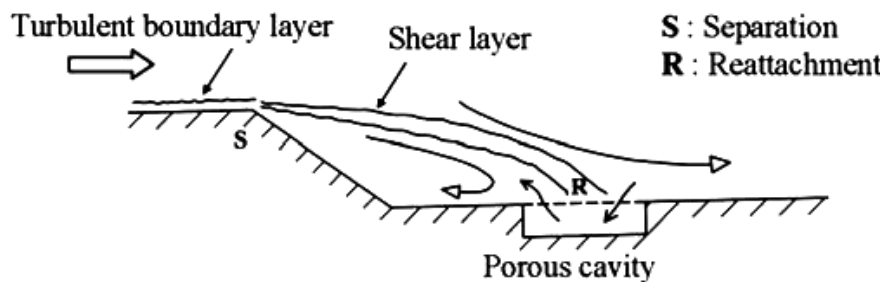


Fig.4.2 Schematic of passive control concept for reattaching flow using porous cavity (after Kumar & Viswanath, 2002)

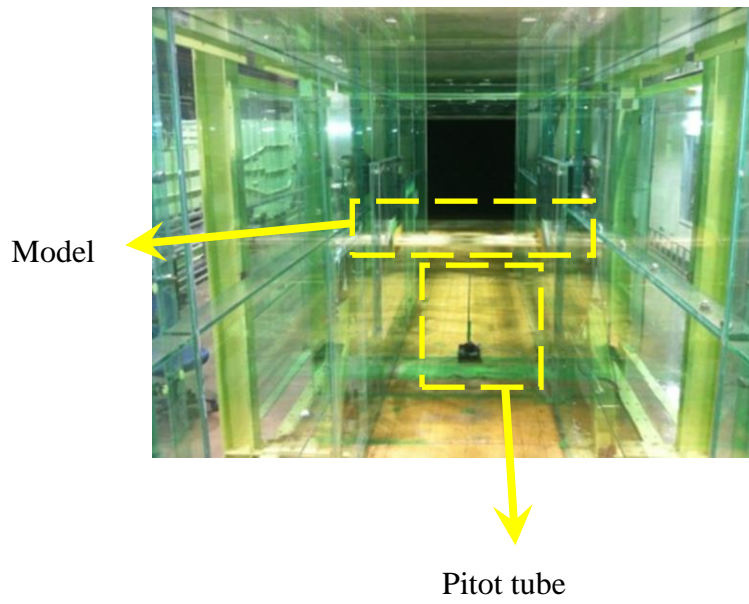


Fig.4.3 Model inside wind tunnel

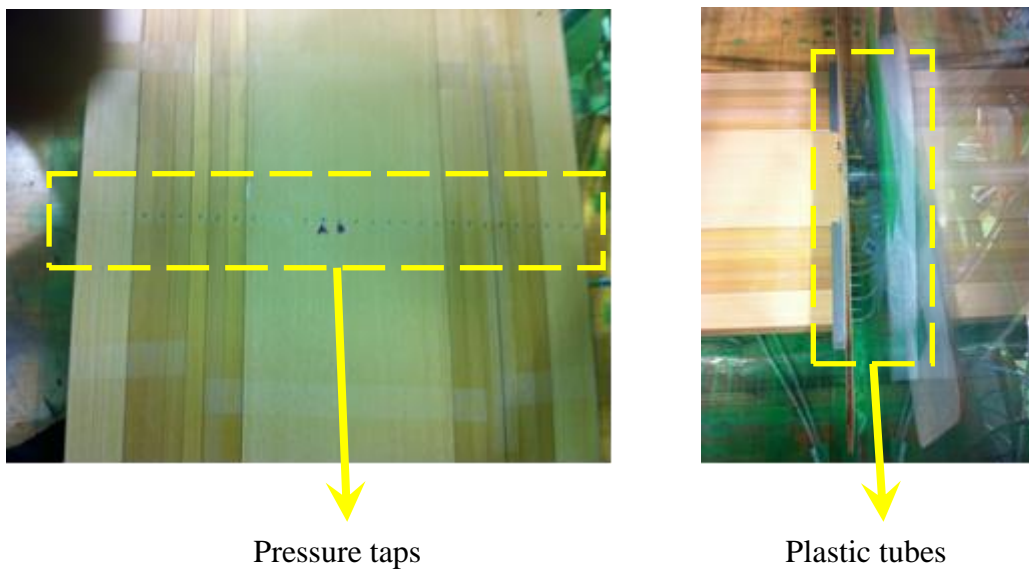


Fig.4.4 Pressure taps at center of model and plastic tubes



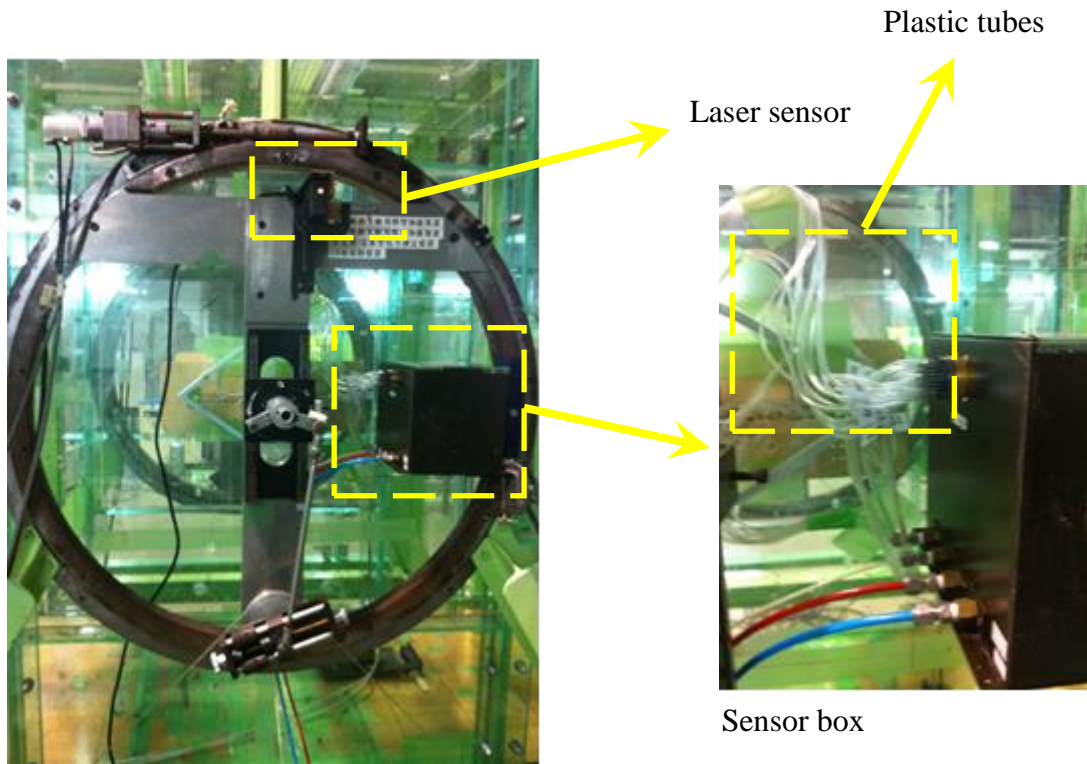


Fig.4.5 Set up of equipment outside wind tunnel for pressure measurement

The basic section, rectangular prism with  $B/D=20$  was modified so double slot and porous cavity with varied width and position can be modeled. Size of basic model is  $B=30$  cm and  $D=1.5$  cm. The prism model consisted of 3 fixed blocks (leading edge or part 1, center or part 3, and trailing edge or part 5) and 12 removable blocks. The removable blocks were arranged in two zones: 6 blocks near leading edge or part 2 and 6 other blocks near trailing edge or part 4. Each removable blocks has 1 cm width, and by removing specific blocks several variations can be developed. Basic section or rectangular prism with  $B/D=20$  is denoted as model F (F means 'full' or without slot), and the naming system for each models were given based on number of blocks removed to create slot and their position, as shown in Fig. 4.6.

The same basic model for double slot can be modified, and variation of width and size of porous cavity can be developed. The models have porous cavity with size of 2 cm, 4 cm, 6 cm and 9 cm width. Section with 9 cm width of porous cavity has different side conditions which are without solid blockage (9A) and with solid blockage (9B). The naming system for these section is as follows: x-y-z means width of porous cavity x cm, y is depth the cavity (0.25 cm and 0.50 cm), and z is 'grating' or 'no grating'.

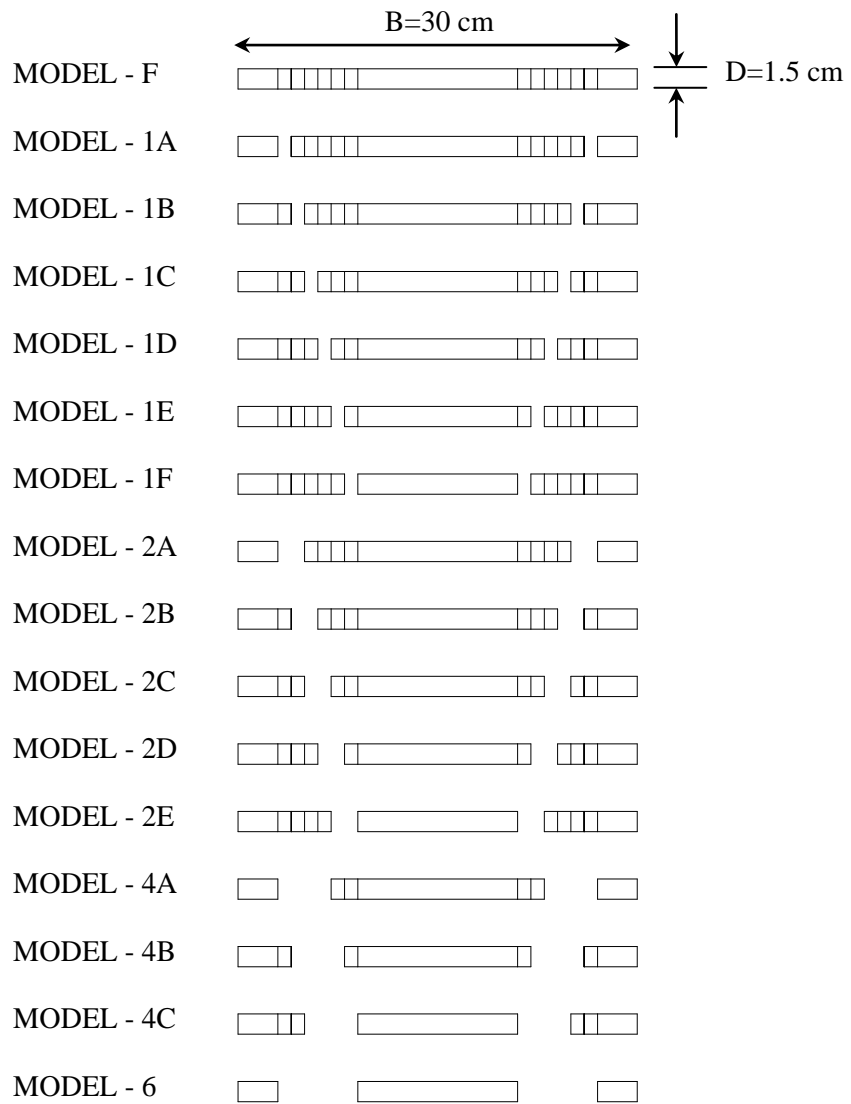


Fig.4.6 Details and naming system of models with double slot

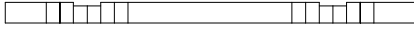


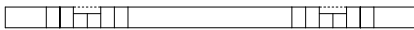
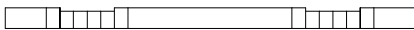


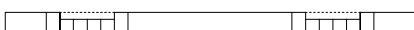








MODEL - 2-025-no grating	
MODEL - 2-025-grating	
MODEL - 2-050-no grating	
MODEL - 2-050-grating	
MODEL - 4-025-no grating	
MODEL - 4-025-grating	
MODEL - 4-050-no grating	
MODEL - 4-050-grating	
MODEL - 6-025-no grating	
MODEL - 6-025-grating	
MODEL - 6-050-no grating	
MODEL - 6-050-grating	
MODEL - 9A-050-no grating	
MODEL - 9A-050-grating	
MODEL - 9B-050-no grating	
MODEL - 9B-050-grating	

Fig.4.7 Details and naming system of models with porous cavity

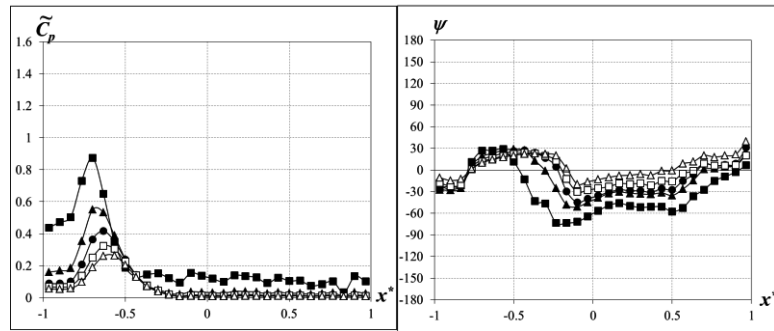


Fig.4.8 Model with double slot (left) and porous cavity (right) during testing

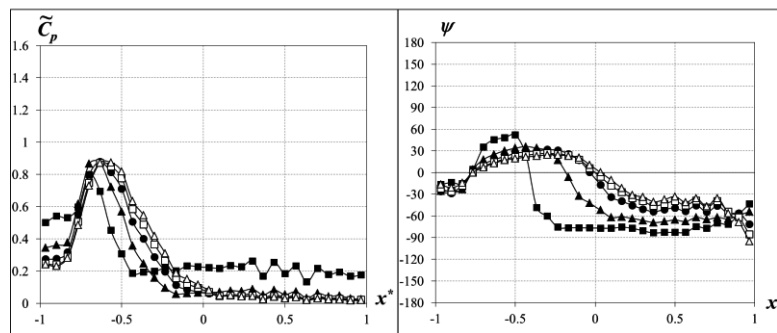
### 4.3 Results: Unsteady Pressure Characteristics and Aerodynamic Derivatives

#### 4.3.1 Unsteady Pressure Characteristics and Aerodynamic Derivatives of Prism with Double Slot

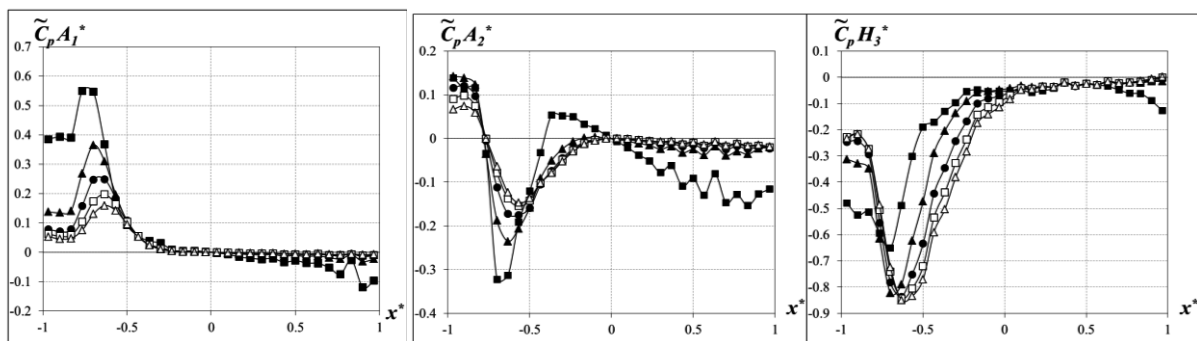
The results of unsteady pressure characteristics are presented in Fig. 4.9 to Fig. 4.24.



(a) heaving



(b) torsional



(c)  $\tilde{C}_p A_1^*(x^*)$ ,  $\tilde{C}_p A_2^*(x^*)$  and  $\tilde{C}_p H_3^*(x^*)$

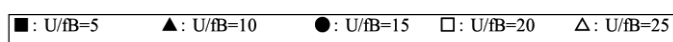
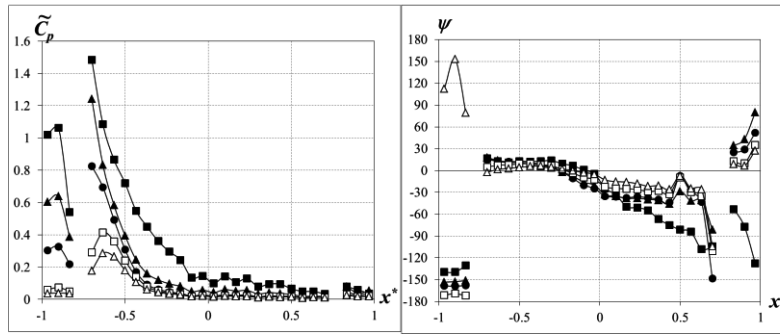
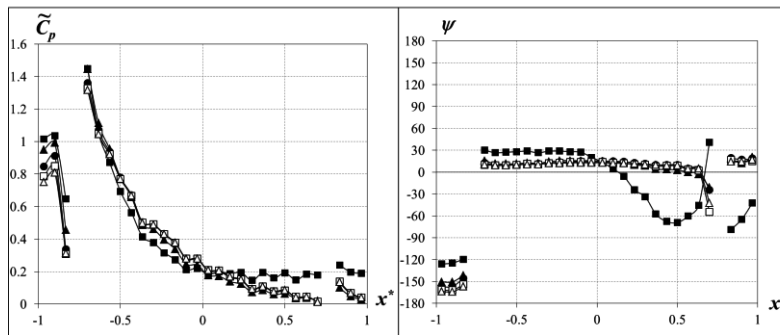


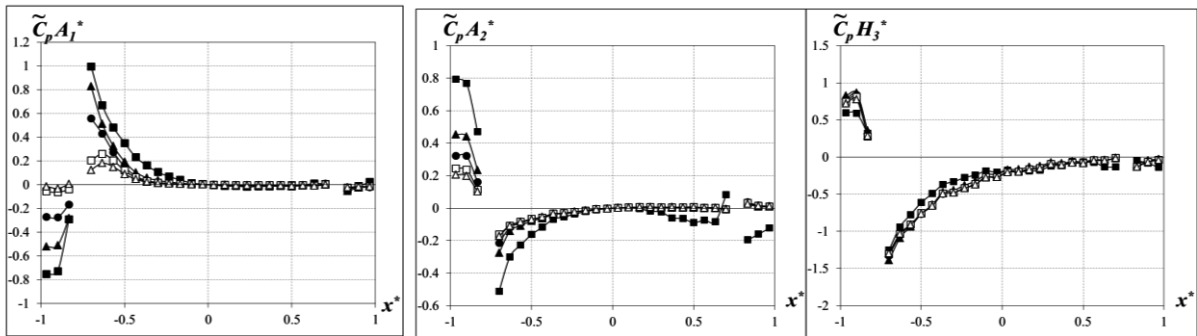
Fig.4.9 Unsteady pressure characteristics of Model F



(a) heaving



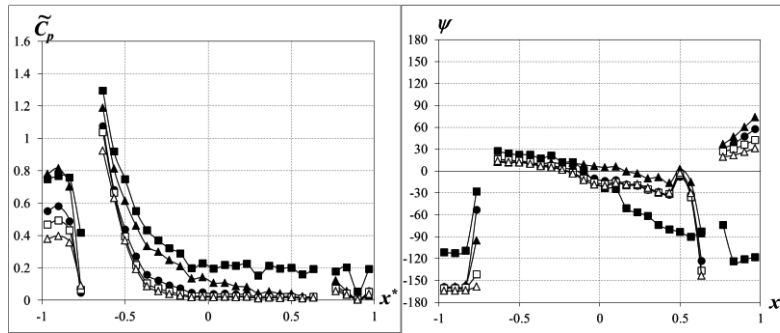
(b) torsional



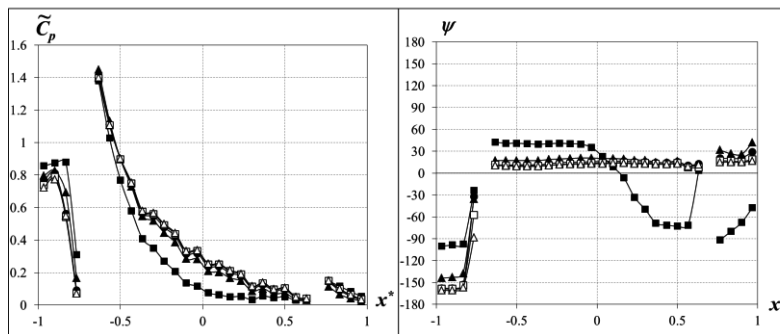
(c)  $\tilde{C}_p A_1^*(x^*)$ ,  $\tilde{C}_p A_2^*(x^*)$  and  $\tilde{C}_p H_3^*(x^*)$



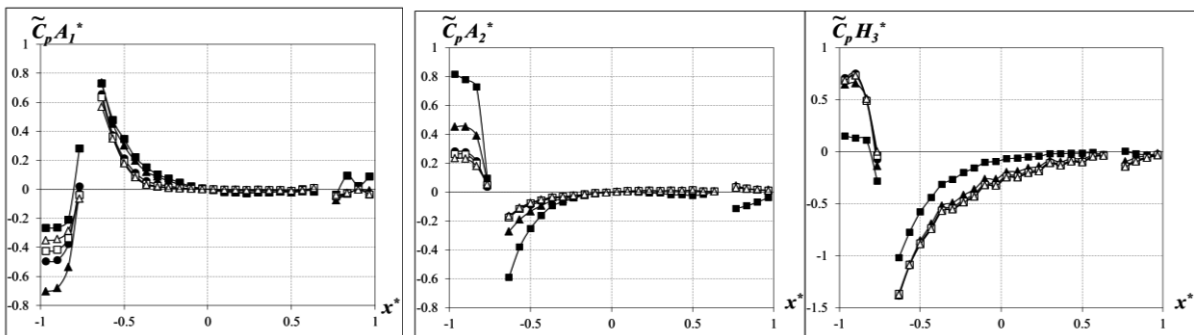
Fig.4.10 Unsteady pressure characteristics of Model 1A



(a) heaving



(b) torsional



(c)  $\tilde{C}_p A_1^*(x^*)$ ,  $\tilde{C}_p A_2^*(x^*)$  and  $\tilde{C}_p H_3^*(x^*)$

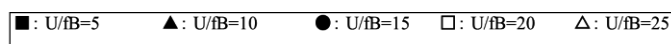
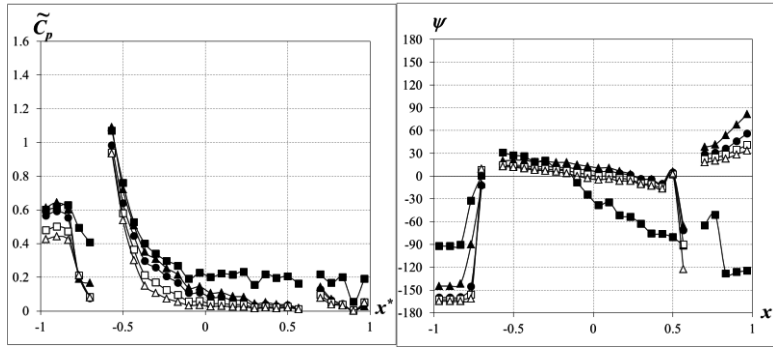
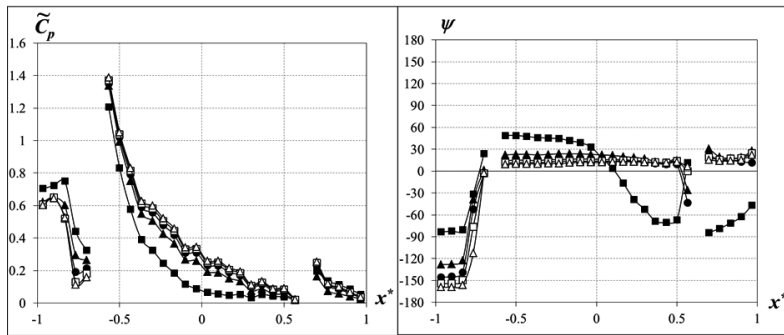


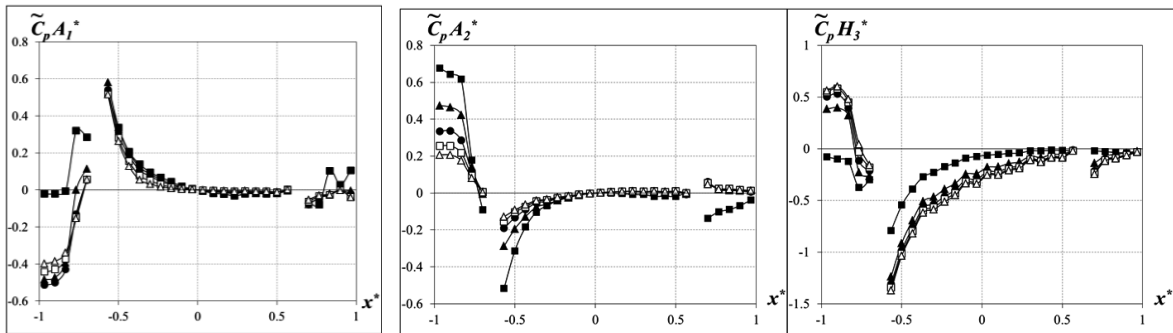
Fig.4.11 Unsteady pressure characteristics of Model 1B



(a) heaving



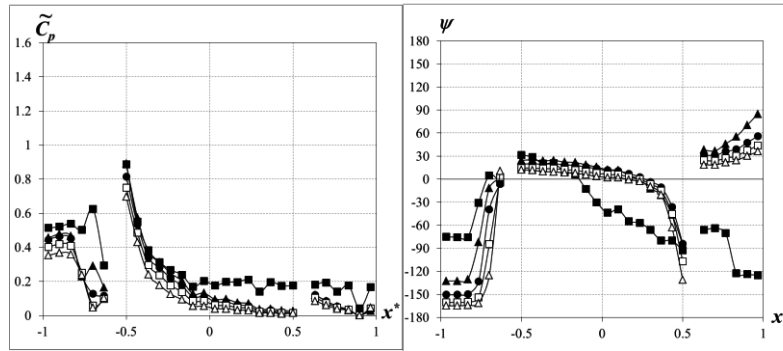
(b) torsional



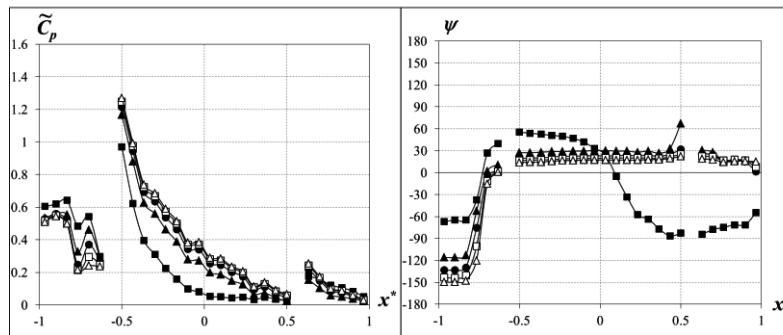
(c)  $\tilde{C}_p A_1^*(x^*)$ ,  $\tilde{C}_p A_2^*(x^*)$  and  $\tilde{C}_p H_3^*(x^*)$



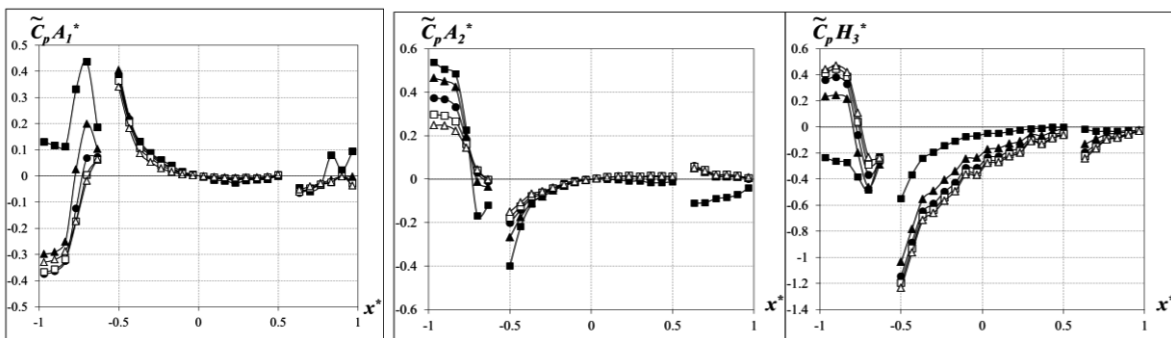
Fig.4.12 Unsteady pressure characteristics of Model 1C



(a) heaving



(b) torsional

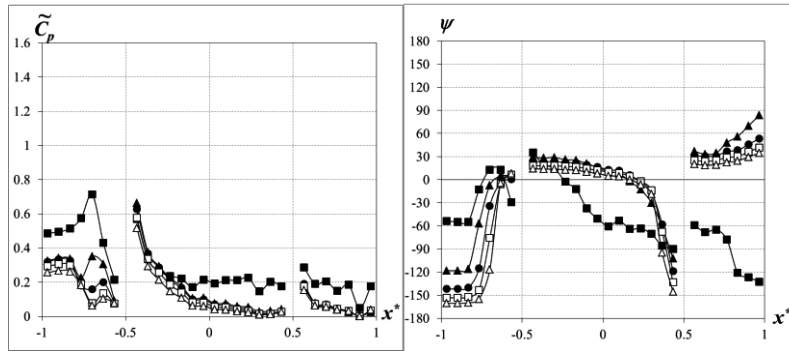


(c)  $\tilde{C}_p A_1^*(x^*)$ ,  $\tilde{C}_p A_2^*(x^*)$  and  $\tilde{C}_p H_3^*(x^*)$

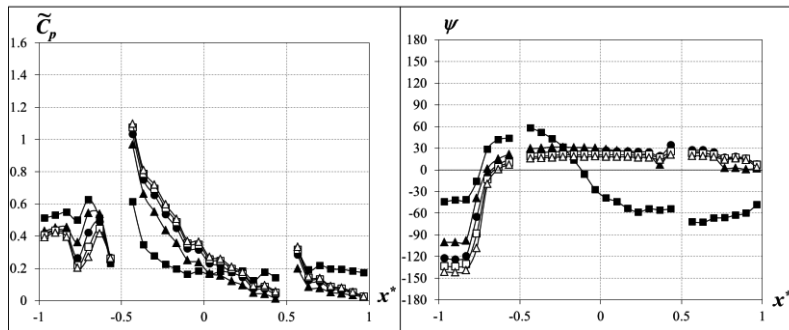


Fig.4.13 Unsteady pressure characteristics of Model 1D

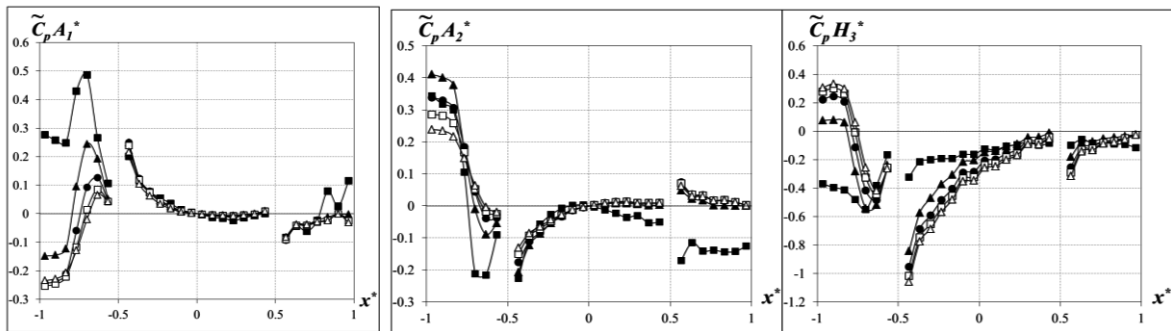




(a) heaving



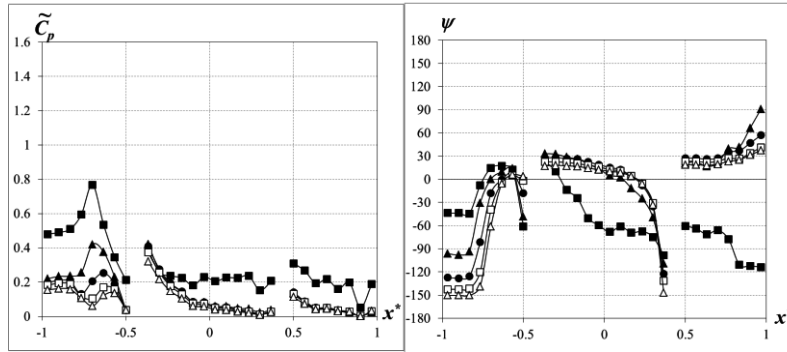
(b) torsional



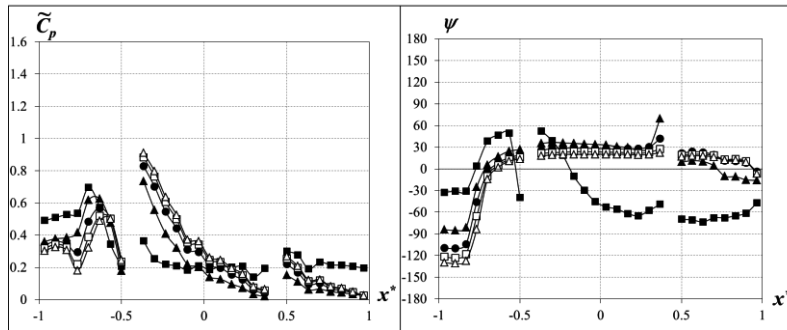
(c)  $\tilde{C}_p A_1^*(x^*)$ ,  $\tilde{C}_p A_2^*(x^*)$  and  $\tilde{C}_p H_3^*(x^*)$



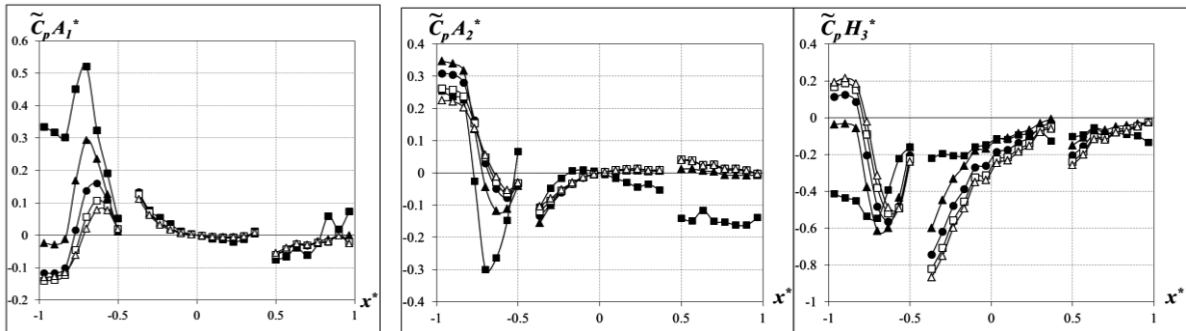
Fig.4.14 Unsteady pressure characteristics of Model 1E



(a) heaving



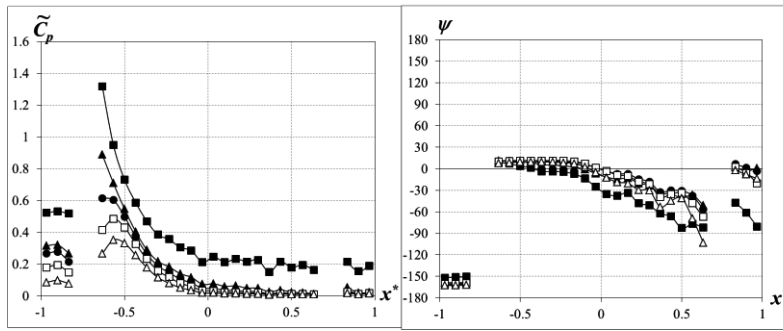
(b) torsional



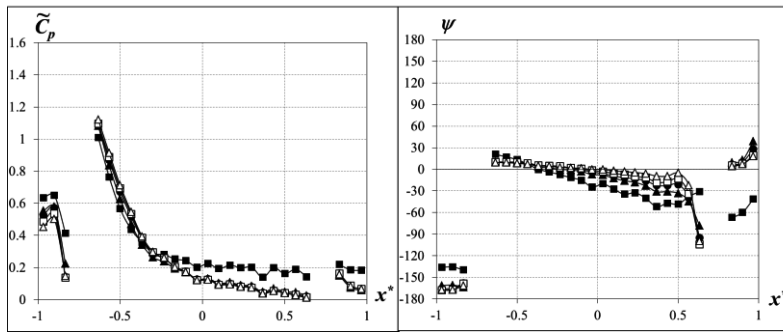
(c)  $\tilde{C}_p A_1^*(x^*)$ ,  $\tilde{C}_p A_2^*(x^*)$  and  $\tilde{C}_p H_3^*(x^*)$



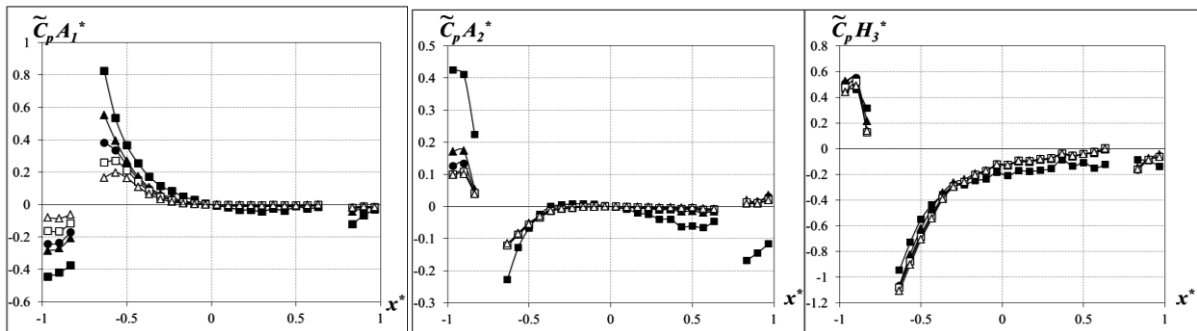
Fig.4.15 Unsteady pressure characteristics of Model 1F



(a) heaving



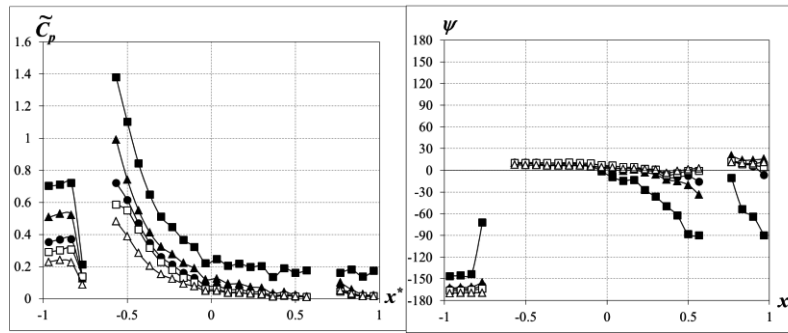
(b) torsional



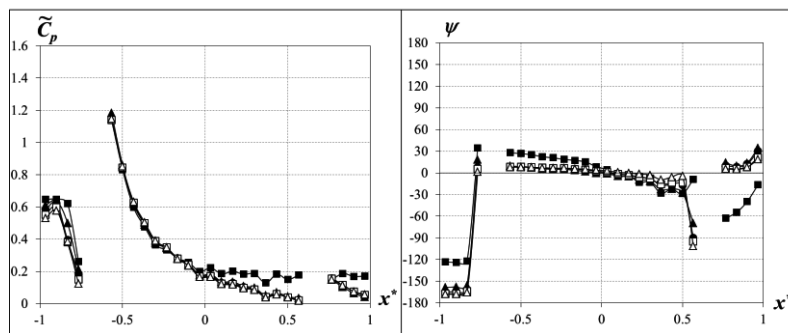
(c)  $\tilde{C}_p A_1^*(x^*)$ ,  $\tilde{C}_p A_2^*(x^*)$  and  $\tilde{C}_p H_3^*(x^*)$



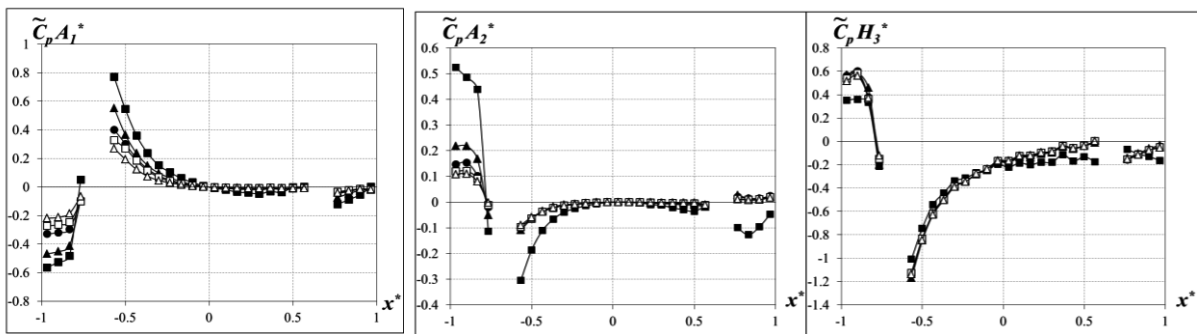
Fig.4.16 Unsteady pressure characteristics of Model 2A



(a) heaving



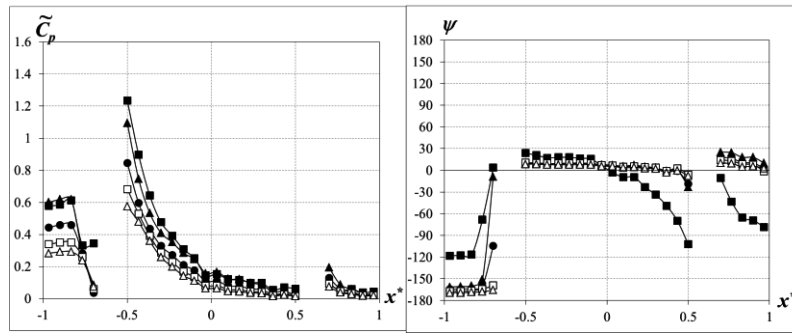
(b) torsional



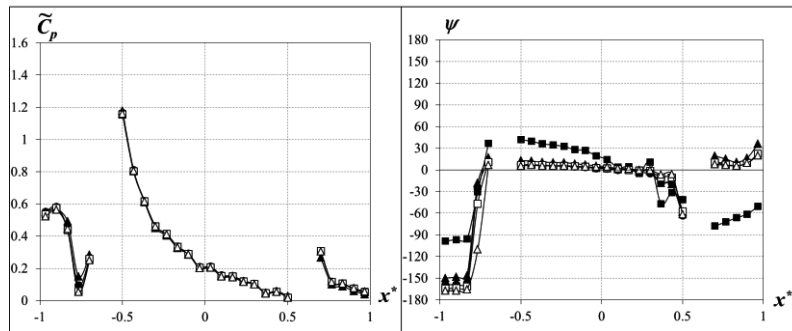
(c)  $\tilde{C}_p A_1^*(x^*)$ ,  $\tilde{C}_p A_2^*(x^*)$  and  $\tilde{C}_p H_3^*(x^*)$



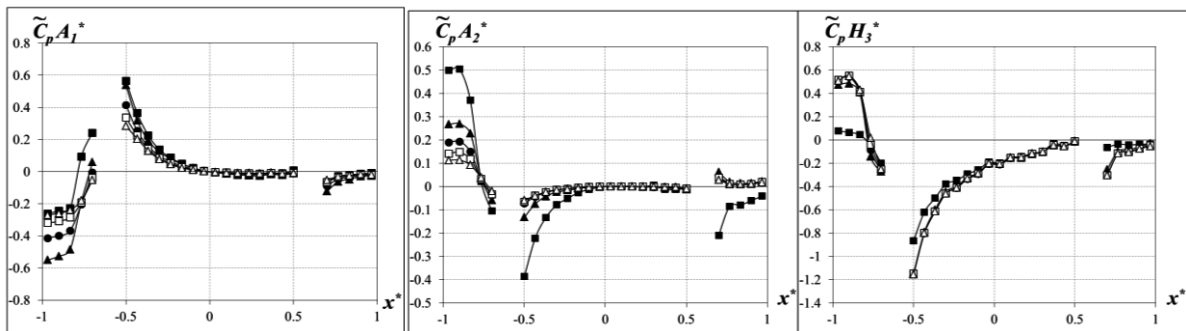
Fig.4.17 Unsteady pressure characteristics of Model 2B



(a) heaving



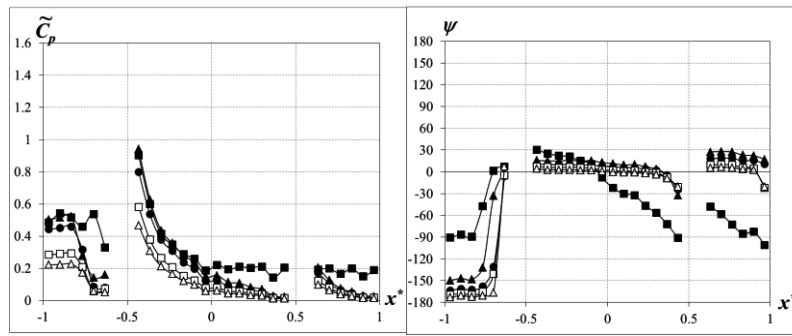
(b) torsional



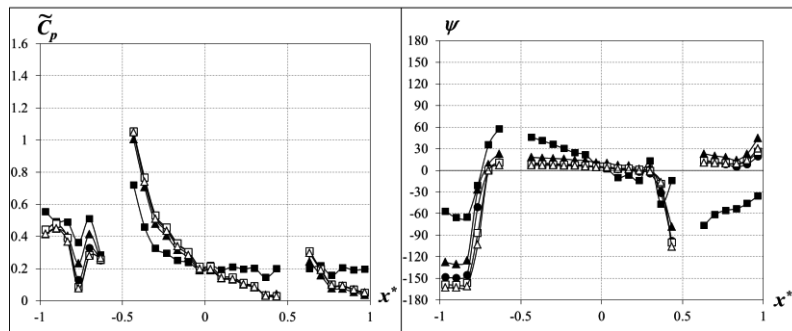
(c)  $\tilde{C}_p A_1^*(x^*)$ ,  $\tilde{C}_p A_2^*(x^*)$  and  $\tilde{C}_p H_3^*(x^*)$



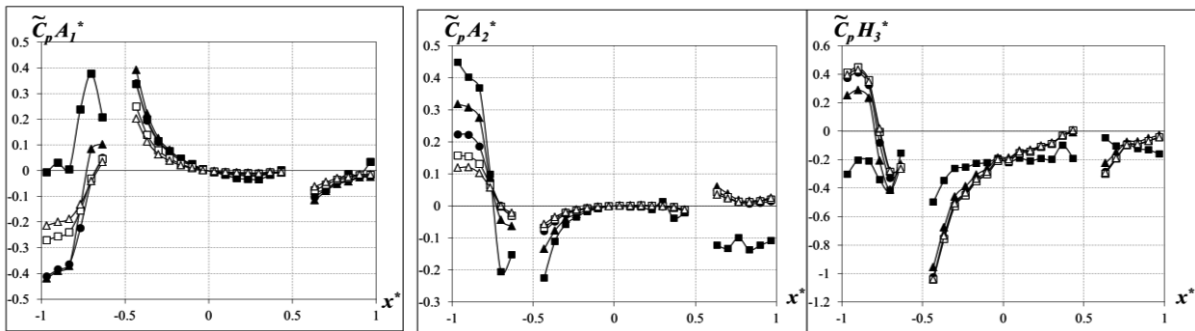
Fig.4.18 Unsteady pressure characteristics of Model 2C



(a) heaving



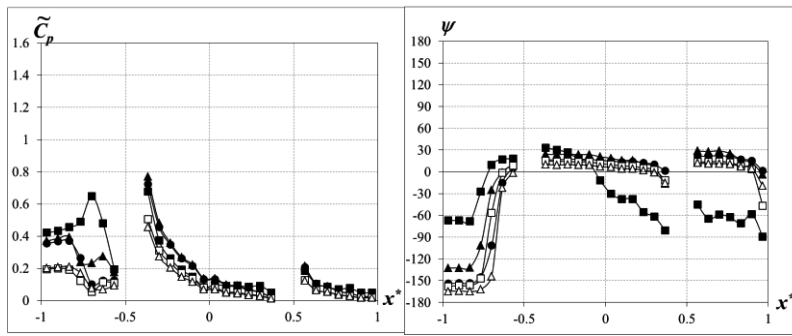
(b) torsional



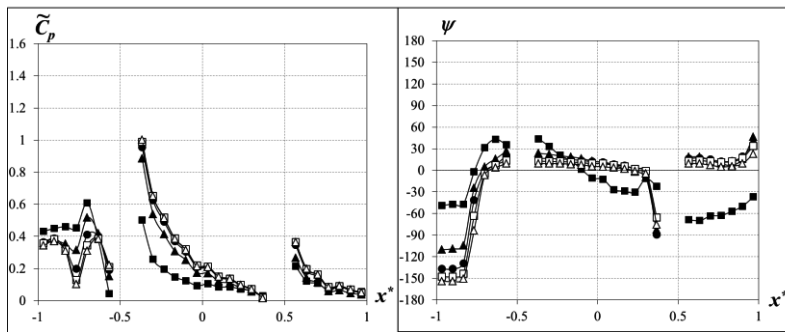
(c)  $\tilde{C}_p A_1^*(x^*)$ ,  $\tilde{C}_p A_2^*(x^*)$  and  $\tilde{C}_p H_3^*(x^*)$



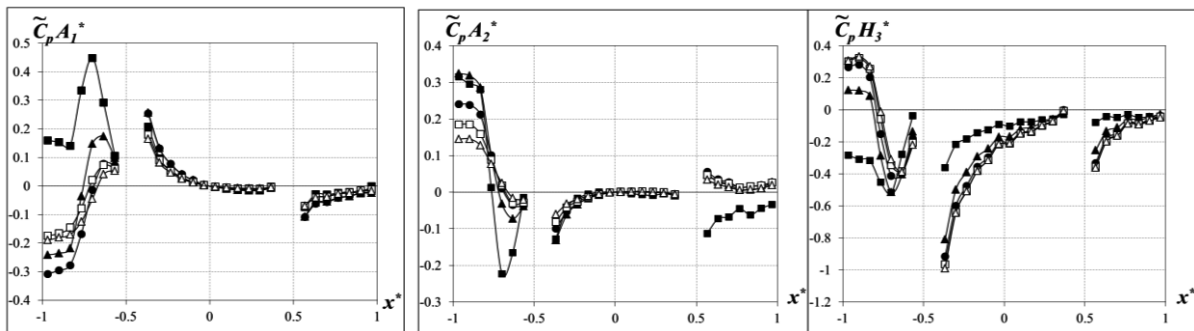
Fig.4.19 Unsteady pressure characteristics of Model 2D



(a) heaving



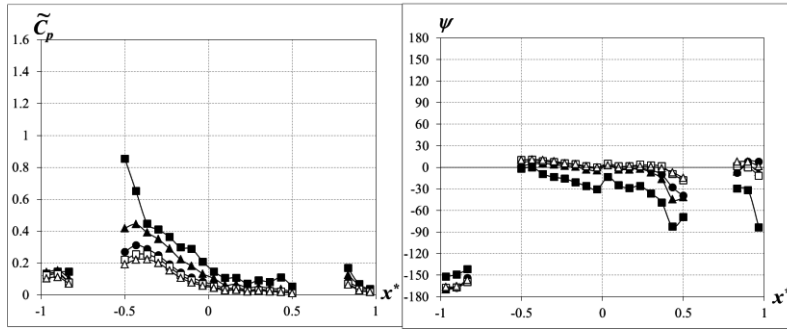
(b) torsional



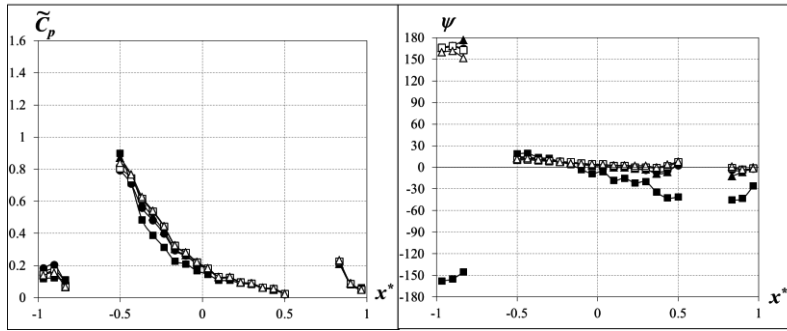
(c)  $\tilde{C}_p A_1^*(x^*)$ ,  $\tilde{C}_p A_2^*(x^*)$  and  $\tilde{C}_p H_3^*(x^*)$



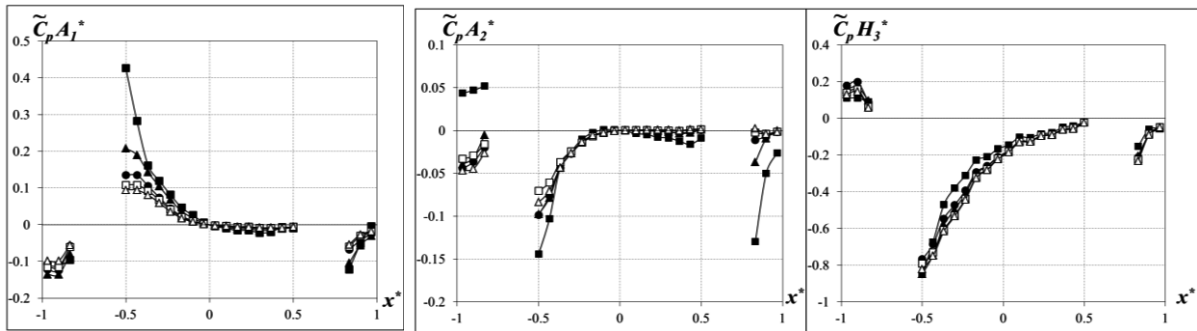
Fig.4.20 Unsteady pressure characteristics of Model 2E



(a) heaving



(b) torsional



(c)  $\tilde{C}_p A_1^*(x^*)$ ,  $\tilde{C}_p A_2^*(x^*)$  and  $\tilde{C}_p H_3^*(x^*)$

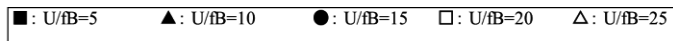
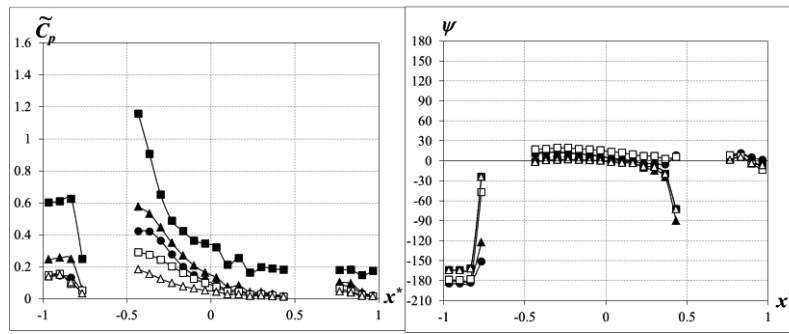
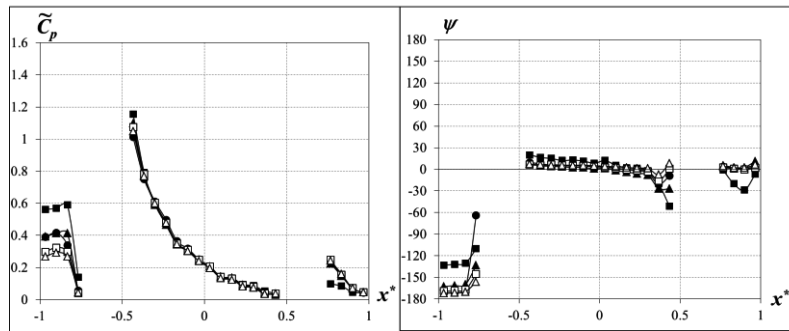


Fig.4.21 Unsteady pressure characteristics of Model 4A

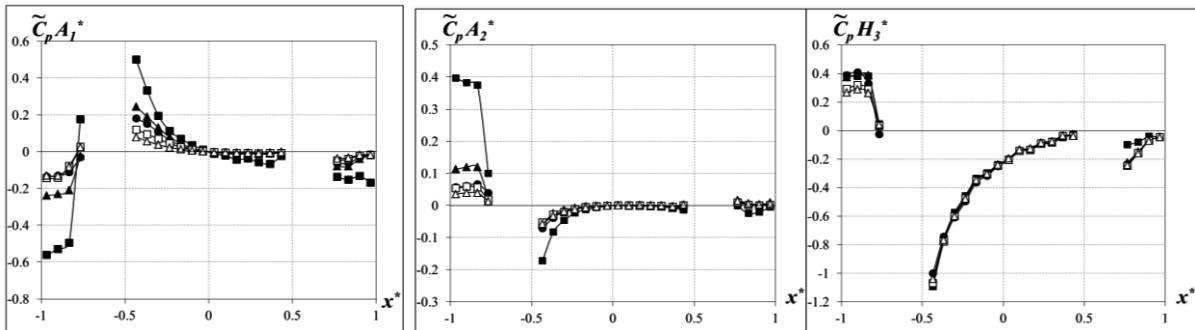




(a) heaving



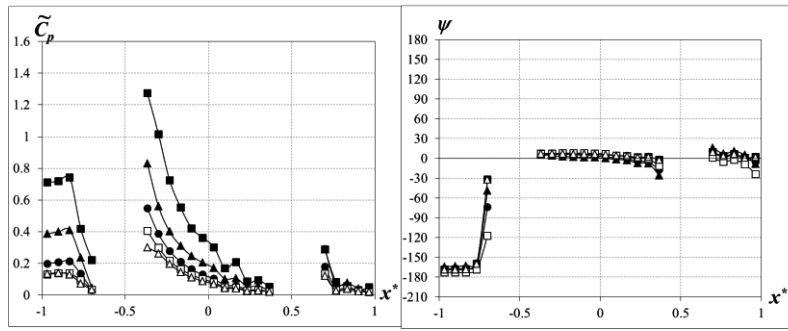
(b) torsional



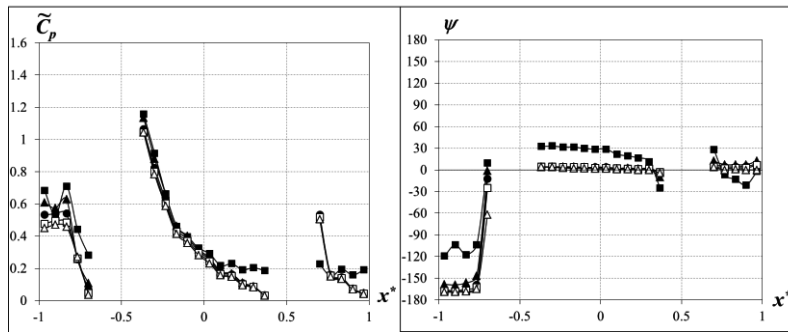
(c)  $\tilde{C}_p A_1^*(x^*)$ ,  $\tilde{C}_p A_2^*(x^*)$  and  $\tilde{C}_p H_3^*(x^*)$



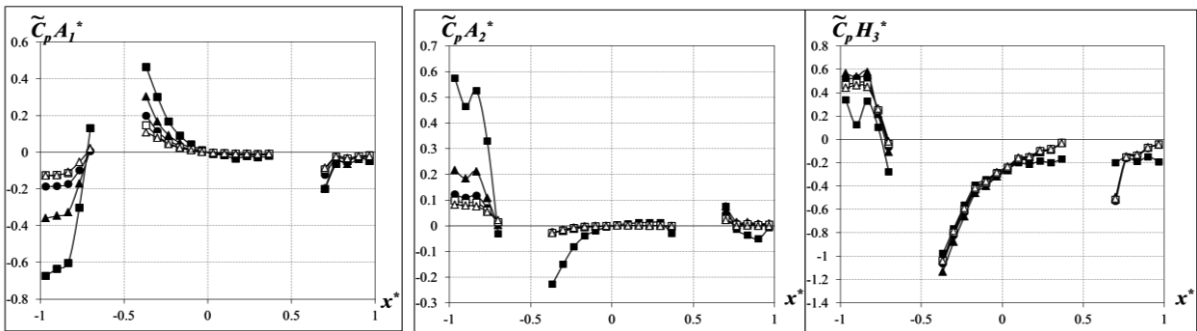
Fig.4.22 Unsteady pressure characteristics of Model 4B



(a) heaving



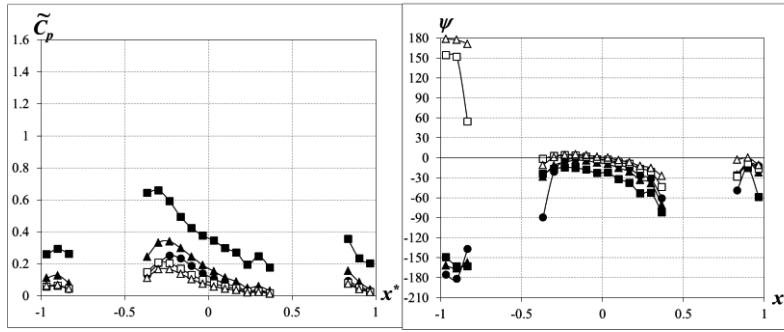
(b) torsional



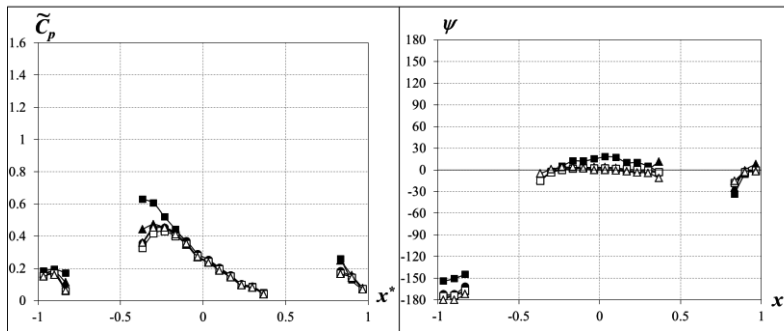
(c)  $\tilde{C}_p A_1^*(x^*)$ ,  $\tilde{C}_p A_2^*(x^*)$  and  $\tilde{C}_p H_3^*(x^*)$



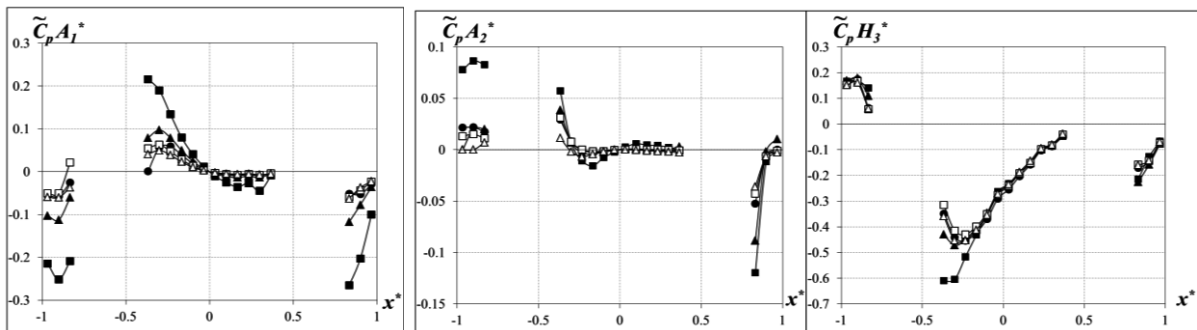
Fig.4.23 Unsteady pressure characteristics of Model 4C



(a) heaving



(b) torsional



(c)  $\tilde{C}_p A_1^*(x^*)$ ,  $\tilde{C}_p A_2^*(x^*)$  and  $\tilde{C}_p H_3^*(x^*)$



Fig.4.24 Unsteady pressure characteristics of Model 6

Aerodynamic derivatives of basic section and section with porous cavity are calculated by using Eq. (2.22a) to (2.22h), and the results are presented in Fig. 4.25 to Fig. 4.29.

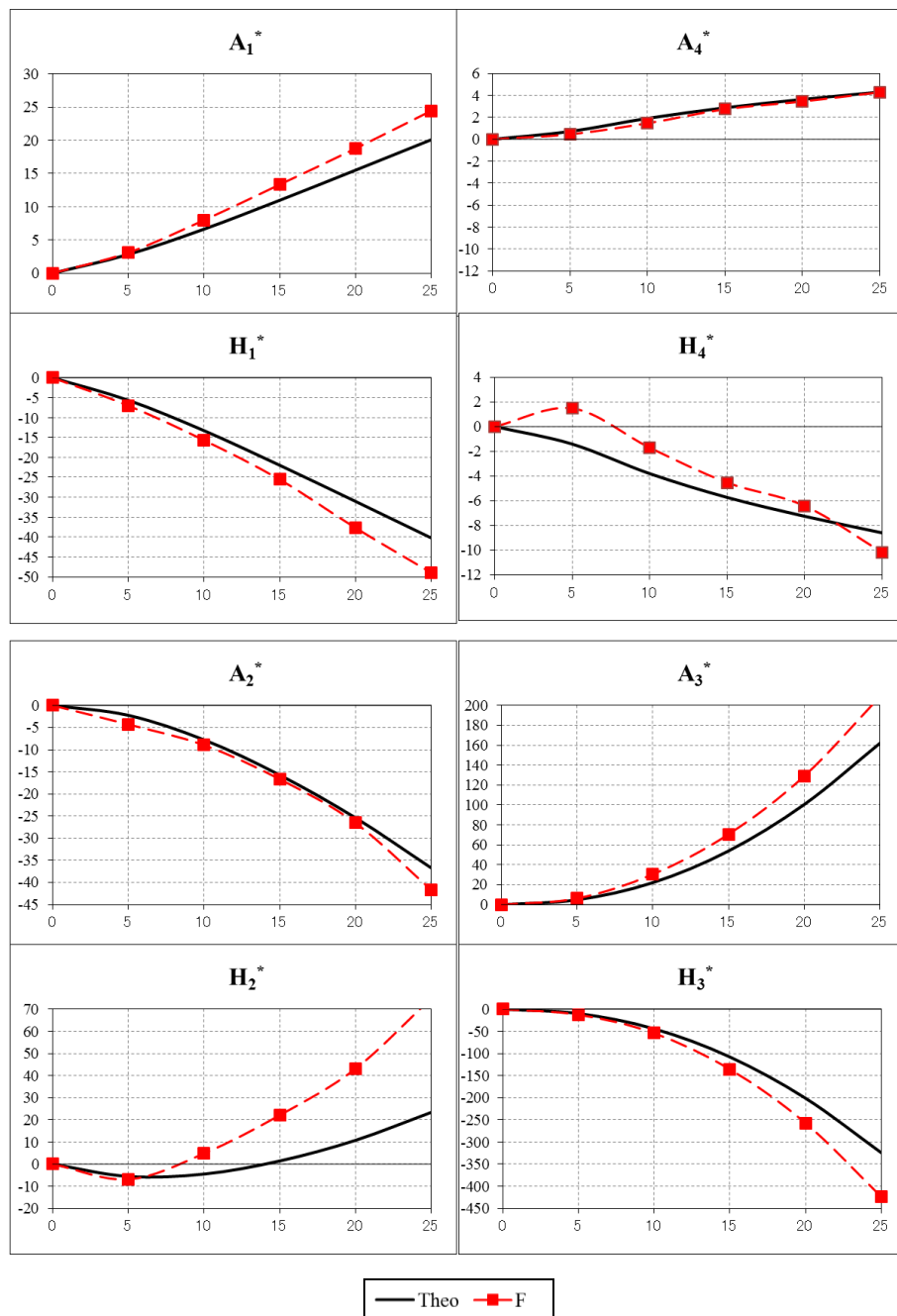


Fig.4.25 Aerodynamic derivatives of Model F or rectangular prism with B/D=20

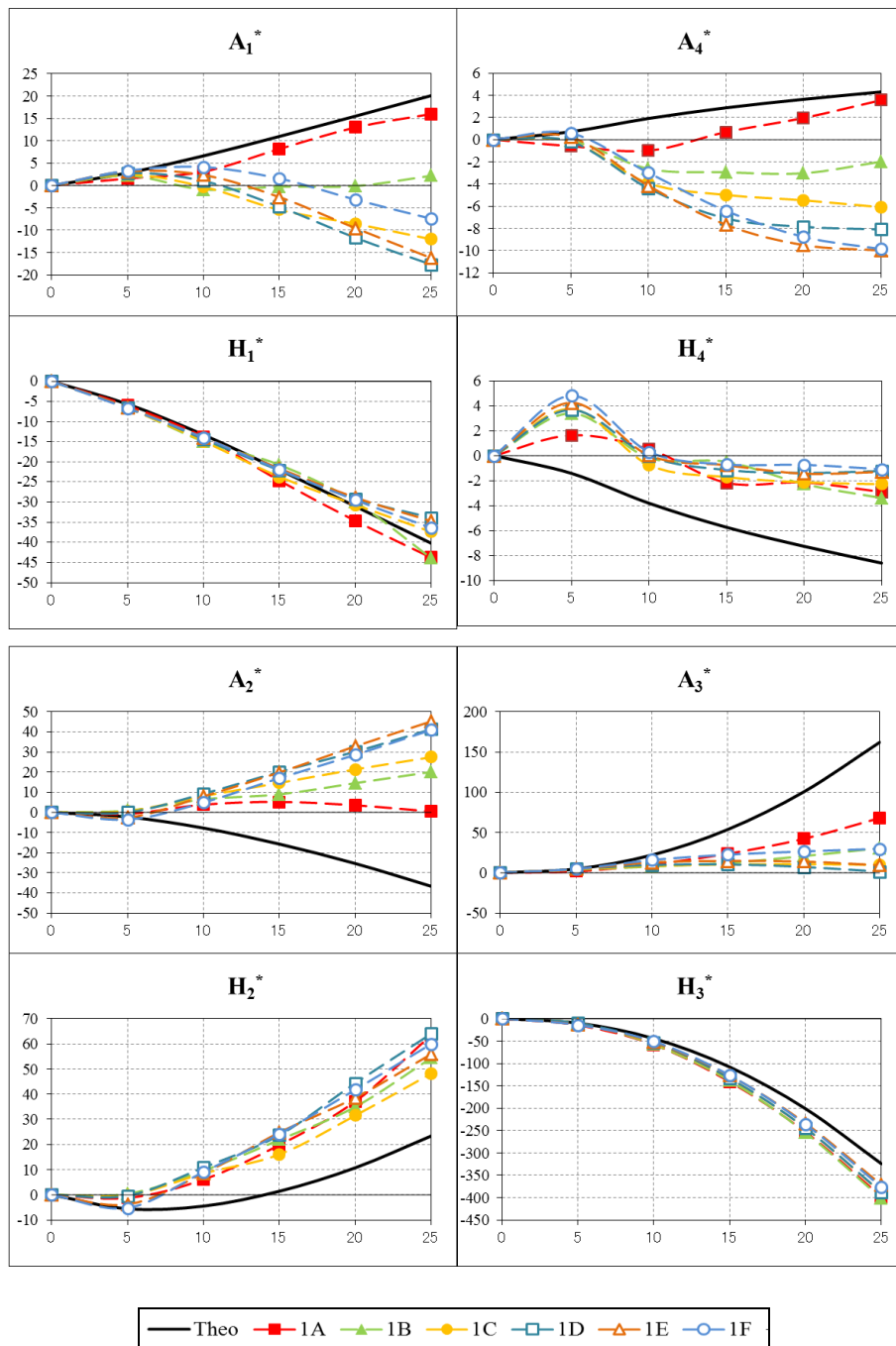


Fig.4.26 Aerodynamic derivatives of Model 1A to 1F

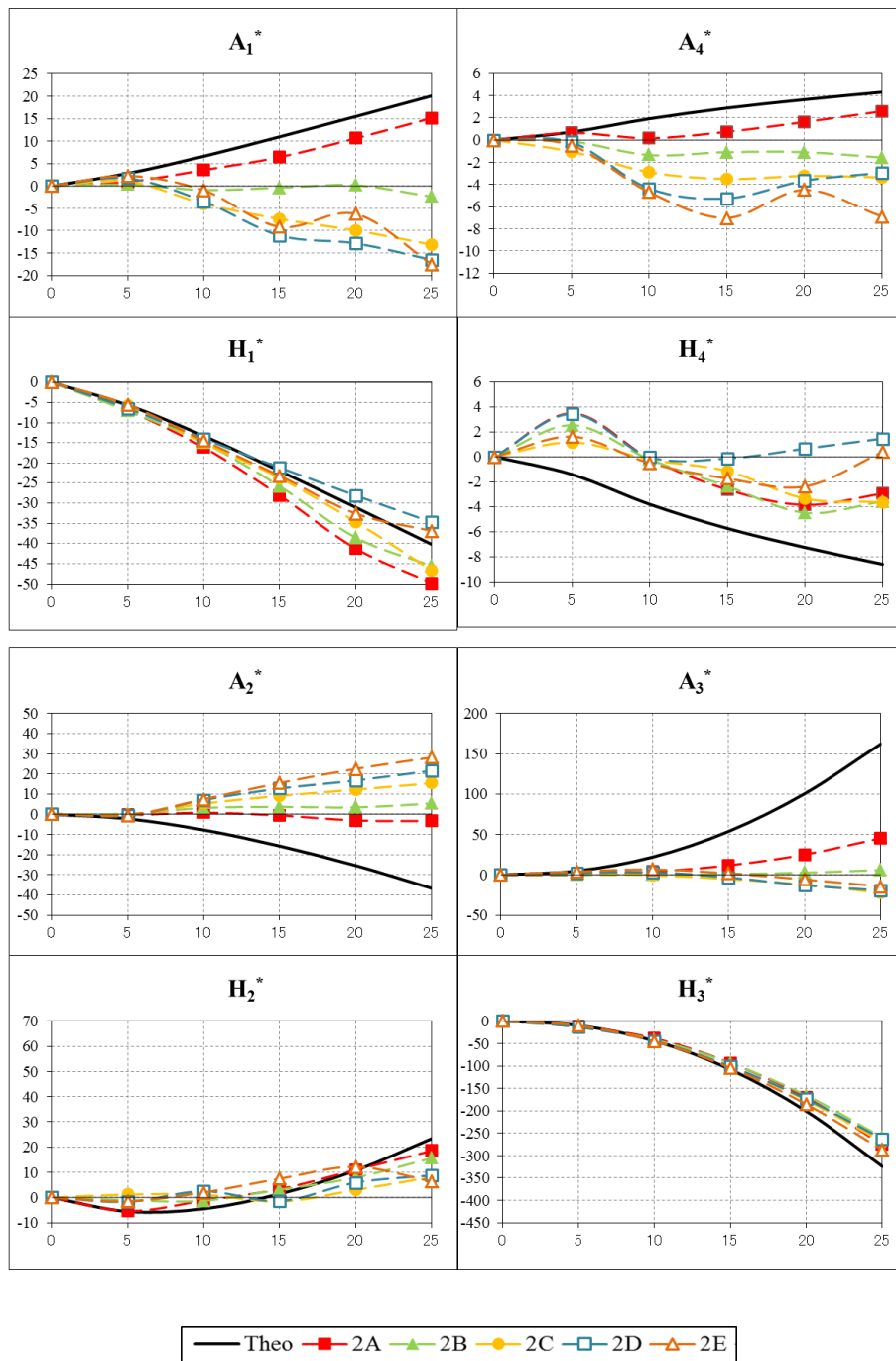


Fig.4.27 Aerodynamic derivatives of Model 2A to 2E

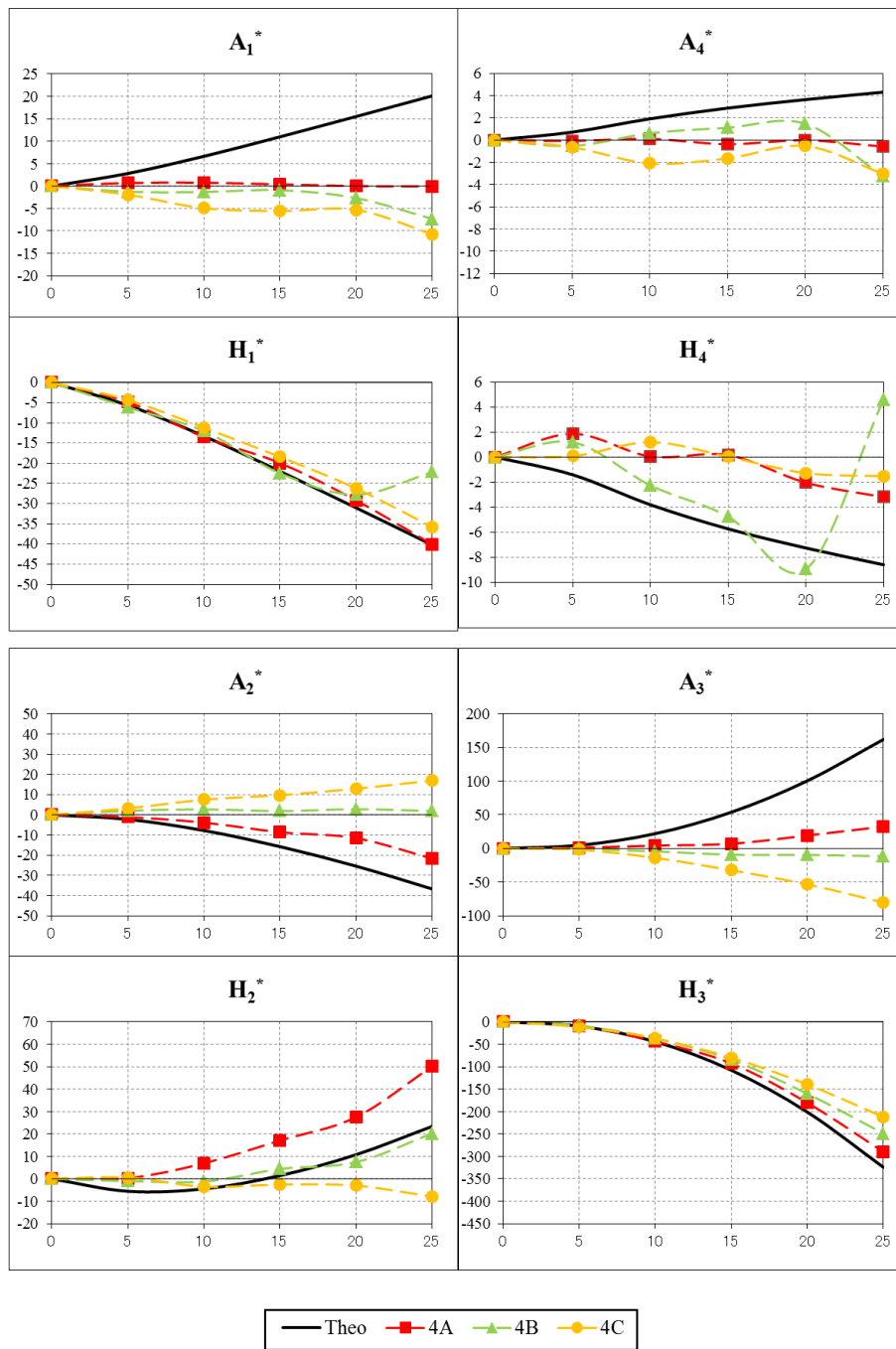


Fig.4.28 Aerodynamic derivatives of Model 4A to 4C

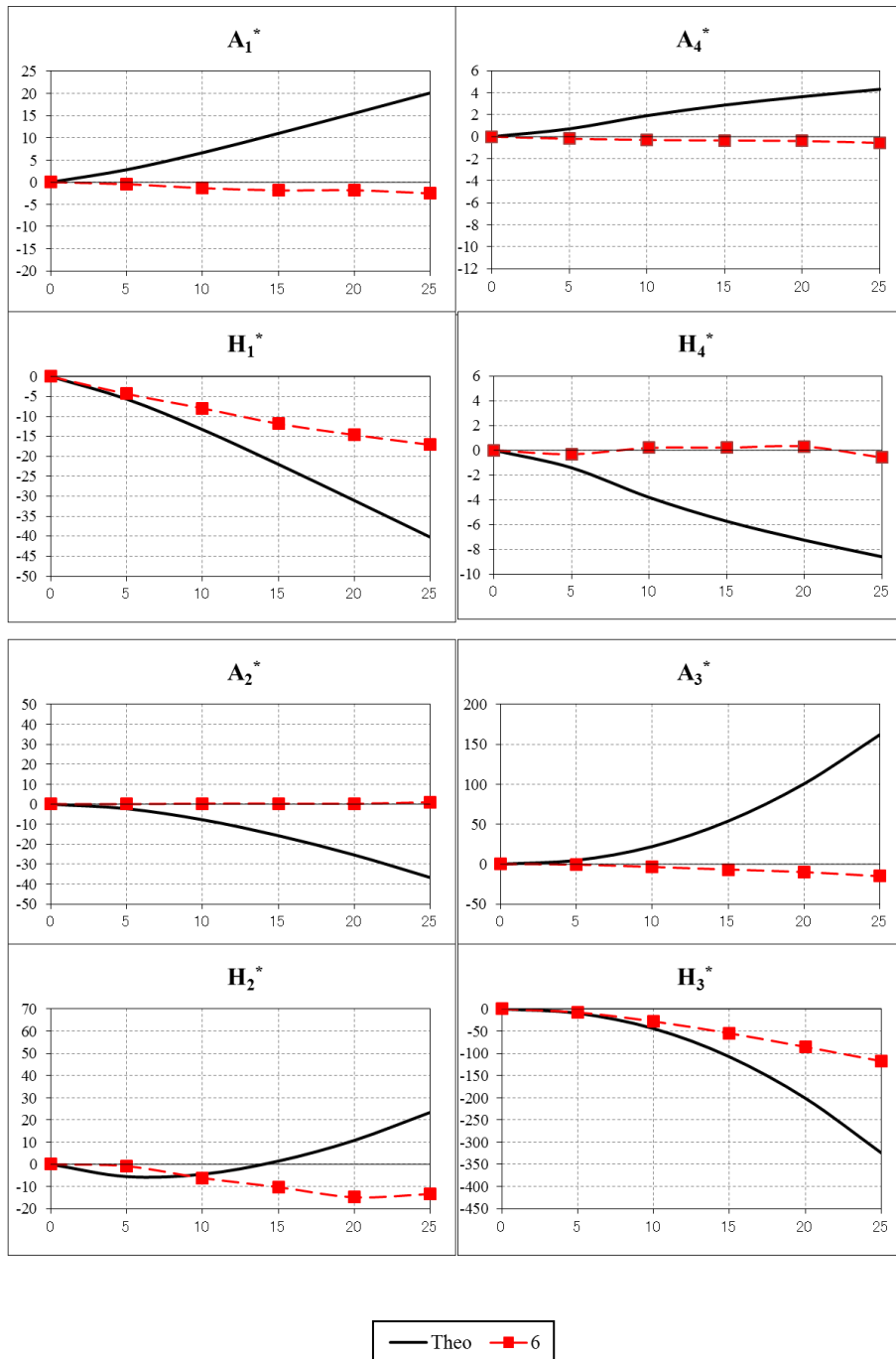


Fig.4.29 Aerodynamic derivatives of Model 6



From the above figures, several patterns of unsteady pressure characteristics and aerodynamic derivatives regarding the position of the slots can be observed:

1. Near leading edge slot plays important role in the aerodynamic derivatives of each section, while near trailing edge slot is less significant. These results are as expected that placing the slot where separation bubble occurred will change the aerodynamic derivatives significantly.
2. Moving the near leading edge slot to the mid-chord position up to certain position tends to change  $A_1^*$  more negative and  $A_2^*$  more positive. For section with narrow slot (Model 1x), moving the slot further will give opposite results.

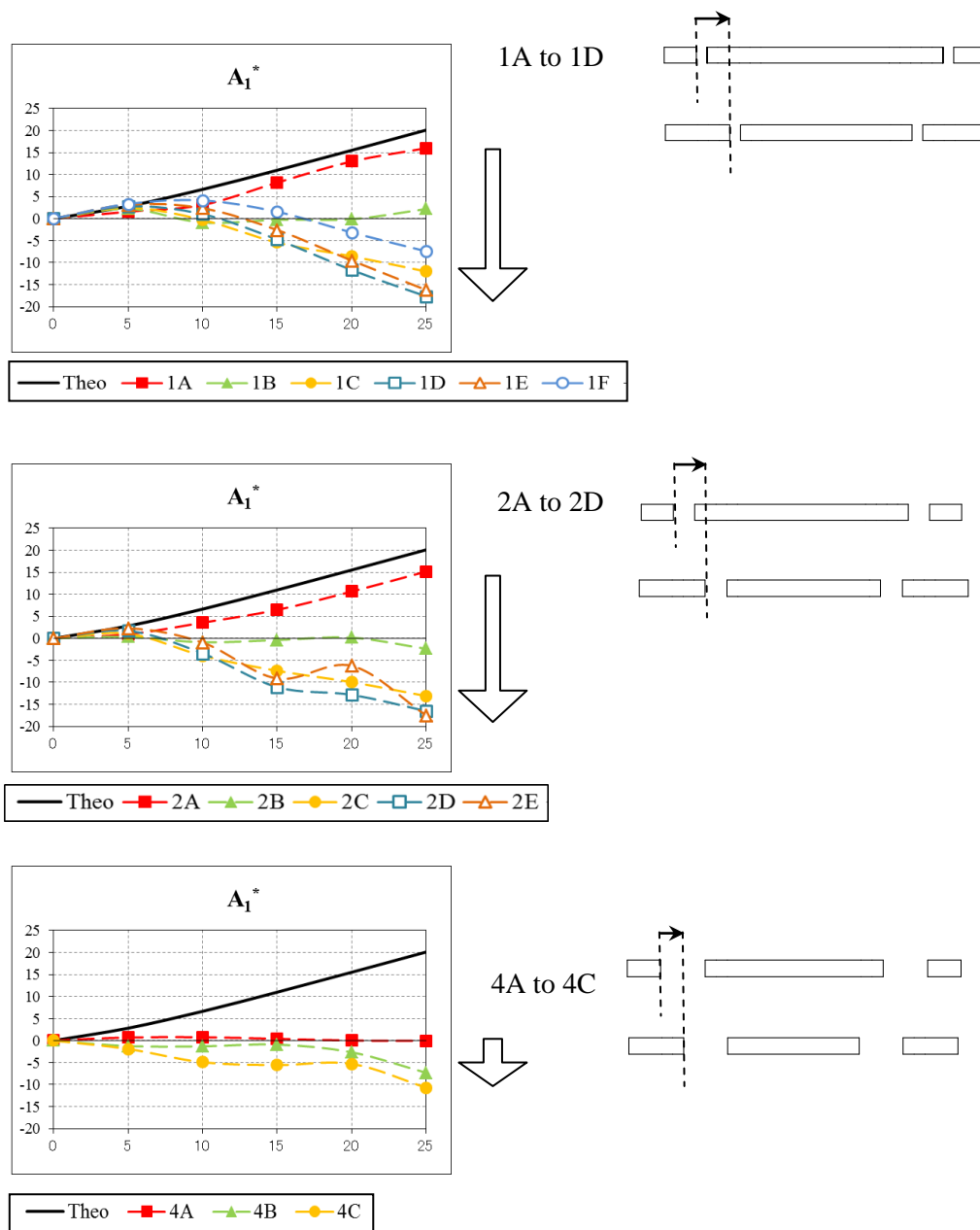


Fig.4.30 Effects of slot position to  $A_1^*$

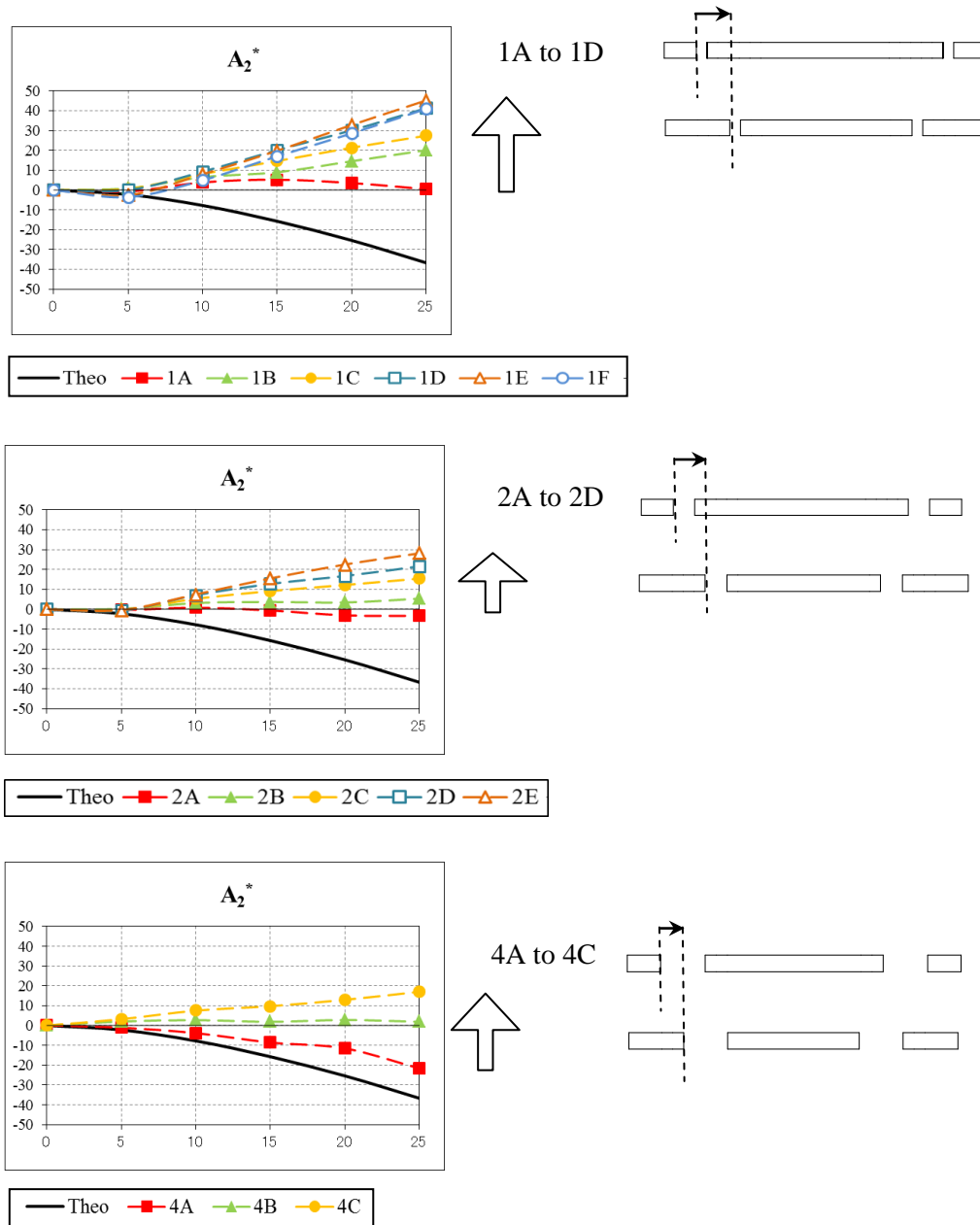


Fig.4.31 Effects of slot position to  $A_2^*$

There are 4 sections that have low absolute value of  $A_1^*$ : Model 1B, Model 2B, Model 4A and Model 6. But only Model 4A that has negative  $A_2^*$ , while the other 3 models have positive value of  $A_2^*$  which means that those sections are prone to torsional flutter at low reduced wind velocity.

3. Aerodynamic derivatives  $H_3^*$  is hardly affected by position of slot for Model 1x and Model 2x. For Model 4x,  $H_3^*$  tends to become more positive or lower in absolute value as position of slot moving toward mid-chord. In Model 6,  $H_3^*$  is significantly lower in absolute value compared to model 1x and Model 2x. These results show that values of  $H_3^*$  are more affected by width instead of position of slots.

It can be expected that Model 4A has the optimal position and width of slots. It has low absolute value of  $A_1^*$  and negative  $A_2^*$ , but  $H_3^*$  is similar to result from Theodorsen function. Further explanation about these aerodynamic derivatives values can be obtained from the unsteady pressure characteristics data.

The effect of near leading edge slot can be clearly seen by comparing unsteady pressure characteristics of Model F with other model. Introducing slot near leading edge completely change the flow field that it produces large pressures upstream of slot and have opposite direction with pressures downstream the slot. For model 1B, 2B, 4A and 6, resultant of these pressures are lower torsional moment. More comprehensive explanation can be get by calculating time history of pressure distribution along the surface and the resultant torsional moment during one cycle of heaving motion. The comparison of time history pressure distribution of Model F and Model 1B is shown in Fig. 4.32. The same phenomena also occurred for Model 2B, 4A and 6. In other words, finding the best slot position to get low absolute value of  $A_1^*$  is simply by tuning the  $P_{1.x_1}$  equals to  $P_{2.x_2}$  as described in Fig. 4.30. This is quite different concept with optimum unsteady pressure characteristics distribution that proposed by Trein & Shirato (2010), which more stable section is attained by balancing the contribution of upwind and downwind half of the section.

For rotational or torsional motion, almost all models with slot have positive  $A_2^*$ . Aerodynamic derivative  $A_2^*$  is related to damping of torsional motion of the system. The pressures will act as stabilizing source if the direction of the pressures are against the motion or oppose the rotational velocity, and they will act as exciting source if otherwise. This can be quantified by calculating the non-dimensional work of each pressure at point-i ( $W_{r,i}$ ) over one cycle of rotational vibration with period  $T$ :

$$W_{r,i} = \int_0^T P_i(t) d\eta_i \quad (4.1)$$

where  $P_i$ : surface force at point-i and  $d\eta_i$ : vertical velocity at point-i. From this definition, positive  $W_{r,i}$  means that force  $P_i$  input the energy into the vibration and vice versa. The non-dimensional work for rotational motion at position  $x^*$  is:

$$W_r(x^*) = x^* \cdot \tilde{C}_{pT}(x^*) \cdot \varphi_0 \cdot \sin \psi_T \cdot \pi \quad (4.2)$$

Non-dimensional work of upper surface for Model F, 1B, 2B, 4A and 6 are presented in Fig. 4.31.

Fig. 4.33 shows that pressures at upstream of near leading edge slot play important role. Pressures at that zone for Model 1B, 2B and 6 act as exciting source and stabilizing source for Model 4A. Although the amplitude of pressures in that zone is lower than the downstream side of the slot, but their effects to global behavior is significant due to larger

arm length. As can be seen in Fig. 4.19, the phase difference values in near leading edge zone is positive, but the values are close to  $180^0$  which imply the near critical condition of stability of Model 4A.

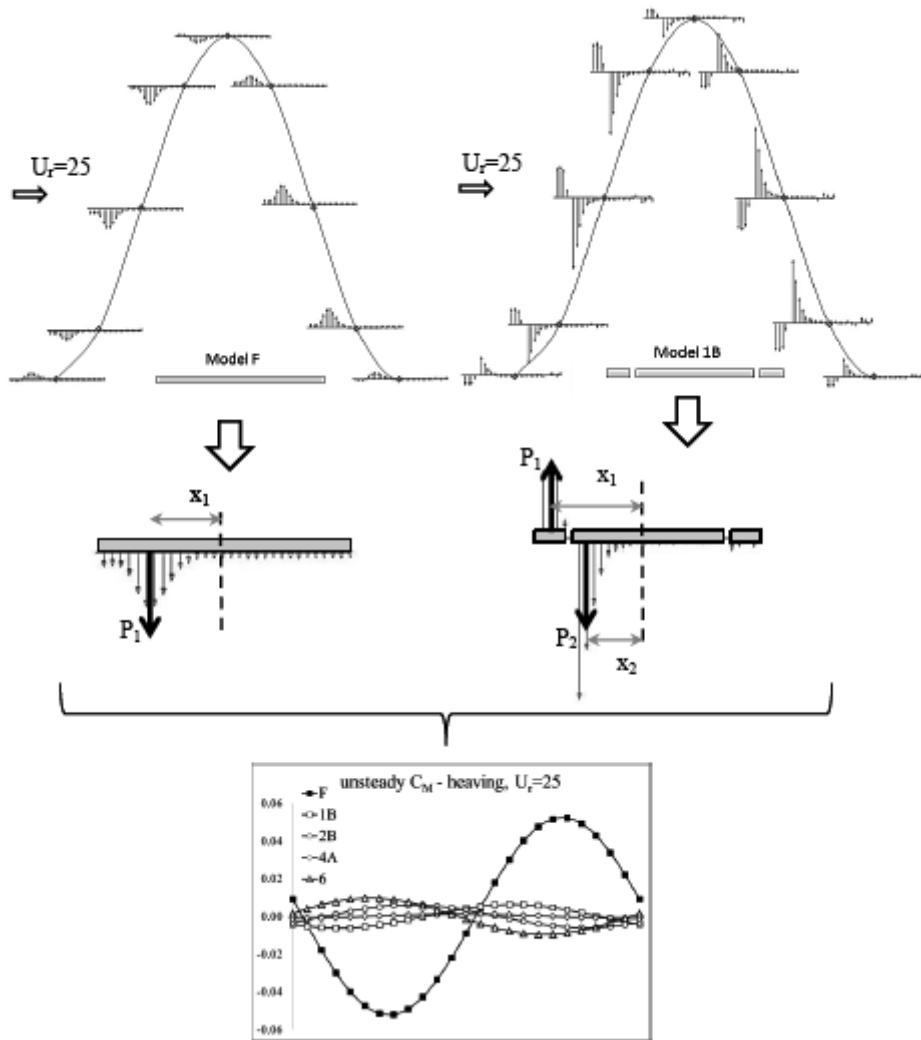


Fig.4.32 Explanation of low absolute value of  $A_I^*$  for Model 1B, 2B, 4A and 6

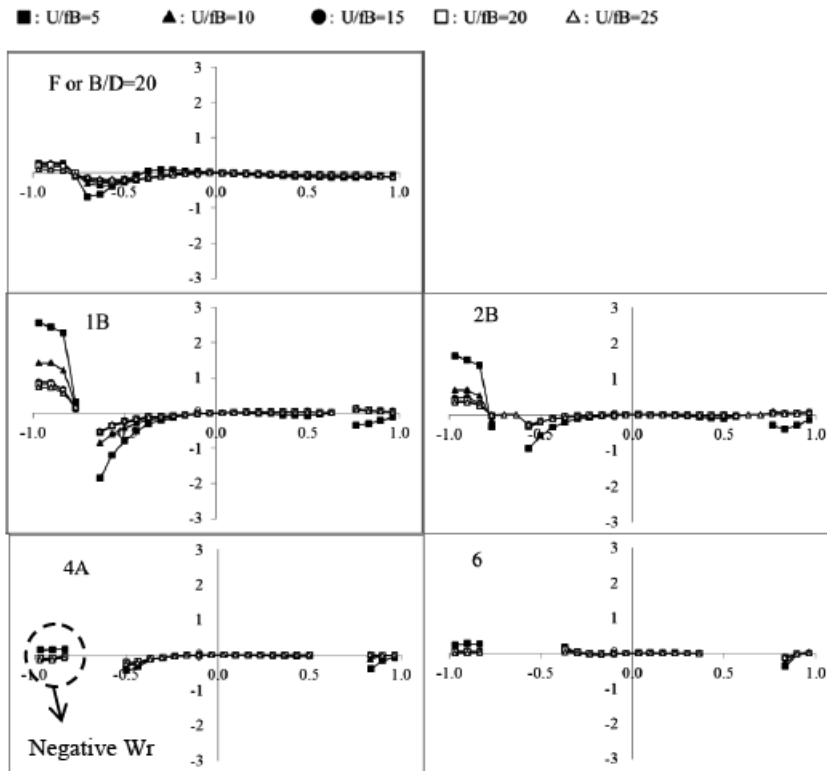


Fig.4.33  $W_r$  of upper surface for Model 1B, 2B, 4A and 6

In order to make general pattern of slot position and width that give optimum condition for flutter stability, Fig. 4.30 and 4.31 are rearranged as seen in Fig. 4.34. Position and width of slot is expressed with variable  $D$  (thickness of prism). Model 1x has slot width  $0.67D$ , Model 2x:  $1.33D$ , and Model 4A:  $2.67D$ . Position A is  $2D$  from leading edge, position B:  $2.67D$ , position C:  $3.33D$ , position D:  $4D$ , position E:  $4.67D$ , and position F:  $5.33D$ .

It can be seen that for slot width  $0.67D$ , optimum position can never be achieved since low  $A_1^*$  occurred along with positive  $A_2^*$  for reduced velocity up to 25. Moving the slot toward mid-chord will produce larger absolute value of  $A_1^*$  and more positive  $A_2^*$ . The same condition also found in section with slot width  $1.33D$ . In section with slot width  $2.67D$ , optimum position is when slot position is  $2D$  from leading edge, as in Model 4A.

Position of slot that gives low absolute value of  $A_1^*$  is strongly related with reattachment point of separation bubble on the surface of the prism. The possible flow field for Model F, Model 1B and Model 4A is shown in Fig. 4.35 to 4.37. The large values of pressures at upstream of leading edge slot with opposite direction with downstream of slot can be attributed with the occurrence of inner circulatory flow in the smaller separation bubble on the surface of the prism.

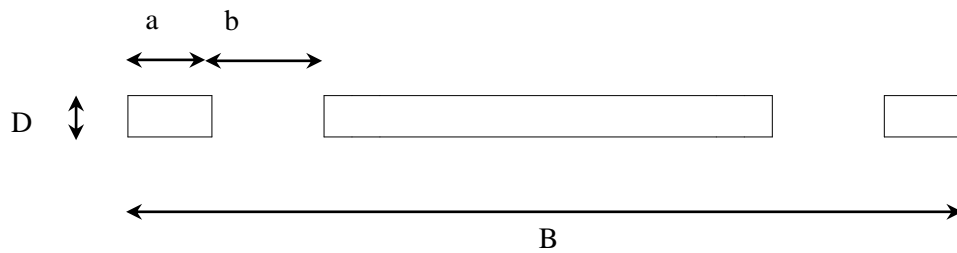
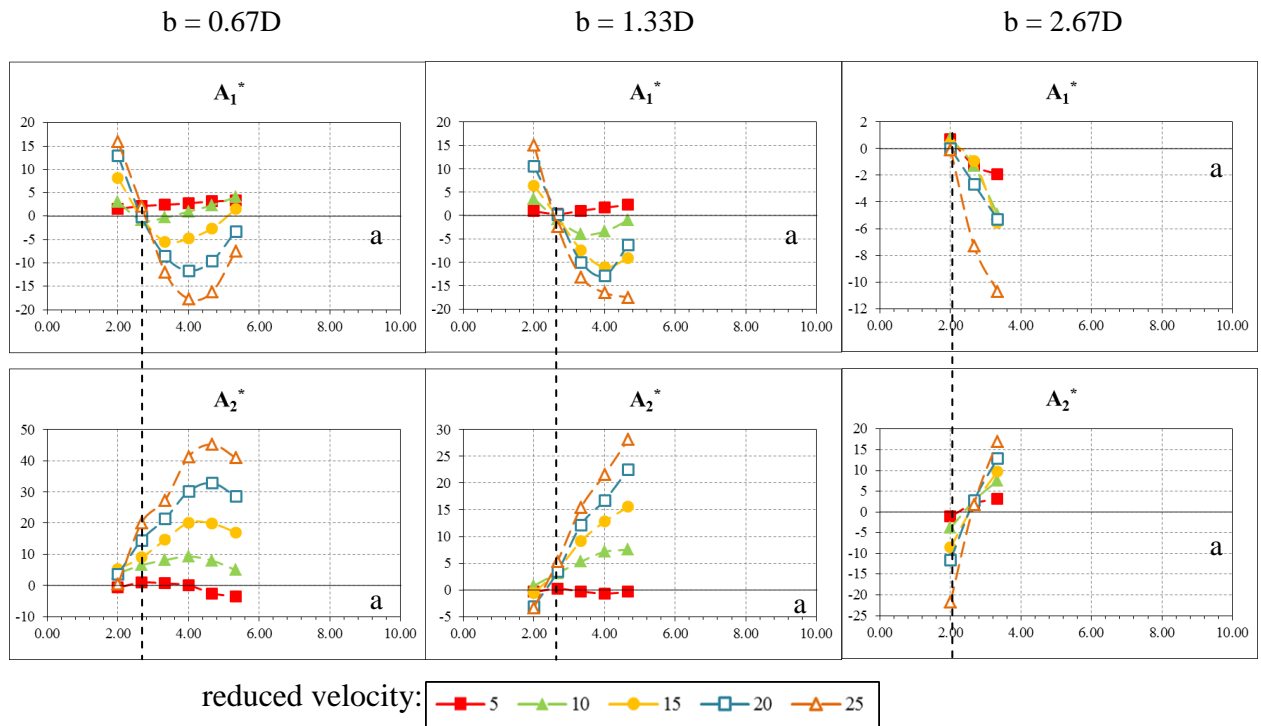


Fig.4.34 Aerodynamic derivatives  $A_1^*$  and  $A_2^*$  for Model 1x (slot width  $0.67D$ , left); Model 2x (slot width  $1.33D$ , center) and Model 4x (slot width  $2.67D$ , right)

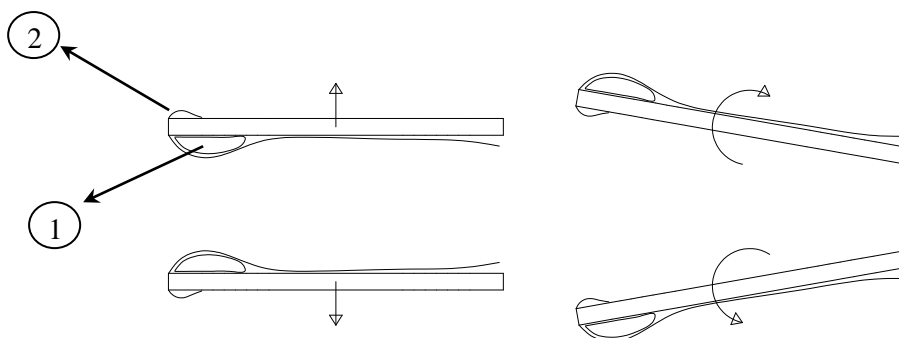


Fig.4.35 Flow field around Model F

Fig.4.33 shows the flow field of basic section, rectangular prism with  $B/D=20$ . Large separation bubble (1) produces negative pressure on the surface, while weaker separation (2) also occurred on the opposite surface.

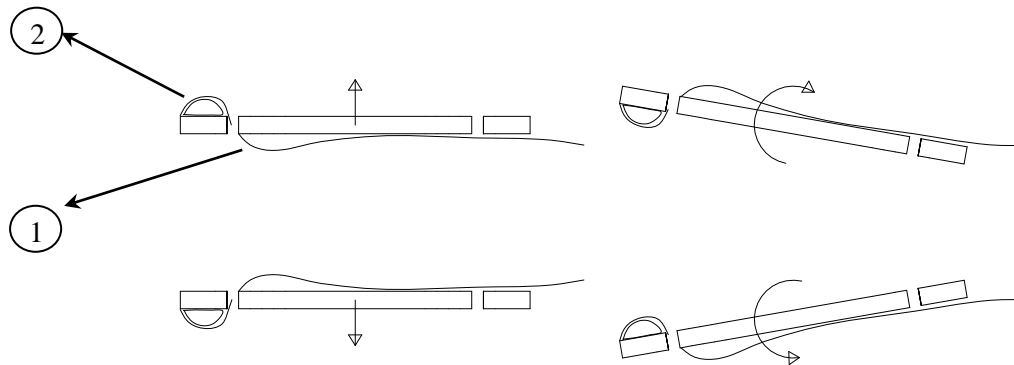


Fig.4.36 Flow field around Model 1B

In Model 1B, the flow field is very much differ from basic section. There is no large separation bubble near leading edge like in basic section. On the other side, the weaker separation on basic section grows into inner circulatory flow, then the flow goes through the slot and produces separation bubble downstream the slot on the opposite surface. This phenomena is similar with mechanism of galloping: the presence of inner circulatory flow on the surface due to motion. This flow produces large negative pressure on the surface. From several model (1A to 1E, 2A to 2D, and 4A to 4C), it can be said that this inner circulatory flow is occurred only when the slot is at certain distance from the leading edge. Large pressure at upstream of slot can be found in Model 1B, 2B which have slot at distance of  $2.67D$ . If the slot is moved to leading edge (Model 1A, 2A, 4A), the pressures become much lower.

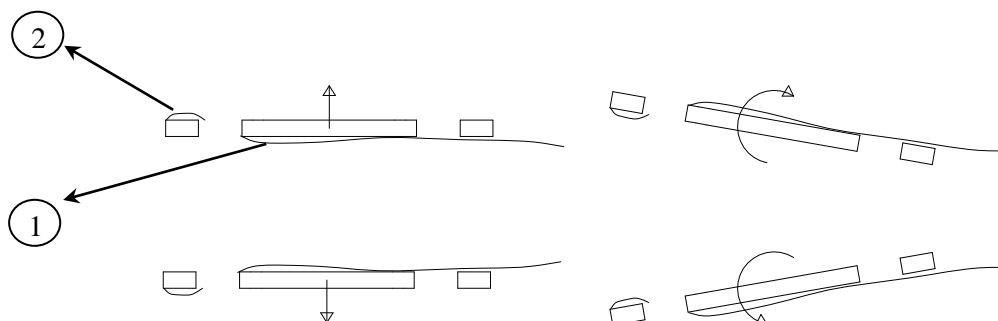


Fig.4.37 Flow field around Model 4A

In Model 4A, the large pressures at near leading edge do not occurred, so it can be said the inner circulatory flow (2) does not have the same intensity as the Model 1B. Separation (2) has the same condition with Model 1B: does not grow into large separation bubble due to the presence of slot.

### 4.3.2 Unsteady Pressure Characteristics and Aerodynamic Derivatives of Prism with Porous Cavity

The unsteady pressure characteristics for upper surface of rectangular prism with cavity are presented in Fig. 4.39 to Fig. 4.54. It can be seen that even large reduction of peak amplitude is possible (up to 59% for section 9A-050-grating), but the effects also felt as increasing of pressure amplitude in the upstream of the peak pressure position. General pattern of the amplitude of pressures of section with porous cavity compared with basic section is as shown in Fig. 4.38. This phenomenon was not observed for transonic flow as reported by Kumar & Viswanath (2002). Therefore, this characteristic might be related with different physical behaviour between transonic flow and very much lower wind velocity flow used for this study. This condition results in no significant change in the contribution of upper surface to aerodynamic derivatives values as shown in Fig. 4.55 to Fig. 4.58. Therefore, no significant effect of porous cavity to flutter stability is expected.

From the unsteady pressure characteristics figures, it can be said that the reduction of amplitude of pressures is affected by the width of cavity, the existence of porous surface and depth of cavity. Further studies are needed to explain in detail the physical process behind this phenomena.

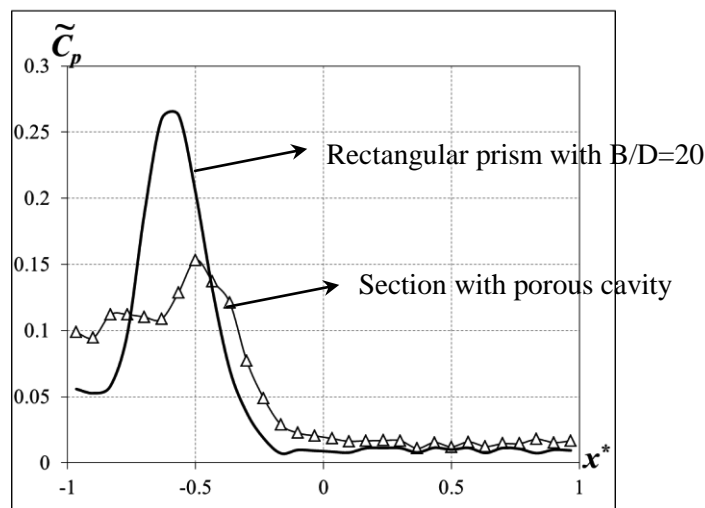
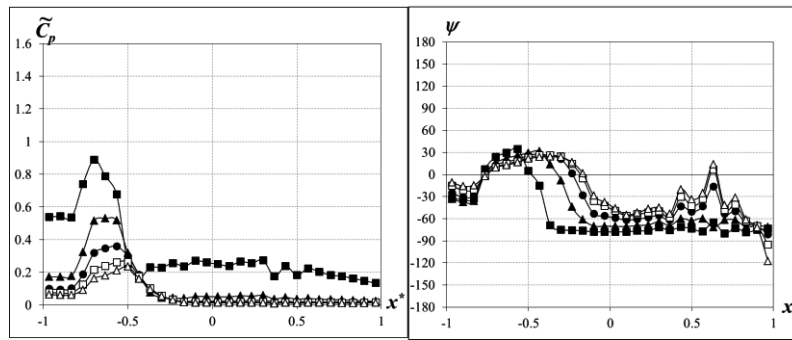
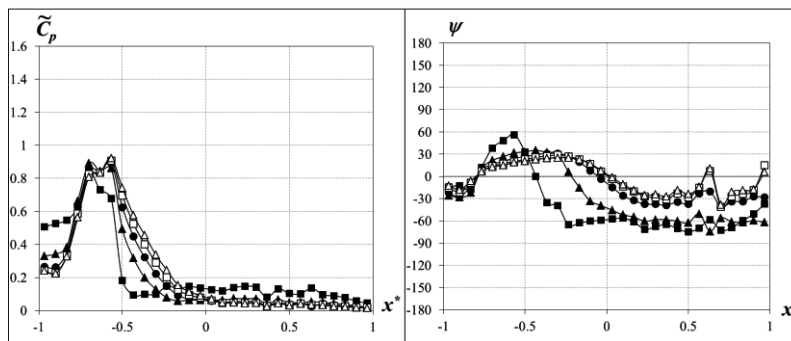


Fig.4.38 Comparison of amplitude of pressures of section with porous cavity compared with rectangular prism with B/D=20 (at high  $U_r$ )

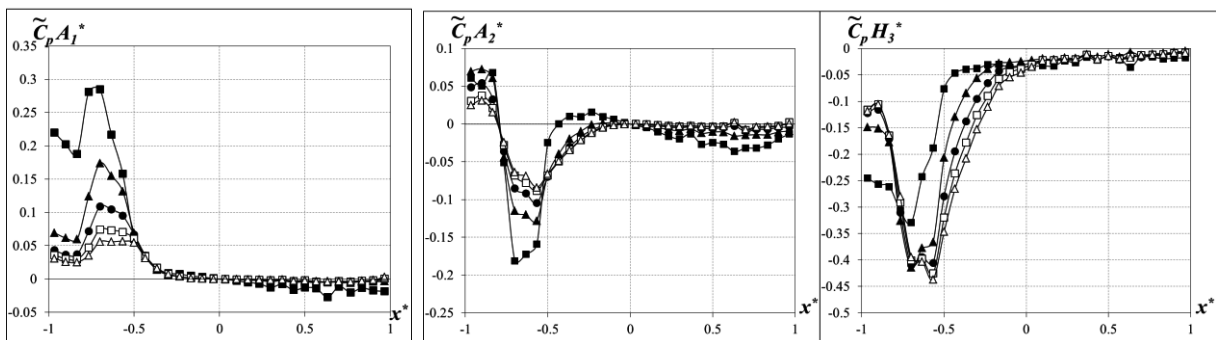




(a) heaving



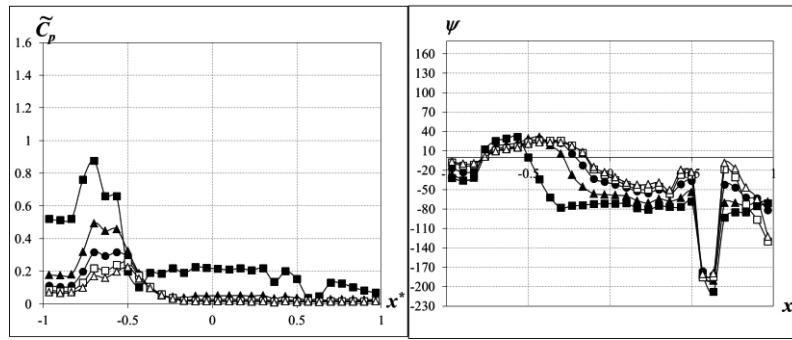
(b) torsional



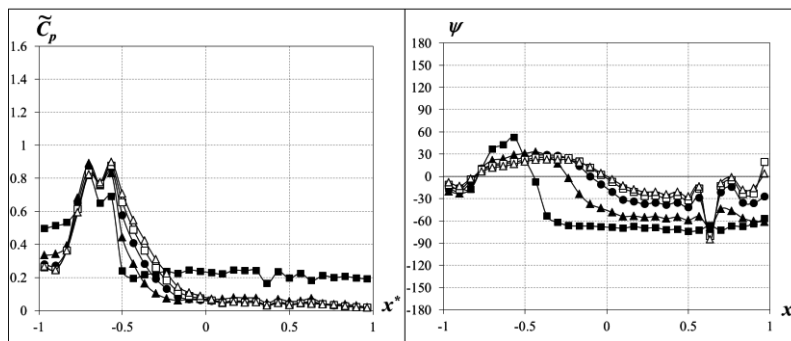
(c)  $\tilde{C}_p A_1^*(x^*)$ ,  $\tilde{C}_p A_2^*(x^*)$  and  $\tilde{C}_p H_3^*(x^*)$



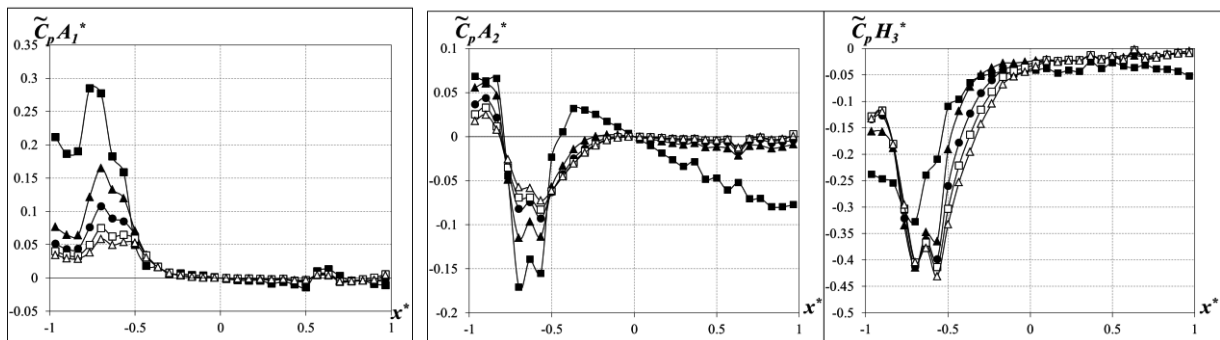
Fig.4.39 Unsteady pressure characteristics of Model 2-025-no grating (upper surface)



(a) heaving



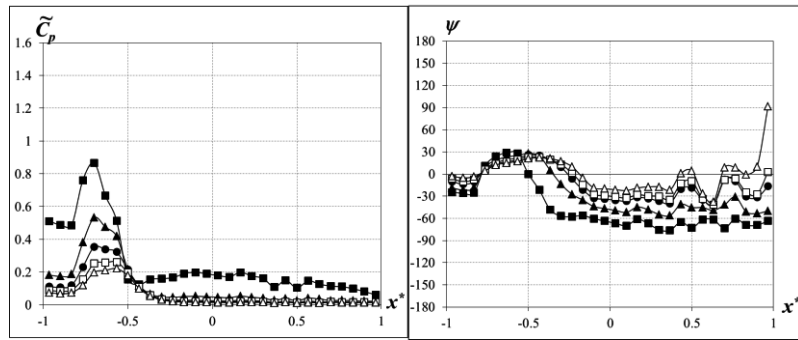
(b) torsional



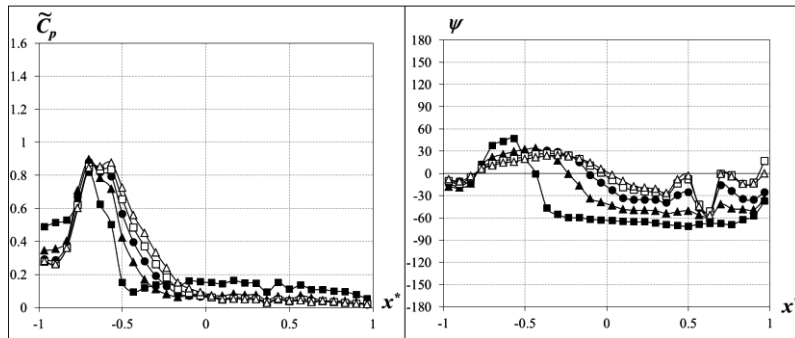
(c)  $\tilde{C}_p A_1^*(x^*)$ ,  $\tilde{C}_p A_2^*(x^*)$  and  $\tilde{C}_p H_3^*(x^*)$



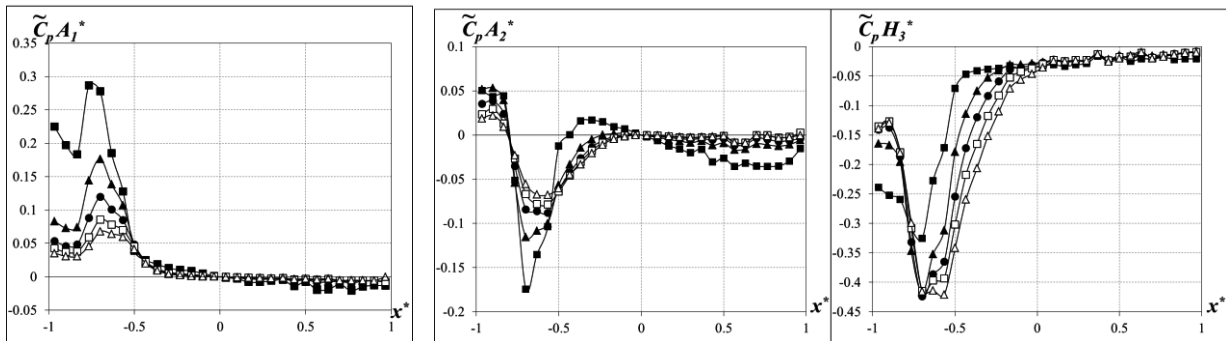
Fig.4.40 Unsteady pressure characteristics of Model 2-050-no grating (upper surface)



(a) heaving



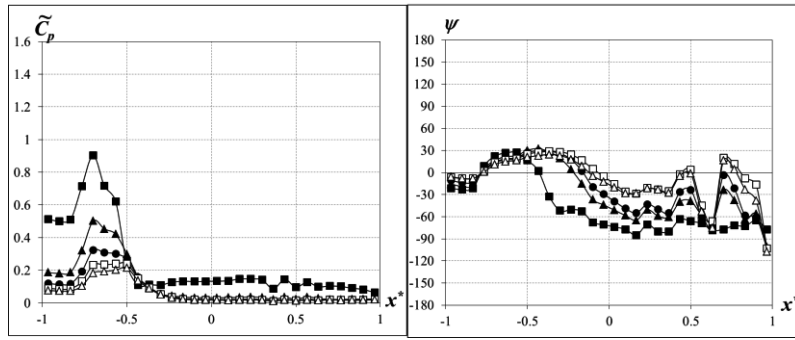
(b) torsional



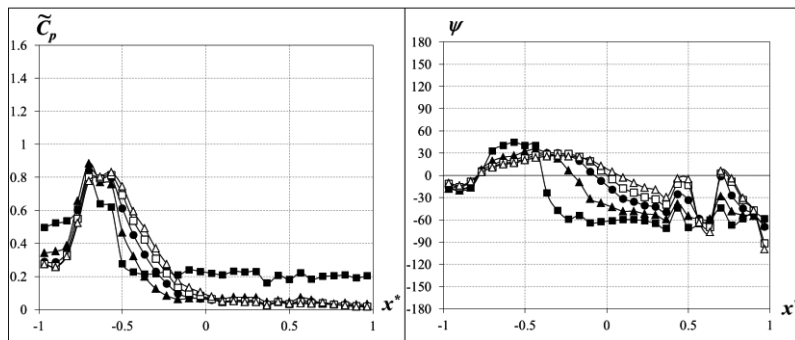
(c)  $\tilde{C}_p A_1^*(x^*)$ ,  $\tilde{C}_p A_2^*(x^*)$  and  $\tilde{C}_p H_3^*(x^*)$



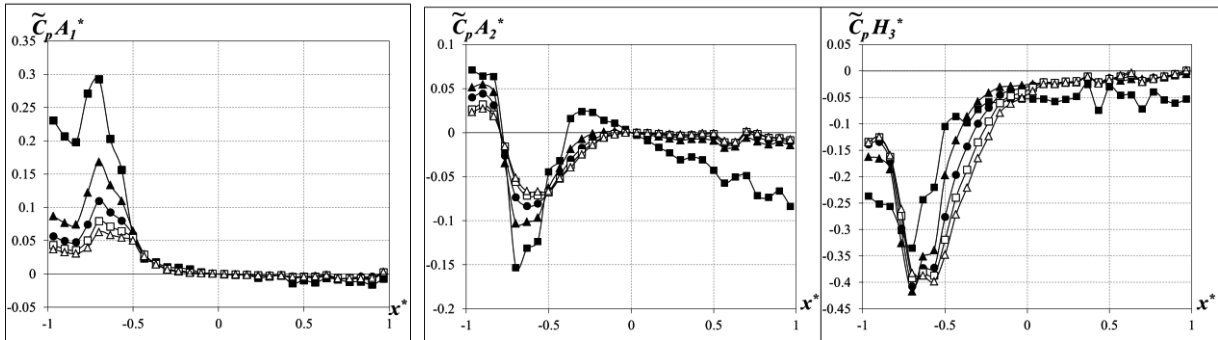
Fig.4.41 Unsteady pressure characteristics of Model 2-025-grating (upper surface)



(a) heaving



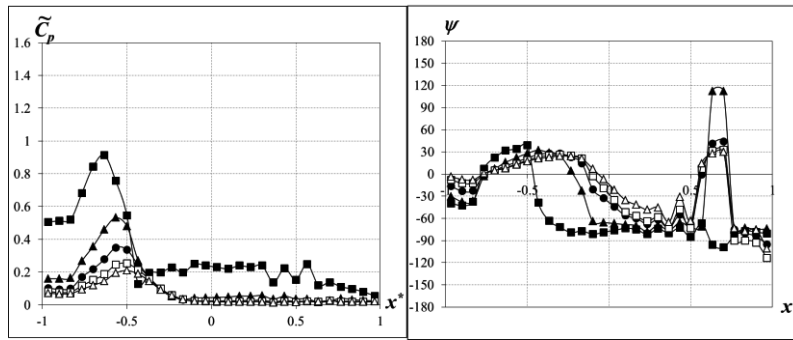
(b) torsional



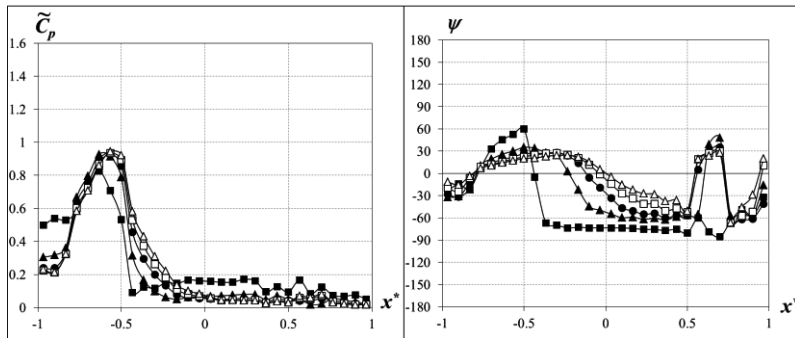
(c)  $\tilde{C}_p A_1^*(x^*)$ ,  $\tilde{C}_p A_2^*(x^*)$  and  $\tilde{C}_p H_3^*(x^*)$



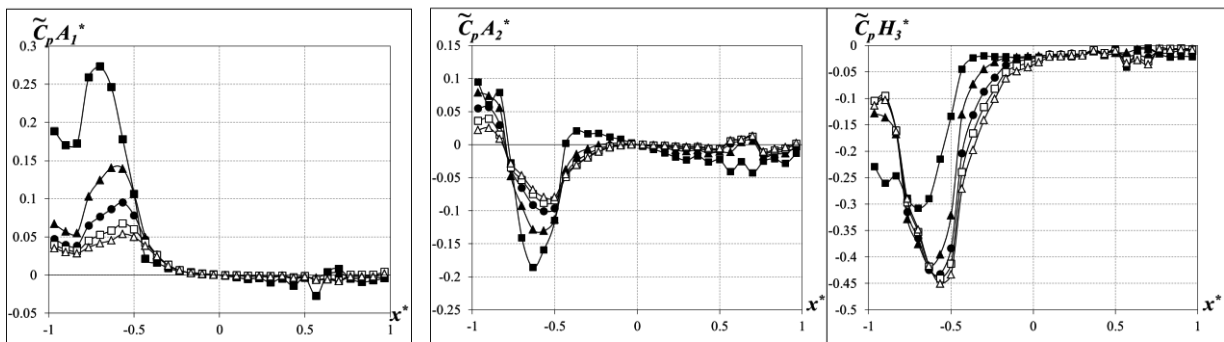
Fig.4.42 Unsteady pressure characteristics of Model 2-050-grating (upper surface)



(a) heaving



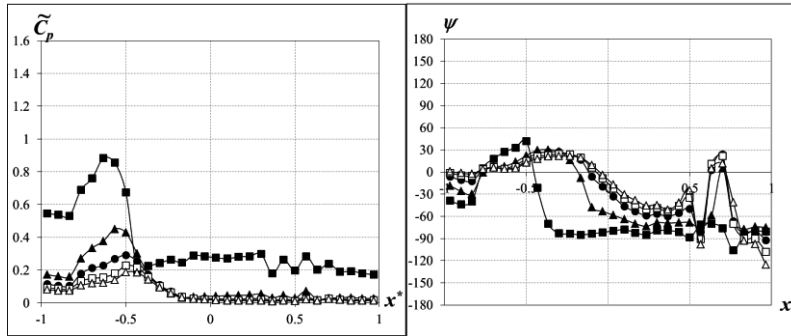
(b) torsional



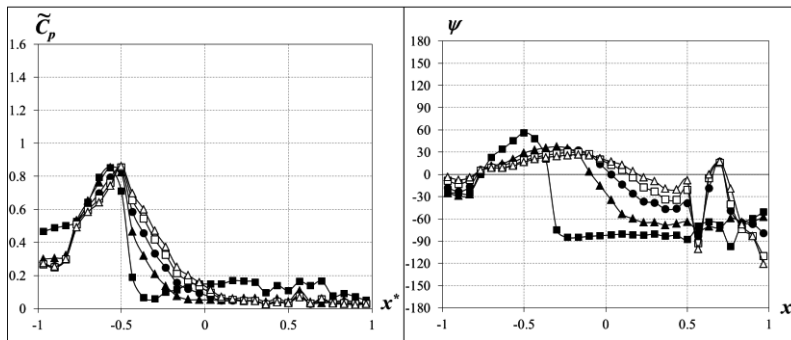
(c)  $\tilde{C}_p A_1^*(x^*)$ ,  $\tilde{C}_p A_2^*(x^*)$  and  $\tilde{C}_p H_3^*(x^*)$



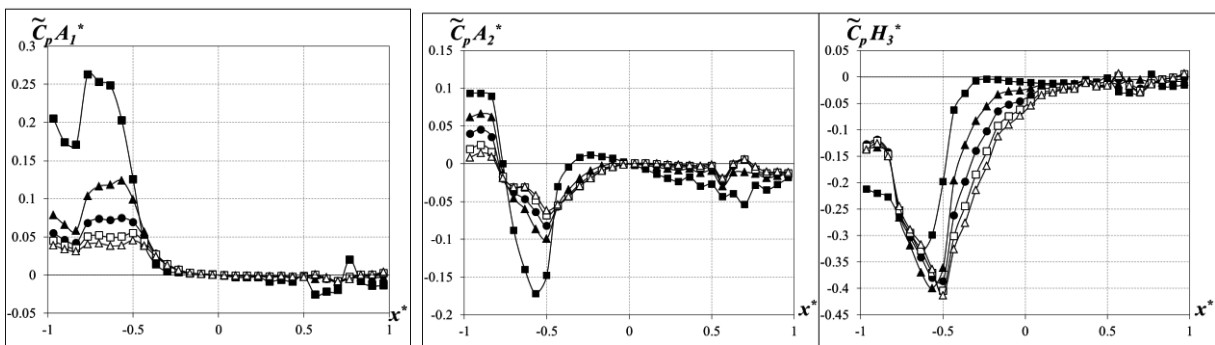
Fig.4.43 Unsteady pressure characteristics of Model 4-025-no grating (upper surface)



(a) heaving



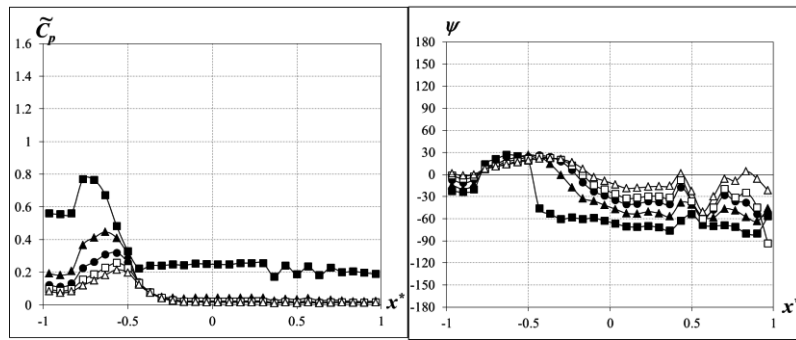
(b) torsional



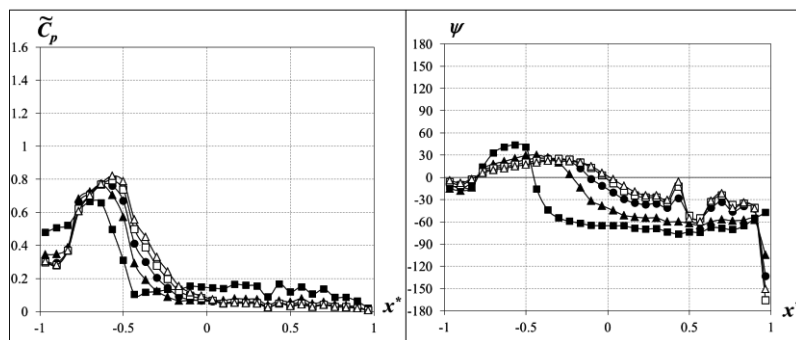
(c)  $\tilde{C}_p A_1^*(x^*)$ ,  $\tilde{C}_p A_2^*(x^*)$  and  $\tilde{C}_p H_3^*(x^*)$



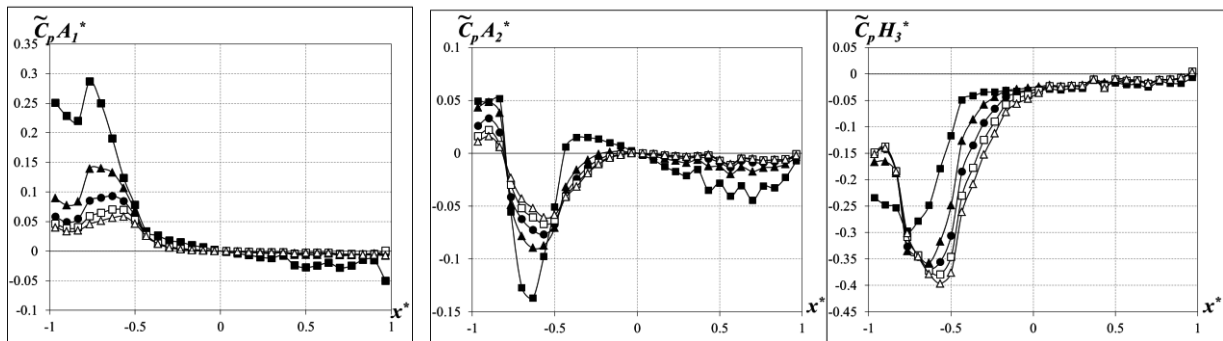
Fig.4.44 Unsteady pressure characteristics of Model 4-050-no grating (upper surface)



(a) heaving



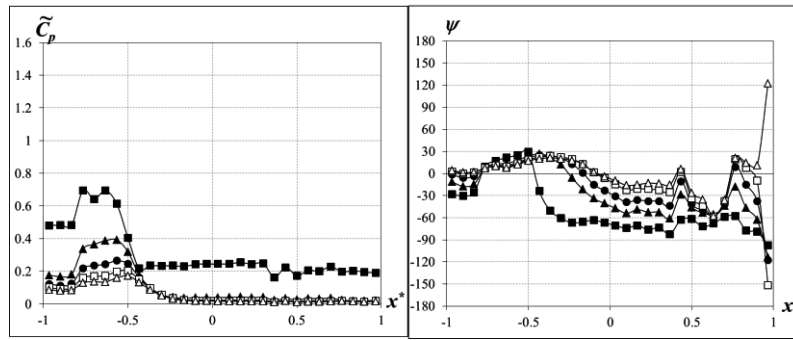
(b) torsional



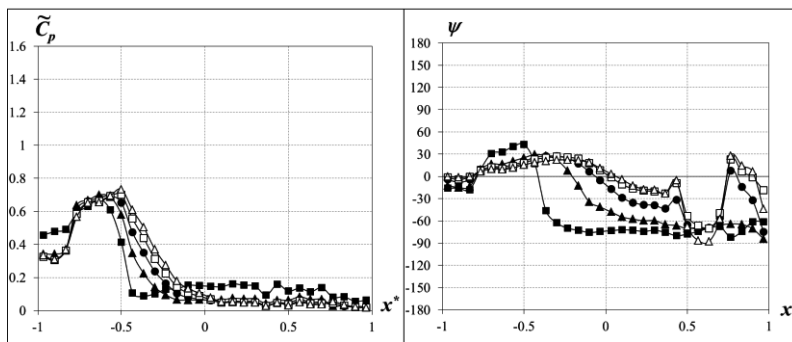
(c)  $\tilde{C}_p A_1^*(x^*)$ ,  $\tilde{C}_p A_2^*(x^*)$  and  $\tilde{C}_p H_3^*(x^*)$



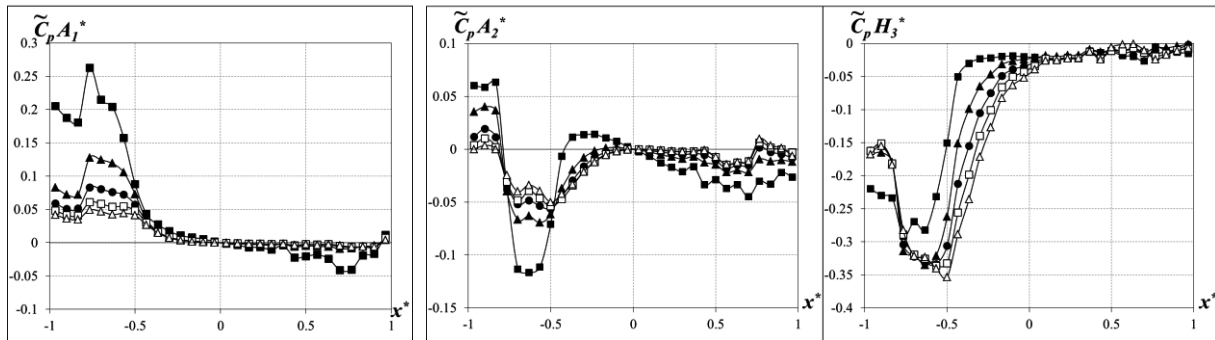
Fig.4.45 Unsteady pressure characteristics of Model 4-025-grating (upper surface)



(a) heaving



(b) torsional



(c)  $\tilde{C}_p A_1^*(x^*)$ ,  $\tilde{C}_p A_2^*(x^*)$  and  $\tilde{C}_p H_3^*(x^*)$

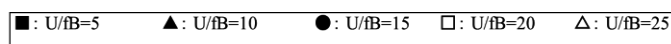
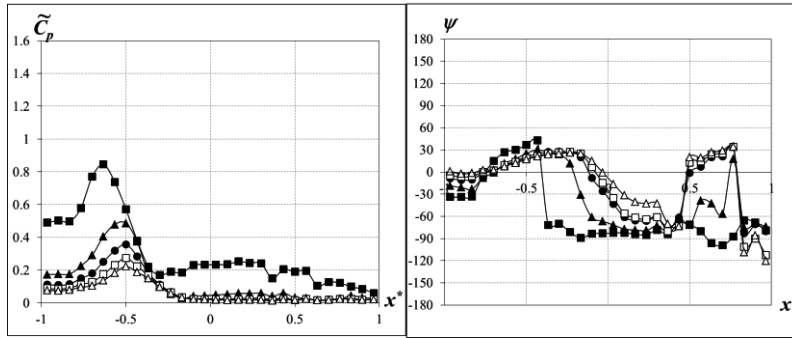
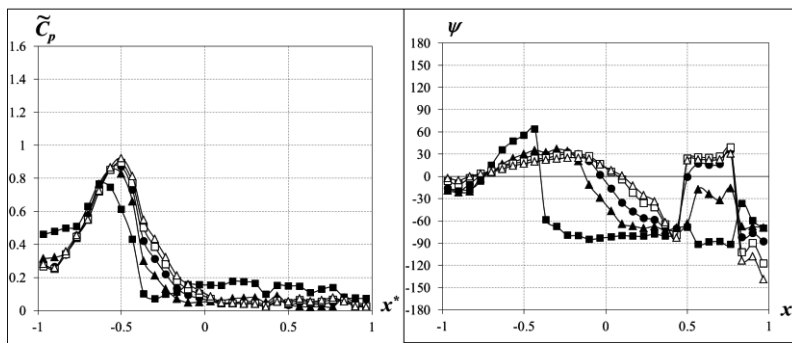


Fig.4.46 Unsteady pressure characteristics of Model 4-050-grating (upper surface)

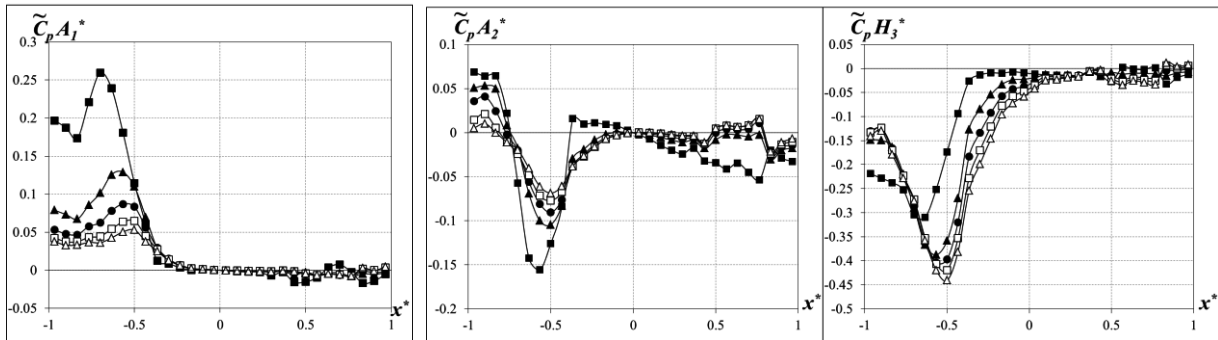




(a) heaving



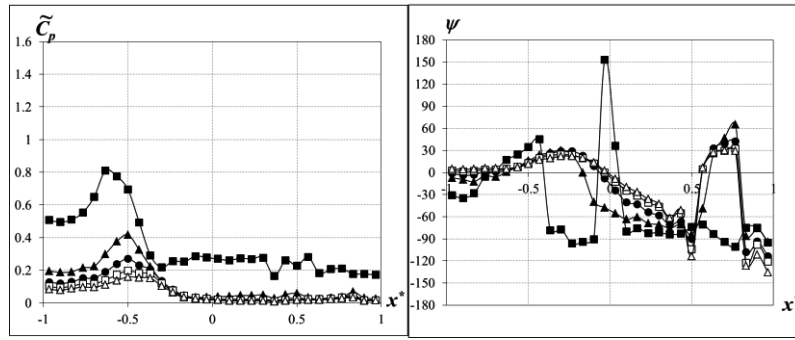
(b) torsional



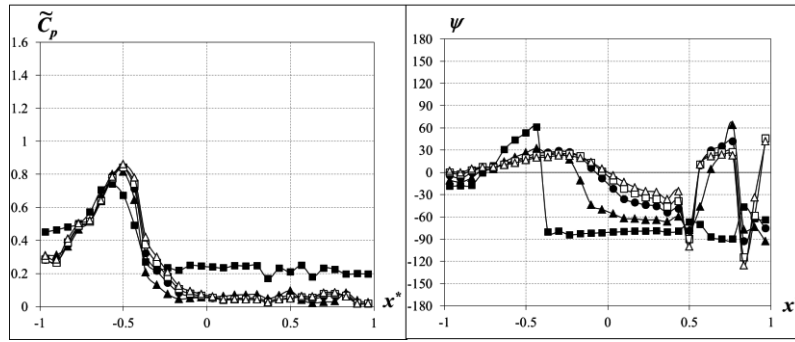
(c)  $\tilde{C}_p A_1^*(x^*)$ ,  $\tilde{C}_p A_2^*(x^*)$  and  $\tilde{C}_p H_3^*(x^*)$



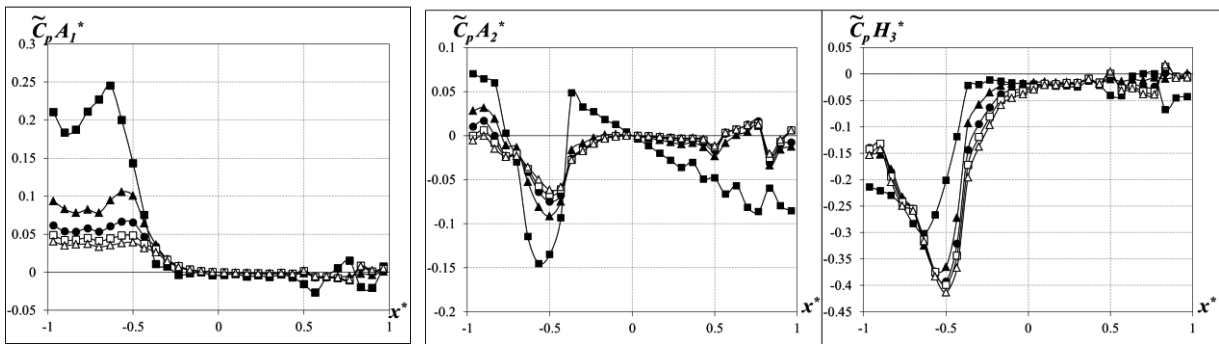
Fig.4.47 Unsteady pressure characteristics of Model 6-025-no grating (upper surface)



(a) heaving



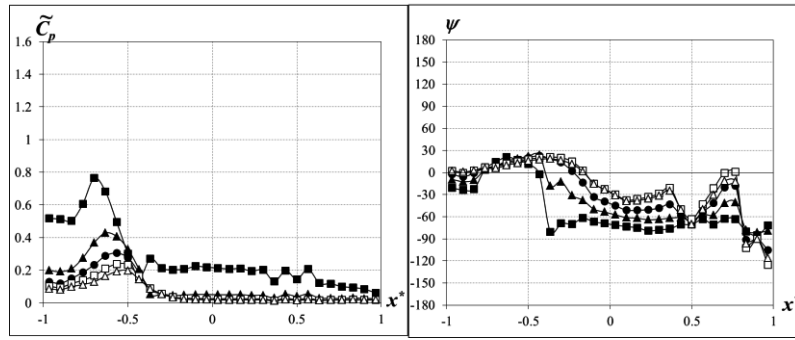
(b) torsional



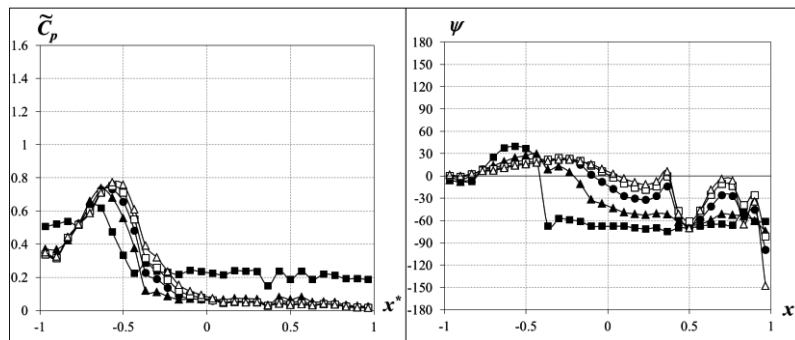
(c)  $\tilde{C}_p A_1^*(x^*)$ ,  $\tilde{C}_p A_2^*(x^*)$  and  $\tilde{C}_p H_3^*(x^*)$



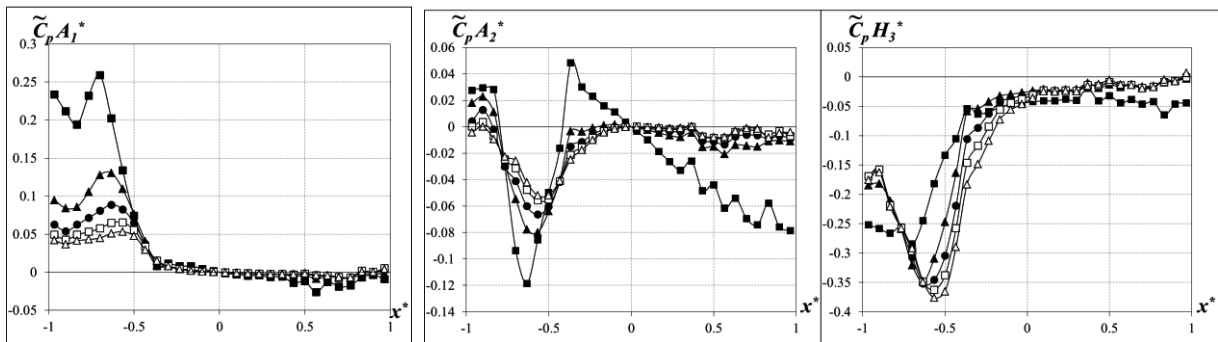
Fig.4.48 Unsteady pressure characteristics of Model 6-050-no grating (upper surface)



(a) heaving



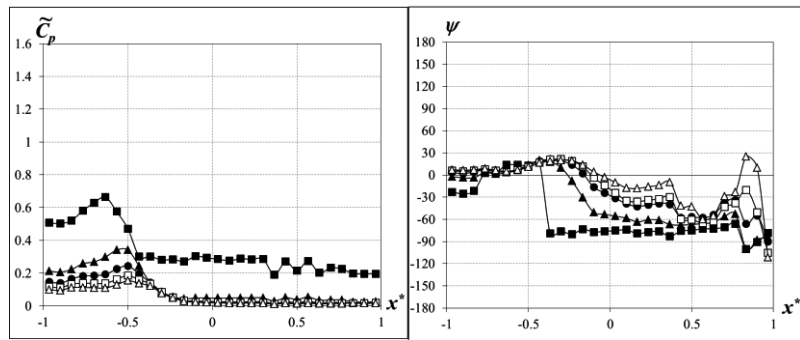
(b) torsional



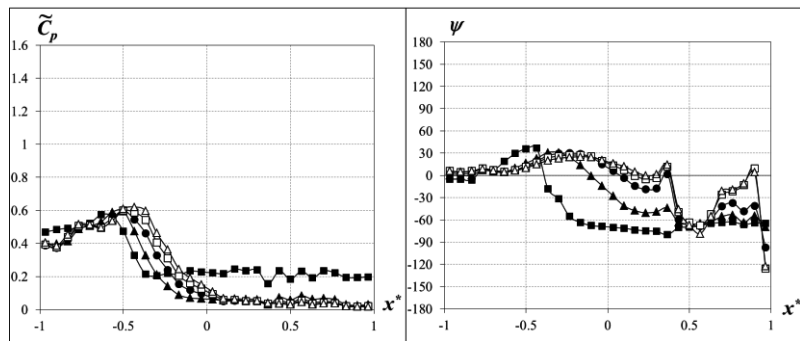
(c)  $\tilde{C}_p A_1^*(x^*)$ ,  $\tilde{C}_p A_2^*(x^*)$  and  $\tilde{C}_p H_3^*(x^*)$



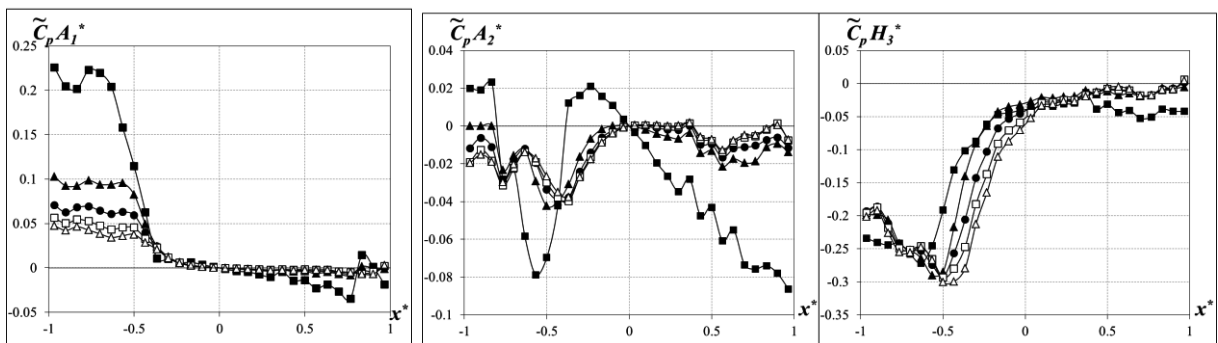
Fig.4.49 Unsteady pressure characteristics of Model 6-025-grating (upper surface)



(a) heaving



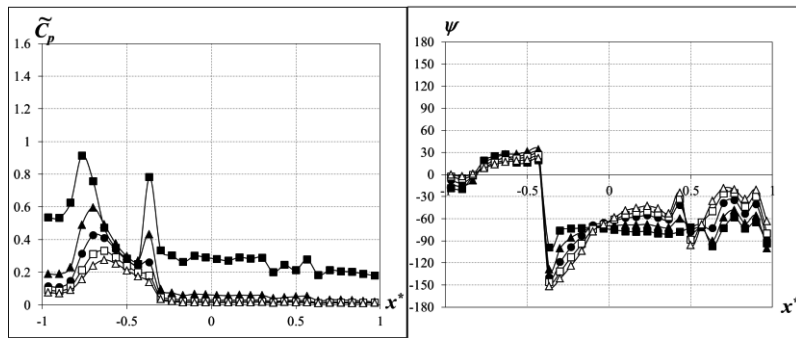
(b) torsional



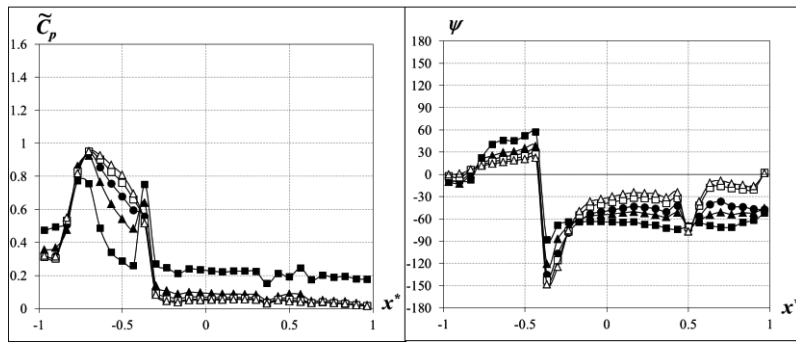
(c)  $\tilde{C}_p A_1^*(x^*)$ ,  $\tilde{C}_p A_2^*(x^*)$  and  $\tilde{C}_p H_3^*(x^*)$



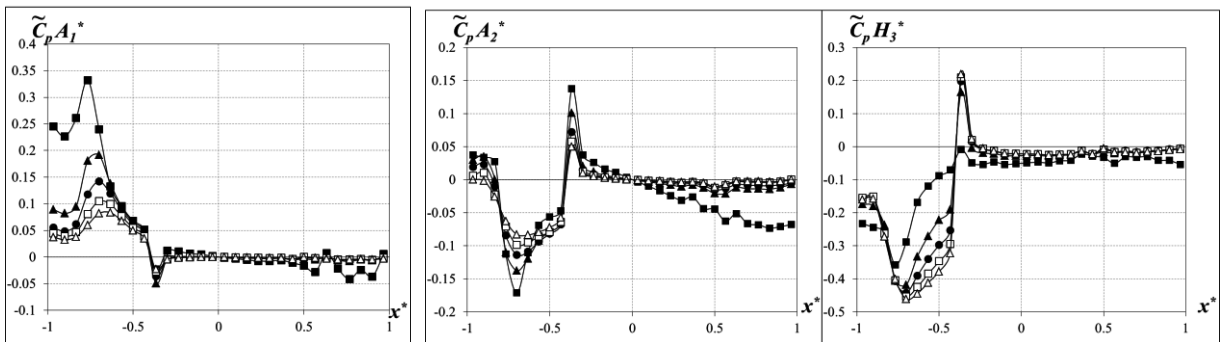
Fig.4.50 Unsteady pressure characteristics of Model 6-050-grating (upper surface)



(a) heaving



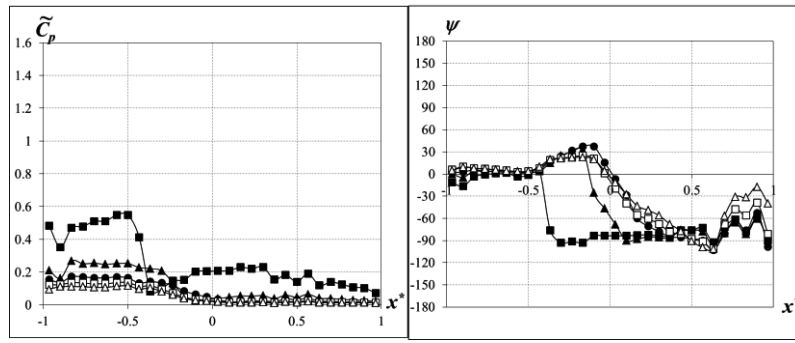
(b) torsional



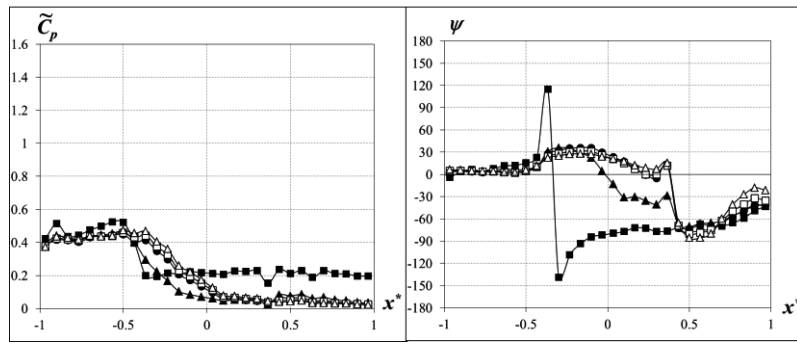
(c)  $\tilde{C}_p A_1^*(x^*)$ ,  $\tilde{C}_p A_2^*(x^*)$  and  $\tilde{C}_p H_3^*(x^*)$



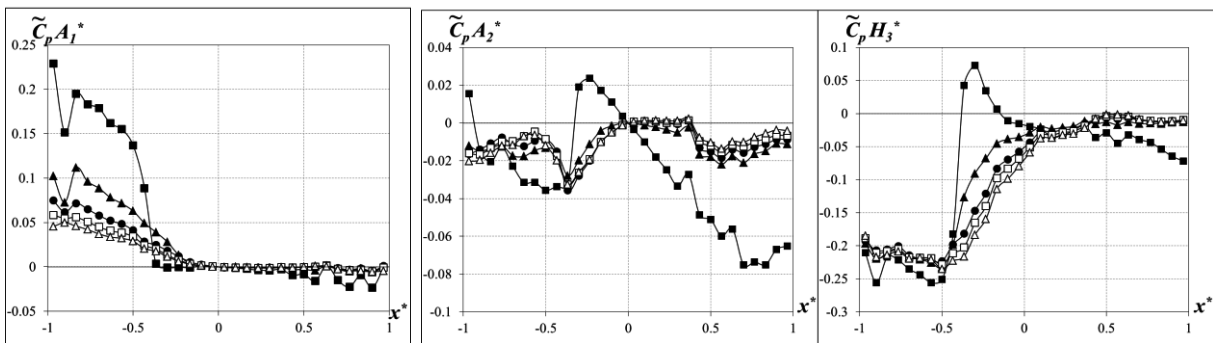
Fig.4.51 Unsteady pressure characteristics of Model 9A-050-no grating (upper surface)



(a) heaving



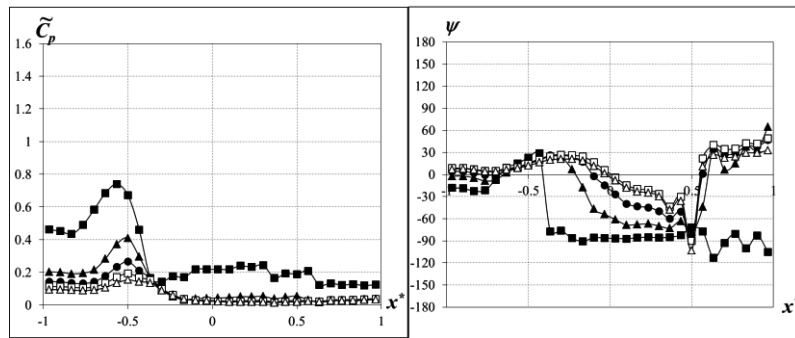
(b) torsional



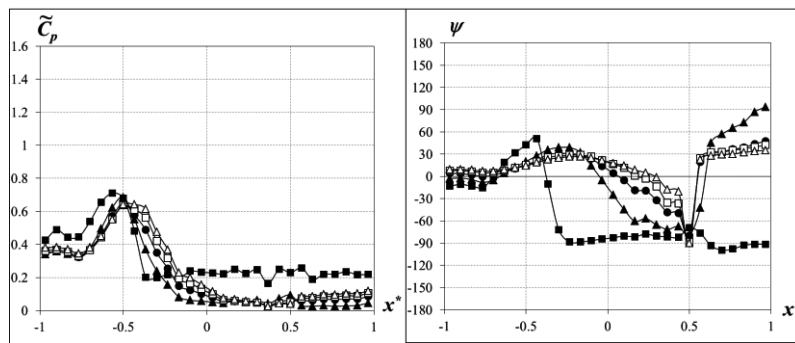
(c)  $\tilde{C}_p A_1^*(x^*)$ ,  $\tilde{C}_p A_2^*(x^*)$  and  $\tilde{C}_p H_3^*(x^*)$



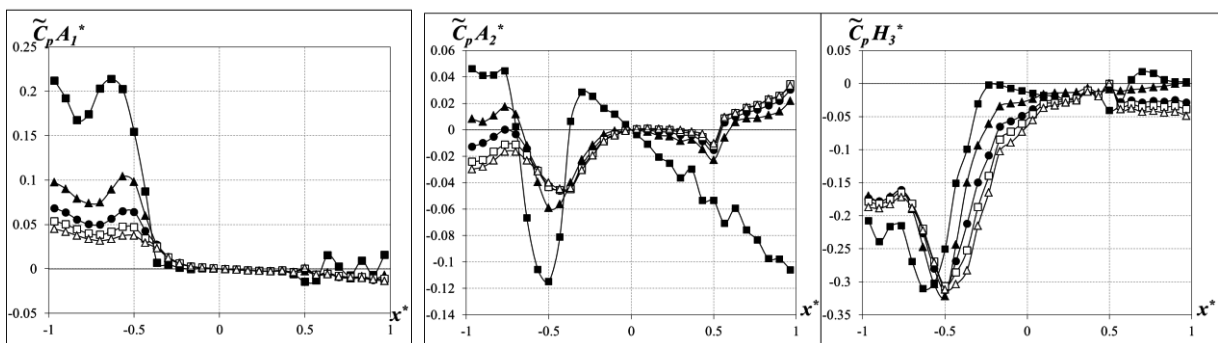
Fig.4.52 Unsteady pressure characteristics of Model 9A-050-grating (upper surface)



(a) heaving



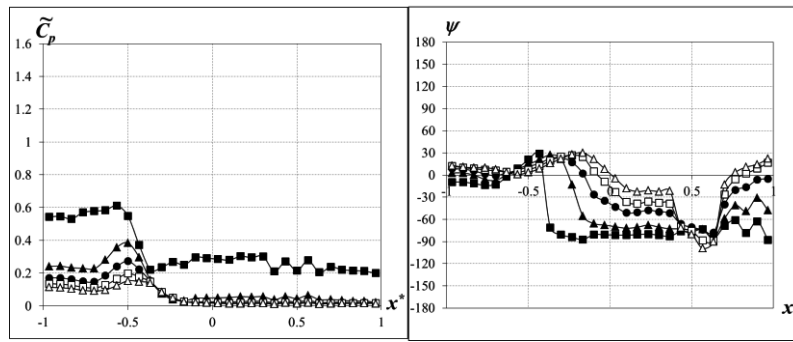
(b) torsional



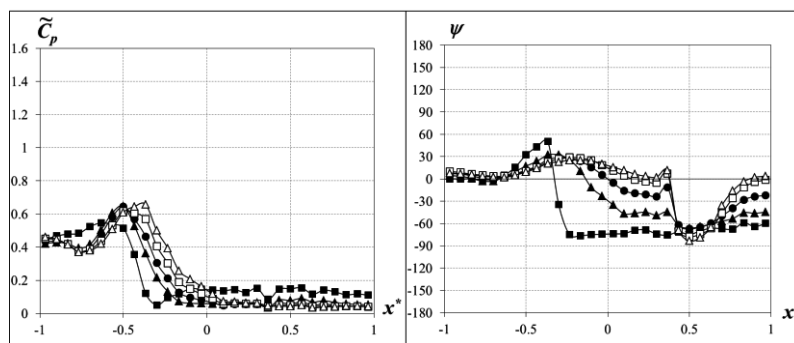
(c)  $\tilde{C}_p A_1^*(x^*)$ ,  $\tilde{C}_p A_2^*(x^*)$  and  $\tilde{C}_p H_3^*(x^*)$



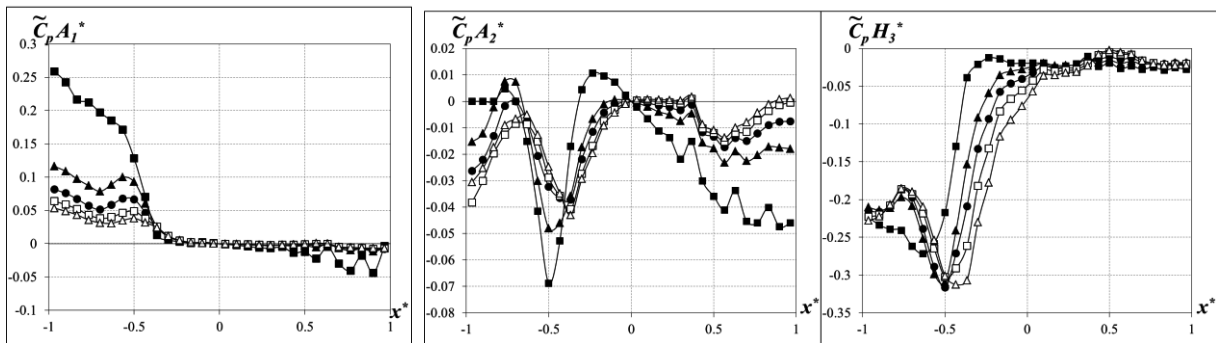
Fig.4.53 Unsteady pressure characteristics of Model 9B-050-no grating (upper surface)



(a) heaving



(b) torsional



(c)  $\tilde{C}_p A_1^*(x^*)$ ,  $\tilde{C}_p A_2^*(x^*)$  and  $\tilde{C}_p H_3^*(x^*)$

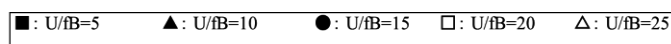


Fig.4.54 Unsteady pressure characteristics of Model 9B-050-grating (upper surface)



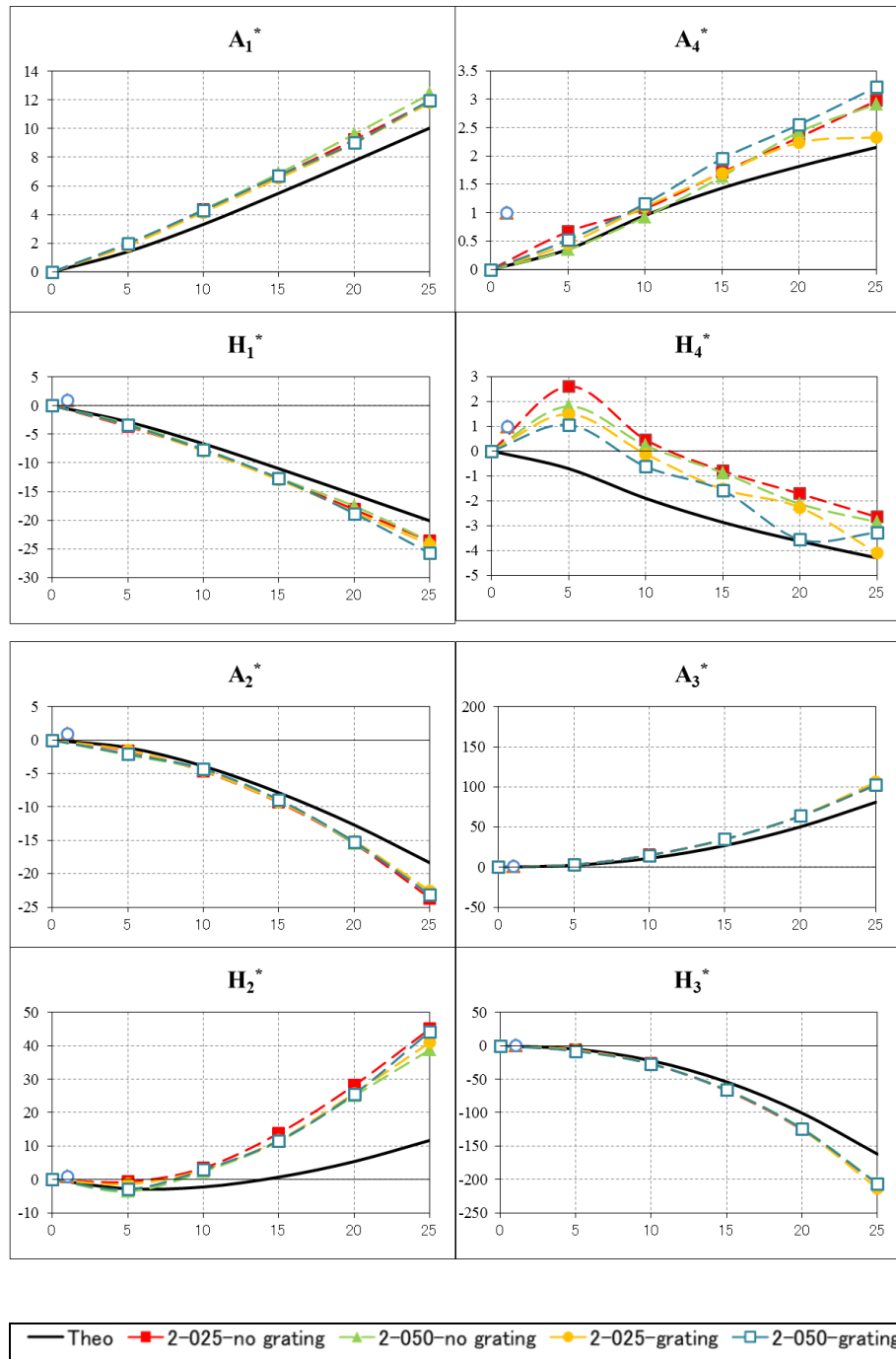


Fig.4.55 Aerodynamic derivatives (calculated from upper surface only) of Model 2-x-y

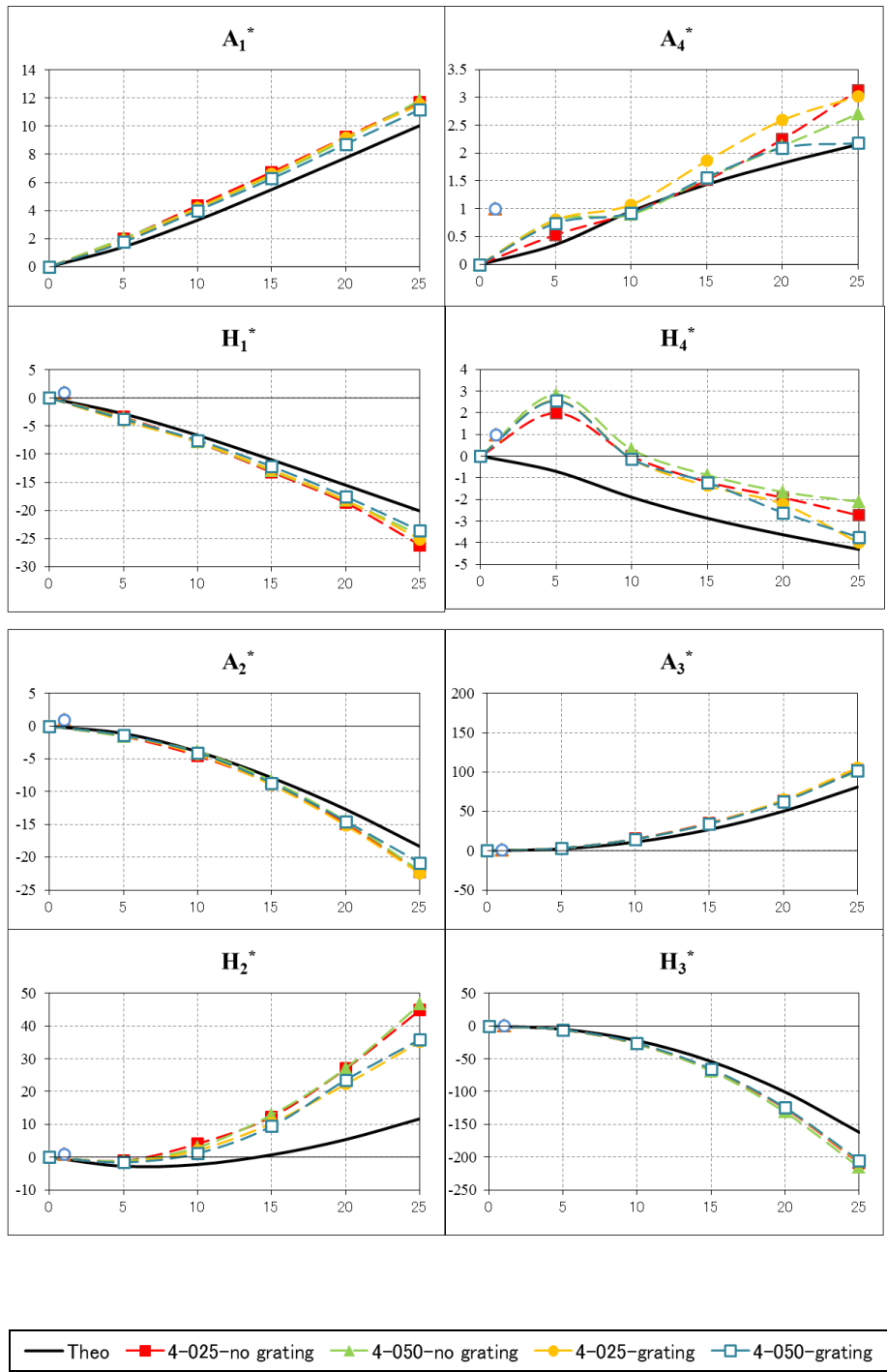


Fig.4.56 Aerodynamic derivatives (calculated from upper surface only) of Model 4-x-y

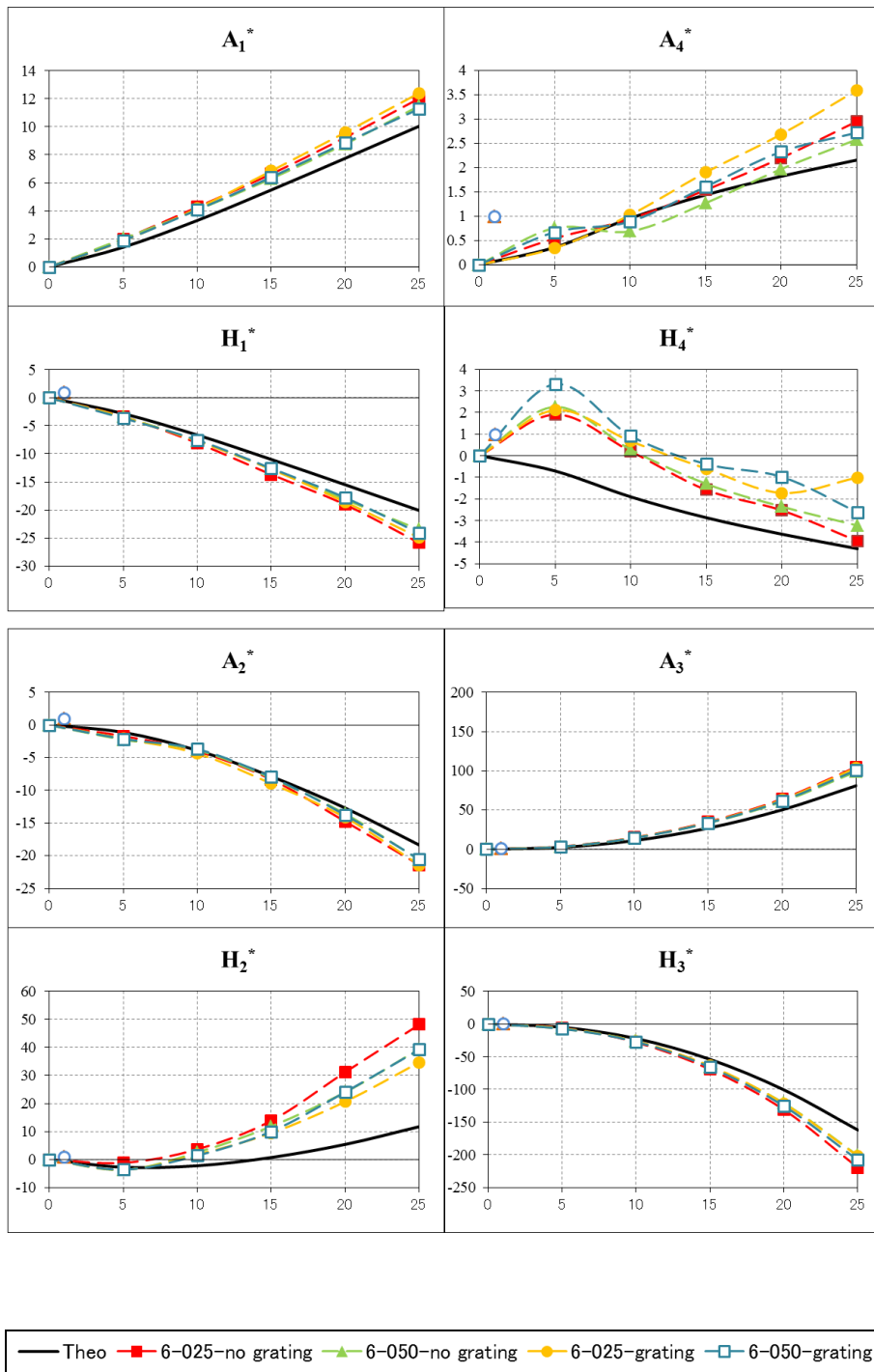


Fig.4.57 Aerodynamic derivatives (calculated from upper surface only) of Model 6-x-y

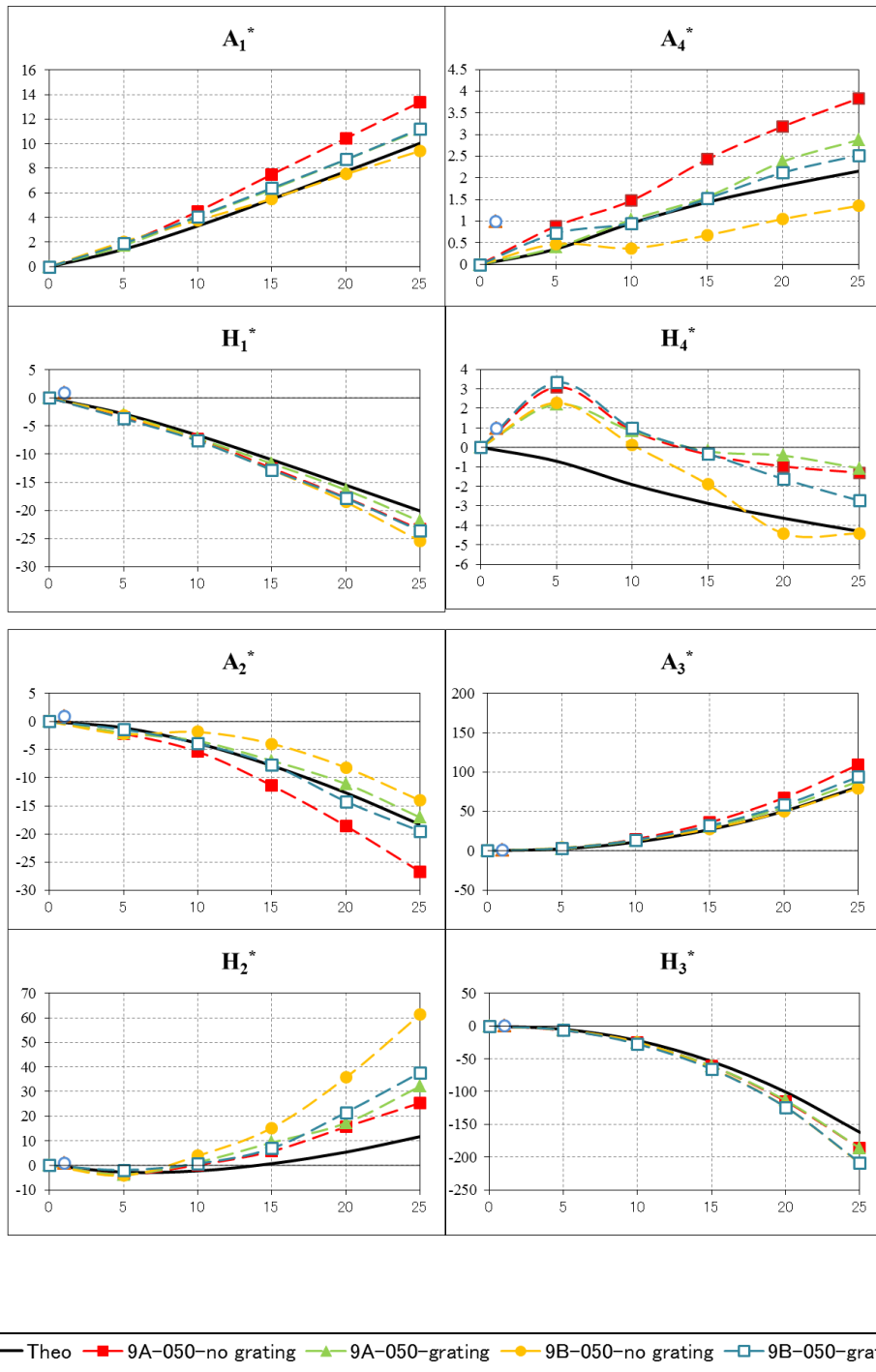

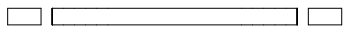
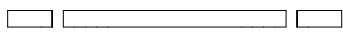
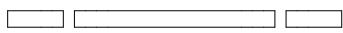
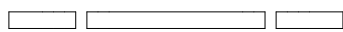
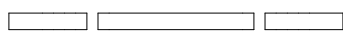

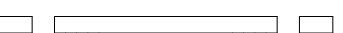




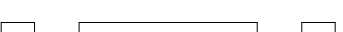


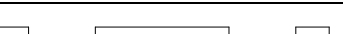


Fig.4.58 Aerodynamic derivatives (calculated from upper surface only) of Model 9-x-y

#### 4.4 Results: Flutter Stability

Flutter onset velocity can be calculated for section with double slot, since models with cavity are non-symmetric so the pressures on the lower surface are different from the upper surface. Moreover from the comparison of aerodynamic derivatives from upper surface with half-value of derivatives from Theodorsen function, no significant change in stability is expected. For model with double slot, as expected, Model 4A is the most stable section with very high increase in flutter onset velocity ( $v_{r\ cr} > 3.52$ ). Structural parameter used are:  $B=0.3$  m;  $m=2.42$  kg/m;  $I=0.0181$  kg.m<sup>2</sup>/m,  $f_{\phi}=5.2$  Hz,  $f_{\eta}=4$  Hz,  $f_{\phi}/f_{\eta}=1.3$ . Structural damping are set as zero.

Table 4.3 Flutter onset velocity of model with double slot (calculated with CEV)

Section	void ratio	$U_{cr}$ (m/s)	$U_{r\ cr}$	$v_{r\ cr}$	ratio $U_r$ to basic section
Theodorsen thin plate	0	9.80	7.11	1.00	
Model F 	0	9.80	7.39	1.04	1.00
Model 1A 	0.07	8.00	5.26	0.74	0.71
Model 1B 	0.07	unstable	-	-	-
Model 1C 	0.07	unstable	-	-	-
Model 1D 	0.07	6.00	4.08	0.57	0.55
Model 1E 	0.07	8.50	5.90	0.83	0.80
Model 1F 	0.07	9.10	6.44	0.91	0.87
Model 2A 	0.13	7.90	5.05	0.71	0.68
Model 2B 	0.13	unstable	-	-	-
Model 2C 	0.13	7.60	5.01	0.70	0.68
Model 2D 	0.13	7.80	5.18	0.73	0.70
Model 2E 	0.13	7.00	4.75	0.67	0.64
Model 4A 	0.27	> 31.20	> 25.00	> 3.52	> 3.38
Model 4B 	0.27	unstable	-	-	-
Model 4C 	0.27	unstable	-	-	-
Model 6 	0.4	unstable	-	-	-

Several questions raise from this study:

1. How to improve the stability of Model 4A? From unsteady pressure characteristics of Model 4A, it can be seen that the stability or negative  $A_2^*$  is due to positive but near  $180^\circ$  value of phase differences in near leading edge zone. This values are considered near critical and another countermeasure to ensure  $A_2^*$  values are always negative.

2. How to modify Model 1B, 2B so the values of  $A_2^*$  become negative? Although optimum arrangement of slot is obtained in Model 4A, but the void ratio is still relatively wide (0.27). Therefore, finding other countermeasures to keep low absolute values of  $A_1^*$  and change  $A_2^*$  to negative is an interesting and challenging task.

## 4.5 Concluding Remarks

This chapter study about flutter stabilization of rectangular prism with side ratio  $B/D=20$  from unsteady pressure characteristics point of view. This approach gives better understanding about the physical process behind stabilization or destabilization of the section when any countermeasures is installed.

Based on the results of prism with double slot, the presence of the slot affects aerodynamic derivatives significantly. Improper arrangement of slot can lead to unstable deck section due to positive value of  $A_2^*$ . The effect of near leading edge slot can be clearly seen by comparing unsteady pressure characteristics of Model F with other model. Introducing slot near leading edge completely change the flow field that it produces large pressures upstream of slot and have opposite direction with pressures downstream the slot. By calculating time history of pressure distribution along the surface and the resultant torsional moment during one cycle of heaving motion, the physical process behind low absolute  $A_1^*$  for Model 1B, 4A and 6 can be explained. For torsional motion,  $A_2^*$  values are affected by the phase difference value in near leading edge zone (upstream the slot). Model 4A is found as the most stable section with flutter stability index  $v_{r\ cr} > 3.52$ .

The presence of porous cavity near leading edge also change the flow and reduction of peak amplitude is obtained. However, there are also increasing of pressures at near leading edge zone. Resultant of these pressures are aerodynamic derivatives that have almost the same value compared with Model F or rectangular prism with  $B/D=20$ . It is interesting to note that local change of flow do not always change the global behavior in term of flutter stability.

## Bibliography

- Brancaleoni, F., Diana, G., Faccioli, E., Fiammenghi, G., Firth, I. P. T., Gimsing, N. J., Jamiolkowski, M., Sluska, P., Solari, G., Valensise, G., and Vullo, E. (2010) *'The Messina Strait Bridge : a challenge and a dream'*, CRC Press.
- Brown, W. C. (1996), 'Development of The Deck for The 3300m Span Messina Crossing', *Congress Report of The 15<sup>th</sup> Congress, IABSE*, Copenhagen, Denmark, pp. 1019-1030.
- Kumar, R., Viswanath, P. R. (2002) 'Passive control of surface pressure fluctuations in reattaching flows', *The Aeronautical Journal*, 106, pp. 669-674.
- Sato, H., Toriumi, R., Sekiya, M., Watanabe., S. (1994), 'Study on Aerodynamic Stability of Super Long-span Bridge', *Proceeding of 13<sup>th</sup> National Symposium on Wind Engineering, Japan Association for Wind Engineering*, pp. 419-424 (in Japanese).
- Tokoro, S., Honda, A., Masuda, I., Nakashima, Y., Murakoshi, J., Fumoto, K. (2002), 'Aerodynamic Improvement of One Box Girder for Super Long Suspension Bridge', *The 2<sup>nd</sup> International Symposium on Wind and Structures*, Busan, Korea, August 21-23 2002, pp. 235-242.
- Yoneda, M., Ohno, K., Tamaki, Y., Kimura., K., Miyachi, S. (1996), 'On aerodynamic stability of a 2500m class streamlined box girder suspension bridge with open spaces or open gratings of bridge deck', *Proceeding of 14<sup>th</sup> National Symposium on Wind Engineering, Japan Association for Wind Engineering*, pp. 401-406 (in Japanese).





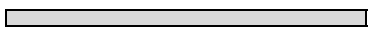




# Chapter 5

## Flutter Stabilization of Slender Bridge Deck Section Using Combination of Double Slot with Fairings and Winglets

Based on results obtained in Chapter 4, it is already known that introducing double slot to rectangular prism with  $B/D=20$  can produce very low value of  $A_1^*$ , lower absolute value of  $H_3^*$  (for section with wide slot). These conditions are favorable for improving flutter stability. Unfortunately, double slot also has tendency to produce more positive value of  $A_2^*$  which is not good for flutter stability. Optimum arrangement of the slot was found as Model 4A, which has very low absolute value of  $A_1^*$ , and negative  $A_2^*$ . Further improvement is studied by combining double slot with additional countermeasures. These additional countermeasures are expected to produce negative  $A_2^*$  while maintaining low absolute value of  $A_1^*$ .

Selected results from Chapter 4 are summarized in Table 5.1.

Table 5.1 Summary of selected model with double slot

Model ID.	aerodynamic derivatives characteristic	Stability performance (calculated using CEV)
 Model F or $B/D=20$ rectangular prism	basic section	$U_f=7.4$
 Model 1B ( $b/B=0.06$ )	very low absolute value of $A_1^*$ , positive $A_2^*$	unstable
 Model 2B ( $b/B=0.13$ )	very low absolute value of $A_1^*$ , positive $A_2^*$	unstable
 Model 4A ( $b/B=0.26$ )	very low absolute value of $A_1^*$ , negative $A_2^*$	$U_f>25$
 Mode 6 ( $b/B=0.4$ )	very low absolute value of $A_1^*$ , lower absolute value of $H_3^*$ , positive $A_2^*$	unstable

$b$ =total width of slot

$B$ =total width of deck section

CEVA=Complex Eigenvalue Analysis

## 5.1 Background

The physical process behind specific aerodynamic derivatives values of models with double slot were pointed out in Chapter 4. Low absolute  $A_1^*$  of model 1B, 2B, 4A and 6 were explained as low torsional moment in heaving motion resulted from opposite direction of unsteady surface pressure upstream and downstream of slot near leading edge. Positive  $A_2^*$  of model 1B, 2B and 6 were due to unsteady surface pressure at upstream of near leading edge slot which have the same direction with body motion during torsional motion, so these pressures input energy into the vibration.

Two additional countermeasures: fairings and winglets are selected to improve these conditions. Both fairings and winglets can produce more negative  $A_2^*$  but with different mechanism:

- Fairings modify flow near the leading edge and produce positive  $\psi$  in the region (Trein, 2009).
- Winglets provide additional lift force that act as aerodynamic damping during torsional motion (Liu *et al.*, 2006). Several literatures assumed no flow interference between the main body of the section and the winglets (del Arco & Aparicio, 1999; Liu *et al.*, 2006). Graham *et al.* (2011) opposed this assumption and showed by using vortex panel code calculation that the lift force of trailing edge side winglet is significantly reduced by the downwash from the main body while leading edge side winglet destabilize the section. Study by Hong (2012) also found that flow interference occurred when winglets are positioned at close position to the main body. This close position was due to practical concern that it is impossible to introduce winglets far from the main body.

In this study, triangular type fairing is used. Position and size of winglets follows results by Hong (2012), where the winglets are positioned right at the edge of the main section and produce more negative  $A_2^*$  for rectangular prism with B/D=20 with moderate increase of  $A_1^*$ .

## 5.2 Description of Experiment and Models

Several models were tested in the wind tunnel to measure the aerodynamic derivatives. The measurements were performed using load cell. Measuring aerodynamic derivatives using load cell is more straightforward and simple than pressure measurement. Amplitude and frequency of each motion were the same as test for pressure measurement. Aerodynamic derivatives were calculated using Eq. (2.14a) to Eq. (2.14h). Fig. 5.1 shows the set up outside wind tunnel, which is less complicated than set up for experiment that used for pressure measurement (Fig. 4.5).

The basic section are designated as Model F, Model 1B, Model 1C, Model 1D, Model 2B, Model 2C, Model 2D, Model 4A and Model 6. Those basic section were combined with fairings (model+f), winglets (model+w) and both fairings and winglets (model+f+w) as shown in Table 5.2. Size of basic model is 30 cm x 1.5 cm. fairings is equilateral shape and size of winglets is 4 x 0.2 cm. Winglets are positioned 3 cm above the rectangular prism.



Fig. 5.1 Set up of equipment outside wind tunnel for direct force measurement

Table 5.2 Models tested in wind tunnels

Basic section	F	1B	1C	1D	2B	2C	2D	4	6
+ fairings	F+f	1B+f	1C+f	1D+f	2B+f	2C+f	2D+f	4+f	6+f
+ winglets	F+w	1B+w	1C+w	1D+w	2B+w	2C+w	2D+w	4+w	6+w
+fairings and winglets	F+f+w	1B+f+w	1C+f+w	1D+f+w	2B+f+w	2C+f+w	2D+f+w	4+f+w	6+f+w

Details of models are shown in Fig. 5.2 to Fig. 5.10. In total, there were 36 models.

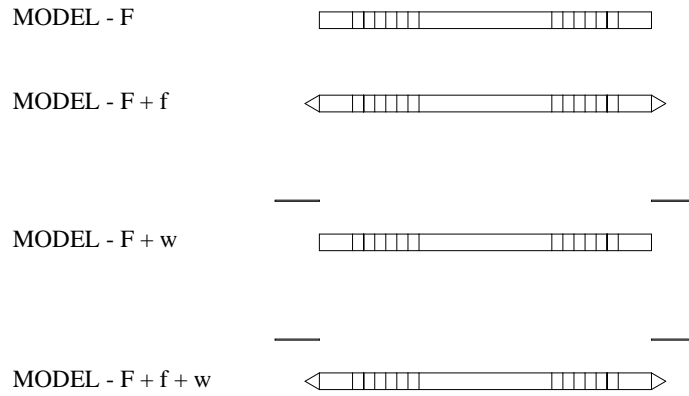


Fig. 5.2 Model F, F+f, F+w and F+f+w

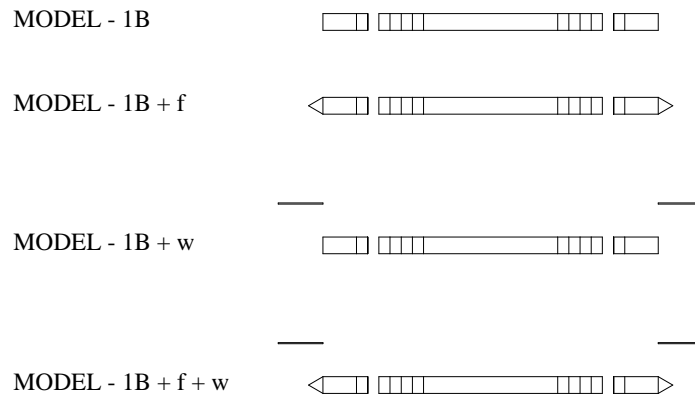


Fig. 5.3 Model 1B, 1B+f, 1B+w and 1B+f+w

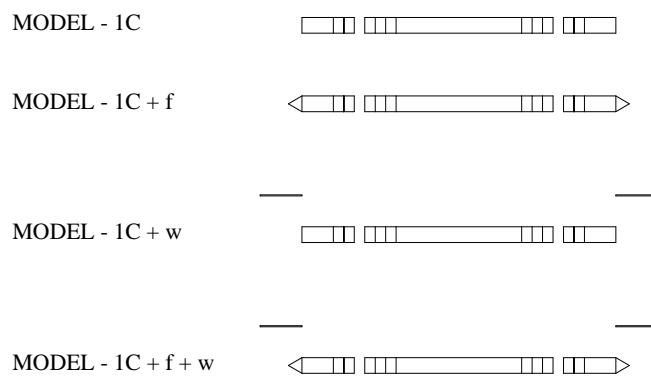


Fig. 5.4 Model 1C, 1C+f, 1C+w and 1C+f+w

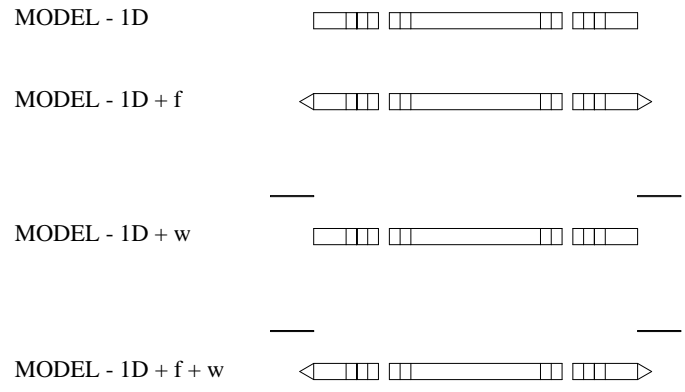


Fig. 5.5 Model 1D, 1D+f, 1D+w and 1D+f+w

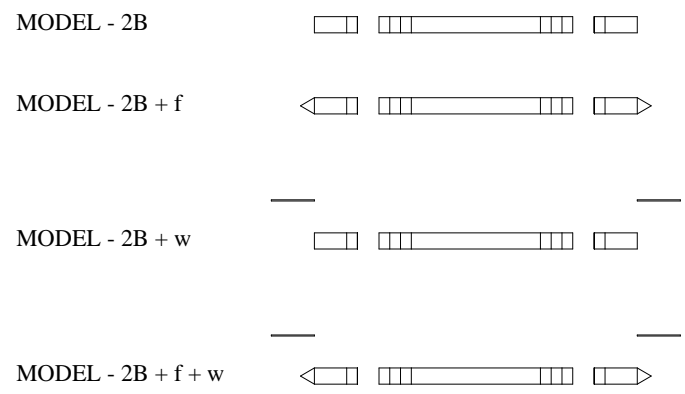


Fig. 5.6 Model 2B, 2B+f, 2B+w and 2B+f+w

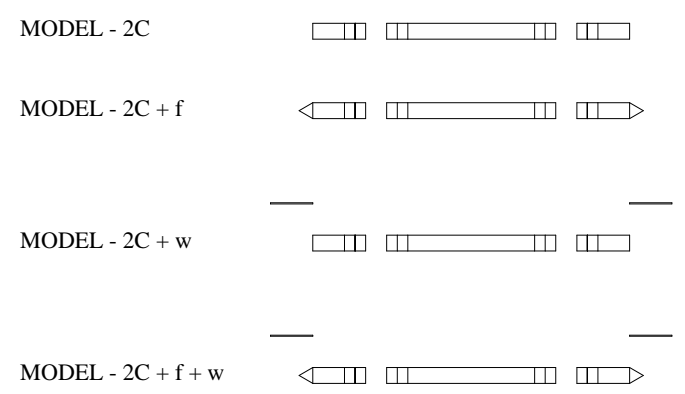


Fig. 5.7 Model 2C, 2C+f, 2C+w and 2C+f+w

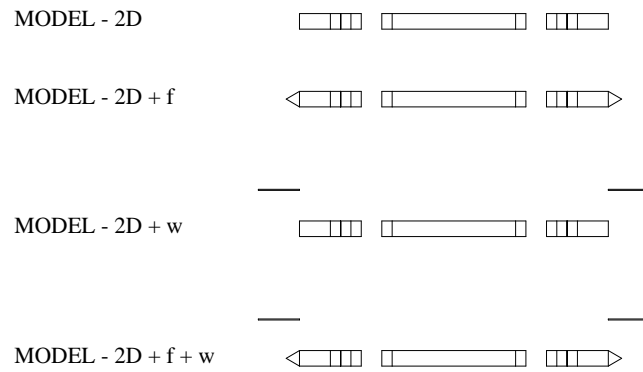


Fig. 5.8 Model 2D, 2D+f, 2D+w and 2D+f+w

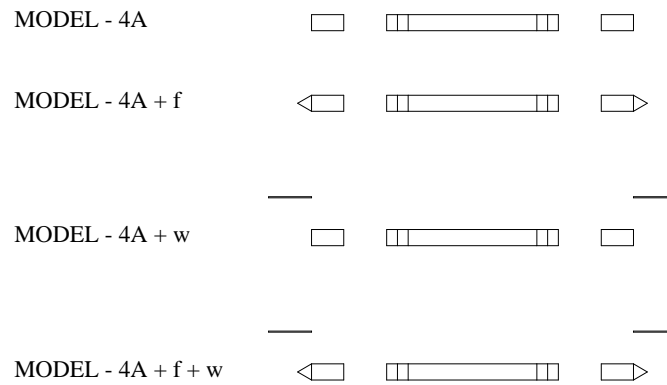


Fig. 5.9 Model 4A, 4A+f, 4A+w and 4A+f+w

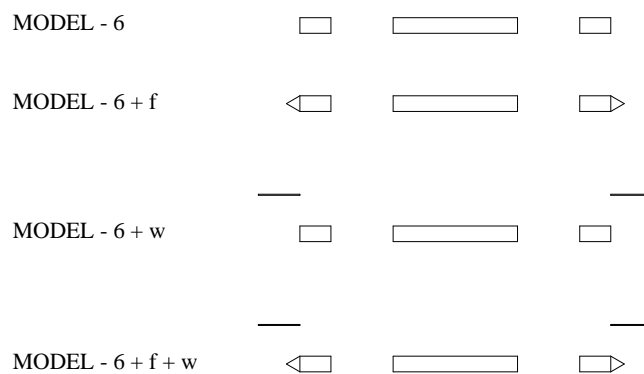


Fig. 5.10 Model 6, 6+f, 6+w and 6+f+w

In order to get more understanding of the physical process behind the change of aerodynamic derivatives due to presence of countermeasures, additional wind tunnel tests were also performed to measure unsteady pressure characteristics of selected models.

One of the disadvantages of pressure measurement experiment is that it cannot be applied to obtain aerodynamic derivatives of general section. For section with appendages like railings, winglets, guide vanes, pressure measurement technique cannot be used to calculate aerodynamic derivatives since only the surface pressures on the main body or section are measured. Otherwise, direct measurement using load cell is applicable to general section even with small appendages since the resultant forces are measured.

### **5.3 Results: Aerodynamic Derivatives and Unsteady Pressure Characteristics**

#### **5.3.1 Comparison of Aerodynamic Derivatives from Pressure Measurement and Direct Force Measurement**

It is interesting to study the difference between aerodynamic derivatives from direct force measurement using loadcell with indirect method from pressure measurement. Fig. 5.11 to Fig. 5.15 show the comparison for Model F, 1B, 2B, 4A and 6. It can be said that in general both results are similar, and several points also highlighted:

1.  $A_1^*$  values of all models are in good agreement.
2.  $H_1^*$  values of Model 4A and 6 have relative large discrepancies, but still in the same pattern (negative values).
3.  $H_3^*$  values from direct force measurement tend to have smaller values than results from pressure measurement. Since  $H_3^*$  is one of important aerodynamic derivatives for flutter analysis, different results in flutter onset velocity are expected.
4. Absolute values of  $A_2^*$  of Model F and 4A from direct force measurement are smaller than results from pressure measurement. These can also lead to different results of flutter onset velocity.
5. Values of  $H_4^*$  show large discrepancy for Model 1B, 2B and 6.
6. Values of  $H_2^*$  show large discrepancy for almost all models. In Model 4A the differences are very clear.
7.  $A_3^*$  and  $A_4^*$  values of all models are in good agreement, except  $A_4^*$  of Model 6.

Overall, both results are confirming each other but with notes that the results of flutter onset velocity calculation might be different. The calculation results are showed in subchapter 5.4.

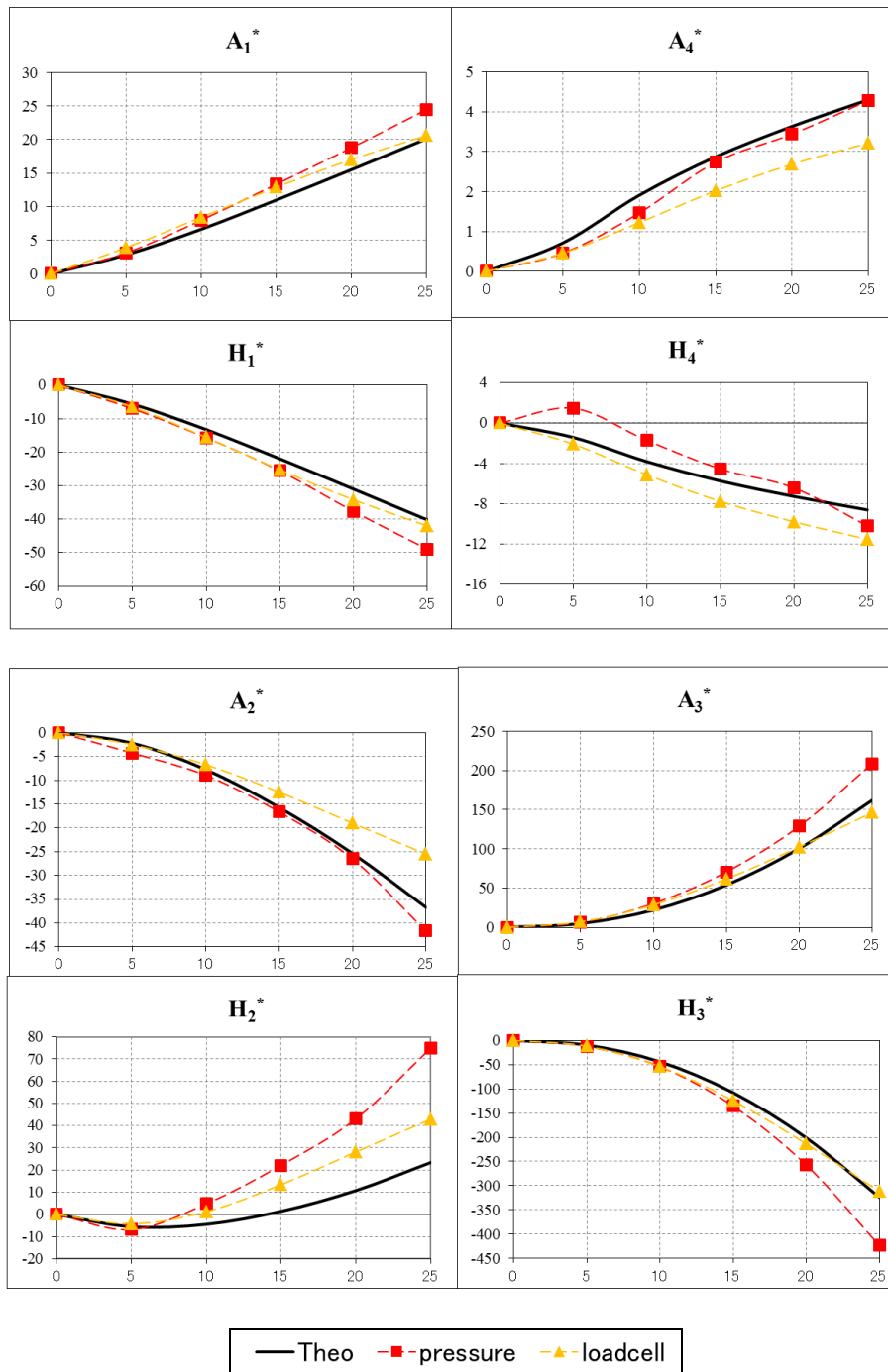


Fig. 5.11 Comparison of aerodynamic derivatives of Model F



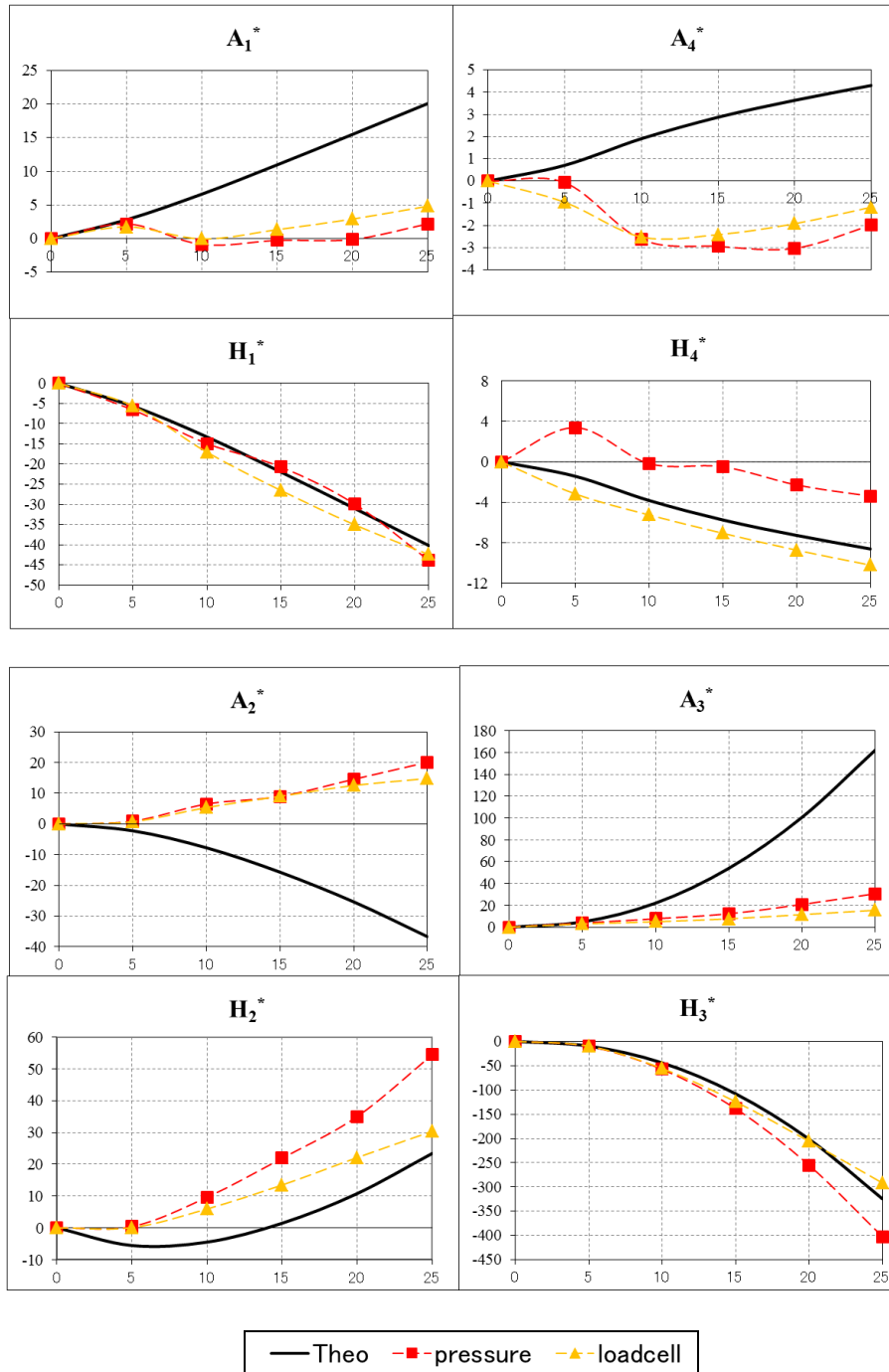


Fig. 5.12 Comparison of aerodynamic derivatives of Model 1B

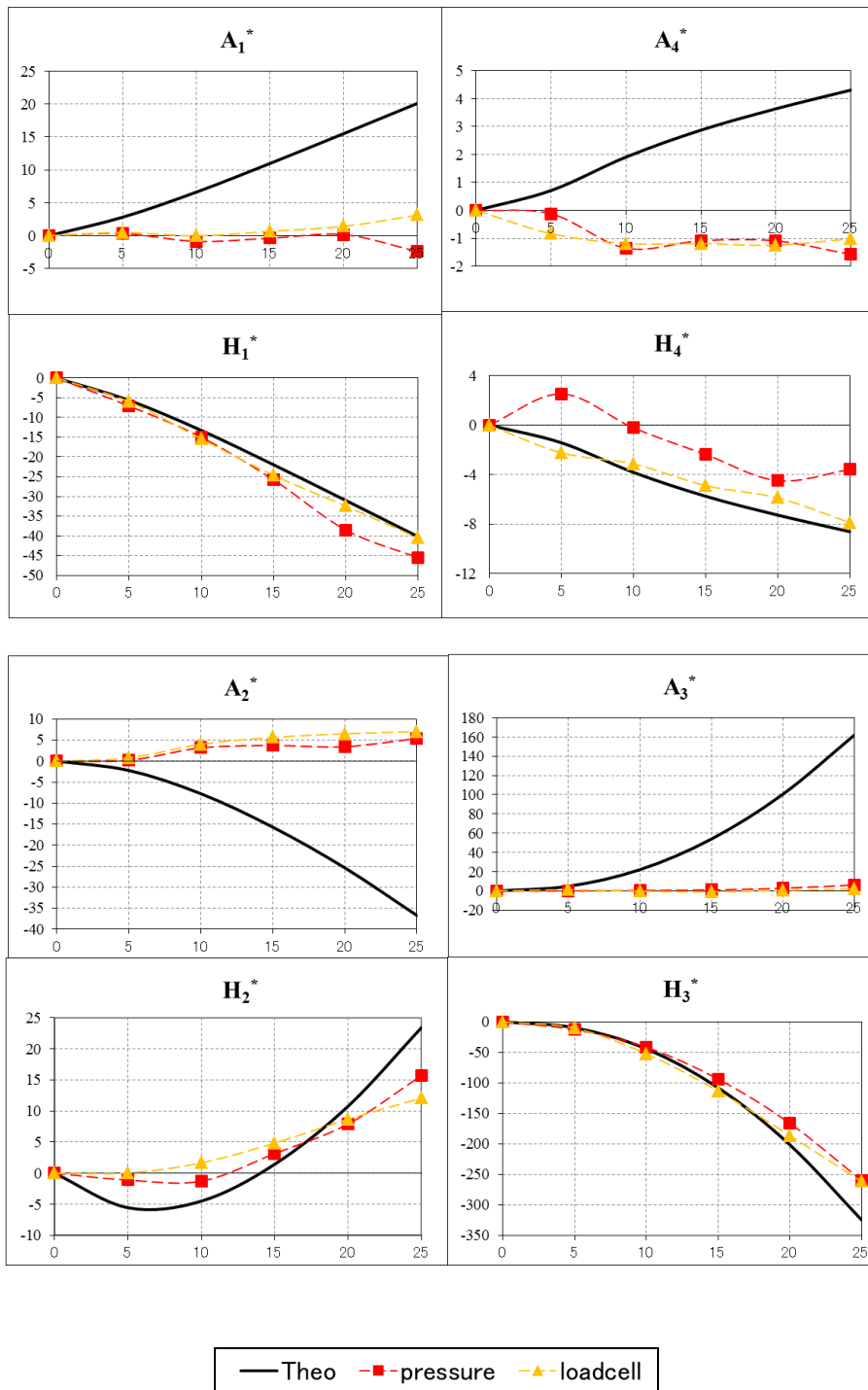


Fig. 5.13 Comparison of aerodynamic derivatives of Model 2B

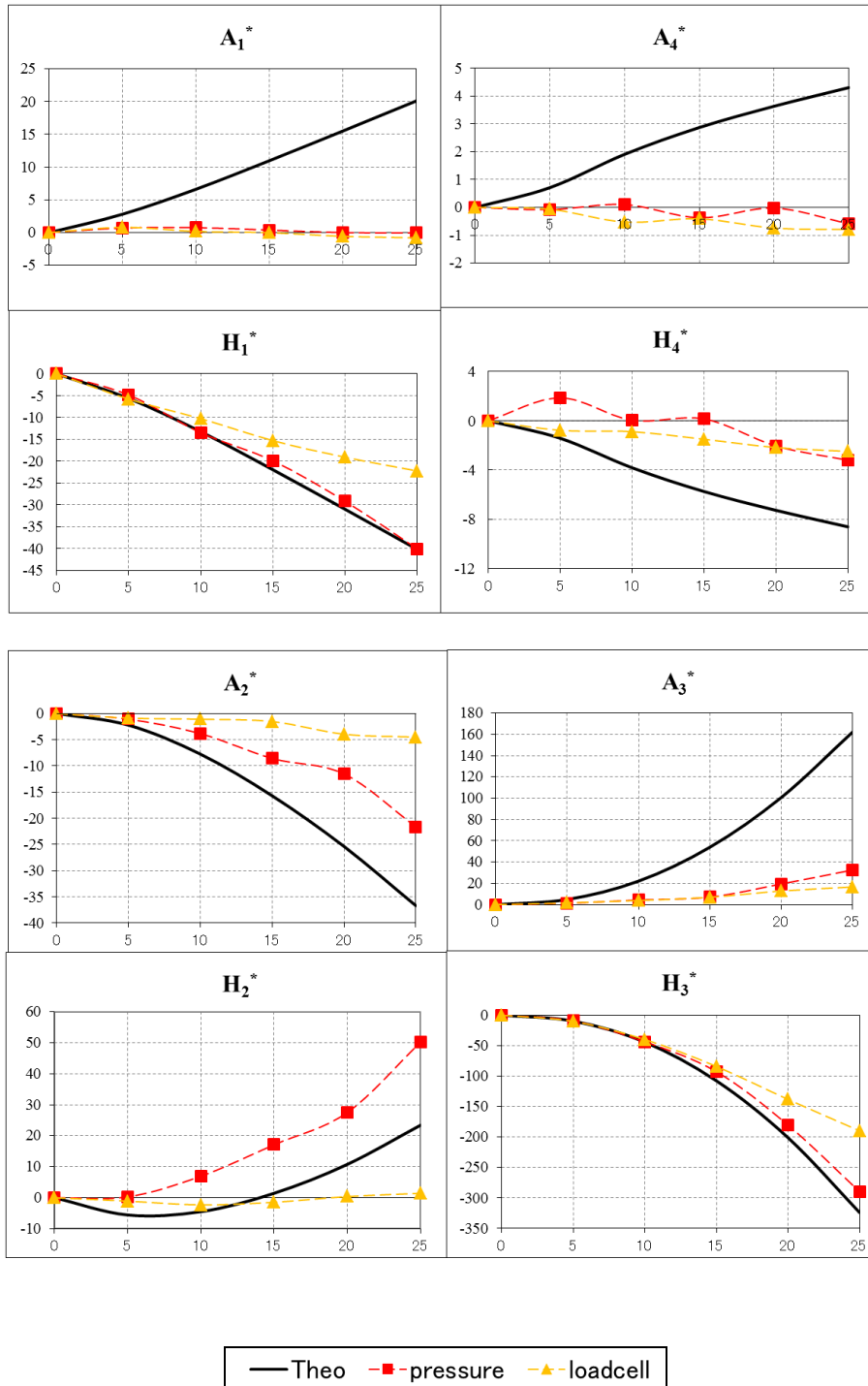


Fig. 5.14 Comparison of aerodynamic derivatives of Model 4A

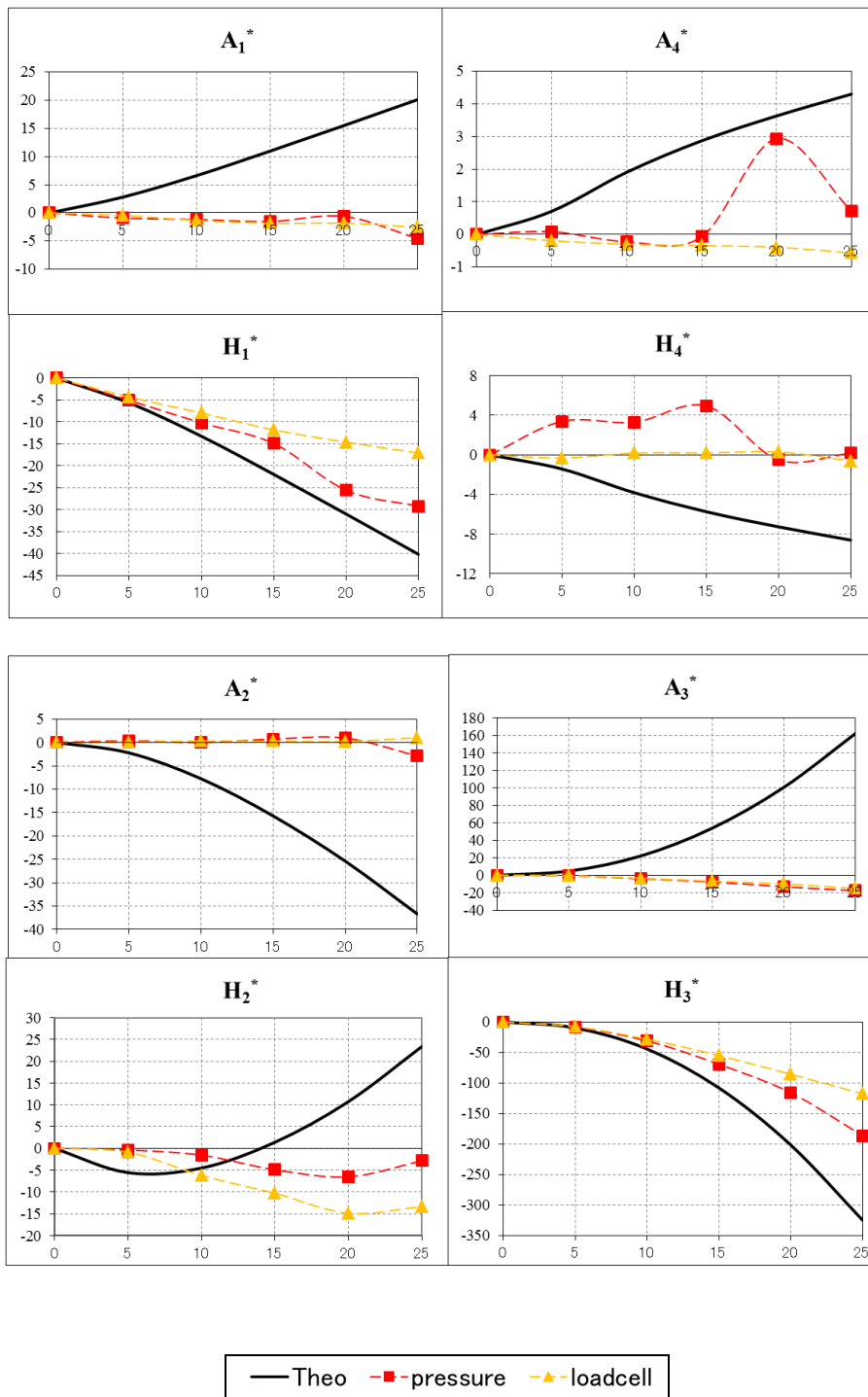


Fig. 5.15 Comparison of aerodynamic derivatives of Model 6

### 5.3.2 Aerodynamic Derivatives of Prism Using Combination of Double Slot with Fairings and Winglets

Aerodynamic derivatives of models are presented in Fig. 5.16 to Fig. 5.24.

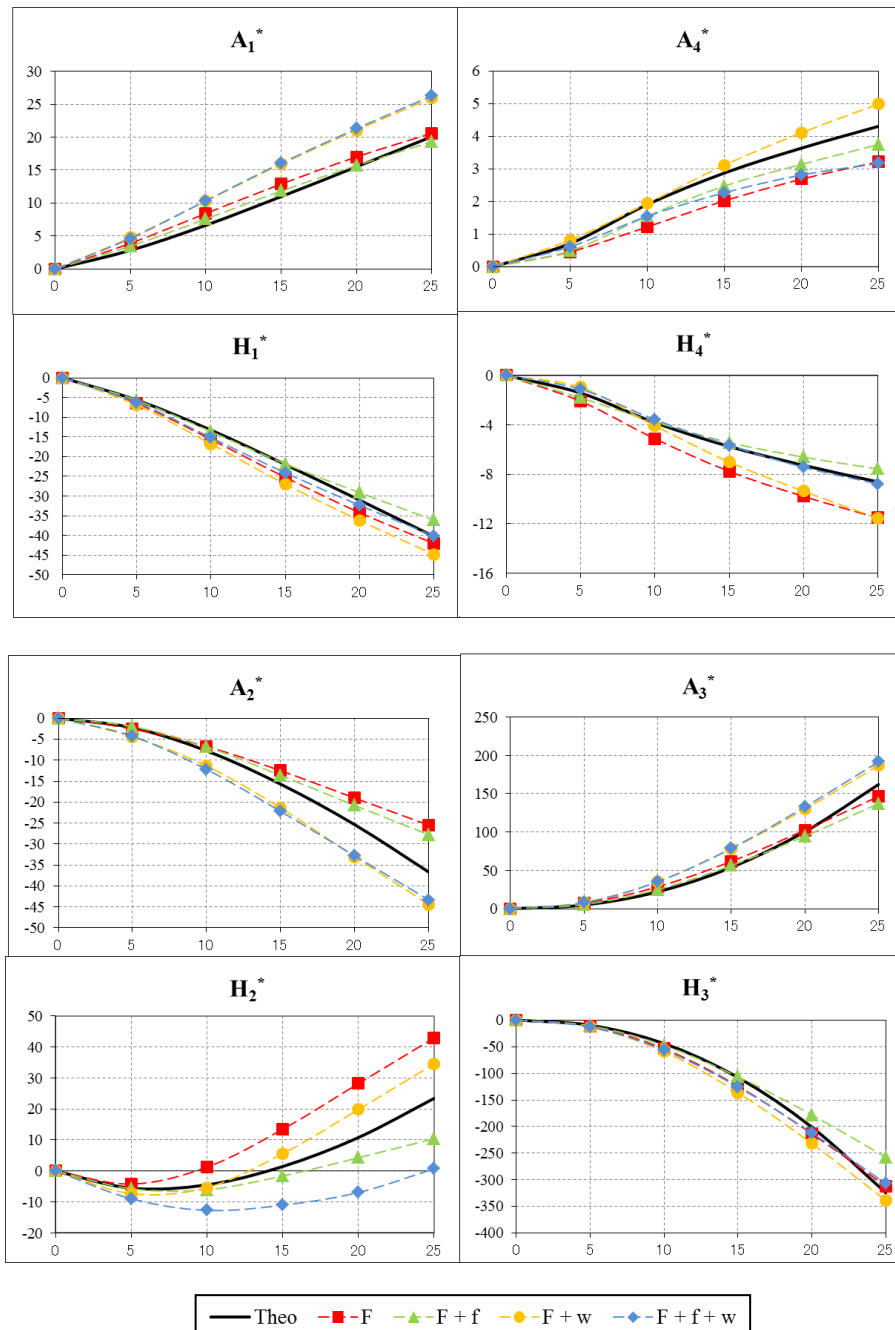


Fig. 5.16 Aerodynamic derivatives of Model F, F+f, F+w and F+f+w

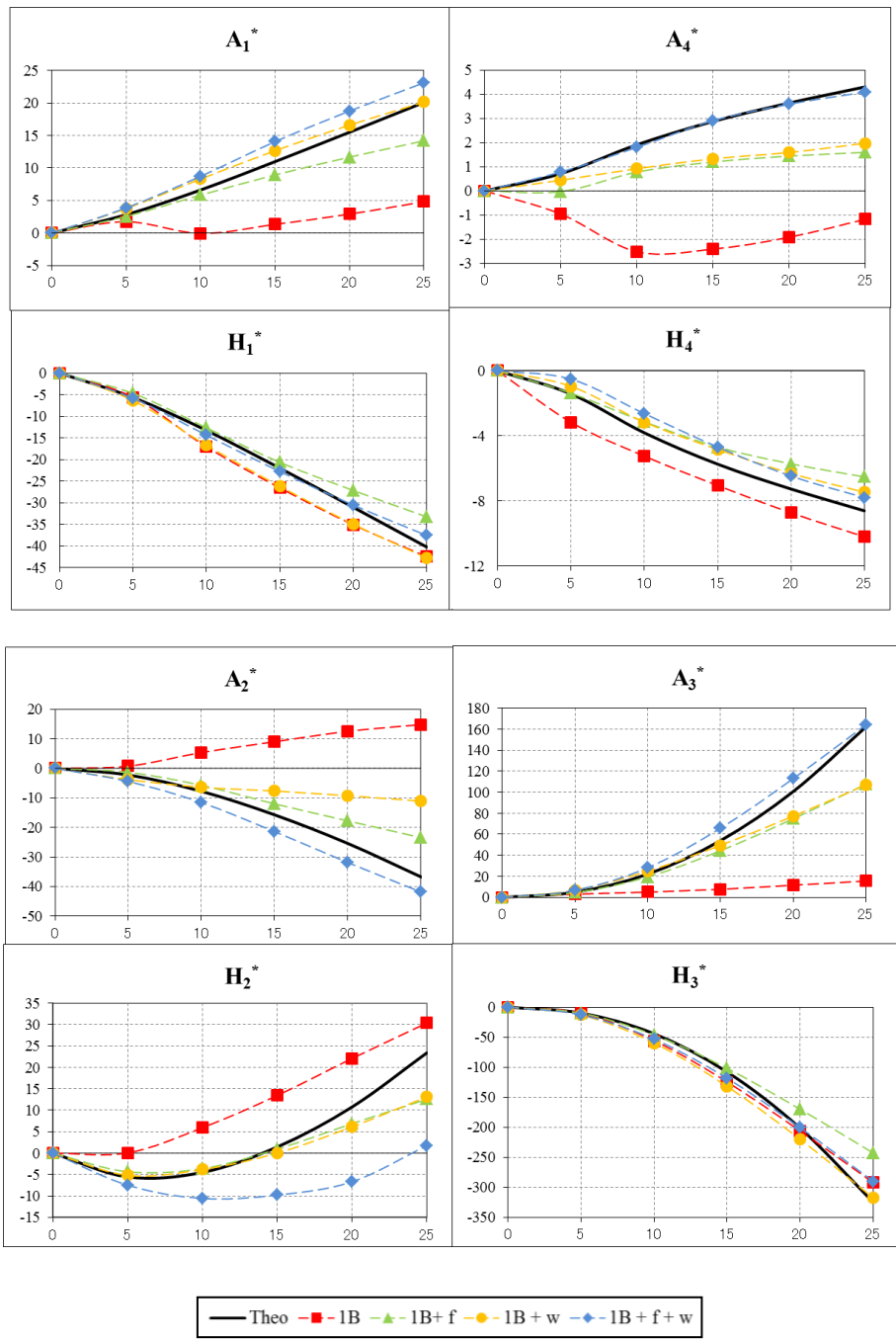


Fig. 5.17 Aerodynamic derivatives of Model 1B, 1B+f, 1B+w and 1B+f+w

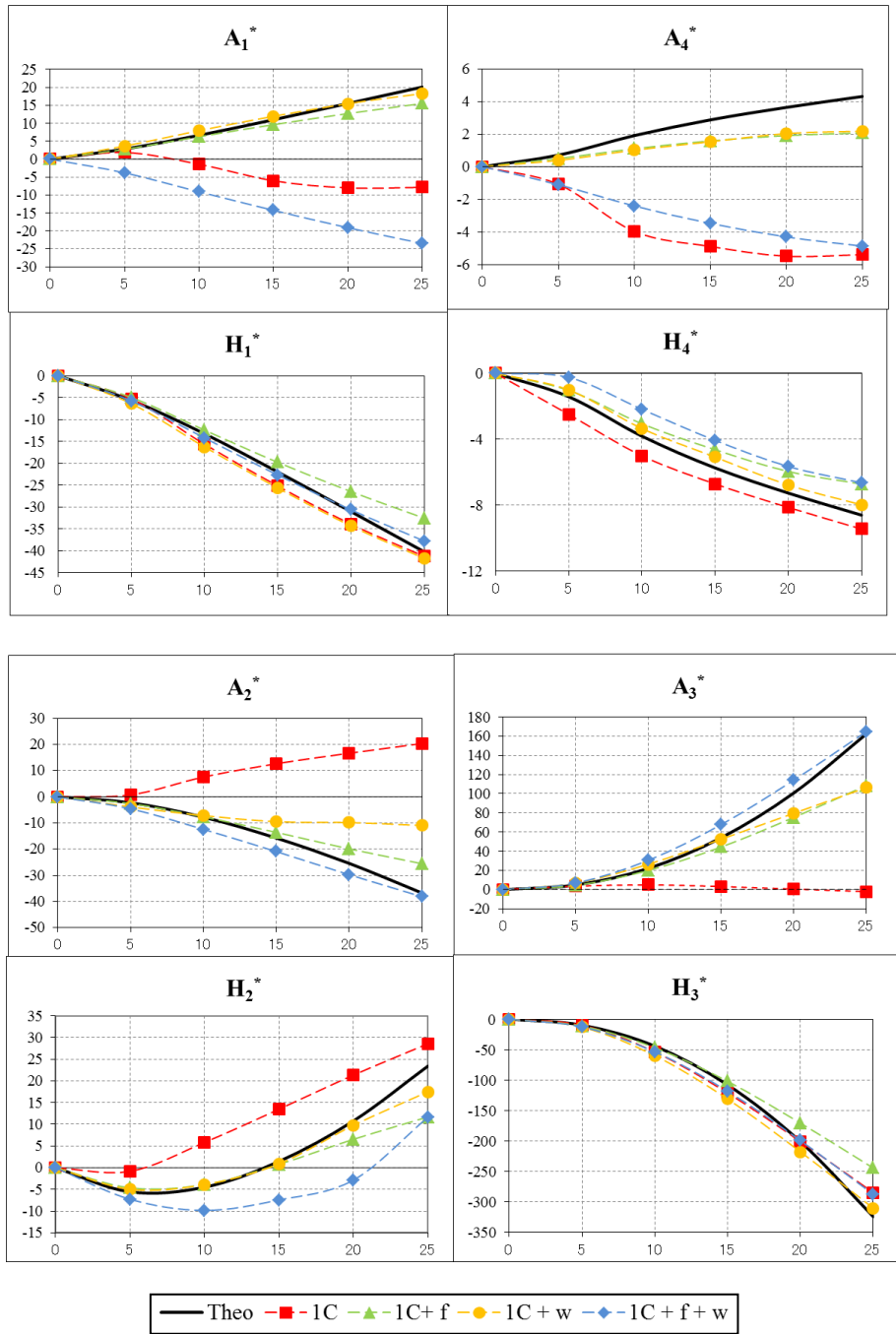


Fig. 5.18 Aerodynamic derivatives of Model 1C, 1C+f, 1C+w and 1C+f+w

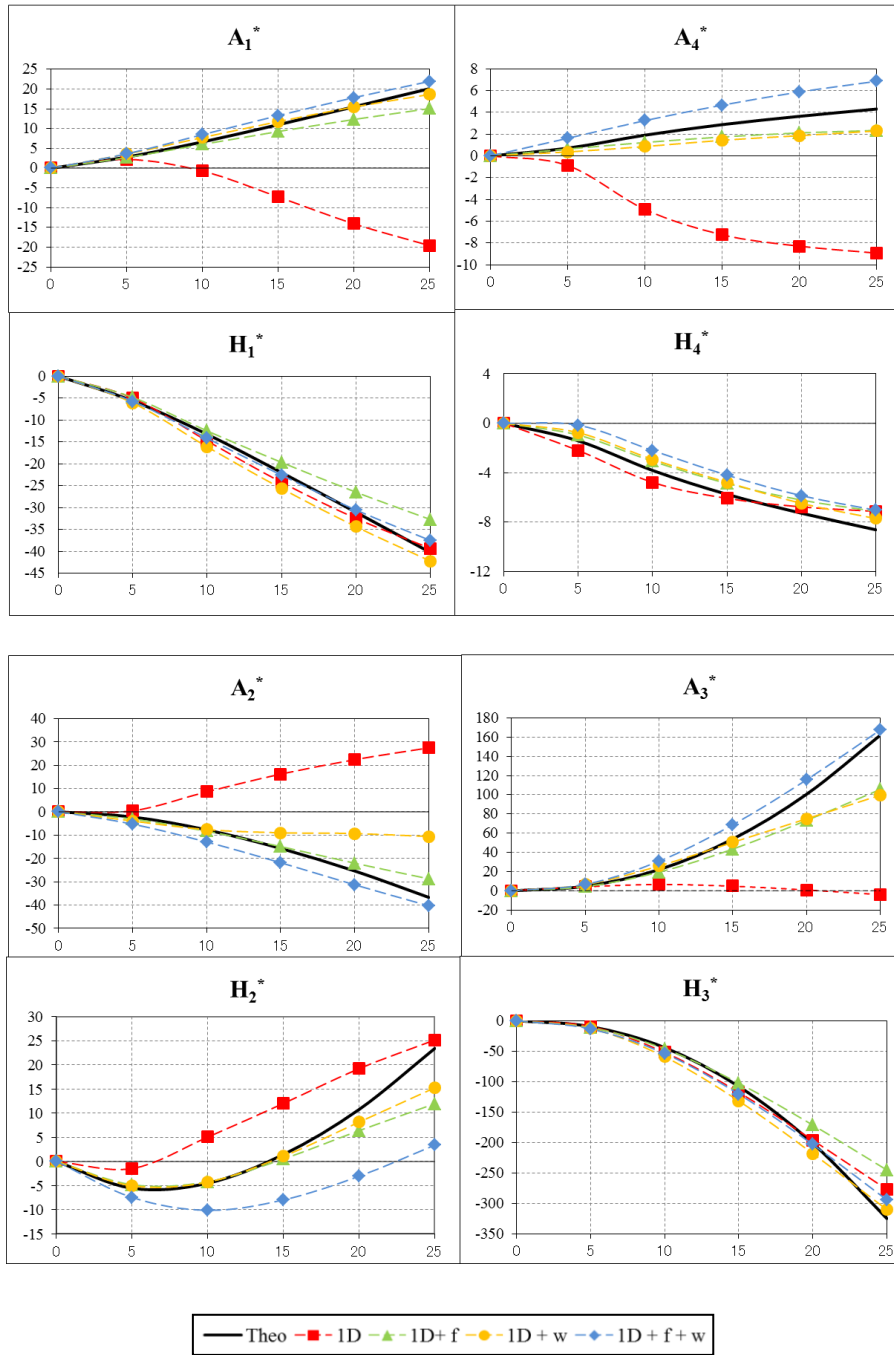


Fig. 5.19 Aerodynamic derivatives of Model 1D, 1D+f, 1D+w and 1D+f+w



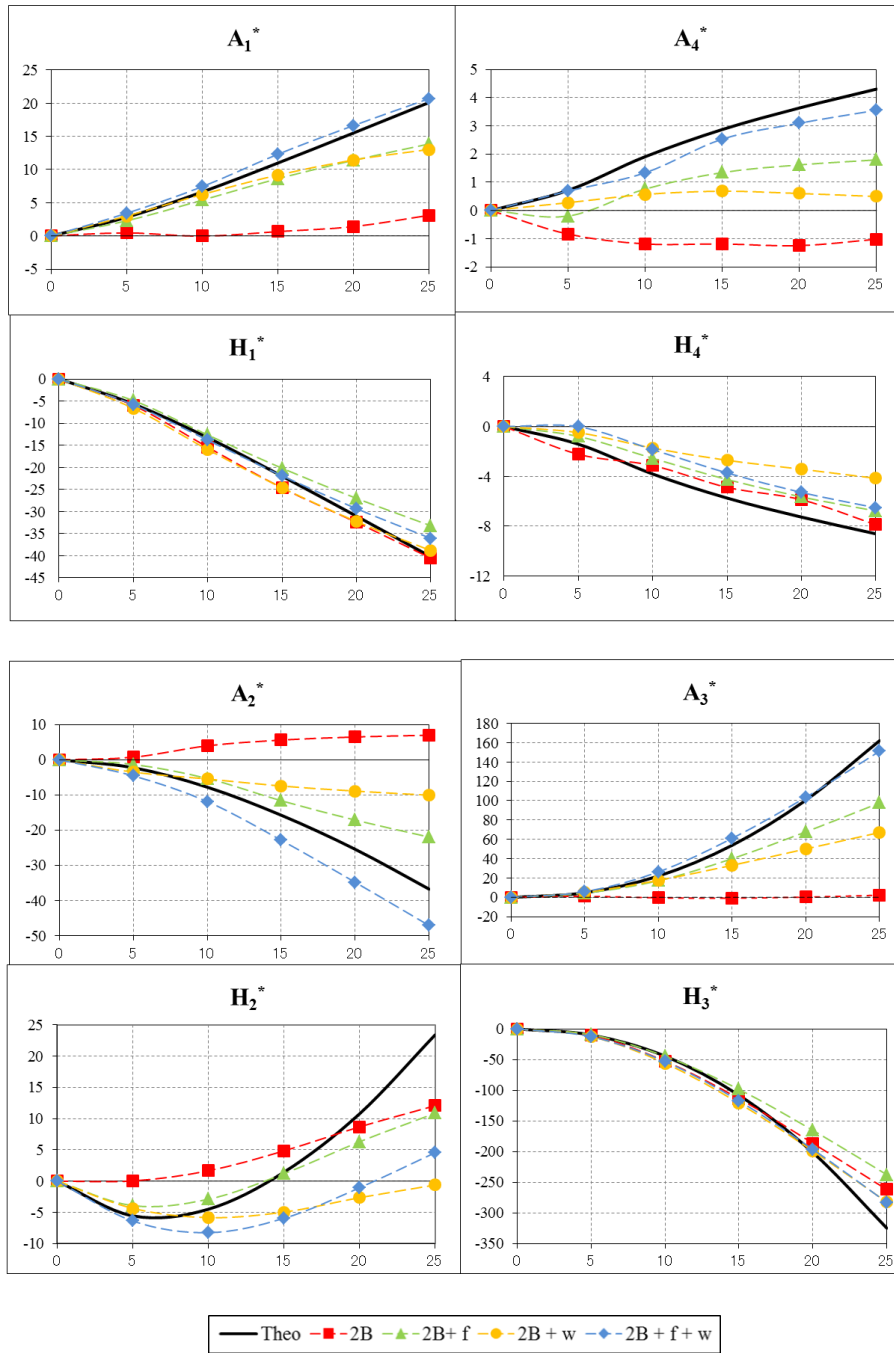


Fig. 5.20 Aerodynamic derivatives of Model 2B, 2B+f, 2B+w and 2B+f+w

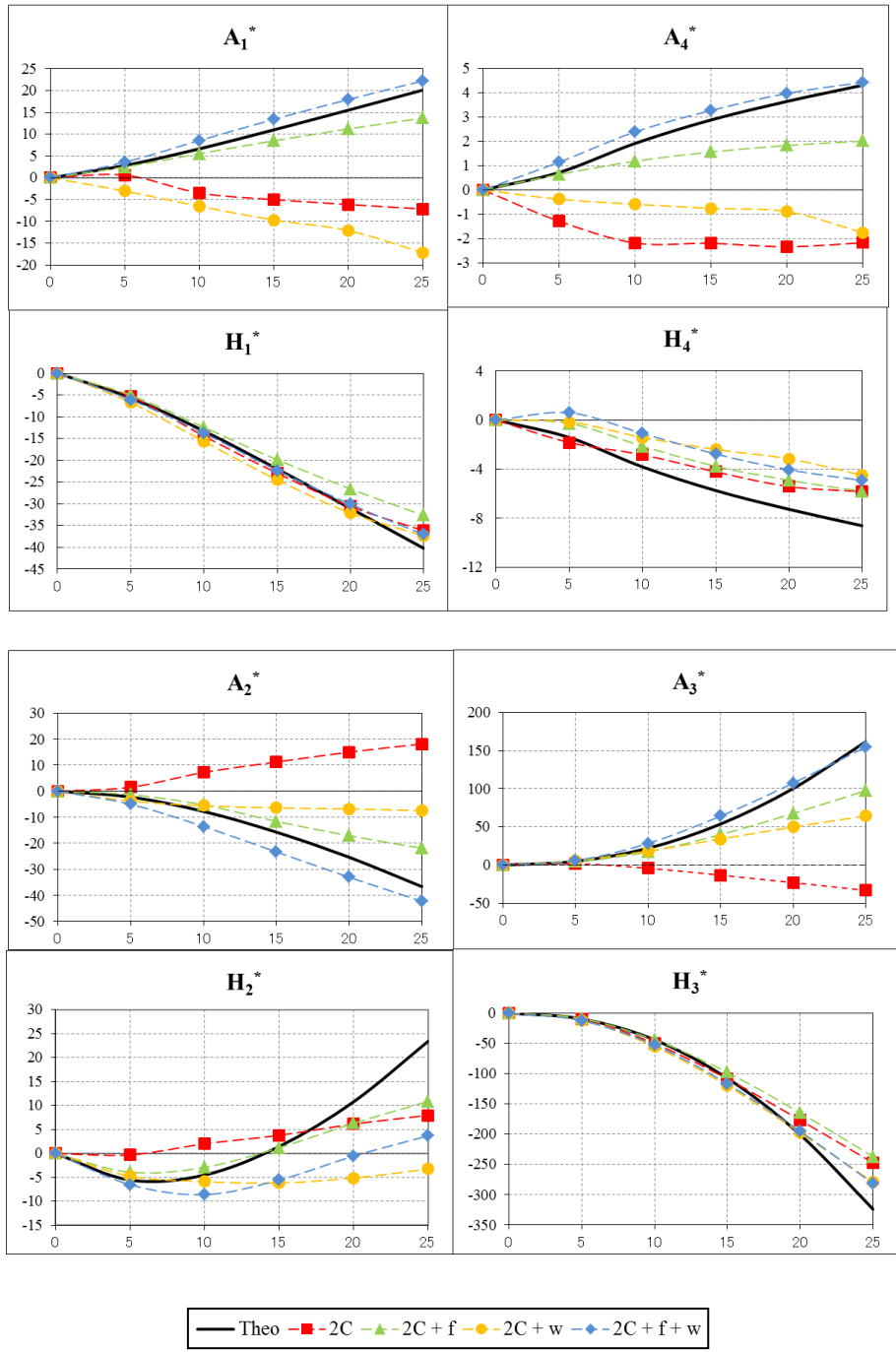


Fig. 5.21 Aerodynamic derivatives of Model 2C, 2C+f, 2C+w and 2C+f+w

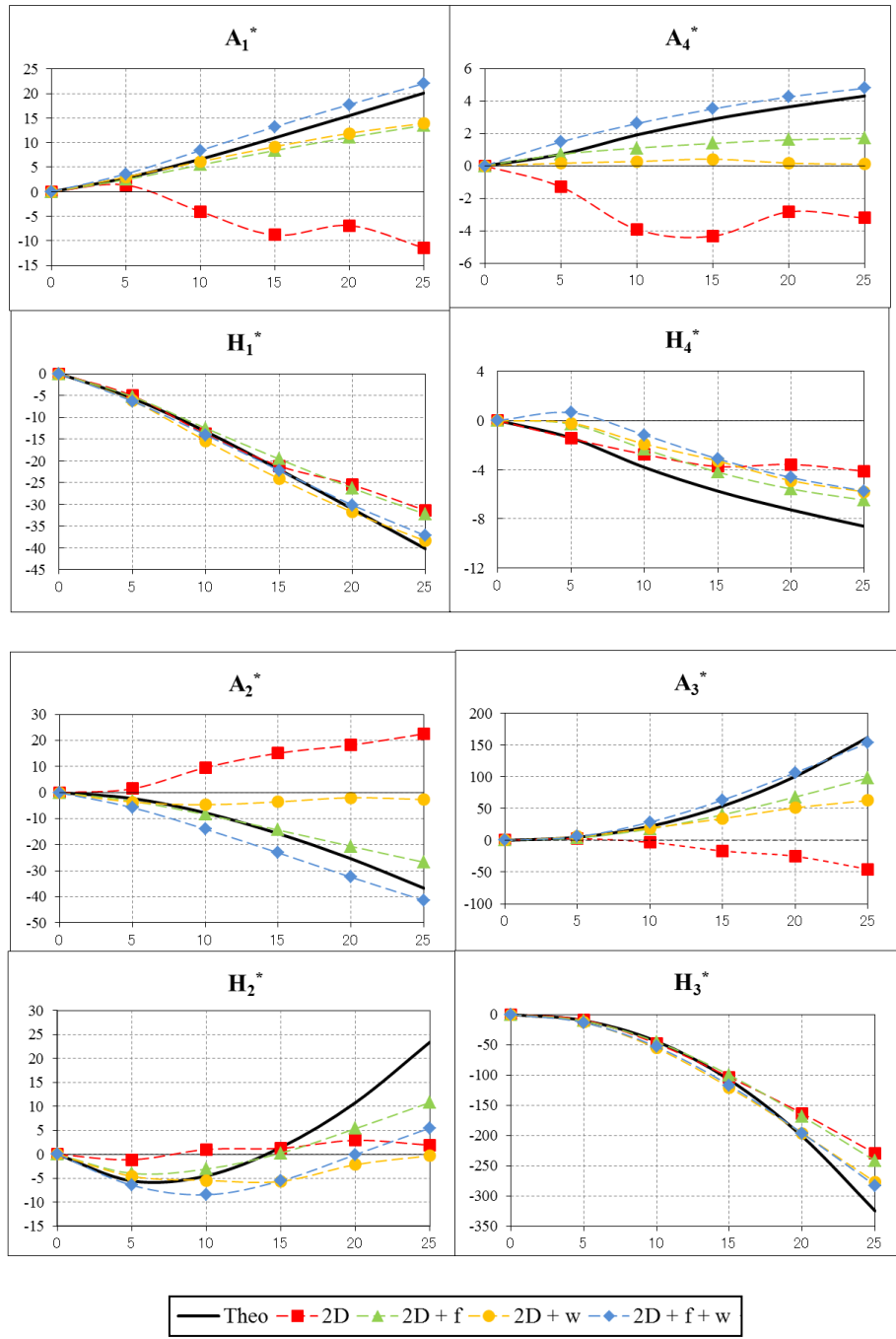


Fig. 5.22 Aerodynamic derivatives of Model 2D, 2D+f, 2D+w and 2D+f+w

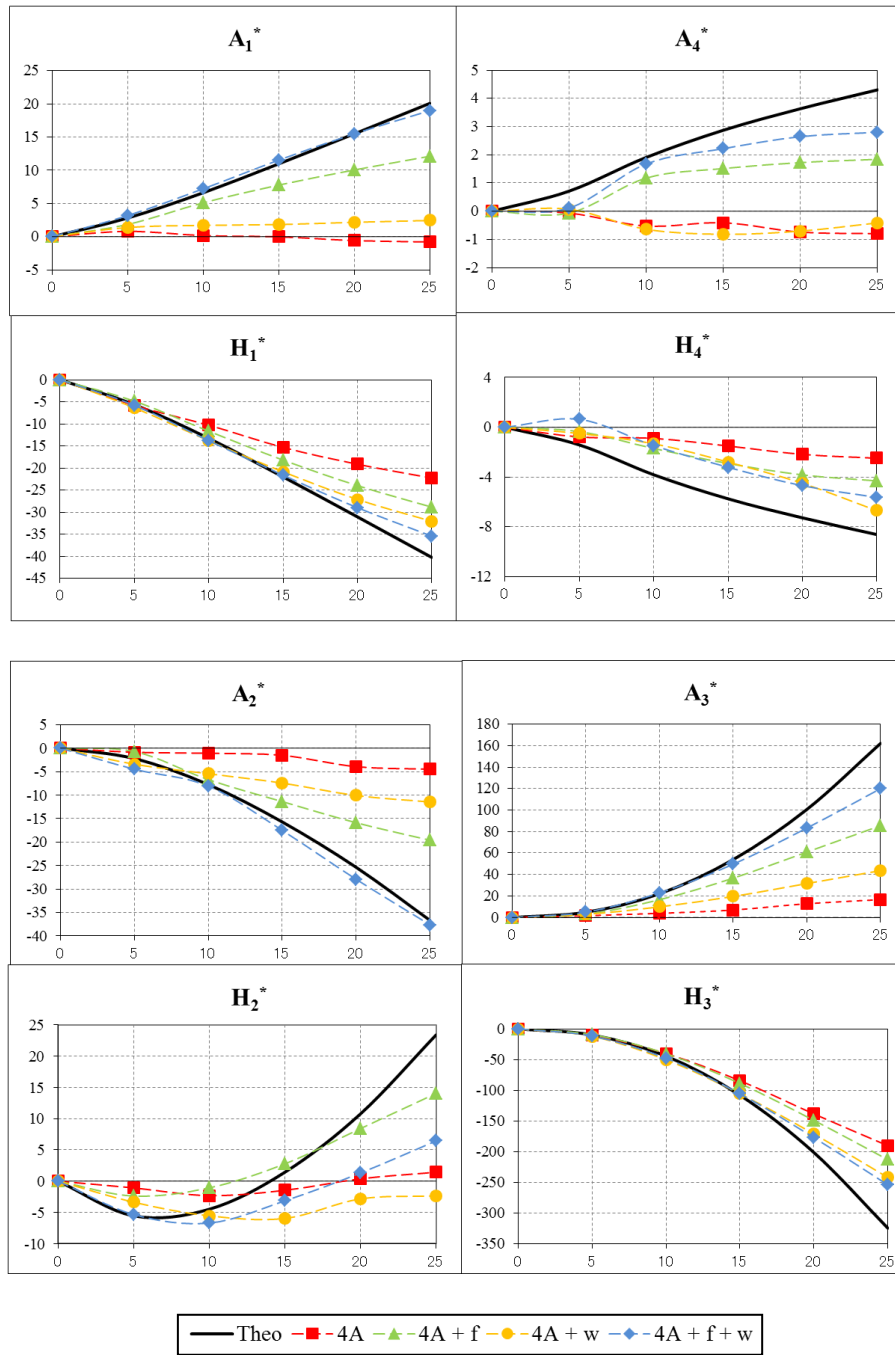


Fig. 5.23 Aerodynamic derivatives of Model 4A, 4A+f, 4A+w and 4A+f+w

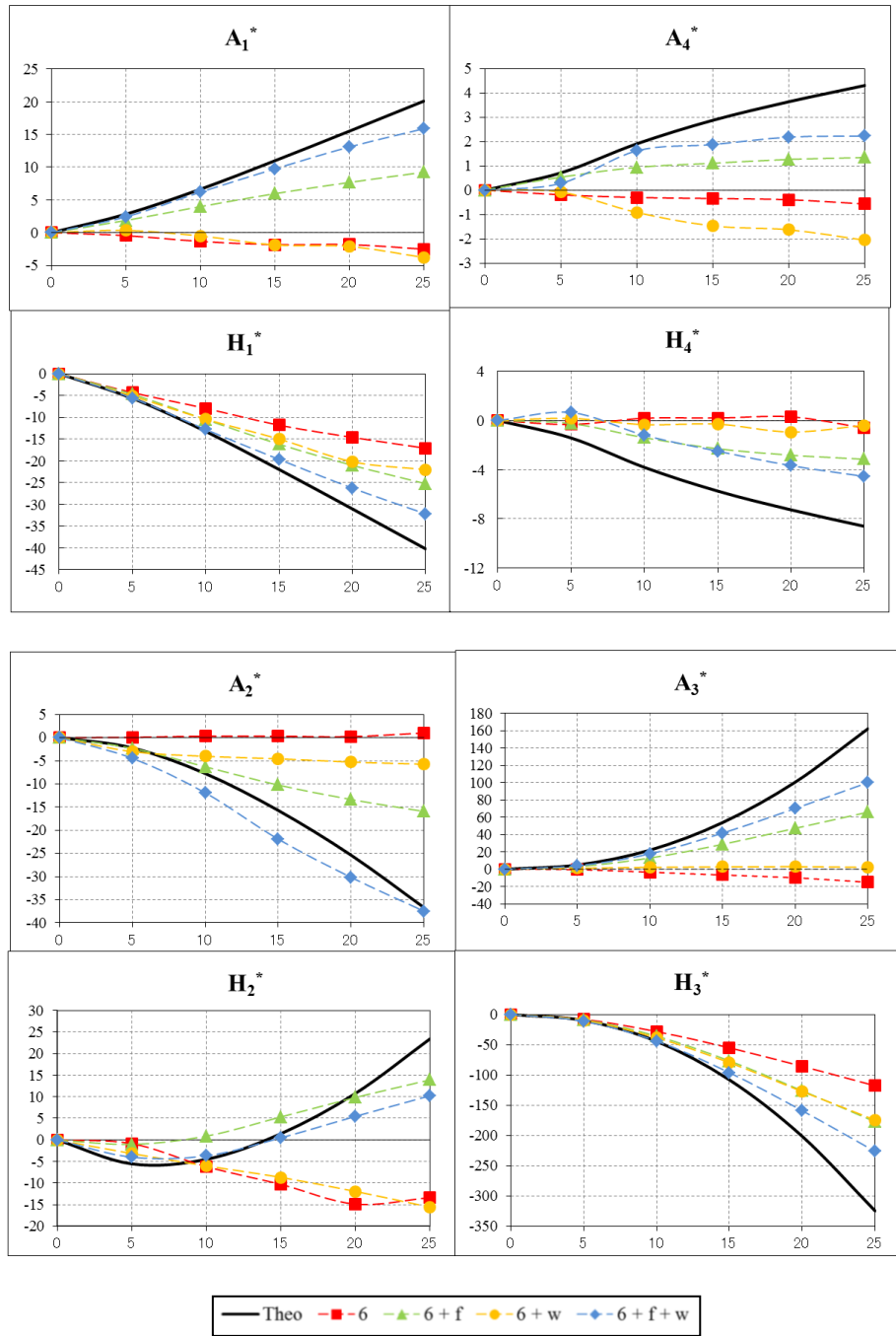


Fig. 5.24 Aerodynamic derivatives of Model 6, 6+f, 6+w and 6+f+w

Several patterns can be observed from above figures:

1. For section with narrow slot (Model 1B and 2B), adding fairings or winglets will change the  $A_1^*$  significantly, make it closer to the value of  $A_1^*$  of  $B/D=20$  rectangular prism. In other words, the benefit of using double slot from flutter stabilization point of view is reduced by the effects of fairings or winglets.
2. For section with wide slot (Model 4A and 6), the effects of fairings is also significant, but the effect of winglets to  $A_1^*$  is insignificant. For these section, adding winglets will change the value of  $A_1^*$  slightly, and produce more negative value of  $A_2^*$ .

3. For most cases,  $H_3^*$  is not affected much by all countermeasures, except for Model 6.

### 5.3.3 Unsteady Pressure Characteristics of Prism Using Combination of Double Slot with Fairings and Winglets

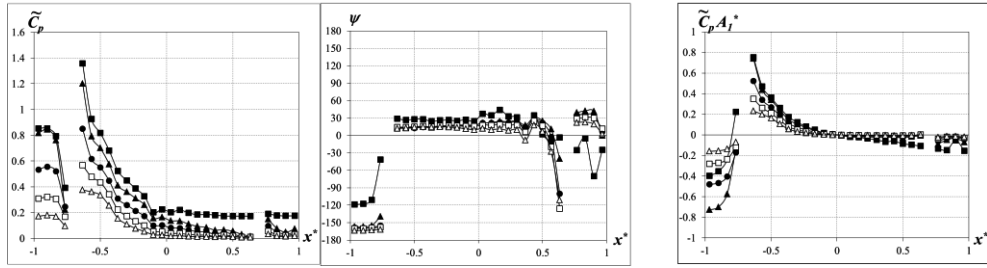
The effects of additional countermeasures to values of aerodynamic derivatives can be explained by analyzing the unsteady pressure characteristics. Fairing at leading edge reduces the amplitude of surface pressure significantly, and also produces positive and near zero phase lag in near leading edge zone.

This pattern of  $\tilde{C}_p(x^*)$  and  $\psi(x^*)$  is related with reduction of size of separation bubble or weak separation at leading edge. It can be said that fairings make the separation at leading edge becomes weaker. This eliminates near zero resultant of pressures in upwind of near leading edge slot with the downwind pressures, since now the pressures have the same direction. Therefore large values of  $A_1^*$  are produced. Similar results also found in torsional motion. In this case, positive  $\psi(x^*)$  near leading edge produces more negative  $A_2^*$ .

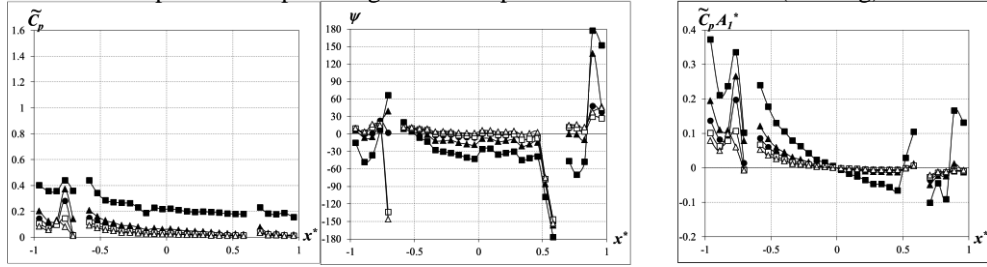
The effects of winglets cannot be understood fully from unsteady pressure data, because measurement only done for surface of main body of the section, not including on the surface of the winglets. Therefore, the lift and moment acting on winglets are still unknown. Unsteady pressure characteristics data can only give explanation about effects of aerodynamic interference between winglets and main body. From Fig. 5.27, it can be said that similar results with fairings also occurred: low amplitude and positive phase lag near leading edge, although for model 4A+w the value of phase lag near leading edge approach  $180^\circ$ . This results are related with the position of winglets that close to the edge of the main body, and therefore also acting like guide vanes.

.Another interesting results from using winglets, is that the effects of winglets are more significant in section with narrow slot (1B and 2B) compared to section with wide slot (4A and 6). From Fig. 5.29, it can be seen that aerodynamic forces on winglets are larger for model 1B+w than for model 4A+w, especially for moment due to heaving motion (related with  $A_1^*$ ). The explanation is still not clear, but it confirms that the effects of each countermeasure cannot be generalized because it depends on the aerodynamics of the basic section itself.

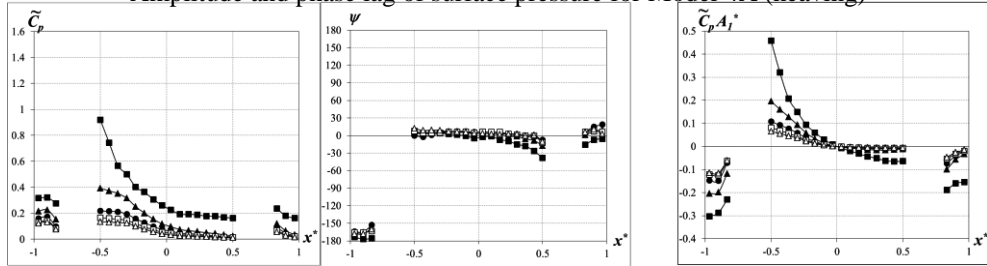
Amplitude and phase lag of surface pressure for Model 1B (heaving)



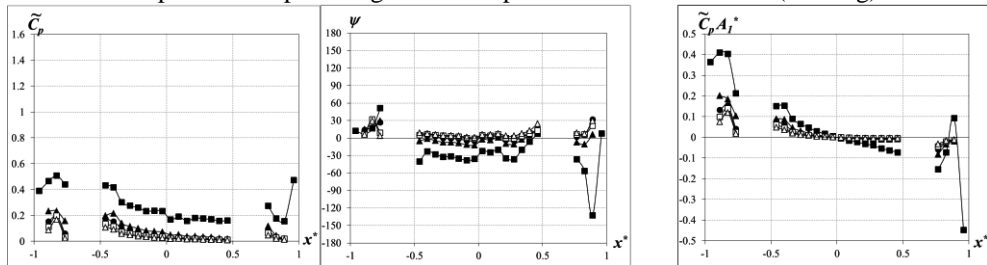
Amplitude and phase lag of surface pressure for Model 1B+f (heaving)



Amplitude and phase lag of surface pressure for Model 4A (heaving)



Amplitude and phase lag of surface pressure for Model 4A+f (heaving)



■ :  $U/fB=5$     ▲ :  $U/fB=10$     ● :  $U/fB=15$     □ :  $U/fB=20$     △ :  $U/fB=25$

Fig. 5.25 Effects of fairings to  $A_I^*$

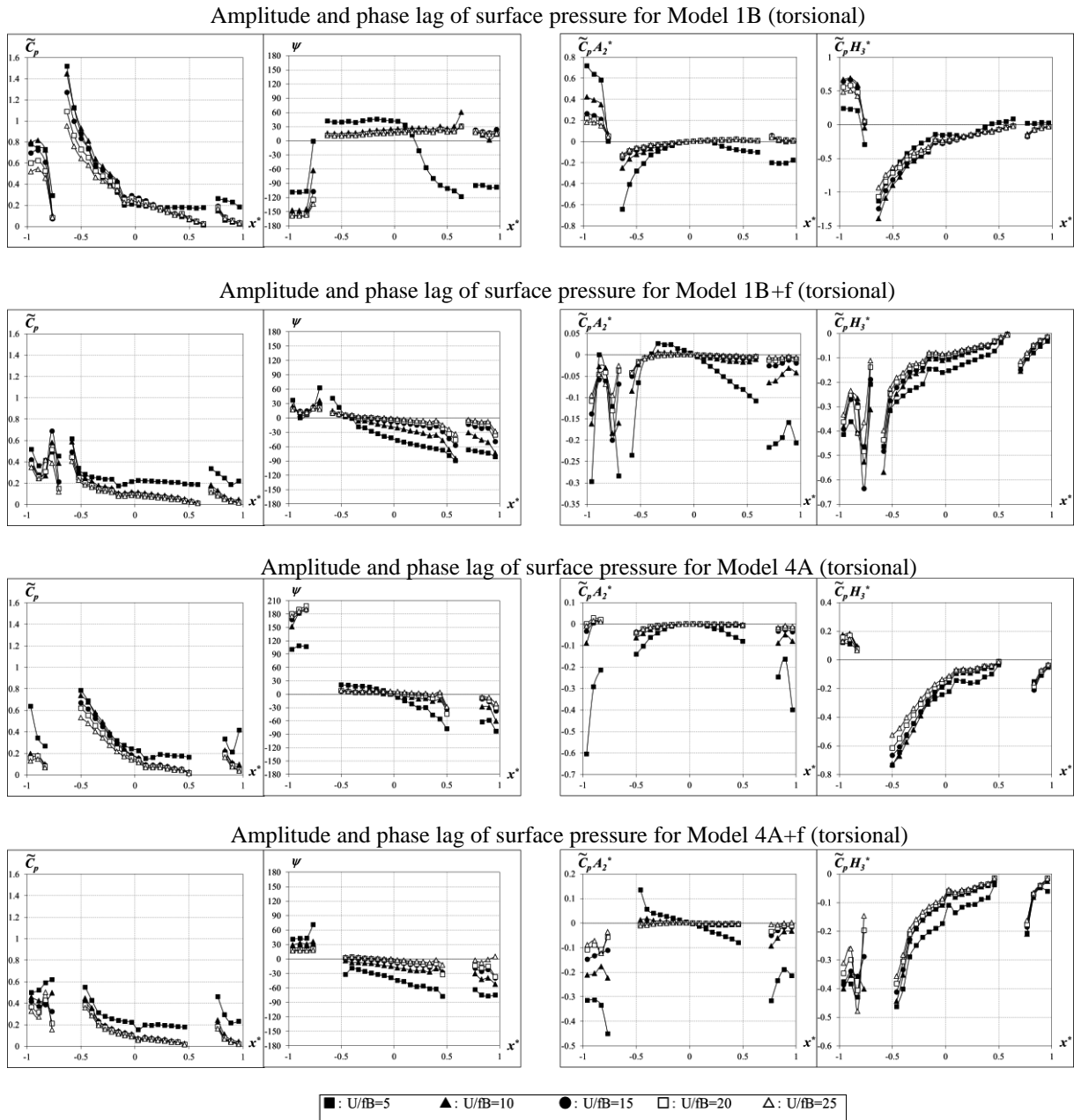
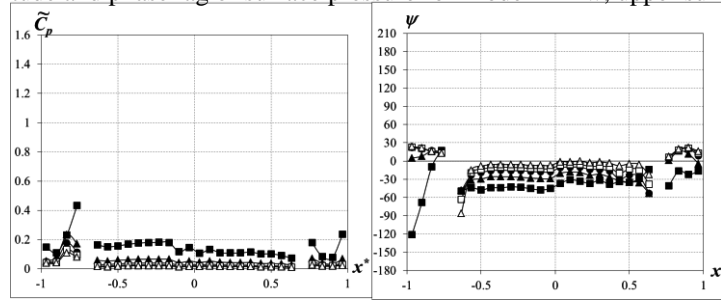


Fig. 5.26 Effects of fairings to  $A_2^*$  and  $H_3^*$

As a conclusion based on aerodynamic derivatives and unsteady pressure characteristics data, it can also be pointed out that different effect of winglets to each model implies that analytical approximation is not applicable in these cases. It can be said that the presence of winglets change the flow field and obviously interference occurred between winglets and main body. The effects of fairing are relatively more predictable. The change of  $\psi$  (phase difference) at upstream of slot near leading zone due to the presence of fairings produces negative  $A_2^*$  (in rotational motion) and relatively large  $A_1^*$  (in heaving motion). Furthermore, pressure measurement test is necessary to confirm the effects of fairings and winglets to unsteady pressure characteristics of each model



Amplitude and phase lag of surface pressure for Model 1B+w, upper surface (heaving)



Amplitude and phase lag of surface pressure for Model 4A+w, upper surface (heaving)

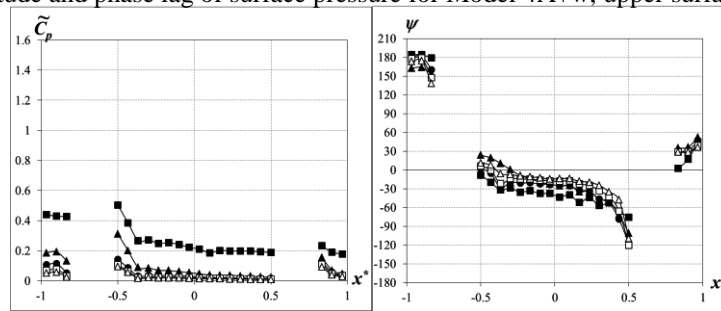
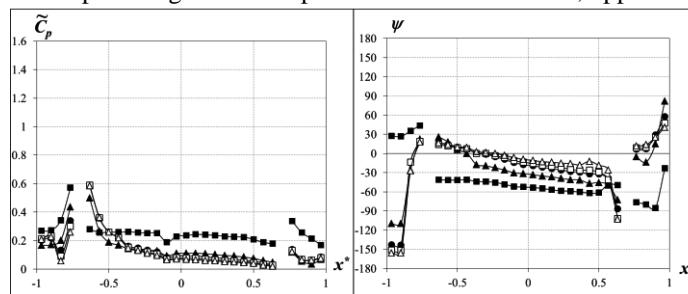


Fig. 5.27 Effects of winglets to  $\tilde{C}_p(x^*)$  and  $\psi(x^*)$ (heaving)

Amplitude and phase lag of surface pressure for Model 1B+w, upper surface (torsional)



Amplitude and phase lag of surface pressure for Model 4A+w, upper surface (torsional)

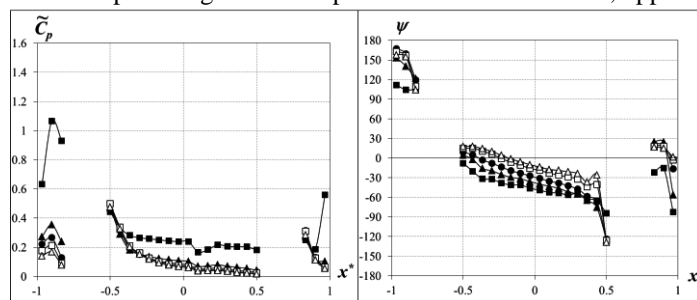


Fig. 5.28 Effects of winglets to  $\tilde{C}_p(x^*)$  and  $\psi(x^*)$ (torsional)

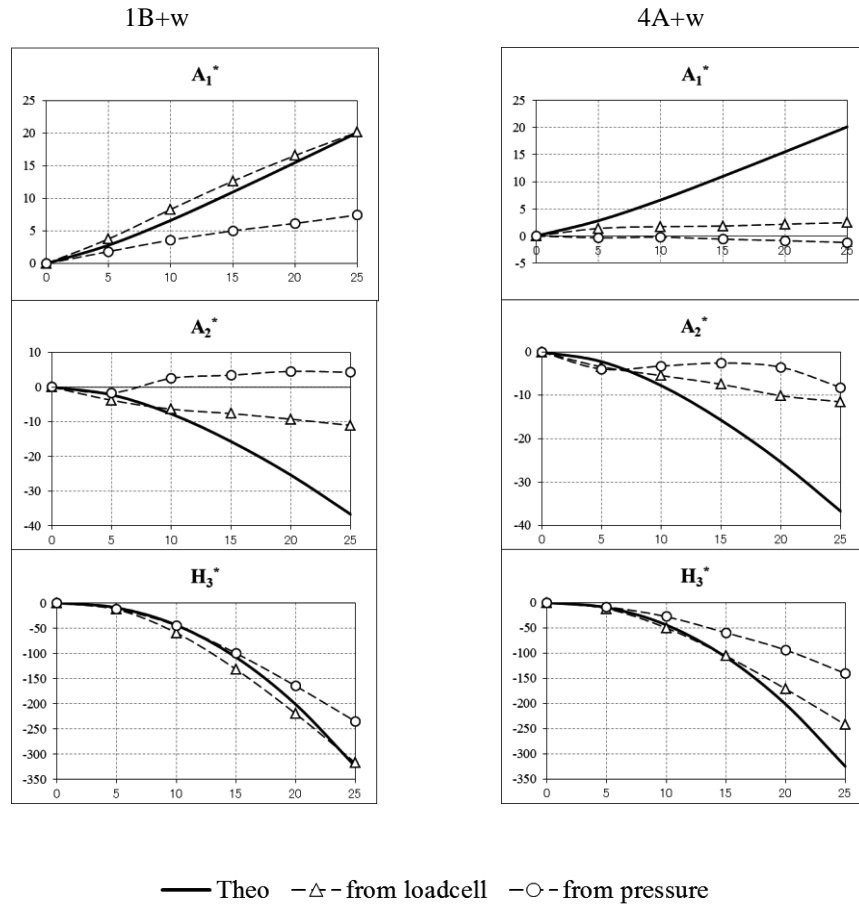


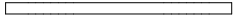
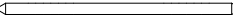


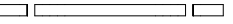
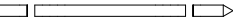


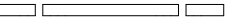
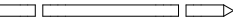


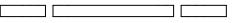



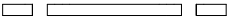



Fig. 5.29 Comparison of aerodynamic derivatives from direct measurement (using loadcell) and from integration of surface pressures (without pressures on winglets)


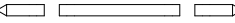

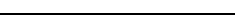


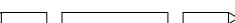

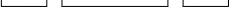



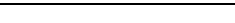
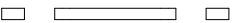


### 5.4 Results: Flutter Stability

Based on the aerodynamic derivatives data, it can be expected that even though fairings and winglets could stabilize section with narrow slot (change  $A_2^*$  to negative), but the improvement of stabilization compared to basic section, Model F, would be moderate. The flutter onset velocities of these models were calculated using CEVA, and the results are presented in Table 5.3. The result of flutter onset velocity for Model F in Table 5.3 is slightly different from Table 4.1 and table 5.1, due to discrepancy of aerodynamic derivatives from different measurement or experiment.

Results from Table 5.3 also in good agreement with previous study as shown in Table 4.1 and 4.2, that combination of slot near leading edge and fairings will increase stability or slender rectangular prism moderately. It also shown that fairings are not always favorable for flutter stabilization.

Table 5.3 Flutter onset velocity of model with combination of double slot with fairings and winglets (calculated with CEV)

	Section	void ratio	$U_{cr}$ (m/s)	$U_{r cr}$	$v_{r cr}$	ratio $U_r$ to basic section
Theodorsen		0	9.80	7.11	1.00	
Model F		0	8.00	5.74	0.81	1.00
Model F+f		0	8.60	6.10	0.86	1.06
Model F+w		0	8.90	6.55	0.92	1.14
Model F+f+w		0	9.50	6.98	0.98	1.22
Model 1B		0.07	unstable	-	-	-
Model 1B+f		0.07	9.10	6.41	0.90	1.12
Model 1B+w		0.07	9.10	6.59	0.93	1.15
Model 1B+f+w		0.07	10.20	7.52	1.06	1.31
Model 1C		0.07	unstable	-	-	-
Model 1C+f		0.07	10.20	7.38	1.04	1.29
Model 1C+w		0.07	9.10	6.63	0.93	1.16
Model 1C+f+w		0.07	7.10	5.98	0.84	1.04
Model 1D		0.07	unstable	-	-	-
Model 1D+f		0.07	10.70	7.81	1.10	1.36
Model 1D+w		0.07	9.50	6.95	0.98	1.21
Model 1D+f+w		0.07	9.60	7.18	1.01	1.25
Model 2B		0.13	unstable	-	-	-
Model 2B+f		0.13	9.80	6.96	0.98	1.21
Model 2B+w		0.13	10.20	7.31	1.03	1.27
Model 2B+f+w		0.13	11.00	8.21	1.15	1.43

Model 2C		0.13	unstable	-	-	-
Model 2C+f		0.13	9.00	6.34	0.89	1.10
Model 2C+w		0.13	8.70	7.37	1.04	1.28
Model 2C+f+w		0.13	10.50	7.88	1.11	1.37
Model 2D		0.13	unstable	-	-	-
Model 2D+f		0.13	11.60	8.57	1.21	1.49
Model 2D+w		0.13	10.00	7.23	1.02	1.26
Model 2D+f+w		0.13	10.60	7.99	1.12	1.39
Model 4A		0.27	> 34.30	> 25.00	> 3.52	> 4.36
Model 4A+f		0.27	10.90	7.92	1.11	1.38
Model 4A+w		0.27	> 31.47	> 25.00	> 3.52	> 4.36
Model 4A+f+w		0.27	10.50	7.73	1.09	1.35
Model 6		0.4	unstable	-	-	-
Model 6+f		0.4	12.70	9.40	1.32	1.64
Model 6+w		0.4	27.50	24.84	3.49	4.33
Model 6+f+w		0.4	13.30	9.96	1.40	1.74

Logarithmic damping for Model F, Model 4A and Model 4A+w are shown in Fig. 5.30. It can be seen that winglets can improve damping for heaving motion of Model 4A, while for torsional motion both have comparable damping values.

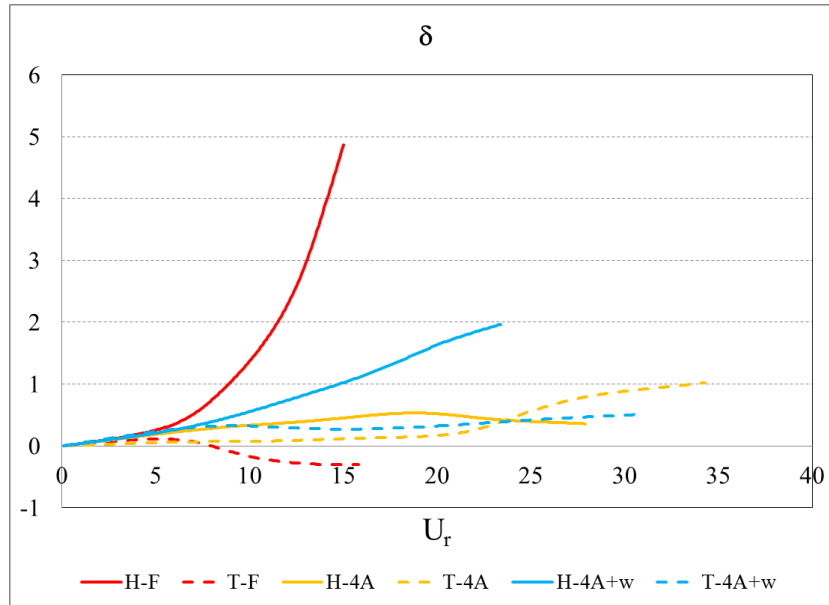


Fig. 5.30 Logarithmic damping for Model F, Model 4A and Model 4A+w

## 5.5 Concluding Remarks

This chapter is a continuation of Chapter 4. The focus of this study is to find additional countermeasures that can produce negative  $A_2^*$  for section with narrow slot that has low absolute value of  $A_1^*$ : Model 1B, 2B. Also Model 6 that has wide slot is studied. Two additional countermeasures: fairings and winglets are selected to improve these conditions. Both fairings and winglets can produce more negative  $A_2^*$  but with different mechanism: fairings modify flow near the leading edge and produce positive  $\psi$  in the region while winglets provide additional lift force that act as aerodynamic damping during torsional motion.

The results show that both fairings and winglets can stabilize the section. Fairings produce negative  $A_2^*$  but at the same time also produce large  $A_1^*$  for all models. These are due to the change of phase difference as expected and lower pressure amplitude at near leading edge zone (upstream the slot). These are attributed to weaker flow separation at leading edge due to presence of fairings. Winglets on the other hand, affects  $A_1^*$  significantly only for section with narrow slot. For section with wide slot (Model 4A and 6), winglets produce more negative  $A_2^*$  but the values of  $A_1^*$  are hardly affected. Unsteady pressure characteristics data show that winglets at position as used in this study also affect the flow field. Low pressure amplitude and almost constant phase difference are produced in Model 1B, which attributed to the weaker flow separation at leading edge. This can be explained that since the position of winglets are close to the surface of main body of the section, they also act like guide vanes.

Flutter onset velocity analysis results are in similar pattern with previous studies by other researchers. Therefore, this study can explain the moderate stabilization that produced by fairings and slots studied before.

## Bibliography

Del Arco, D. C., Aparicio, A. C. (1999), 'Improving suspension bridge wind stability with aerodynamic appendages', *Journal of Structural Engineering*, 125(12), pp. 1367-1375.

Graham, J. M. R., Limebeer, D. J. N., Zhao, X. (2011), 'Aeroelastic control of long-span suspension bridges', *ASME Journal of Applied Mechanics*, 78 (4), pp. 041018.

Hong, J. W. (2012), Study of Stabilization Against Coupled Flutter for Long Span Bridge Deck, Master thesis, Kyoto University, Kyoto, Japan (in Japanese).

Liu, G., Meng, F., Wang, X. (2006), "Mechanism of flutter control of suspension bridge by winglets", *Proceedings of the Fourth International Symposium on Computational Wind Engineering*, Yokohama, Japan, July 16-19, 2006.

Trein, C. A. (2009), 'Study on the Unsteady Pressure Characteristics of Bluff Bodies Focusing on Flutter Stabilization of Long-span Bridges', PhD thesis, Kyoto University, Kyoto, Japan.





# Chapter 6

## Feasibility of Using Slender Deck for Long Span Suspension Bridges

As stated in Chapter 2, there are two ways in practice to improve stability against flutter:

1. Modify structural configuration to improve structural parameter
2. Modify shape of deck to improve aerodynamic derivatives value

All the studies in this thesis are concerning only the aerodynamic derivatives of the deck. Rectangular prism with  $B/D=20$  is used as basic section since it has good aerodynamic properties that similar to thin plate and can be modified to obtain deck with excellent aerodynamic properties. In practice, the idea of using slender deck is still being questioned due to its unconventional form. This chapter provides preliminary analysis of the effects of using slender bridge deck, from structural parameters point of view.

### 6.1 Problems of Slender Bridge Deck

The behavior of long span suspension bridge had been already explained in several literatures (Brancaleoni *et al*, 2010; Gimsing and Georgakis, 2011), but several questions about the use of slender bridge deck still need to be clarified quantitatively, such as :

1. Effects of mass  
Several study reported the effect of dead weight or mass to the performance of suspension bridge (Kawada, 2010; Yoneda & Ito, 1986) and concluded that dead weight increases the stiffness of the bridge, which is due to the increase in tension of the main cable (known as gravity stiffness). Therefore, slender deck that has less weight will be more flexible and experience larger deflection, and the use of box girder with  $B/D$  more than 15 is questioned due to its lack of mass.
2. Stiffness and natural frequency  
It is obvious that stiffness of the deck becomes lower as the deck become slender, so that the behavior and stiffness of the bridge become more similar to stand alone cable element, which is heaving mode and torsional mode have the same frequency, or frequency ratio is equal to 1. The significant effects from other dynamic properties such as  $m_{eq}$  and  $I_{eq}$  was studied by Wu (2004) by performing parametric sensitivity analysis, and found that higher  $m_{eq}$  and  $I_{eq}$  could improve flutter stability. But in real bridge structure all of the parameters are interrelated, and such parametric study is not realistic from practical point of view. Dynamic properties from FEM model could give the insight of effect of deck slenderness quantitatively.
3. Reduction of steel

This is the main advantage of using slender bridge deck, but still there is question about the amount of saving. For rigid truss and slender deck, the saving of steel material is obvious (Brancaleoni *et al*, 2010), but less significant saving is expected for the case of slender deck with more slender deck section, for example between box girder with B/D=10 and B/D=20).

## 6.2 Approach of Study

In order to clarify the above mentioned problems, a series of analysis are done as detailed below :

1. FEM simulation (using commercial software MIDAS) of suspension bridge with variation of span length and deck cross section. Main span length are 1500m, 2000m, 3000m, and 3500m whilst side span is taken as 0.3\*main span. The sag ratio is fixed as n=1/11. Side span satio and sag ratio values are selected based on consideration of optimum configuration as reported by Gimsing and Georgakis (2011), Miyata *et al* (2001), Xiang & Ge (2007). Deck cross sections are rectangular prism box girder with side ratio B/D=10, 15, 20. Total width of deck is 45 m. The 45 m width is selected so that the depth of deck with B/D=20 is 2.25 m. It is commonly accepted that minimum depth of box girder is around 2.20 m, based on requirement for maintenance and internal inspection (Brancaleoni *et al*, 2010).
2. Although this study is not for detail design, but to get reasonable dimensions and sectional forces, a proper live load is used. The recommended live load from ASCE is used (Buckland *et al*, 1980), with 30% HV (heavy vehicle) since it represents average routes with relative large numbers of trucks. The comparison of 30% HV ASCE live load with other code can be found in Buckland (1991).
3. Size of main cables are calculated using an approximate formula (Gimsing and Georgakis, 2011) as follows:

$$A_m = \frac{\{(g+p)l_m + 2.P\}\sqrt{l_m^2 + 16.k_m^2}}{8.\bar{\sigma}_c.k_m - \gamma_c.l_m\sqrt{l_m^2 + 16.k_m^2}} \quad (6.1)$$

where  $A_m$ =area of main cable,  $g$ =dead load,  $p$ =uniform live load,  $P$ =point live load,  $l_m$ =length of main span,  $k_m$ =vertical distance of sag point to top of pylon,  $\bar{\sigma}_c$ =allowable stress of main cable=810 MPa,  $\gamma_c$ =weight density of main cable=84 kN/m<sup>3</sup>.

4. Mass and mass moment of inertia equivalent ( $m_{eq}$  and  $I_{eq}$ ) for selected mode shape are calculated by :

$$m_{eq,i} = \frac{\{\phi\}_i^T [M] \{\phi\}_i}{\int_D \{\phi^z\}_i^2 dx} \quad (6.2)$$

$$I_{eq,j} = \frac{\{\phi\}_j^T [M] \{\phi\}_j}{\int_D \{\phi^{rx}\}_j^2 dx} \quad (6.3)$$

where  $m_{eq,i}$  and  $I_{eq,j}$  are mass equivalent for fundamental heaving mode-i and torsional mode-j,  $\{\phi\}_i$ =mode shape-i,  $\{\phi^z\}_i$ = vertical component of mode shape-i,  $\{\phi\}_j$ =mode shape-j,  $\{\phi^{rx}\}_j$ =rotational component of mode shape-j, [M]=mass matrix.

5. The effect of deck stiffness to flutter instability is analysed by using 2-D bi-modal complex eigenvalue (CEV) analysis as explained in Chapter 3. This type of flutter analysis that involves only two fundamental modes is a simplified method. In CEV analysis, flutter wind speed is determined by eigenvalue method in the frequency domain, by iteratively solve the flutter equation (Agar, 1989). CEV analysis has several weaknesses, particularly due to its inability to explain the flutter generation mechanism, but its accuracy is good if the only concern is flutter onset velocity.
6. Aerodynamic derivatives values for all deck section are fixed, calculated from Theodorsen function, as explained in Chapter 2. These values are corresponding to the classical theoretical case of linearized thin airfoil (thin plate) that undergoes heaving and pitching motion, and have been used as benchmark for bridge decks. These values can be calculated analytically by substituting the Theodorsen function with formula proposed by Scanlan & Tomko (1971). By using fixed aerodynamic derivatives for all deck section, comparison of results and analysis can be limited only to the effects of structural dynamic properties.

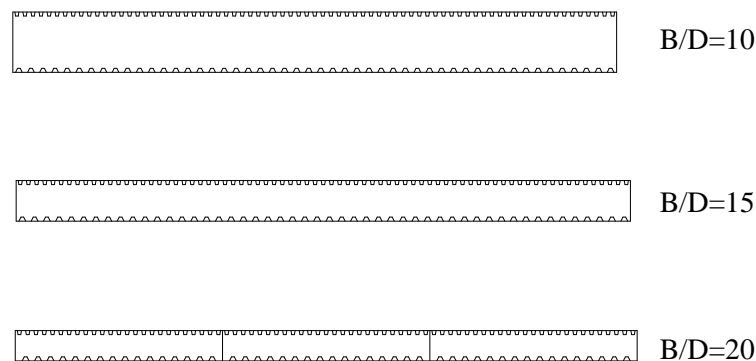


Fig.6.1 Deck cross section for analysis

### 6.2.1 Analysis of Suspension Bridge

Nowadays with the advance of computing power and analysis software, a complete three dimensional finite element model for suspension bridges can be developed utilizing a nonlinear catenary or truss element with large displacement capability. In this thesis, MIDAS commercial structure analysis software is used. MIDAS employs elastic catenary cable element for shape finding analysis, and use the linearized finite displacement method or second order analysis from tangential stiffness matrix at the dead load equilibrium state for live load analysis (MIDAS IT, 2009).

Semi-analytic method is usually used for preliminary analysis in order to determine the behavior of suspension bridge under gravity load. This method is very useful and attractive since it can connect between complex and unpractical analytic solution (Steinman, 1953; Ulstrup, 1993) and powerful but expensive finite element model (Kim & Lee, 2001). Clemente *et al* (2000) and Wollmann (2001) proposed simple formulations and procedures, although the applicability are limited compared to the finite element model, but still act as a good tool for the preliminary analysis or for educational purposes. Permata & Essen (2013) compared the results of semi-analytic solution using Wollmann proposed procedure with MIDAS, and concluded that Wollmann's method is sufficient for preliminary analysis despite its inaccuracy for special cases related with flexibility of hangers.

### 6.2.1.1 Theory of Cable

The static behavior of a suspension bridge depends on the stiffness and mass contribution of the main cable. In the suspension bridges, basic theory of cable must be fully understood first. Based on Fig. 6.2 and assuming the self weight load on cable is uniformly distributed ( $g$ ), the equation of equilibrium of the cable is given as follows :

$$\frac{d^2 y_g(x)}{dx^2} = \frac{-g}{H_g} \quad (6.4)$$

Eq. (6.4) can be characterized as equilibrium equation for parabolic cable that gives small margin of error compared to catenary cable for practical sag to span ratio usually used in real suspension bridge structures.

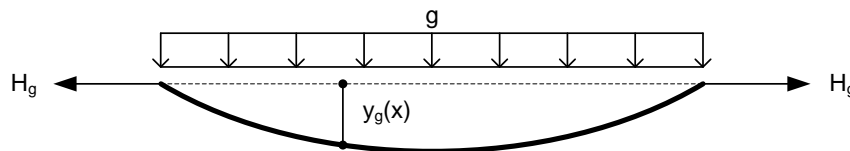


Fig.6.2 Cable load and geometry

### 6.2.1.2 Theory of Suspension Bridge: Deflection Theory and Solution by Wollmann

Fig. 6.2 is extended by considering the stiffening effect of the deck and hangers and several basic assumptions are made as follows to formulate more simple equilibrium equation :

- a) the weight of cable, hanger and stiffening deck are assumed to be uniformly distributed via hanger and taken by the cable, thus the cable shape is parabolic which validates Eq. (6.4).
- b) any arbitrarily live load ( $p$ ) applied to the deck is transferred to the main cable via hangers which are assumed as inextensible and the hanger force ( $s$ ) is uniformly distributed. Hanger force ( $s$ ) is pulling up the deck and pulling down the cable.

Based on Fig. 6.3, the equilibrium equation for cable is given as:

$$\left( \frac{d^2 y_g(x)}{dx^2} + \frac{d^2 y_p(x)}{dx^2} \right) = \frac{-(g + s)}{H_g + H_p} \quad (6.5)$$

The equilibrium equation for stiffening deck is given as:

$$EI \frac{d^4 y_p(x)}{dx^4} = p(x) - s \quad (6.6)$$

Substituting Eq (6.4) and (6.5) into Eq. (6.6) will give

$$EI \frac{d^4 y_p(x)}{dx^4} - (H_g + H_p) \frac{d^2 y_p(x)}{dx^2} - p(x) - H_p \frac{d^2 y_g(x)}{dx^2} = 0 \quad (6.7)$$

Eq. (6.7) can be characterized as an equilibrium equation based on deflection theory with two unknowns. One compatibility equation is needed to connect the two unknowns: cable horizontal tension  $H_p$  and suspension bridge deflection due to live load  $p$ ,  $y_p$  :

$$\frac{H_p}{E_c A_c} L_c + \frac{d^2 y_g(x)}{dx^2} \int_l y_p(x) dx = \delta_j - \delta_i \quad (6.8)$$

Where  $\delta_j$  and  $\delta_i$  are the displacements at cable ends.

The derivation of Eq. (6.8) can be seen in Wollmann (2001). It relates the compatibility of the cable with the horizontal tension of the cable and pylon stiffness. The integral formula can be analytically calculated using Simpson's rule with minimum ten discretization points that will also be used as output stations.

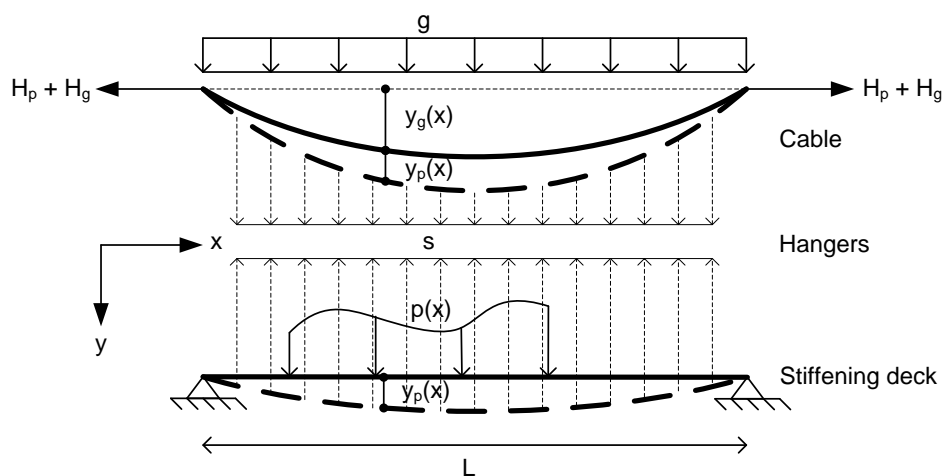


Fig.6.3 Suspension bridge load and geometry

Mathematically Eq. (6.7) can be rearranged to give a formula that analogous to flexural beam under axial tension as shown in Fig. 6.4.

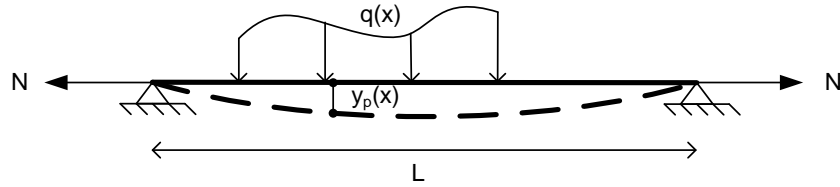


Fig.6.4 Flexural beam with axial tension under arbitrary load

The moment equilibrium can be given as follows:

$$M(x) = M_o(x) + Ny_p(x) \quad (6.9)$$

Differentiating Eq. (6.9) twice will give:

$$EI \frac{d^4 y_p(x)}{dx^4} = q + N \frac{d^2 y_p}{dx^2} \quad (6.10)$$

By analogy based on Eq. (6.7) and Eq. (6.10), it can be said that:

$$N = H_g + H_p \quad (6.11)$$

$$q = p(x) + H_p \frac{d^2 y_g(x)}{dx^2} \quad (6.12)$$

By applying a boundary condition, Eq. (7) can be solved numerically to give the response in the deck once the cable tension and deflection due to live load is obtained. Additional minimization function is added to solve the compatibility equation for the case where cable horizontal tension is different for the side spans and main span. The flowchart describing the solution for calculating the deck response using Wollmann's method is shown in Fig. 6.5.

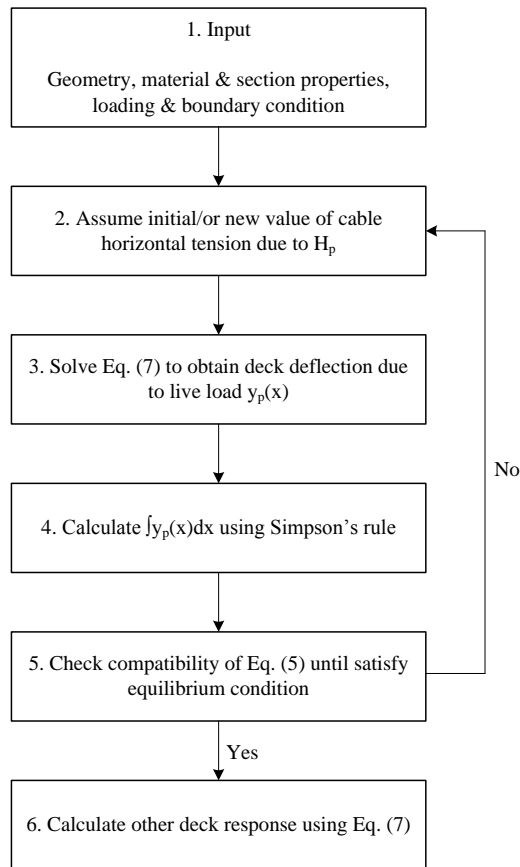


Fig.6.5 Flowchart for solution algorithm using Wollman's method

### 6.2.1.3 Finite Element Model of Suspension Bridge

A brief and comprehensive explanation of finite element modelling of suspension bridge structure can be found in Al-Assaf (2006). There are two main issues in finite element modelling of suspension bridge: formulation of the element (cable element) and initial condition of the element. The stiffness matrix of a cable element should take into account the effect of geometric nonlinearity. The initial internal forces should be calculated first. These forces are due to the deflection under self-weight or total dead load of the cables, deck and superimposed dead loads. A shape finding process is required to estimate the final shape of a cable and the internal forces.

The process of modelling suspension bridge structure using MIDAS software is summarized in Fig. 6.6. The elastic catenary element model is used only for finding the initial forces in the main cables and hangers. After the initial shape and forces are determined, the cable elements are transformed into equivalent truss element, which stiffness is function of elastic stiffness and initial forces.

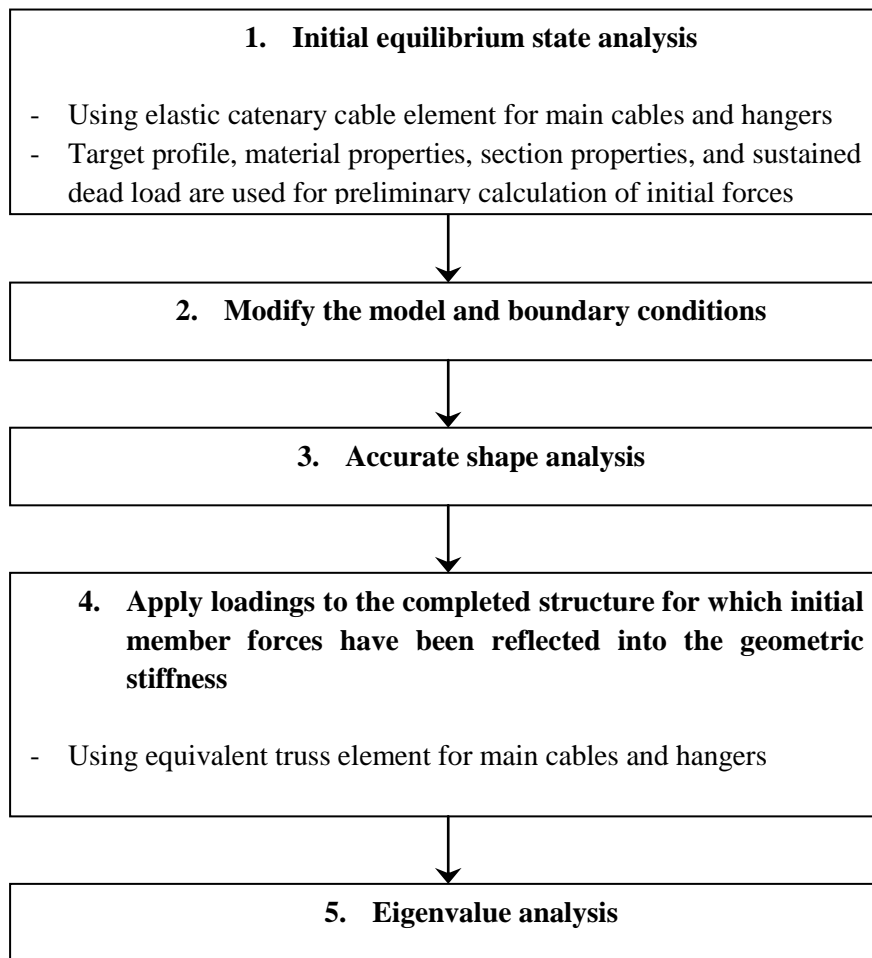


Fig.6.6 Flowchart for develop finite element model of suspension bridge using MIDAS

The derivation of stiffness matrix for elastic catenary cable element, equivalent truss element and details of shape finding process are beyond the scope of this thesis.



Fig.6.7 FEM model of suspension bridge with main span 1500 m





Fig.6.8 FEM model of suspension bridge with main span 2000 m



Fig.6.9 FEM model of suspension bridge with main span 3000 m

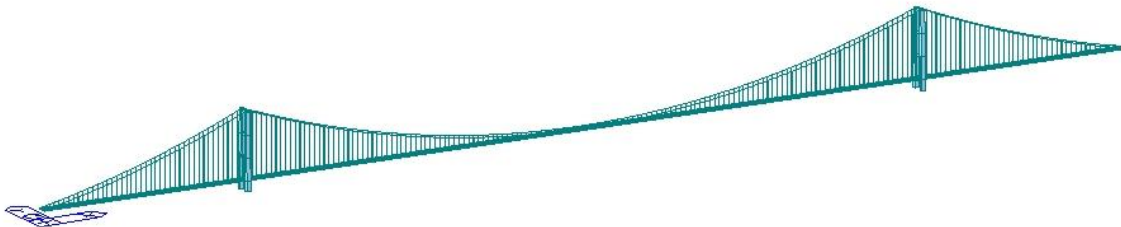


Fig.6.10 FEM model of suspension bridge with main span 3500 m

### 6.2.2 Live Load for Long Span Bridge

Most of the bridge loading code are intended for short or moderate span bridge, like AASHTO that covers only bridge with span less than 500 ft or about 150 m. Therefore, special code that covers long span bridge is used in this study. The ASCE loading (Buckland *et al.*, 1980) is used to its simplicity and applicability up to 2000 m span. Beyond this span, extrapolation is used.

The ASCE loading –like other bridge loading codes- proposed a uniform load and a concentrated load to give moments and shears. Unlike aother traditional codes, the concentrated load is increase with loaded length (Fig. 6.11).

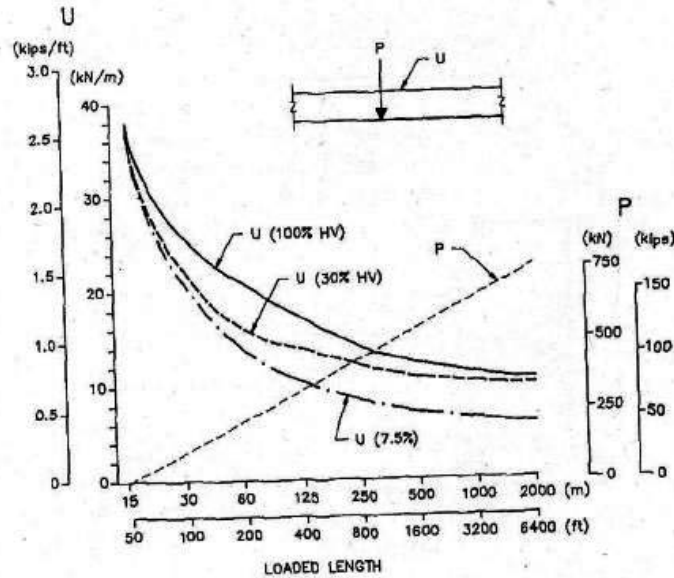


Fig.6.11 Live load for bridges as suggested by ASCE (after Buckland, 1991)

## 6.3 Results and Discussion

### 6.3.1 Weight of Steel Deck and Main Cable

Total weight of steel decks are presented in Table. 6.1. It can be seen that although total reduction can achieved 10000 ton for bridge with main span 3500m, but actually this is relatively small compared to the total volume. The reduction is only 2.75% for B/D=15, 7.46% for B/D=20. One important note is that these volume values are based on cross sections that are not designed by detail analysis. Total weight of main cables are presented in Table. 6.2. The average reduction of main cable volume are 2.06% for B/D=15, 5.52% for B/D=20.

Table 6.1 Total weight of steel deck

$l_m = 1500m$			$l_m = 2000m$		
Section	Total weight (ton)	Reduction (ton)	Section	Total weight (ton)	Reduction (ton)
B/D=10	58534.56	-	B/D=10	78046.08	-
B/D=15	56927.22	1607.34	B/D=15	75902.96	2143.12
B/D=20	54170.03	4364.53	B/D=20	72226.71	5819.37

$l_m = 3000m$			$l_m = 3500m$		
Section	Total weight (ton)	Reduction (ton)	Section	Total weight (ton)	Reduction (ton)
B/D=10	117069.11	-	B/D=10	136580.63	-
B/D=15	117069.11	3214.68	B/D=15	132830.17	3750.46
B/D=20	108340.06	8729.05	B/D=20	126396.74	10183.89

Table 6.2 Total weight of main cable

$l_m = 1500m$			$l_m = 2000m$		
Section	Total weight (ton)	Reduction (ton)	Section	Total weight (ton)	Reduction (ton)
B/D=10	14807.95	-	B/D=10	46672.66	-
B/D=15	14489.82	318.13	B/D=15	45683.11	989.55
B/D=20	13963.85	844.11	B/D=20	43992.40	2680.26

$l_m = 3000m$			$l_m = 3500m$		
Section	Total weight (ton)	Reduction (ton)	Section	Total weight (ton)	Reduction (ton)
B/D=10	130062.04	-	B/D=10	201785.25	-
B/D=15	127526.28	2535.77	B/D=15	197590.87	4194.38
B/D=20	123082.32	6979.72	B/D=20	190685.97	11099.28

### 6.3.2 Stress and Deflection at Mid-span due to Live Load

Results of stress and deflection calculation shown in Fig. 6.12. It shows that stress and deflection is mainly controlled by the cable and the stiffness of deck is less significant. The stress even get smaller as the deck get more slender. Although the deflection of more slender deck are larger, but the changes are insignificant and the values are still acceptable.

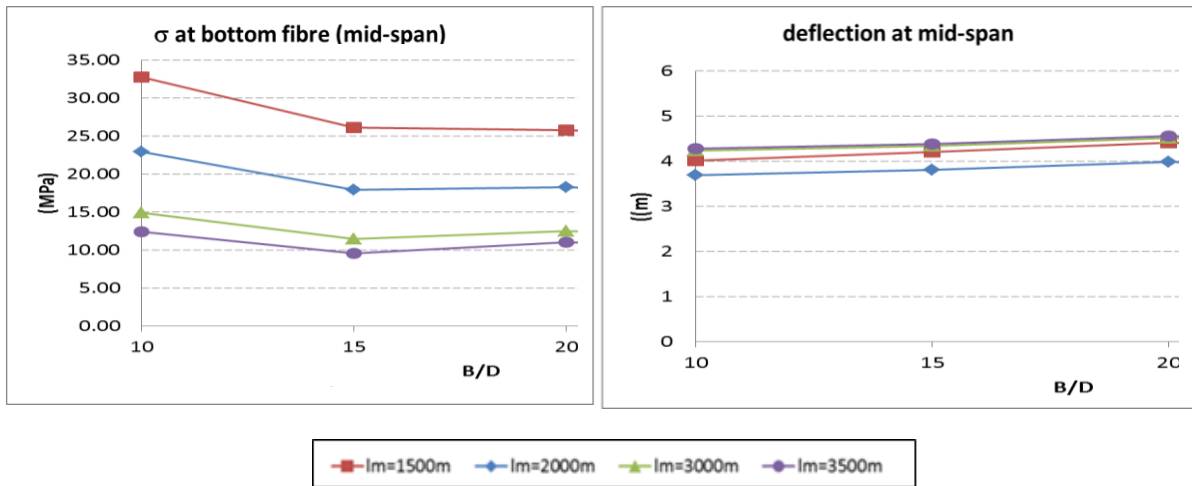


Fig.6.12 Stress and deflection at bottom fibre at mid-span due to live load

### 6.3.3 Structural Dynamic Properties

Mass equivalent ( $m_{eq}$ ) and mass moment of inertia equivalent ( $I_{eq}$ ) for fundamental symmetric heaving and torsional modes are shown in Fig. 6.13.

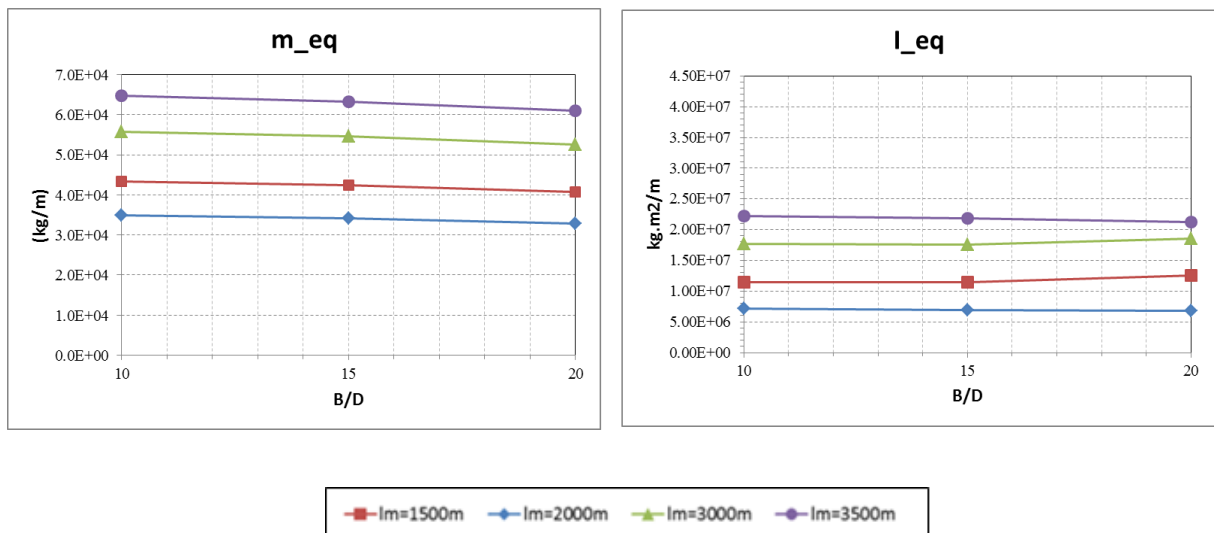


Fig.6.13 Mass equivalent and moment of inertia equivalent for 1<sup>st</sup> symmetric heaving and torsional modes

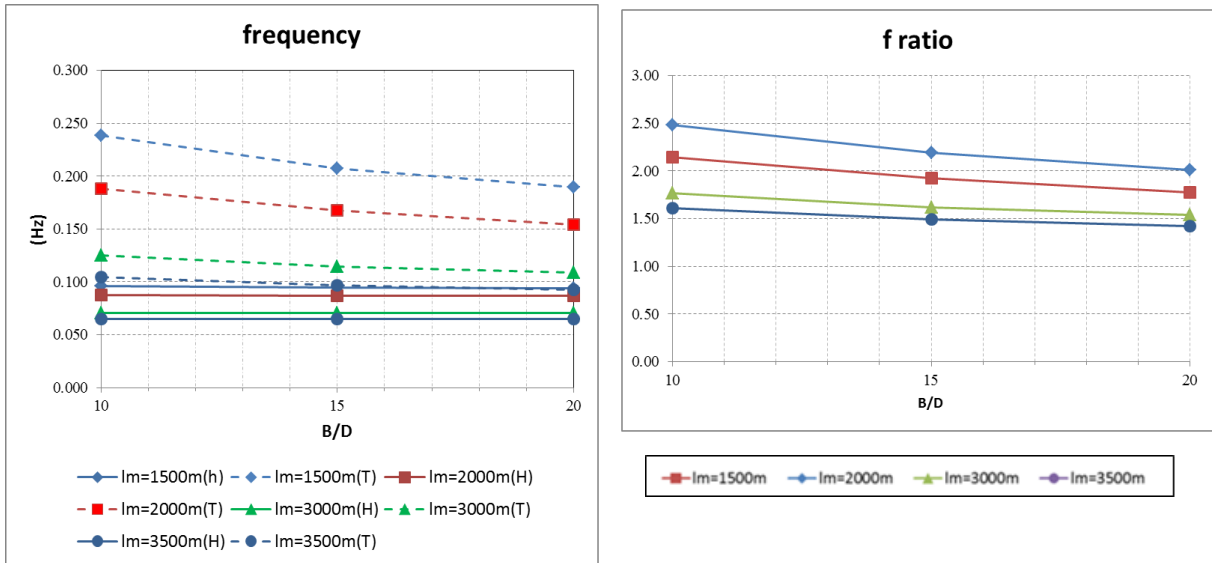


Fig.6.14 Frequency and frequency ratio for 1<sup>st</sup> symmetric heaving and torsional modes

Based on Fig. 6.13 and Fig. 6.14, the effects of deck stiffness to dynamic properties are clearly shown. Effects of slenderness is more significant to torsional frequency than heaving frequency. Frequency ratio is an important parameter for stability against coupled flutter. In order to get more clear understanding of effects of these dynamic parameters to coupled flutter onset velocity, flutter analysis is carried out by using fixed aerodynamic derivatives from Theodorsen function. The results are shown in Fig. 6.15.

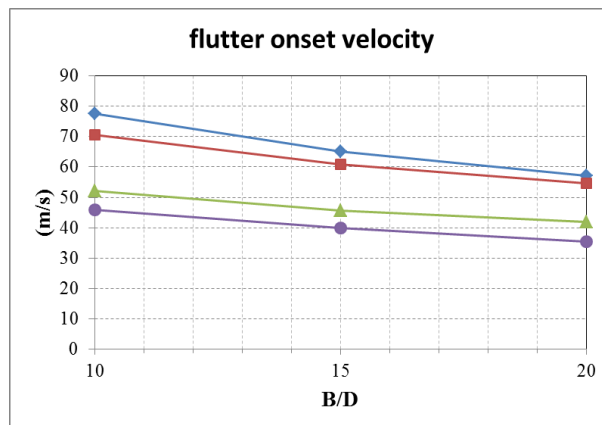


Fig.6.15 Flutter onset velocity of the models, with aerodynamic derivatives from Theodorsen function

The hexagonal box girder with vertical plate that described in Appendix B has flutter stability index or  $U_{r\ cr}/U_{r\ cr\ plate} > 2.5$  (Matsumoto *et al*, 2007). This section is based from rectangular prism with  $B/D=20$ . As explained previously, the aerodynamic derivatives of rectangular prism are similar to thin plate from Theodorsen function, and since model

$l_m=3500\text{m}$  with deck  $B/D=20$  has flutter onset velocity  $35.5\text{ m/s}$ , it could be estimated that if hexagonal box girder with vertical plate is used for  $l_m=3500\text{m}$ , the flutter onset velocity will be  $> 2.5*35.5=88.75\text{ m/s}$ , which meets the requirement from most of the typhoon-prone country in the world.




This result shows that slender deck section that has side ratio  $B/D=20$  is feasible for candidate of deck for future long span suspension bridges.

### 6.3.4 Frequency Ratio of Long Span Suspension Bridge Using Slotted Deck

As explained in Chapter 3, the latest development of using slotted deck is the triple box girder deck (as for proposal of Messina Bridge) and double box girder (as for proposal of future long span bridges in Japan). Model 4A that proposed in this thesis is basically a triple box girder section with wider central box. This section has favorable feature for structural dynamic properties, that the mass of the deck is more concentrated at the mid-chord of the deck. This will lead to lower moment of inertia, and produce larger torsional frequency.

In order to quantify this benefit, other FEM model also developed with the same procedures as mentioned in sub-chapter 6.2. Three deck sections are used: twin box girder, triple box girder and Model 4A. The results are presented in Table 6.3. It can be said that Model 4A, beside its superior aerodynamic properties for flutter stabilization, also has advantages than other slotted deck type due to its larger frequency ratio. Therefore, Model 4A can be used for further studies as candidate for deck section for future long span bridges.

Table 6.3 Comparison of frequency ratio of long span suspension bridge with slotted deck

Bridge deck	$l_m=1500\text{m}$	$l_m=2000\text{m}$	$l_m=3000\text{m}$	$l_m=3500\text{m}$
Twin girder 	1.81	1.65	1.43	1.33
Triple box girder with equal width 	1.83	1.66	1.43	1.34
Model 4A 	1.92	1.73	1.47	1.37

## 6.4 Concluding Remarks

This chapter not directly related with other chapters, it aims to give brief insight about use of slender bridge deck for long span suspension bridges. Basic theory of analysis of suspension bridges also presented.

Finite element model using MIDAS software are developed to calculate and check the effects of using slender deck. As expected, parameters that related to the static analysis of the bridge (stress, deformation) are not affected significantly by the slenderness of the deck. In fact, stress are reduced as the slenderness of the deck increased. The reduction of weight of steel decks and main cables also presented, as the reduction are less than 10%.

Frequency of first torsional mode is affected by the slenderness, as the deck become more slender the torsional frequency get lower. However, the frequency of first heaving mode is almost constant. This is unfavorable for flutter stability of the bridge deck, but preliminary analysis shows that excellent flutter stability can be achieved by using slender deck with superior aerodynamic properties.

Model 4A is compared to other slotted box girder deck: twin box girder and triple box girder. Results show that Model 4A has better structural parameter value (higher frequency ratio) than the other slotted deck. This confirms that advantages of using Model 4A for long span suspension bridge are not just from aerodynamic properties but also from structural point of view.

## Bibliography

- Agar, T. J. A. (1989) 'Aerodynamic flutter analysis of suspension bridges by a modal technique', *Engineering Structures*, 11, pp. 75-82.
- Brancaleoni, F., Diana, G., Faccioli, E., Fiammenghi, G., Firth, I. P. T., Gimsing, N. J., Jamiolkowski, M., Sluszk, P., Solari, G., Valensise, G., and Vullo, E. (2010) *The Messina Strait Bridge : a challenge and a dream*, CRC Press.
- Buckland, P. G., Navin, F. P. D., Zidek J. V., and McBryde, J. P. (1980) 'Proposed vehicle loading of long-span bridges', *Journal of the Structural Division*, ST4, pp. 915-932.
- Buckland, P. G. (1991) 'North American and British long-span bridge loads', *Journal of Structural Engineering*, 117(10), pp. 2872-2987.
- Clemente, P., Nicolosi, G., and Raithel, A. (2000) 'Preliminary design of very long-span suspension bridges', *Engineering Structures*, 22, pp. 1699-1706.
- Gimsing, N. J., Georgakis, C. T. (2011) *Cable supported bridges : concept and design 3ed.*, Wiley.
- Kawada, T. (2010) *History of the modern suspension bridges : solving the dilemma between economy and stiffness*, ASCE Press
- Kim, K. S., and Lee, H. S., (2001) 'Analysis of target configurations under dead loads for cable-supported bridges', *Computers and Structures*, 79, pp. 2681-2692
- Matsumoto, M., Mizuno, K., Okubo, K., Ito, Y., and Matsumiya, H. (2007) 'Flutter instability and recent development in stabilization of structures', *Journal of Wind Engineering and Industrial Aerodynamics*, 95, pp. 888-907.
- MIDAS Information Technology (2009) 'Midas civil-integrated solution system for bridge and civil structures'.
- Miyata, T., Yamada, H., Katsuchi, H., and Suangga, M. (2001) 'Optimum suspension bridge configuration against flutter and construction cost', *EASEC 8*, Singapore, December 5-7 2001.
- Permata, R., Essen, D. (2013) 'Static analysis of suspension bridges under gravity load', *CECAR 6*, Jakarta, Indonesia.
- Scanlan, R. H., and Tomko, J. J. (1971) 'Airfoil and bridge deck flutter derivatives', *Journal of Engineering Mechanic Division*, ASCE 97, EM6, pp. 1717-1737.
- Steinman, D. B. (1953) *A practical treatise on suspension bridges*, Wiley.
- Ulstrup, C. C. (1993) 'Rating and preliminary analyss of suspension bridges', *Journal of Structural Engineering*, 119 (9), pp. 2653-2679.
- Wu, H. (2004) *The effects of structural dynamics for the flutter instability of fundamental structural sections*, PhD thesis, Kyoto University.
- Wollman, G. P. (2001) 'Preliminary analysis of suspension bridges', *Journal of Bridge Engineering*, 6 (4), pp. 227-233.
- Xiang, H. F., and Ge, Y. J. (2007) 'Aerodynamic challenges in span length of suspension bridges', *Front. Archit. Civ. Eng. China*, 1(2), pp. 153-162



Yoneda, M., and Ito, M. (1986) 'Effects of dead weight on aerodynamic stability of long-span suspension bridges', *Structural Eng. / Earthquake Eng.*, 3(1), pp. 123s-133s



# Chapter 7

## Concluding Remarks

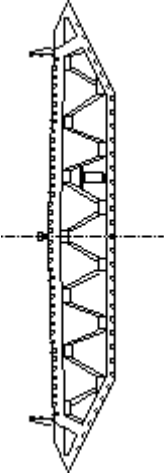
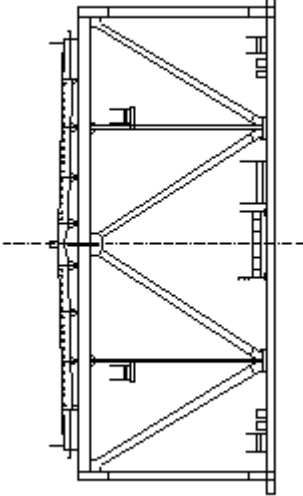
The concluding remarks for each chapter already presented the important notes obtained from this thesis. Several points are highlighted from this thesis:

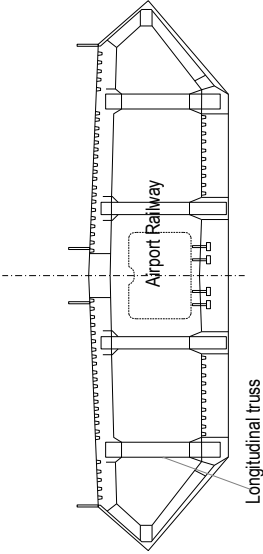
1. Suspension bridge structures are flexible structures as the main cables are the ‘backbone’ of the structure. Its flexibility make it prone to aerodynamic-related excitation. Flutter instability is one of the main concern in designing long span suspension bridges. Engineers and researchers are continuing search for better deck shape option for future long span bridges that can achieved 3000 m. Latest trend in this field is the use of slotted box girder deck section, that has advantages attributed to lower weight but disadvantages for aerodynamic stability.
2. CEV and SBS analysis are two practical method for analysis of flutter stability. Selberg formula has limited applicability, because it is intended only for thin plate. Selberg formula will give inaccurate results when the aerodynamic derivatives of the deck differs significantly from derivatives values from Theodorsen function. CEV is more like ‘purely’ mathematical approach to flutter problem, while SBS is based on the physics of the process that involved heaving and torsional branch of motion. CEV and SBS will give the same results for flutter onset velocity, which is the main concern of this thesis. But for future studies, SBS is a better option since it can give the information about role of each aerodynamic derivatives for damping of the motion.
3. This thesis study about flutter stabilization of rectangular prism with side ratio  $B/D=20$  from unsteady pressure characteristics point of view. This approach gives better understanding about the physical process behind stabilization or destabilization of the section when any countermeasures is installed.
4. Section with double slot with proper arrangement (as Model 4A) can be a candidate for further study in search for better deck shape. This section is not just good from aerodynamic properties point of view, but also provide better structural parameter (higher frequency ratio) that is favorable for flutter stability. One important note is, that the good aerodynamic properties of this section is reduced when fairings are used. Fairings at leading edge will produce weaker flow separation at leading edge and make the flow around the body more smooth (reflected by almost constant phase difference and lower pressure amplitude). This raises another question about the occurrence of vortex-induced vibration. This point is certainly need attention for further study.

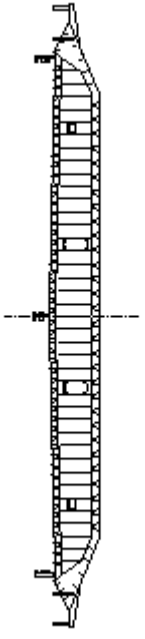
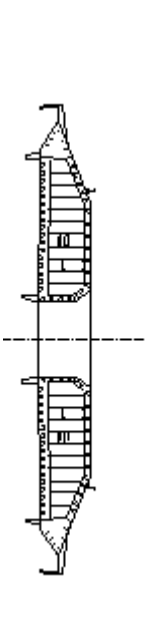
5. Porous cavity is not effective for countermeasures against flutter since the aerodynamic derivatives value of the deck with porous cavity are similar with the aerodynamic derivatives of rectangular prism with  $B/D=20$ . The presence of porous cavity near leading edge also change the flow and reduction of peak amplitude is obtained. However, there are also increasing of pressures at near leading edge zone. Resultant of these pressures are aerodynamic derivatives that have almost the same value compared with Model F or rectangular prism with  $B/D=20$ .
6. Fairings and winglets are studied as additional countermeasures for prism with double slot. The results show that both can stabilize the deck, but the improvement is only at moderate level for section with narrow slot. One interesting result is that the effects of winglets is more significant for section with narrow slot than section with wide slot. Further study is needed to clarify the effects of winglets to rectangular prism.
7. A brief analysis is also carried out as preliminary check for feasibility of using slender deck for long span suspension bridges. However, many important parameters are still need more detail study: the vibration of deck due to vehicle-bridge interaction, fatigue resistance of slender deck, and vibration due to vortex shedding.
8. All the analysis of flow field around the deck in this thesis is based on unsteady pressure characteristics data. Flow visualization is also suggested for future study in order to get better understanding of flow field around the slotted deck section and to confirm the relation of unsteady pressure characteristics to flow field.

# **Appendix A**

## **Cross Section of Deck for Long Span Suspension Bridges**

<p>Storebaelt East Bridge (Denmark)</p>  <p>Finished : 1998 Main span : 1642 m</p>	<p>Deck type : single box girder with fairings</p> <p>Additional countermeasures :</p> <ul style="list-style-type: none"> <li>- Wind screen with 2.4 m height and 50% porosity ratio</li> <li>- Guide vanes</li> </ul> <p>Flutter onset velocity : 70 – 75 m/s</p> <p>B/D : 7.75</p> <p>Weight of deck : 0.40 ton/m<sup>2</sup></p>	<p>1. From the previous experiences of Danish bridges, it was revealed that construction and maintenance costs for box girder are much lower than truss or plate girder (Larsen &amp; Gimsing, 1992). Therefore at the start of Storebaelt bridge design phase, it was decided to concentrate the study on the single box concept for deck section, and only include other options like trusses or twin boxes if it turned out to be impossible to achieve a sufficient aerodynamic stability with the single box. The result of the initial model tests was that several of the box configurations provide adequate aerodynamic stability so other girder options were never studied (Gimsing, 1998).</p> <p>2. During the final phase of construction, large amplitude vibration was observed at relatively low wind speed, 5-10 m/s. Studies and modifications had been made by adding guide vanes at the bottom corner of the deck. These guide vanes improve aerodynamic behaviour and also flutter onset velocity from 69 m/s to 73 m/s (Larsen <i>et al.</i>, 2000)</p>
<p>Akashi Kaikyo Bridge (Japan)</p> 	<p>Deck type : truss girder</p> <p>Additional countermeasures :</p> <ul style="list-style-type: none"> <li>- Grating at shoulder and centre of road</li> <li>- Vertical stabilizer below the grating at road centre</li> </ul> <p>Flutter onset velocity : 80 m/s</p> <p>B/D : 2.5</p>	<p>1. Several findings were concluded during studies and design of this bridge (Miyata <i>et al.</i>, 1992):</p> <ul style="list-style-type: none"> <li>- Single box girder fails to meet the aerodynamic stability requirement</li> <li>- Two box girder deck with narrow slot can meet the stability requirement, but large torsional vortex excitation occurs at low wind speed and also the weight of steel needed is larger than a truss girder.</li> <li>- The longitudinally non-uniform section box girder (bluffer section near the pylon) meet the aerodynamic stability and has economic steel use,</li> </ul>

<p>Finished : 1998 Main span : 1991 m</p>	<p>Weight of deck : 0.85 ton/m<sup>2</sup></p>	<p>but due to construction method consideration the truss girder was selected. 2. From the full bridge wind tunnel tests, it was found that the large torsional displacement must be taken into account to verify the aerodynamic stability. And also it was found that the effect of unsteady aerodynamic drag force is important on flutter instability (Kitagawa, 1998).</p>
<p>Tsing Ma Bridge (Hongkong)</p>  <p>Finished : 1997 Main span : 1377 m</p>	<p>Deck type : double deck truss girder with fairings</p> <p>Additional countermeasures :</p> <ul style="list-style-type: none"> <li>- Vented surface covered with grating on the upper and lower surface</li> <li>- Utilization of double deck provide 'all weather' capability for traffic</li> </ul> <p>Flutter onset velocity : 75 m/s</p> <p>B/D : 5.39</p> <p>Weight of deck : 0.55 ton/m<sup>2</sup></p>	<p>1. From wind tunnel tests, it was found that the wind speed within the lower deck will be kept low, at 40% of external wind speed.</p>
<p>Runyang Bridge (China)</p>	<p>Deck type : single box girder with fairings</p> <p>Additional countermeasures :</p> <ul style="list-style-type: none"> <li>- Central stabilizer</li> </ul>	<p>1. Central stabilizer improves the flutter stability. The improvement is significant from sectional model test, for +3° angle of attack, flutter onset velocity without and with central stabilizer is 50.8 m/s and 64.9 m/s, respectively. But from full bridge model tests, the improvement is not so significant for the</p>

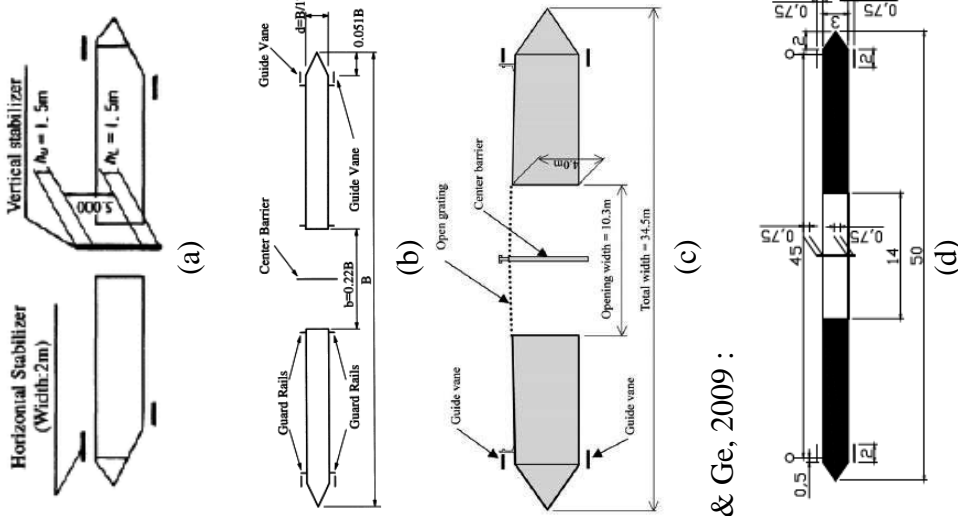
 <p>Finished : 2005</p> <p>Main span : 1490 m</p> <p>Xihoumen Bridge (China)</p>	<p>Flutter onset velocity : 55 m/s</p> <p>B/D : 12.1</p> <p>Weight of deck : -</p>	<p>same case, 52.5 m/s and 55.1 m/s (Ge &amp; Xiang, 2009).</p>
 <p>Finished : 2009</p> <p>Main span : 1650 m</p> <p>Messina Bridge (Italy)</p>	<p>Deck type : twin box girder with fairings and narrow slot <math>b/B = 0.17</math></p> <p>Additional countermeasures :</p> <ul style="list-style-type: none"> <li>- Inboard edges use <math>45^{\circ}</math> chamfer</li> <li>- Position of inspection rail under the bottom slab is optimized</li> </ul> <p>Flutter onset velocity : 89 m/s</p> <p>B/D : 10.6</p> <p>Weight of deck : 0.76 ton/m<sup>2</sup></p> <p>Deck type : triple box girder</p> <p>Additional countermeasures :</p> <ul style="list-style-type: none"> <li>- Aerodynamic dampers</li> <li>- Grid wind screen</li> <li>- Curved inboard edges with trip wire to control</li> </ul>	<p>1. From sectional model tests, it was found that single box girder with central stabilizer can also meet the aerodynamic stability requirement, which is 78 m/s . But the stability is very sensitive to the height of stabilizer for <math>+3^{\circ}</math> angle of attack case (Ge &amp; Xiang, 2009) :</p> <ul style="list-style-type: none"> <li>Single box girder → <math>U_c=48</math> m/s</li> <li>With 1.2 m stabilizer → <math>U_c=37</math> m/s</li> <li>With 1.7 m stabilizer → <math>U_c=43</math> m/s</li> <li>With 2.2 m stabilizer → <math>U_c=88</math> m/s</li> </ul> <p>2. On the other side, twin box girder solution has more consistent stability performance if some variation of the deck detail are made, although improvement also can be achieved with 'tuning' the deck details.</p>
		<p>1. This deck section based from the idea of vented deck and twin deck.</p> <p>2. The excellent aerodynamic performances are results of :</p> <ul style="list-style-type: none"> <li>- Low aerodynamic static coefficient</li> <li>- Low absolute value of important aerodynamic derivatives <math>A_1^*</math> and <math>H_3^*</math> (Matsumoto et al.,</li> </ul>





<p style="text-align: center;">(c)</p> <p style="text-align: center;">(d)</p>	<p>Main span = 5000 m → <math>U_c=67</math> m/s</p> <p>Xiang and Ge (2009) studied deck (d) for suspension bridge with main span 5000 m. They found that minimum flutter onset velocity of 82.9 m is possible.</p>	
<p>Enclosed elliptic deck (Richardson, 1988)</p>	<p>Elliptic tubular deck with 30% thick was proposed to completely protect the traffic at any weather condition, and its large torsional stiffness can eliminate any torsional vibration problems. Also this shape has relatively low drag coefficient.</p>	<p>Matsumoto <i>et al.</i> (1999) reported that ellipse and diamond shape have good aerodynamic performance. Stabilization of ellipse deck due to its low <math>A_J^*</math> derivatives while diamond shape from its low <math>H_3^*</math> derivatives value. Both sections have reduced flutter onset velocity comparable to flat plate section. Keep in mind that their torsional stiffness is very much larger than flat plate, therefore high flutter onset velocity can be expected.</p>
<p>Double pear shaped deck (Richardson, 1988)</p>	<p>If the twin deck and elliptic deck are merged, the result will be a double pear shaped deck. The pear shape is chosen instead of ellipse due to aerodynamic consideration.</p>	<p>Based on qualitative analysis, Richardson believed that this deck will have small pitching moment and thus the torsional frequency can be kept almost constant even in high wind speed. Therefore flutter and torsional divergence can be avoided.</p>

Twin box girder with narrow slot, vertical and horizontal stabilizer (Ueda *et al.*, 1998, Sato *et al.*, 2000, Sato *et al.*, 2002)



Xiang & Ge, 2009 :

Ueda *et al.* (1998) reported that multi-mode flutter analysis of a 2500 m main span bridge using section (a) obtain flutter onset velocity around 80 m/s.

Full model tests and analysis of a 2800 m main span bridge with deck (c) by Public Works Research Institute proved the effectiveness of this concept, flutter onset velocity around 85 m/s was achieved (Sato *et al.*, 2002). Relatively large static deformation was also observed.

Xiang & Ge (2009) adopted this concept by studying deck (d) for a 5000 m suspension bridge. They found that minimum flutter onset velocity 74.7 m is possible.

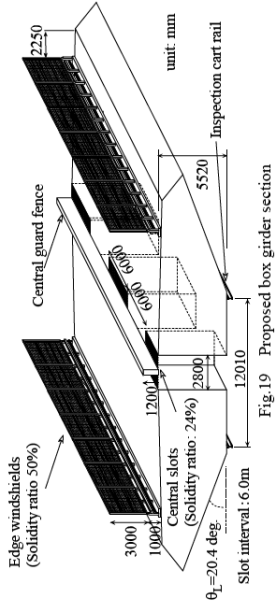
After the completion of Akashi Kaikyo Bridge, Japanese bridge engineers are intensively studying the feasibility of longer span bridge. Although there are several ideas, but most notably is combination of twin girder with narrow slot, vertical stabilizer and horizontal stabilizer.

From aerodynamic derivatives point of view, the stabilization of this deck comes from  $A_1^*$  and  $H_3^*$ . The section has low value of  $A_1^*$  and  $H_3^*$  which favourable for coupled flutter stability.

The mechanism of stabilization is studied by Matsumoto *et al.* (2003) and reported that adding vertical stabilizer at the centre of slot changes the flow field and results different unsteady pressure characteristics distribution. Vertical plate reduces unsteady pressure on upwind girder, and induces phase on downwind girder between  $-180^\circ$  and  $-90^\circ$ . This pattern results low absolute value of  $H_3^*$ .

Ueda *et al.* (1998) showed that adding horizontal stabilizer results lower absolute value of  $A_1^*$ .

Single box girder with narrow slot (Mukarami *et al.*, 2002, Tokoro *et al.*, 2002, Fumoto *et al.*, 2005)



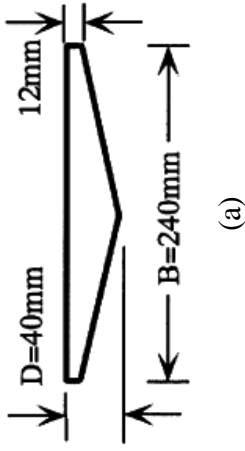
Suspension bridge with main span 2800 m using single box girder section with flutter onset velocity 45 m/s can be improved by combination of several optimized countermeasures, produce deck with flutter onset velocity around 85 m/s.

Intensive studies also conducted by Japanese engineers and researchers under cooperation of PWRI (Public Works Research Institute), HSBA (Honshu Shikoku Bridge Authority) and several private companies. The aim was to find optimization for single box girder so it can be feasible for super long span bridge.

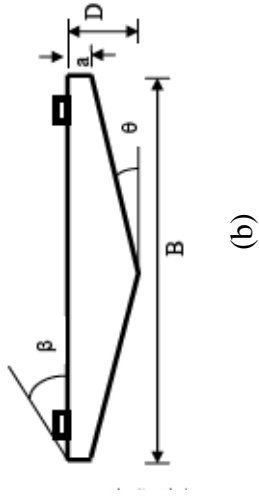
The optimization include several optimized countermeasures :

- Center narrow slot with 6 m interval
- wind shields (50% porosity ratio and 4 m height)
- Central guard fence (block with 1.2 m height)
- Positioning of inspection cart rail
- Slope of inclined lower web (slope value of around 20° was found as optimum)

Triangle box girder (Matsumoto *et al.*, 1997)



Kubo *et al.*, 2007 :



Larsen & Wall, 2012 :



Matsumoto *et al.* (1997) studied the unsteady pressure characteristics distribution of section model (a) with  $B/D=6$ . The results show that this section has comparable flutter onset reduced velocity with thin rectangular plate.

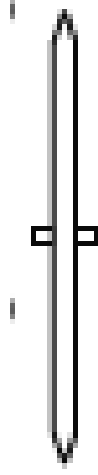
Kubo *et al.* (2007) studied deck (b) with variation of  $\beta$  and lower plate slope  $\theta$ . They found that proper arrangement of  $\beta$  can improve aerodynamic performance, and for small  $\theta$  -which means more streamlined deck- the vortex induced vibration is not observed and flutter onset velocity is relatively high. They also applied this section for a study of 1300 m suspension bridge, with  $\theta=12^\circ$  and  $\beta=27^\circ$ , flutter onset velocity is higher than 77 m/s.

Larsen & Wall (2012) reported that section (c) is one of section that free of vortex shedding vibration.

Triangle section has unique unsteady pressure characteristics pattern :

- On upper surface the distributions are similar with rectangular plate, and the thickness of the side vertical surface might be an important variable.
- On the lower surface, the unsteady pressure are almost constant and have very low value, except a local peak close to leading edge.

Hexagonal plate with vertical plate (Matsumoto *et al.*, 2002 and Matsumoto *et al.*, 2007)



The idea of this deck section is from rectangular plate  $B/D=20$ . Further studies results that countermeasures such as vertical plates and fairings can improve flutter onset velocity more than 200% of basic rectangular plate  $B/D=20$ .

Mechanism of stabilization are :

- control the peak unsteady pressure and phase near leading edge with fairing
- induce new pressure peak on downwind side surface and anti-symmetric phase distributions by installing vertical plates at the centre
- This manipulation results low absolute value of  $H_3^*$

However, the application of this section has to be studied in more detail since it has low torsional stiffness for aerodynamic purpose and low bending stiffness against vertical dead and traffic load.

# Appendix B

## Scientific Production

1. Permata, R., Trein, C. A., Hong, J. W., Shirato, H., *Control of Flutter Stability In The Case of B/D=20 Rectangular Prism by Manipulating Unsteady Pressure Characteristics*, 1<sup>st</sup> Symposium on Flutter, 2011, Tokyo, Japan.
2. Permata, R., Trein, C. A., Hong, J. W., Shirato, H., *Effects of Fairings and Vertical Plates on Unsteady Pressure Characteristics and Flutter Stability of B/D=20 Rectangular Prism*, 24<sup>th</sup> KKCNN Symposium on Civil Engineering, 2011, Hyogo, Japan.
3. Hong, J. W., Yonamine, K., Permata, R., Shirato, H., *Study of Stabilization Against Coupled Flutter Using Combination of Cylindrical Members*, 24<sup>th</sup> KKCNN Symposium on Civil Engineering, 2011, Hyogo, Japan.
4. Permata, R., Yonamine, K., Hattori, H., Shirato, H., *Effects of Double Slot to Unsteady Pressure Characteristics and Flutter Stability of B/D=20 Rectangular Prism*, 25<sup>th</sup> KKCNN Symposium on Civil Engineering, 2012, Busan, Korea.
5. Permata, R., Yonamine, K., Hattori, H., Shirato, H., *Use of Double Slot as Countermeasure Against Coupled Flutter Instability of Bridge Deck*, 62<sup>nd</sup> National Conference on Theoretical and Applied Mechanics, 2013, Tokyo, Japan.
6. Permata, R., Yonamine, K., Hattori, H., Shirato, H., *Use of Double Slot as Countermeasure Against Coupled Flutter Instability of Bridge Deck*, 12<sup>th</sup> Americas Conference on Wind Engineering (12ACWE), 2013, Seattle, Washington, USA.
7. Permata, R., Yonamine, K., Hattori, H., Shirato, H., *Aerodynamics and Flutter Stability of Slender Bridge Deck with Double Slot and Porous Cavity*, 6<sup>th</sup> Civil Engineering Conference in Asia Region (CECAR6), 2013, Jakarta, Indonesia.
8. Permata, R., Hattori, H., Shirato, H., *Feasibility and Behavior of Long Span Suspension Bridges with Slender Deck*, 6<sup>th</sup> Civil Engineering Conference in Asia Region (CECAR6), 2013, Jakarta, Indonesia.
9. Permata, R., Essen, D., *Static Analysis of Suspension Bridges Under Gravity Load*, 6<sup>th</sup> Civil Engineering Conference in Asia Region (CECAR6), 2013, Jakarta, Indonesia.
10. Permata, R., Zain, M. R. M., Hattori, H., Shirato, H., *Flutter Stabilization of Slender Bridge Deck Section Using Combination of Double Slot with Fairings and Winglets*, 8<sup>th</sup> Asia-Pacific Conference on Wind Engineering (APCWE8), 2013, Chennai, India.